

Quantum Monte Carlo calculations with chiral effective field theory interactions

Quanten-Monte-Carlo-Rechnungen mit Wechselwirkungen basierend auf chiraler effektiver Feldtheorie

Zur Erlangung des Grades eines Doktors der Naturwissenschaften (Dr. rer. nat.)

genehmigte Dissertation von M.Sc. Ingo Tews aus Greifswald

Tag der Einreichung: 14.07.2015, Tag der Prüfung: 12.10.2015

2015 — Darmstadt — D 17

1. Gutachten: Prof. Ph.D. Achim Schwenk

2. Gutachten: Prof. Dr. Hans-Werner Hammer



TECHNISCHE
UNIVERSITÄT
DARMSTADT

Fachbereich Physik
Institut für Kernphysik
Theory Center

Quantum Monte Carlo calculations with chiral effective field theory interactions
Quanten-Monte-Carlo-Rechnungen mit Wechselwirkungen basierend auf chiraler effektiver Feldtheorie

Genehmigte Dissertation von M.Sc. Ingo Tews aus Greifswald

1. Gutachten: Prof. Ph.D. Achim Schwenk
2. Gutachten: Prof. Dr. Hans-Werner Hammer

Tag der Einreichung: 14.07.2015

Tag der Prüfung: 12.10.2015

2015 — Darmstadt — D 17

Bitte zitieren Sie dieses Dokument als:

URN: urn:nbn:de:tuda-tuprints-50110

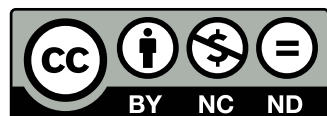
URL: <http://tuprints.ulb.tu-darmstadt.de/5011>

Dieses Dokument wird bereitgestellt von tuprints,

E-Publishing-Service der TU Darmstadt

<http://tuprints.ulb.tu-darmstadt.de>

tuprints@ulb.tu-darmstadt.de



Die Veröffentlichung steht unter folgender Creative Commons Lizenz:

Namensnennung – Keine kommerzielle Nutzung – Keine Bearbeitung 3.0 Deutschland

<http://creativecommons.org/licenses/by-nc-nd/3.0/de/>

Abstract

The neutron-matter equation of state connects several physical systems over a wide density range, from cold atomic gases in the unitary limit at low densities, to neutron-rich nuclei at intermediate densities, up to neutron stars which reach supranuclear densities in their core. An accurate description of the neutron-matter equation of state is therefore crucial to describe these systems. To calculate the neutron-matter equation of state reliably, precise many-body methods in combination with a systematic theory for nuclear forces are needed. Chiral effective field theory (EFT) is such a theory. It provides a systematic framework for the description of low-energy hadronic interactions and enables calculations with controlled theoretical uncertainties. Chiral EFT makes use of a momentum-space expansion of nuclear forces based on the symmetries of Quantum Chromodynamics, which is the fundamental theory of strong interactions. In chiral EFT, the description of nuclear forces can be systematically improved by going to higher orders in the chiral expansion. On the other hand, continuum Quantum Monte Carlo (QMC) methods are among the most precise many-body methods available to study strongly interacting systems at finite densities. They treat the Schrödinger equation as a diffusion equation in imaginary time and project out the ground-state wave function of the system starting from a trial wave function by propagating the system in imaginary time. To perform this propagation, continuum QMC methods require as input local interactions. However, chiral EFT, which is naturally formulated in momentum space, contains several sources of nonlocality.

In this Thesis, we show how to construct local chiral two-nucleon (NN) and three-nucleon (3N) interactions and discuss results of first QMC calculations for pure neutron systems. We have performed systematic auxiliary-field diffusion Monte Carlo (AFDMC) calculations for neutron matter using local chiral NN interactions. By comparing these results with many-body perturbation theory (MBPT), we can study the perturbative convergence of local chiral interactions. We have shown that soft, low-cutoff potentials converge well and can be reliably used in MBPT, while harder potentials are less perturbative and have to be treated within AFDMC. We have also derived consistent local chiral 3N interactions and study these forces in detail. Our results show that local regulators lead to less repulsion from 3N forces compared to nonlocal 3N forces. Finally, we present the neutron-matter equation of state based on local chiral NN and 3N interactions using the AFDMC method as well as results for light nuclei and neutron drops. This work paves the way for systematic QMC calculations with chiral EFT interactions for nuclei and nucleonic matter.

Zusammenfassung

Die Zustandsgleichung für Neutronenmaterie verbindet verschiedene physikalische Systeme über einen weiten Dichtebereich, von kalten atomaren Gasen im unitären Grenzfall bei geringen Dichten, über neutronenreiche Kerne bei mittleren Dichten, bis hin zu Neutronensternen, in deren Innern supranukleare Dichten erreicht werden. Eine akkurate Beschreibung der Zustandsgleichung für Neutronenmaterie ist daher entscheidend für die Beschreibung dieser Systeme. Um die Zustandsgleichung für Neutronenmaterie verlässlich zu berechnen, werden präzise Vielteilchenmethoden in Verbindung mit einer systematischen Theorie der Kernkräfte benötigt. Die chirale effektive Feldtheorie (EFT) ist eine solche Theorie. Sie ermöglicht eine systematische Beschreibung von hadronischen Wechselwirkungen bei kleinen Energien mit kontrollierten theoretischen Unsicherheiten. In chiraler EFT wird eine Impulsraumentwicklung der Kernkräfte benutzt, die auf den Symmetrien der Quantenchromodynamik, der fundamentalen Theorie der starken Wechselwirkung, basiert. Die Beschreibung der Kernkräfte in chiraler EFT kann systematisch verbessert werden, indem man höhere Ordnungen in der chiralen Entwicklung berücksichtigt. Kontinuums-Quanten-Monte-Carlo-Methoden (QMC) gehören zu den präzisen Vielteilchenmethoden, die zur Beschreibung stark wechselwirkender Systeme bei endlichen Dichten zur Verfügung stehen. Diese Methoden behandeln die Schrödingergleichung als Diffusionsgleichung in imaginärer Zeit. Durch Entwicklung des Systems in imaginärer Zeit wird die Grundzustandswellenfunktion aus einer Startwellenfunktion heraus projiziert. Für diese Entwicklung benötigen Kontinuums-QMC-Methoden lokale Wechselwirkungen. Chirale EFT ist jedoch im Impulsraum formuliert und enthält daher verschiedene Nichtlokalitäten.

In dieser Dissertation wird gezeigt, wie man lokale chirale Zwei- (NN) und Dreiteilchen-Wechselwirkungen (3N) konstruieren kann. Systematische Auxiliary-Field-Diffusion-Monte-Carlo-Rechnungen (AFDMC) für reine Neutronenmaterie basierend auf den neuen lokalen chiralen NN-Wechselwirkungen werden durchgeführt und die Ergebnisse dieser QMC-Rechnungen diskutiert. Durch Vergleich dieser Ergebnisse mit Vielteilchen-Störungstheorie (MBPT) kann die perturbative Konvergenz der lokalen chiralen Wechselwirkungen untersucht werden. Es wird gezeigt, dass weiche Potenziale mit kleinen Cutoffs gut konvergieren und verlässlich in MBPT verwendet werden können, während harte Potentiale weniger perturbativ sind und mit Hilfe der AFDMC-Methode studiert werden können. Es werden auch konsistente lokale chirale 3N-Kräfte hergeleitet und detailliert untersucht. Die Ergebnisse zeigen, dass lokale 3N-Regulatoren zu geringerer Repulsion, verglichen mit nicht-lokalen 3N-Regulatoren, führen. Schließlich werden die Zustandsgleichung für Neutronenmaterie mit chiralen NN- und 3N-Kräften, die mit der AFDMC-Methode berechnet wurde, sowie Ergebnisse für leichte Kerne und Neutronentropfen präsentiert. Diese Arbeit schafft die Grundlage für systematische QMC-Rechnungen mit chiralen Wechselwirkungen für Kerne und Kernmaterie.

Contents

1	Introduction	7
1.1	Motivation	7
1.2	Neutron-rich systems	10
1.2.1	Neutron stars	10
1.2.1.1	Formation of neutron stars	12
1.2.1.2	Neutron-star modeling, equation of state, and mass-radius relation	13
1.2.1.3	Observations of neutron stars	17
1.2.2	Neutron-rich nuclei	22
1.2.2.1	Neutron-rich nuclei and nucleosynthesis	24
1.2.2.2	Nuclear matter and symmetry energy	27
1.2.2.3	Neutron-matter equation of state and neutron skins	28
1.2.3	Ultracold atoms	29
1.2.3.1	Universality	30
1.2.3.2	Neutron-matter equation of state and ultracold atoms	31
2	Chiral effective field theory for nuclear forces	33
2.1	Quantum chromodynamics	33
2.1.1	Chiral symmetry	34
2.1.2	QCD calculations for neutron matter	35
2.2	Chiral effective field theory for QCD at low energies	37
2.2.1	Basic principles	37
2.2.2	Pionless effective field theory	38
2.2.3	Chiral effective field theory	39
2.2.4	Two-nucleon interactions up to $N^3\text{LO}$	41
2.2.5	Three-nucleon interactions up to $N^3\text{LO}$	46
2.3	Results with chiral EFT interactions	49
2.3.1	Many-body perturbation theory	50
2.3.2	Ab initio results	53
2.3.3	Motivation for nonperturbative benchmarks	55
3	Quantum Monte Carlo	57
3.1	Basic principles	57
3.1.1	Green's function Monte Carlo	59
3.1.2	Auxiliary-field diffusion Monte Carlo	60
3.2	Quantum Monte Carlo results with phenomenological interactions	63
3.2.1	Phenomenological interactions	63
3.2.1.1	Two-nucleon interactions	64
3.2.1.2	Three-nucleon interactions	65
3.2.1.3	Problems of phenomenological interactions	65

3.2.2	Light nuclei	66
3.2.3	Neutron matter and neutron stars	66
3.2.4	Ultracold atoms	67
3.3	Motivation for Quantum Monte Carlo with chiral EFT interactions	68
4	Local chiral NN interactions	71
4.1	Nonlocalities in chiral interactions and strategies for their removal	71
4.2	Derivation of local chiral NN interaction	72
4.2.1	Leading order	72
4.2.2	Next-to-leading order	73
4.2.3	Next-to-next-to-leading order	75
4.2.4	Next-to-next-to-next-to-leading order	75
4.2.5	Regularization and fits of low-energy couplings	76
4.2.6	Phase shifts	79
4.2.7	Deuteron properties	81
5	Quantum Monte Carlo calculations with chiral EFT NN interactions	87
5.1	Neutron matter	87
5.2	Nonperturbative validation of MBPT calculations for soft chiral interactions	91
5.3	Light nuclei	93
5.4	Summary of main results	94
6	Chiral three-body forces for Quantum Monte Carlo calculations	95
6.1	Derivation of local chiral 3N forces	95
6.1.1	Two-pion-exchange interaction V_C	96
6.1.2	One-pion-exchange–contact interaction V_D	98
6.1.3	Three-body contact interaction V_E	98
6.1.4	Regularization of coordinate space 3N interactions	99
6.2	Implementation in Quantum Monte Carlo	99
6.3	Fits of c_D and c_E	105
6.4	Local chiral 3N forces in neutron matter	107
6.5	Local regulators	111
7	Results at N^2LO with local chiral NN and 3N interactions	117
7.1	Equation of state of neutron matter using AFDMC	117
7.2	Variation of the c_i couplings	119
7.3	Light nuclei	120
7.4	Neutron drops	121
8	Summary and outlook	125
A	Fourier transformation of contact interactions	129
B	Partial-wave-decomposed contact interactions	131
C	Two-body matrix elements for MBPT calculations in pure neutron matter	133

D	Fourier transformation of chiral momentum-space 3N forces	137
D.1	Two-pion-exchange interaction V_C	137
D.1.1	$V_C^{c_1}$	137
D.1.2	$V_C^{c_3}$	138
D.1.3	$V_C^{c_4}$	141
D.2	One-pion-exchange–contact interaction V_D	143
E	Fourier transformation of local coordinate-space 3N forces to momentum space	145
	Bibliography	149



1 Introduction

1.1 Motivation

Neutron stars are astrophysical objects of extremes. They contain the largest reservoirs of degenerate fermions, reaching the highest densities we can observe in the cosmos, up to $\sim 10^{15}$ g/cm³ in their core. Neutron stars have typical masses of 1.4 solar masses (M_{\odot}) [1]. However, only recently the two heaviest $2M_{\odot}$ neutron stars have been observed [2, 3] and their masses were determined with a high precision of $\pm 0.04M_{\odot}$. On the other hand, neutron-star radii are so far not determined due to observational difficulties [4]. They are estimated to be 10-15 km [1, 5]. Moreover, there is no neutron star of which we know both mass and radius simultaneously.

The determination of the relation between neutron-star masses and the corresponding radius is an open and fascinating problem of nuclear astrophysics. This so-called mass-radius relation is uniquely fixed by the equation of state (EoS), which links the pressure inside the neutron star with the density of neutron-star matter. The equation of state of neutron stars is mainly governed by the strong interaction and includes many physical effects over a wide density range. Among those are fascinating phenomena like nucleon superfluidity [6], hyperons [7], meson condensates [8, 9, 10], or even possible quark matter in the core [7].

After their creation, neutron stars cool down by emitting neutrinos. In the later stage of their life, because of the high densities, or high Fermi momenta, of the nucleons, neutron-star matter can be assumed as cold $T = 0$ matter and thermal effects are then only a small correction. This simplifies modeling the EoS of neutron stars and makes them an ideal and exciting testing ground for predictions of strongly interacting matter. These predictions have to be tested against astronomical observations of neutron stars to discriminate between different models for the EoS. The neutron-star mass-radius relation has been studied in many works, e.g., using the liquid drop model [11], using relativistic mean-field models [12, 13, 14, 15] or with phenomenological potential models [16]. All of these calculations are based on different models for nuclear interactions that bind neutrons and protons together and lead to a large span in the mass-radius prediction of neutron stars, ranging for a typical $1.4M_{\odot}$ neutron star from 9 – 15 km, see Refs. [5, 17, 18] and references therein. In this Thesis, we will present a way of improving the theoretical predictions for the equation of state of neutron matter, making better predictions of the neutron-star mass-radius relation possible.

In addition, in certain density regimes, various properties of neutron matter can be tested in the laboratories on Earth. For example, neutron matter at low densities can be probed in experiments with ultracold atoms [19, 20, 21, 22, 23, 24, 25, 26] while matter at higher densities can be probed in the heavy ion collisions experiments [27].

At the low-density side, in experiments with ultracold atoms around a Feshbach resonance [20], the parameters of the atomic interaction can be tuned to resemble neutron-neutron interactions. The cold atomic system then behaves like neutron matter at very low densities and provides a possible test for theories of strongly interacting fermions in this regime. A well-known problem for these ultracold systems is the question of the ground-state properties of this many-body

system composed of spin-1/2 fermions interacting via a zero-range, infinite scattering length contact interaction. These properties are all described by universal parameters, such as the Bertsch parameter for the energy per particle, and a lot of theoretical and experimental effort has been put into its determination, see Ref. [28] and references therein.

Besides neutron stars, different models for the strong interaction can be tested in experiments with nuclei. An interesting region are neutron-rich nuclei which are relevant for nucleosynthesis and the creation of elements heavier than iron [29, 30] as well as for modeling of neutron-star crusts [31]. These nuclei are unstable on earth but can be experimentally created with much effort. To explain the solar abundance pattern of elements [32, 33] accurate information on, e.g., half-lives and binding energies of these nuclei is needed.

Due to the difficulties creating these nuclei on earth, there exists only few experimental data for many of them, and our knowledge is mostly based on theoretical predictions. In some cases, these predictions are tested against experiment, see, e.g., the recent work on calcium isotopes [34]. Moving away from nuclear stability, the spread of theoretical predictions grows [35]. Improved nuclear Hamiltonians in combination with accurate many-body methods are needed to obtain controlled theoretical error estimates, which allow for reliable extrapolations into unknown regions of the nuclear chart. This work will enable accurate calculations of light nuclei and provides a basis of calculations of heavier neutron-rich nuclei with controlled theoretical uncertainties.

The key aspect of modern nuclear physics is to gain a better understanding of nuclear forces, a challenge for both experimental and theoretical physics. As shown above, a very fascinating and important ingredient of matter are neutrons: Neutron-rich matter makes up neutron stars, neutron-rich nuclei are key for the creation of all elements in the cosmos, and neutron matter at low densities can be probed in fascinating experiments with ultracold atoms. Nuclear interactions connect these different physical systems in different density regimes. By increasing our knowledge of one system, we can improve our understanding of nuclear forces and also increase our understanding of the other systems.

As mentioned, many different models for nuclear interactions have been suggested. These models have been fit to reproduce certain physical observables, however, they often have certain disadvantages: first, they are created *ad hoc* and cannot be linked to the fundamental theory, Quantum Chromodynamics (QCD). Second, they do not provide a means of assessing the importance of different contributions and, thus, no systematic way of improvement. As a result, they do not allow the estimation of reliable theoretical uncertainties.

One possible framework, which does not suffer from these disadvantages, is chiral effective field theory (EFT), see Refs. [36, 37] for recent review articles. Chiral EFT provides a systematically improvable way of describing low-energy nuclear interactions and is based on the symmetries of QCD. Chiral EFT has been extensively and successfully applied in calculations of the structure and reactions of light nuclei [38, 39, 40, 41, 42], medium-mass nuclei [34, 43, 44, 45, 46, 47, 48, 49, 50, 51], and nucleonic matter [52, 53, 54, 55, 56, 57, 58]. In these calculations, nucleon-nucleon (NN) potentials at next-to-next-to-next-to-leading order (N^3LO) [59, 60] in chiral EFT have been found to give accurate results. In addition to these NN forces, chiral EFT also predicts many body forces. These are key for a correct description of physical observables [34, 39, 41, 42, 43, 48, 49, 50, 51, 61].

The theoretical uncertainties of the state-of-the art calculations of neutron-rich systems with chiral EFT interactions originate from several sources: the many-body Hamiltonian and the many-body method, which is used to study the system. The dominant uncertainty stemming

from the many-body Hamiltonian in the theoretical calculations at present are three-nucleon (3N) forces, see Refs. [38, 62].

Regarding the second point, there is a range of many-body methods available to study nuclear or neutron-rich systems, one of which is many-body perturbation theory (MBPT). Some of the state-of-the-art results with chiral EFT interactions are obtained in MBPT, and it has been shown in neutron matter calculations including all chiral forces up to $N^3\text{LO}$ [57] that a sizeable contribution to the theoretical uncertainty of the calculation originates from the many-body method. Furthermore, a validation of the perturbative convergence of MBPT calculations is needed to assess the quality of those calculations.

A very powerful family of many-body methods are continuum quantum Monte Carlo (QMC) methods, which are very precise for strongly interacting systems [63, 64, 65], including neutron matter [16, 23, 66, 67, 68], and have been successfully used to study light nuclei in pioneering calculations [69, 70]. Furthermore, Quantum Monte Carlo methods have been employed to study cold atomic gases or electronic systems [64, 71, 72].

The standard QMC approach used in the study of light nuclei properties [69], including scattering [73], is the nuclear Green's Function Monte Carlo (GFMC) method. To solve the many-body Schrödinger equation, the integration over the particle coordinates is performed stochastically in nuclear GFMC while summations in spin-isospin space [74, 75] are performed explicitly. As a result, the method is very accurate but computationally very costly and allows one to access only nuclei with $A \leq 12$ [70, 76]. Larger particle numbers can be accessed with auxiliary-field Diffusion Monte Carlo (AFDMC), which in addition to the stochastic approach to the particle coordinates also stochastically evaluates the summations in spin-isospin space [77]. However, the cost is that one uses simpler variational wave functions than those used in nuclear GFMC. The uncertainty of the QMC methods reduces statistically with the number of simulations and, thus, is smaller than the uncertainty of an MBPT calculation.

QMC methods, however, require as an input local interactions to easily sample the many-body propagator and, thus, have not been used with chiral EFT interactions due to nonlocalities in their present implementation in momentum space. The available versions of the chiral potentials are nonlocal because they employ both nonlocal regularizations in momentum space and nonlocal contact interactions. This makes them not suitable for the QMC family of methods. It would be a milestone to use chiral interactions in this nonperturbative many-body method to produce nonperturbative benchmarks for the systems described above. This would allow for a direct comparison with perturbative methods using the same Hamiltonian to assess the quality of different methods and previous results.

In this Thesis, we show how to include chiral NN and 3N interactions into QMC calculations. This will combine the accuracy of QMC methods with the systematic chiral EFT expansion, and will allow for high-precision calculations of neutron matter for astrophysical applications and of light nuclei, where the theoretical uncertainty of the many-body method is small. The results will be compared to current state-of-the-art calculations. Furthermore, this work opens up nonperturbative benchmarks of nuclear matter and nuclei for astrophysics, including studies of hyperons, based on chiral EFT, as well as the matching to the underlying theory of QCD through lattice simulations.

This Thesis is structured as follows: In this Chapter, we will motivate the different physical systems of interest for this work and explain the foundations of chiral EFT in the next Chapter. Furthermore, we will present the current results for different systems using chiral EFT interactions. In Chapter 3, we will present the basic principles of the QMC methods used in this work,

GFMC and AFDMC, and present the recent status of QMC calculations for the physical systems of interest using phenomenological interactions.

In Chapter 4, we will explain how to remove all sources of nonlocality in chiral EFT NN interactions to next-to-next-to-leading order (N^2 LO) based on the work of Ref. [78]. We will present improved local nucleon-nucleon (NN) interactions at leading-order (LO), next-to-leading order (NLO), and N^2 LO. We also show results for phase shifts and deuteron properties. In Chapter 5, we will use the developed chiral NN potentials in QMC calculations to study the neutron matter equation of state up to nuclear densities at different chiral orders with systematic theoretical uncertainties, as well as light nuclei. We will compare our AFDMC simulations of neutron matter to MBPT calculations using the same Hamiltonian, to study the perturbativeness of the interactions.

In Chapter 6, we will show how to additionally include the leading chiral 3N forces into our simulations. These forces are key for the correct reproduction of physical observables. We will show how to fit the low-energy couplings (LECs) accompanying these forces and study the influence of the regulator function on the results for neutron matter. In Chapter 7, we will present results for the full chiral N^2 LO Hamiltonian, including NN and 3N forces, on the equation of state of neutron matter, light nuclei and neutron drops.

1.2 Neutron-rich systems

As stated before, neutron-rich systems are exciting physical systems because they occur naturally in a variety of length scales and densities. Neutron-rich matter is the main building block of neutron stars, which are a final stage of stellar evolution and are born in supernova explosions. Inside of neutron stars the neutron-rich matter is probed at densities of up to several times nuclear saturation density, $n_0 = 0.16 \text{ fm}^{-3} \sim 2.7 \cdot 10^{14} \text{ gcm}^{-3}$. Neutron stars are macroscopic objects, bound by gravitation. We will describe the main properties of neutron star in Sec. 1.2.1. At intermediate densities, neutron-rich nuclei are a current frontier in nuclear physics. They are key for the understanding of the r-process. Currently, many efforts are made to extend the experimental knowledge of these nuclei, e.g., in the future FAIR facility in Darmstadt, Germany, as well as at RIBF at RIKEN, Japan, and the future FRIB facility in Michigan, USA. Neutron-rich nuclei will be subject in Sect. 1.2.2.

At very low densities, pure neutron matter exhibits universality and can be probed in experiments with ultracold atoms. Pioneering experiments have been performed at several institutions worldwide, like Duke, MIT, Rice and more [19, 20, 21, 22, 23, 24, 25]. We will introduce neutron-matter at low densities and ultracold atoms in Sec. 1.2.3.

Because of its connections to ultracold atoms and its importance for the physics of neutron-rich nuclei, neutron stars, and supernovae, neutron matter constitutes an exciting system to study. It furthermore offers an ideal testing ground for many-body methods and nuclear forces and serves as *ab initio* input to energy density functionals [16, 23, 56, 79, 80, 81].

1.2.1 Neutron stars

Neutron stars represent one of the final stages in the stellar evolution. Stars with a mass smaller than approximately $10M_\odot$ will become white dwarfs at the end of their life. Very heavy stars with masses larger than $25M_\odot$ will collapse to Black Holes. Medium mass stars will transform into neutron stars.

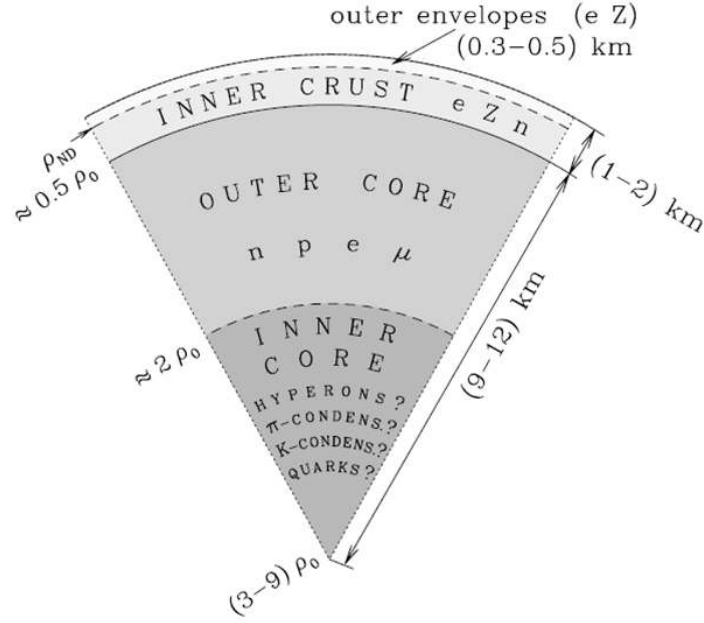


Figure 1.1: Neutron-star structure taken from Ref. [86].

Stars heavier than white dwarfs were already postulated in 1931 by Lev Landau [82], and with the discovery of the neutron by Chadwick in 1932 [83], the idea of neutron stars as the final product of supernova explosions was proposed by Baade and Zwicky [84]. However, until the 1960s, no observational evidence for their existence was found. In 1967 Hewish und Bell discovered a pulsed radio signal with a period of 1.337 s [85]. The signal was identified as being a pulsar, a rapidly rotating neutron star with a strong magnetic field. Since then, many more neutron stars have been discovered, some of them in very interesting binary star systems.

Neutron stars mainly consist of neutrons, whose β decay is blocked due to very high electron chemical potential. They are stabilized against the gravitational collapse due to the degeneracy pressure of neutrons and strong interactions, but are bound by the gravitational force and not by the strong interaction.

Neutron stars have typical masses of $1 - 2M_{\odot}$ with a radius of about $10 - 14$ km [4, 17]. They reach very high densities in their interior, up to several times nuclear saturation density in their core, and are an ideal testing ground for theories of the strong interaction in the cold high-density regime, which is not accessible in Earth's laboratories.

Neutron stars can have very large magnetic fields of $10^{12} - 10^{13}$ G, and can rotate very fast [7]. Since rotating magnetic fields emit radiation along the magnetic field lines, rotating neutron stars resemble giant light houses emitting radio signals along cones at the magnetic north and south pole. If these cones touch the Earth, we can observe the very precisely timed signals with radio telescopes. These neutron stars are pulsars and almost all neutron-star observations have been made with them.

Neutron stars are structured in several layers, which can be seen in Fig. 1.1. The outermost layer, the neutron-star atmosphere, is very thin, up to a few centimeters or even less. It is most likely composed of hydrogen or helium and emits the radiation which can then be observed by Earth's telescopes.

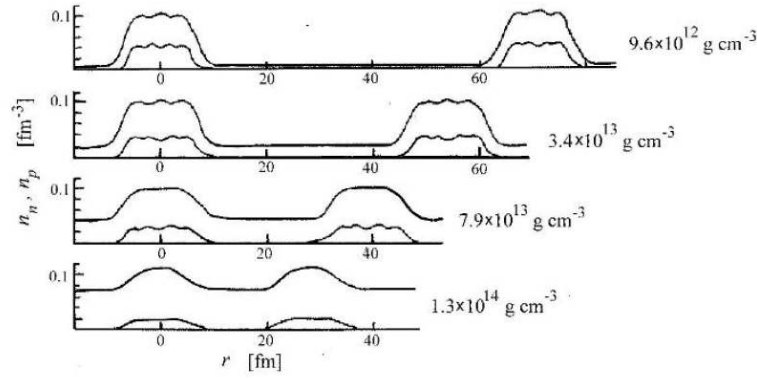


Figure 1.2: Neutron and proton density profiles at several average densities ρ from Ref. [86].

The next layer is the outer crust or envelope, which is several hundred meters thick and contains neutron-rich nuclei of the iron region. When going deeper into the neutron star, the density and, as a consequence, the electron chemical potential increases. This induces electron captures by protons and the nuclei become more and more neutron rich. The outer crust ends, when the density is high enough for neutrons to drip out of the nuclei (neutron-drip). At this density, the electron chemical potential is high enough to block neutron β -decay and neutrons can exist freely in between the nuclei. This neutron-drip density marks the begin of the inner crust.

Deeper in the neutron star, the neutron density in between the nuclei will increase and there will be less and less nuclei. This is visualized in Fig.1.2, where the proton and neutron density profiles are shown at several average densities. In total the crust is about 1 km thick.

At roughly $n \approx 0.5n_0$, all nuclei are dissolved and the matter is in β equilibrium, consisting of free neutrons with a small admixture of protons, electrons, and possibly muons. This region is called outer core and extends to densities of $\approx 2n_0$. Deeper inside the neutron star, in the inner core, the densities can increase up to $10n_0$. It is possible, that new phases of matter may appear, like pion- or kaon-condensates, hyperons, or even quark matter [7, 8, 9, 10].

In the following, we briefly sketch the formation of neutron stars, explain the equation of state of neutron stars and their mass-radius relation and give details on neutron-star observations.

1.2.1.1 Formation of neutron stars

Neutron stars are mostly made in type-II (core-collapse) supernova explosions of medium mass stars with masses between approximately $10M_\odot < M < 25M_\odot$. During the stellar lifetime, all stars process hydrogen into heavier elements in stellar burning cycles in their cores. The stellar burning processes stabilize the star against gravitational collapse. During the hydrogen burning, the largest cycle in the star's lifetime, helium is created in the core. The further life of a star after the hydrogen burning is determined, among others, by the star's total mass.

Stars below $10M_\odot$ will transform into white dwarfs. Most commonly, these stars undergo another burning cycle in their core, the helium burning, where helium is processed to carbon and oxygen. In this phase, hydrogen burning will continue in the star's shell, leading to the star becoming a red giant. In the end of this process, the star will eject its outer layers, and a carbon-oxygen white dwarf will remain. For lower mass stars, also helium white dwarfs can form, if the star's mass is insufficient to support helium burning. Heavier stars may undergo additional burning phases, creating neon or magnesium white dwarfs.

White dwarfs are stabilized against gravitational collapse due to the degeneracy pressure of the electrons in their interior. This pressure is only sufficient to stabilize stars of a certain maximum mass, the so-called Chandrasekhar mass [87]. The Chandrasekhar limit depends on the composition of the star and is typically around $1.4M_{\odot}$.

If the star's mass is higher than $10M_{\odot}$, the star's core temperatures will enable many more fusion processes, like helium burning, then carbon, neon, oxygen, and silicon burning, consequently, until elements around the iron peak are created. These are the heaviest elements which can be created in stellar burning, because fusion processes of these elements are no longer energetically favorable and the Coulomb barriers of these nuclei prevent further fusion processes. These heaviest elements made in stellar burning are collected in the star's center. A typical star in this stage has an iron core, surrounded by several layers in different stellar burning cycles. The closest layer to the core is the one with silicon burning, where the fusion product will add up to the mass of the white-dwarf core.

When the core's mass exceeds the Chandrasekhar limit, the electrons cannot support it against gravitational collapse. The core then collapses and its density increases very fast. During the collapse, the proton fraction decreases, with increasing density leading to higher electron chemical potential. Protons will capture electrons to form neutrons. The incompressibility of nuclear matter stops the collapse and a proto-neutron star is formed.

The infalling matter from the star bounces off the proto-neutron star and creates an outbound shockwave. This shockwave is very energetic and dissociates the nuclei in the star's material, forming optimal conditions for nucleosynthesis processes. The shockwave loses energy and, according to 1D and 2D supernova simulations, may stall, but is most likely reenergized by neutrinos [88, 89].

The resulting explosion pushes the star's outer layers into space and a hot proto-neutron star remains. This whole process is called core-collapse supernova. The neutron star then cools via neutrino emission. Neutron stars absorb a large part of the angular momentum and the magnetic field of the initial star and, thus, can have strong magnetic fields and high rotation frequencies, and can be detected by their emitted radio signals.

Since neutron stars are stabilized by the neutron degeneracy pressure and the strong interaction, they also have a maximum mass they can support against gravitational collapse, see Sec. 1.2.1.2. This mass is not known, but it is larger than $2M_{\odot}$, see Sec. 1.2.1.3. If the initial star is too massive, the collapsing core overcomes this maximum neutron-star mass, and the collapse of the star proceeds until a black hole is formed.

Aside from core-collapse supernovae, neutron stars can also be formed due to a collapse of an accreting white dwarf in a binary system. This event happens, when the white dwarf's mass surpasses the Chandrasekhar limit. However, this mechanism occurs rarely, as white dwarfs close to the Chandrasekhar limit are undergoing a Type Ia supernovae [86].

1.2.1.2 Neutron-star modeling, equation of state, and mass-radius relation

Neutron-star modeling differs from the description of other stellar objects because effects of general relativity become very important. A parameter measuring this importance is the compactness parameter R_S/R with the Schwarzschild radius $R_S = 2MG/c^2$, where M is the star's mass and G the gravitational constant. While this parameter is only about $4 \cdot 10^{-6}$ for the sun, which makes a general relativistic treatment negligible, the parameter is about $0.2 - 0.4$ for

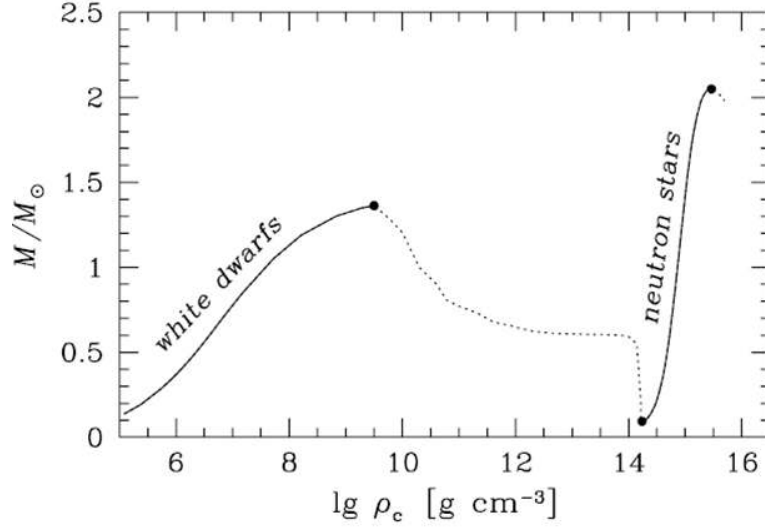


Figure 1.3: Stellar masses vs. central densities from Ref. [86]. In the picture, two stable regimes for stellar models can be seen: white dwarfs, which have small central densities, and neutron stars with larger central densities.

typical neutron stars. Thus, neutron stars are relativistic objects and have to be treated in the framework of general relativity.

The fundamental equations describing a spherically symmetric, hydrostatic body made of isotropic material in the framework of general relativity are the Tolman-Oppenheimer-Volkoff (TOV) equations. The equations relate pressure P , energy density $\varepsilon = \rho + E/V$, mass and the radius and were derived independently by Tolman and Oppenheimer and Volkoff in 1939 [90, 91]. They are given by

$$\frac{dP}{dr} = -\frac{Gm(r)\varepsilon(r)}{r^2} \left(1 + \frac{P(r)}{\varepsilon(r)c^2}\right) \left(1 + \frac{4\pi P(r)r^3}{m(r)c^2}\right) \left(1 - \frac{2Gm(r)}{c^2 r}\right)^{-1}, \quad (1.1)$$

$$\frac{dm}{dr} = 4\pi r^2 \varepsilon(r). \quad (1.2)$$

These equations are valid only for static objects and have to be modified for rotating objects. This effect becomes important for millisecond pulsars. In the following, we will only treat static objects. This is a good approximation for typical neutron stars with a rotational period of ~ 1 s or larger. For fast rotating neutron stars, the pressure in the neutron star will be modified as matter is driven outwards, allowing for heavier stellar objects.

If additionally a relation between P and ε is known, these coupled equations can be solved. This link is the equation of state (EoS) $P = P(\varepsilon, T)$. In neutron stars, although $T \sim 10^8 K$, matter can be assumed to be at $T = 0$, because the thermal energy of ~ 10 keV is small compared to the kinetic and interaction energy of the neutrons, which is several MeV. Thus, $P = P(\rho)$.

The equation of state covers several orders of magnitude in density, and has to incorporate different, and also unknown, physics and particle species as well as different interactions. This is why the equation of state of neutron star matter is so fascinating, but difficult to obtain. While the density range of the equation of state for white dwarfs is experimentally accessible, the neutron-star EoS has large uncertainties. This uncertainty is small for the neutron-star crust, where densities are relatively low and accessible in experiment. The EoS at higher densities,

EOS	M_{max}
	$[M_{\odot}]$
BPAL12	1.46
BGN1H1	1.64
BBB1	1.79
FPS	1.80
BGN2H1	1.82
BBB2	1.92
SLy	2.05
BGN1	2.18
APR	2.21
BGN2	2.48

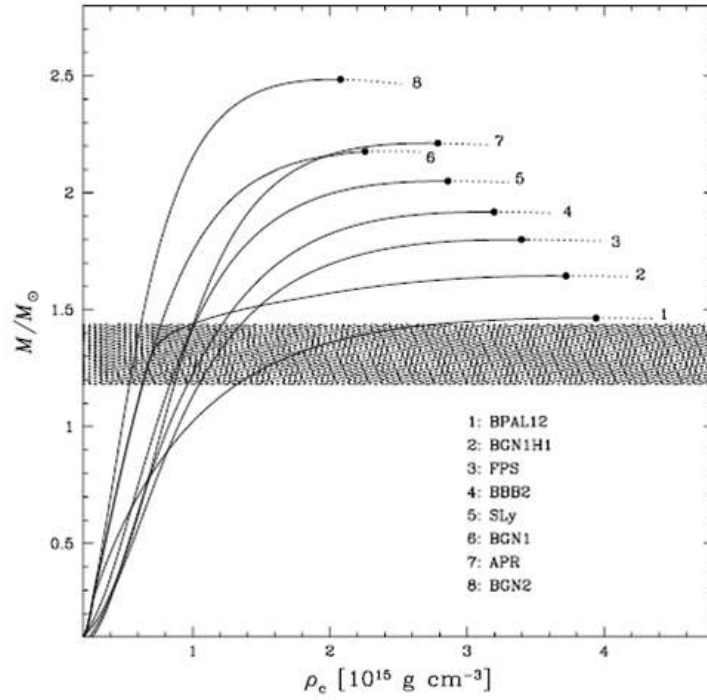


Figure 1.4: Maximum neutron-star masses vs. central densities from Ref. [86] for several equations of state.

however, has a large theoretical uncertainty because above saturation density extrapolations are needed. Furthermore, at intermediate densities, the nuclei involved are too neutron-rich to exist on Earth and are difficult to obtain in experiment. Neutron-star matter at higher densities can be approximated by using neutron-matter results [56, 92], and is very challenging to be studied experimentally.

With a known EoS, the TOV equations are a system of coupled differential equations for $P(r)$ and $m(r)$ and can be solved numerically. For this, one usually employs the following starting conditions: at the stars surface, for $r = R$, the pressure vanishes, $P(R) = 0$, and $P(r) = \rho(r) = 0$ for $r > R$. For infinite distances the metric approaches the Minkowski metric. Inside the star, the pressure stays positive, $P(r) > 0$, it decreases with radius, $dP/dr < 0$, and the density in the center of the star ρ_C is finite. The equation of state, in addition, has to be causal, meaning the speed of sound is smaller than the speed of light, $v_s < c$, with $v_s = \sqrt{dP/d\rho}$.

For every equation of state and for a given central density ρ_C , one finds the neutron-star mass $M(\rho_C)$ and the neutron-star radius $R(\rho_C)$ as a function of the central density. The mass $M(\rho_C)$ is depicted in Fig. 1.3. In this plot from Ref. [86] we show stellar masses vs. central densities for an equation of state from Ref. [86]. A stellar model is only stable, when $dM/d\rho_C > 0$, and otherwise collapses. In the picture, two stable regimes for stellar models can be seen: white dwarfs, which have small central densities, and neutron stars with larger central densities. For both regimes, there are maximum masses for the stars. If the maximum mass of a white dwarf surpasses the Chandrasekhar limit, or the central density is too high, the star collapses and the central density increases. The collapse stops, when the neutron-star branch is reached. If again, the neutron-star mass surpasses the maximum mass of the star, the neutron star will collapse to a black hole.

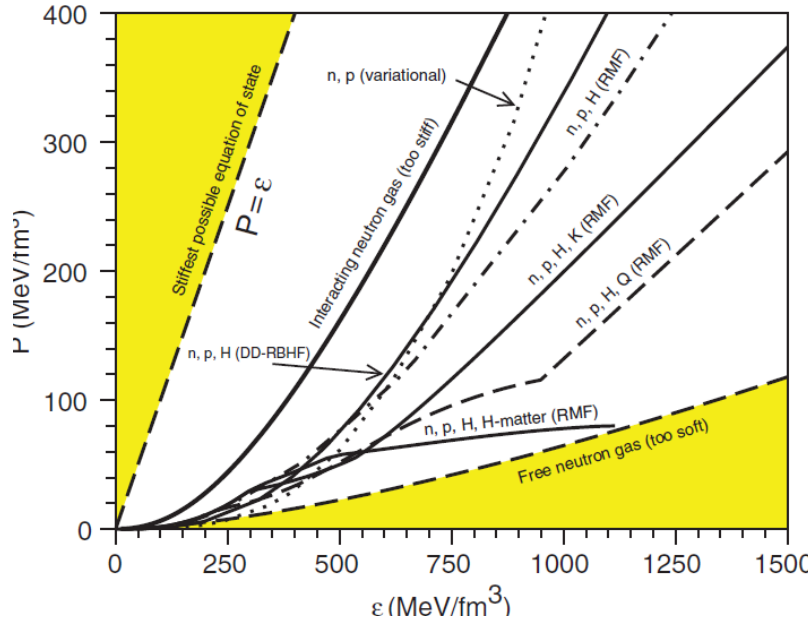


Figure 1.5: Different equations of state from Ref. [93]. The allowed region for the EoS is constrained left by the stiffest possible EoS, where $v_s = c$ and on the lower right by the non-interacting neutron gas. In the picture, RMF means relativistic mean-field model, DD-RBHF is the density-dependent relativistic Brueckner–Hartree–Fock model, n are neutrons, p are protons, H are hyperons, K are meson condensates, and Q means u , d , and s quarks.

The maximum neutron-star mass is unknown and every EoS leads to a different maximum neutron-star mass, see Fig. 1.4, where we show mass vs. central density for several EoS from Ref. [86]. The first calculation of the maximum neutron-star mass was made by Oppenheimer and Volkoff [91]. They assumed an EoS of a free Fermi gas of neutrons at $T = 0$. This EoS leads to a maximum mass of $M_{\text{max}} = 0.71M_{\odot}$. Interestingly, they deduced that neutron stars, thus, cannot play an important role in nature, because the maximum mass would be too small for neutron stars to be formed in collapse scenarios.

In Fig. 1.5 we show different examples for equations of state from Ref. [93]. The Oppenheimer and Volkoff EoS is depicted as the right boundary line, while the left boundary line is given by the stiffest possible equation of state, where $P = \epsilon$ with the energy density ϵ and, thus, the speed of sound $v_s = c$.

Because we can calculate $M(\rho_C)$ and $R(\rho_C)$ for every EoS and a given central density ρ_C , we can compute the so-called mass-radius relation $M = M(R)$. Every initial value for the central density is one point in the mass-radius curve. These mass-radius curves are shown in Fig. 1.6 for the different equations of state from Fig. 1.5 of Ref. [93]. As one can see, in addition to different predictions of the maximum mass of neutron stars, different EoS also lead to different neutron-star radii. The reason is that neutron-star radii are correlated with the pressure of the neutrons inside the neutron star. Nowadays, predictions for maximal neutron-star masses are $2 - 3M_{\odot}$ with radii around 12 km [57]. For every EoS one finds one possible mass-radius curve, while each mass-radius curve also corresponds explicitly to one EoS.

The difference in the predictions of neutron-star properties reflects the fact, that the equation of state at high densities is not well constrained. Thus, a refined theory of the equation of

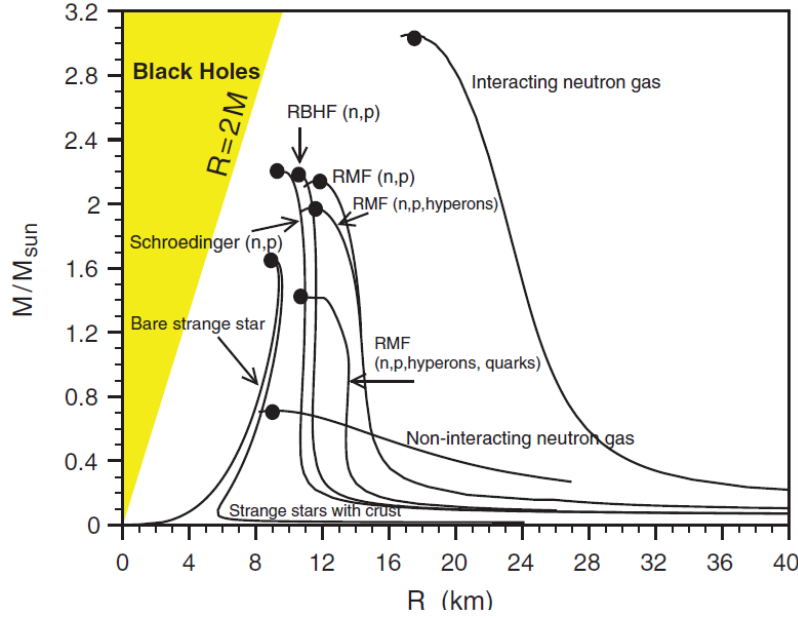


Figure 1.6: Neutron-star mass-radius relations for the different equation of state of Fig. 1.5.

state would improve neutron-star modeling. At the same time neutron-star observations can also help to improve the theories of the strong interaction. For example, from the simultaneous observation of masses and radii of different neutron stars, one would be able to determine the equation of state of neutron-rich matter, which would have great implications for our understanding of nuclear physics. One goal of this work is to improve the predictions of the EoS of neutron matter.

In the next Section, we will present more details on neutron-star observations and their possible impact and constraints on the equation of state of neutron-rich matter.

1.2.1.3 Observations of neutron stars

In our galaxy, we expect a total population of $10^8 - 10^9$ neutron stars, of which about 2000 neutron stars have been observed so far, most of them as pulsars. An optimal observation of a neutron star would be the determination of its mass and radius simultaneously with small error bars. Although there are accurate mass determinations of neutron stars with uncertainties of the order of 10^{-2} or better, so far no radii could be precisely measured.

Precise neutron-star mass measurements have been made in neutron-star binary systems, based on timing measurements of orbital periods, signal delays in binary systems due to the companion, and similar. Since pulsars are precise clocks with an almost constant period and our instruments are accurate enough to determine these times with small uncertainties, masses can be determined with small error bars. We show this in Fig. 1.7, where observed neutron-star masses with the corresponding error bars are shown [1]. Especially in double neutron-star binaries, the mass uncertainty is of the order of 10^{-4} , which is a remarkably precise determination.

The radii, however, can only be accessed indirectly with small accuracy, especially since neutron stars are very faint and small. Thus, so far, no neutron-star radius could be measured with a high accuracy [1]. There is a lot of effort put into the determination of neutron-star radii, and

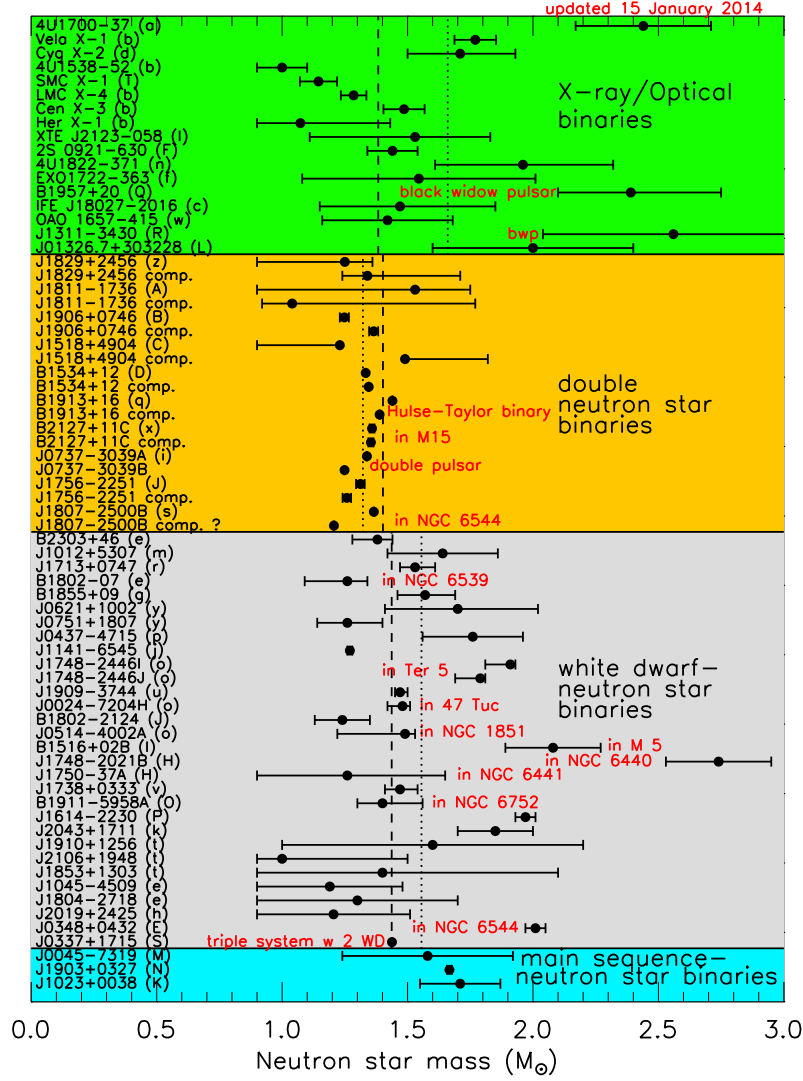


Figure 1.7: Observed neutron-star masses from Ref. [1].

recent statistical analysis suggest typical radii to be around 12 ± 1 km [5]. There are, however, no radius determinations for neutron stars, whose mass is simultaneously known. Thus, the EoS cannot be constrained by a single point, or better box, in the mass-radius diagram.

Although neutron-star radii observations, so far, do not put constraints on the equation of state, neutron-star mass measurements do. For every equation of state we find a maximum mass for neutron stars, as stated before. In Fig. 1.3, for the eight different EoS we find maximum masses ranging from $1.5 - 2.5M_{\odot}$ for example. In the recent years, two neutron stars with well-constrained masses of $1.97 \pm 0.04M_{\odot}$ and $2.01 \pm 0.04M_{\odot}$ have been observed [2, 3]. These are the heaviest observed neutron stars up to now, and their discovery requires every equation of state to support a maximum mass larger than $2M_{\odot}$. For instance, in Fig. 1.3, the equations of state 1-4 can be excluded based on this observation. The variation in the maximum mass reflects the fact that the equation of state is not well constrained above saturation density, where additional phases of matter may appear. However, the discovery of two-solar-mass neutron stars rules out many additional phases, as they soften the EoS and lower the theoretical maximum mass. It is, thus, probable, that neutron stars contain no exotic phases.

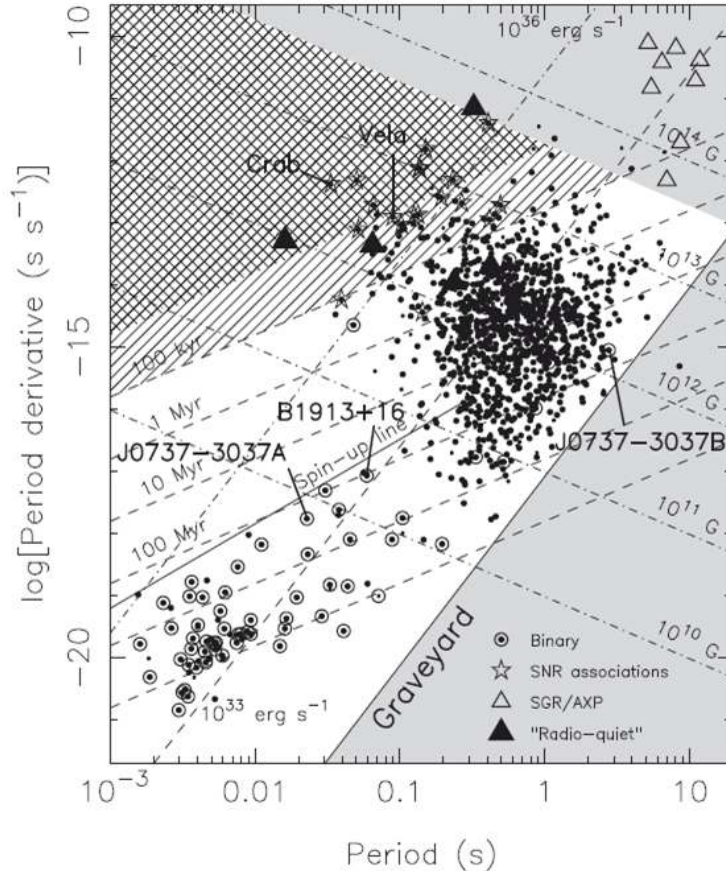


Figure 1.8: Pulsar diagram with the rotational period and its time derivative for observed pulsars, from Ref. [94].

As mentioned before, most neutron stars have been observed as pulsars, which emit radio signals along the magnetic north and south poles. The emitted energy stems from the rotational energy of the neutron star, so over time an isolated pulsar will slow down.

Furthermore, pulsars can also exist in binary star systems. These systems start with two main-sequence stars, where the more massive star will undergo a core-collapse supernova and turn into a neutron star first. If the system is not destroyed in this process, the neutron star will remain in the binary with the second main-sequence star. At some point, the companion will begin the red-giant phase and the neutron star will accrete matter from it, gaining angular momentum and, thus, spinning up [94].

The rotational periods of pulsars can be very different, and the fastest observed pulsar has a period of only 1.4 ms. The observed pulsar spin periods and their time derivative can be plotted into the pulsar diagram, see Fig. 1.8 [94].

In the pulsar diagram, one can see two populations of neutron stars. Most neutron stars have rotational periods around 1s and are isolated. However, there is another population of old neutron stars with very short rotational periods, in the range of 1 – 10ms. These so called millisecond pulsars are mostly in binaries and got spun up by accretion.

The measurement of rotational periods puts another constraint on the EoS. A star of a certain mass and radius can only support a certain rotational frequency before it would be destroyed.

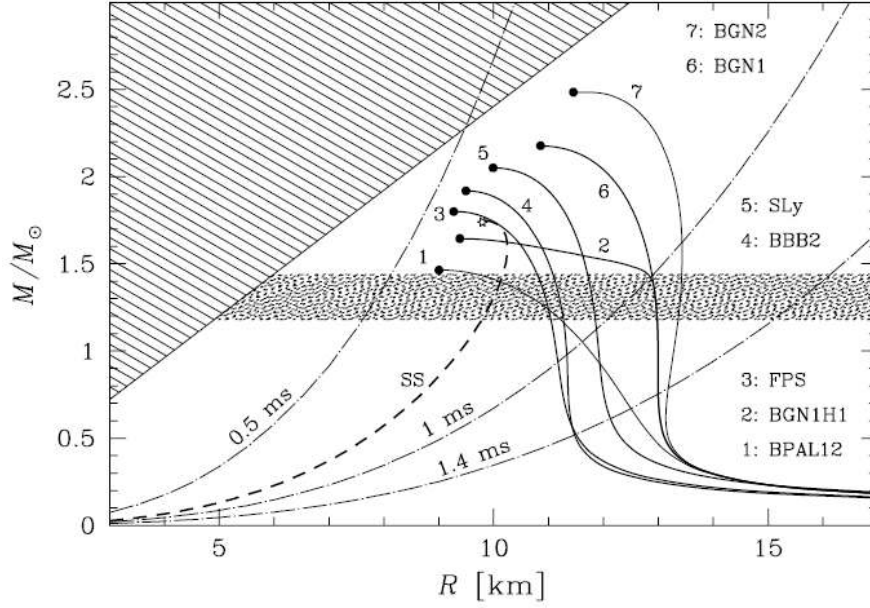


Figure 1.9: Mass-radius relation for several model EoS from Ref. [86]. The region in the upper left corner is excluded by causality. The lines labeled by 0.5ms, 1.0ms, and 1.4ms are the mass-shedding limits for these rotational periods. A stable star with the corresponding rotational period has to lie left of these lines.

This maximal rotation rate is set by the mass-shedding limit. At this limit, the rotational velocity would equal the escape velocity, and in the framework of general relativity one finds

$$P_{\min} = C \left(\frac{R}{10\text{km}} \right)^{3/2} \left(\frac{M_{\odot}}{M} \right)^{1/2} \text{ ms}, \quad (1.3)$$

where $C \sim 1$ is a constant [95], which is only weakly dependent on the EoS. Thus, by observing smaller rotational periods, one can exclude certain areas of the mass-radius diagram. This is depicted in Fig. 1.9, where the mass-shedding curves for three rotational periods are depicted. The measurement of small rotational periods can in principle exclude large parts of the mass-radius diagram, especially in combination with the corresponding mass measurements.

Neutron-star binaries are not only interesting because orbital parameters and constituent masses can possibly be determined very precisely, but also for the fact, that neutron-star binaries emit gravitational waves due to the strong effects of general relativity in these systems. These effects are stronger, if the binary system contains two neutron stars, which we will assume in the following.

Gravitational waves are waves in space-time and have been predicted in the framework of general relativity theory. The direct detection of gravitational waves has not been possible so far, but would be a direct proof of the theory of general relativity. The energy of the emitted gravitational waves is higher, the closer the neutron stars are. As the emission of gravitational waves reduces the systems energy, the neutron star's orbits will change and the stars slowly approach each other. When the neutron stars merge, they will emit gravitational waves with a characteristic frequency. The Advanced LIGO experiment [96] is looking for gravitational waves from such neutron-star mergers and hopefully will detect them in the near future. The characteristic frequency of a merger event can also be used to determine parameters of the neutron-star equation of state, see Ref. [97, 98, 99].

Table 1.1: Two double neutron-star systems with corresponding stellar masses and the ratio of measured and calculated orbital-period time derivative.

System	$M_A[M_\odot]$	$M_B[M_\odot]$	$\dot{P}_b^{\text{meas}}/\dot{P}_b^{\text{GR}}$	Ref.
PSR B1913+16	1.4398(2)	1.3886(2)	0.997(2)	[100]
PSR J0737-3039	1.3381(7)	1.2489(7)	1.003(14)	[101]

Although gravitational waves from neutron-star binaries have not been detected directly yet, they can be used to indirectly check general relativity. The change of orbital parameters due to gravitational wave emission can be calculated from the theory of general relativity while in certain systems the orbital parameters can be measured with high precision over time. The first famous example was the Hulse-Taylor pulsar PSR B1913+16 which was discovered in 1974 by Hulse and Taylor. They were awarded with the Nobel prize in physics in 1993 "for the discovery of a new type of pulsar, a discovery that has opened up new possibilities for the study of gravitation".

The system consists of a pulsar orbited by another neutron star and has a high eccentricity of $e = 0.617$ and a short rotational period of $7.75h$. For these parameters, general relativity effects are strong and can be accurately measured. A comparison of the time derivative of the orbital period \dot{P}_b between the measured value and a general relativistic calculation gives a ratio of $0.997(2)$ [100], which provides evidence for the validity of general relativity.

Another interesting system is the double pulsar J0737-3039, which is the only known neutron-star binary with two pulsars and which was discovered in 2003 [102]. It has a very short orbital period of $2.4h$ [103] and leads to a ratio of the time derivatives of $1.003(14)$ [101]. In fact, this system is ideally suited for testing the effects of general relativity because the mass ratio R as well as five post-Keplerian parameters can be measured: the relativistic orbit precession $\dot{\omega}$, the parameter γ combining gravitational redshift and time dilatation, the time derivative of the orbital period \dot{P}_b , and Shapiro delay parameters s and r , which all depend on the individual masses. By using the mass ratio and one post-Keplerian parameter to determine the masses, these parameters allow four independent tests of general relativity. In Fig. 1.10, these parameters are plotted as functions of the two masses. They all intersect in one single point with high accuracy, which gives evidence of the validity of the theory of general relativity.

There are, of course, more possible constraints on the neutron-star equation of state. As an example, quasi-periodic oscillations (QPOs) in magnetars, neutron stars with very strong magnetic fields, depend on the neutron-star crust thickness and the neutron-star radius. Recently, several oscillation frequencies have been measured [104, 105, 106, 107] and could be used to put constraints on the equation of state [108]. However, it is challenging and presently model dependent to assign oscillation modes to the observed frequencies. A deeper understanding of QPOs and more information on neutron stars obtained with the future NICER mission [109, 110] can lead to additional constraints on the EoS.

To summarize, the key to the description of neutron stars is the neutron-star equation of state. On the other hand, neutron matter is useful as a test case in which different aspects of nuclear interactions can be probed. The neutron-star equation of state is dominated by the properties of neutron matter, which makes its study directly relevant for neutron-star modeling.

In this Thesis, we want to give a better description of neutron matter, which, in combination with improved observational constraints, will allow to determine the neutron star mass-radius

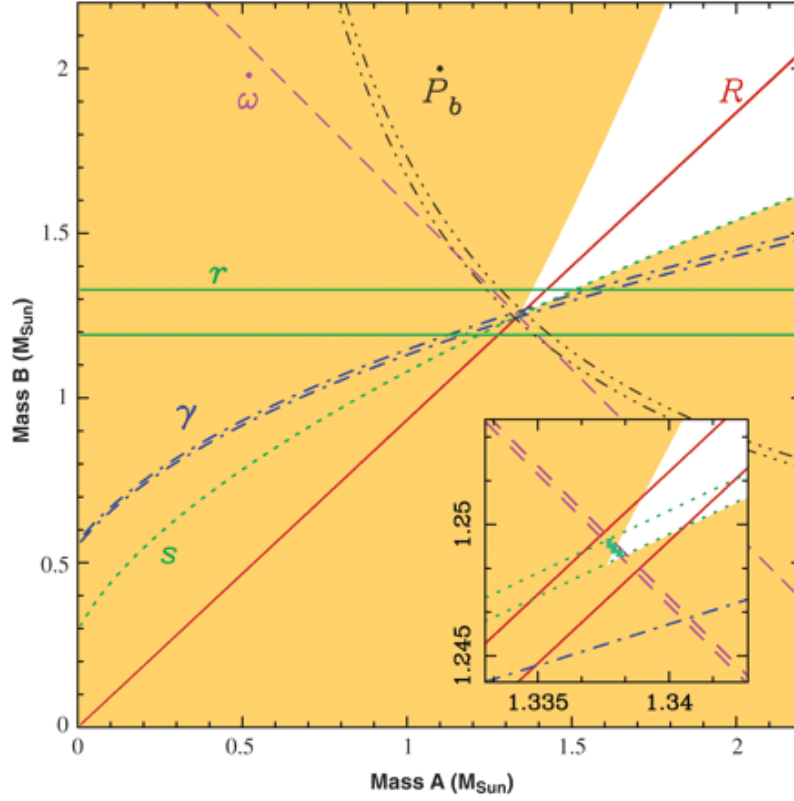


Figure 1.10: Tests of general relativity for several orbital parameters of the system J0737-3039 from Ref. [101]. Shown are the constraints on the pulsar’s masses for the mass ratio R , for the relativistic orbit precession $\dot{\omega}$, for γ combining redshift and time dilatation, for the time derivative of the orbital period \dot{P}_b , and for parameters of the Shapiro delay s and r . Line pairs indicate the measurement uncertainty. All parameters intersect in one point which corresponds to the pulsar’s masses. Shaded regions are excluded by the condition $\sin(i) \leq 1$.

relation with theoretical uncertainties from nuclear physics. The neutron matter results will allow to give an improved estimate for neutron-star radii and serve as a systematically improvable nonperturbative benchmark for model equations of state used in supernova simulations. Additionally, they will also pave the way for a prediction of the signal of neutron-star mergers with nuclear physics uncertainties.

In turn, an accurate simultaneous observation of a neutron star’s mass and radius would enable us to constrain the neutron matter EoS, and doing this, also the fundamental theories of the strong interaction.

1.2.2 Neutron-rich nuclei

In the last Section we introduced neutron stars as a possibility to test theories of the strong interaction in the high-density regime. Since this regime can be probed on Earth only with tremendous effort, neutron stars are important laboratories to test these theories. To verify the same theories at intermediate or nuclear densities, we can apply them to the calculation of properties of nuclei and compare with experimental results.

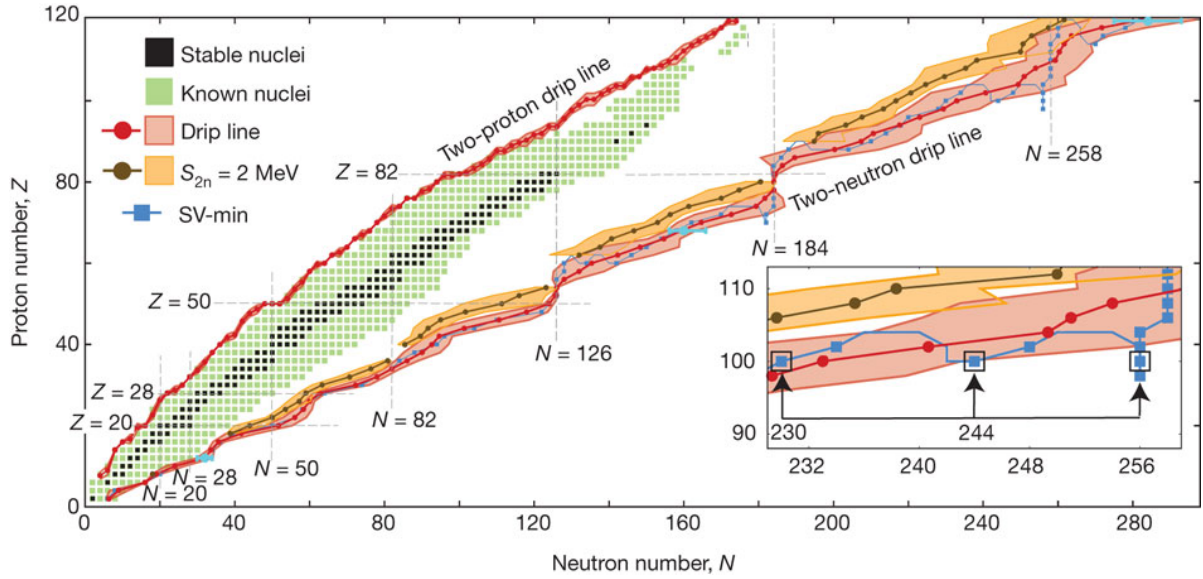


Figure 1.11: Nuclear chart of bound even-even nuclei from Fig. [111]. There exist 767 even-even nuclei which are known experimentally. The stable nuclei are depicted as black squares. The red lines are the proton and neutron drip lines with their uncertainty regions for different models, while the blue line is the drip line for one model. The brown line is the $S_{2n} = 2$ MeV line with its uncertainty. The inset depicts the behavior of the neutron drip line for high N .

Nuclei can be arranged according to the number of protons and neutrons in the nuclear chart, see Fig. 1.11 for the nuclear chart of bound even-even nuclei. Roughly 3000 nuclei have been investigated on Earth [111], which either lie in the valley of stability (black squares in Fig. 1.11) or which are unstable and radioactive (green squares). The stable nuclei follow roughly the maximum of the semi-empirical formula for the binding energy, given by [112, 113]

$$E_B = a_V \cdot A - a_S A^{2/3} - a_C \frac{Z(Z-1)}{A^{1/3}} - a_A \frac{(N-Z)^2}{4A} + \delta(N, Z), \quad (1.4)$$

which is based on the liquid-drop model. This formula describes the binding energies of larger nuclei quite well. The five terms are the volume term with coefficient a_V proportional to the nucleus' size, the surface term a_S taking into account the surface of the nucleus, the Coulomb term a_C which includes the Coulomb repulsion of the protons, the asymmetry term a_A taking into account the different Fermi seas of protons and neutrons, and a pairing term $\delta(N, Z)$ which includes nucleon pairing. Without the Coulomb term, the valley of stability line would follow a diagonal with $N = Z$ in the nuclear chart, but the Coulomb term influences the proton Fermi energy and makes the valley of stability tend to a slight neutron asymmetry for heavier nuclei. Moving away from the valley of stability, the binding energy decreases due to the Coulomb and asymmetry terms. The boundaries of nuclear binding are the neutron and proton drip lines. These are marked in the case of the neutron drip line by the one-neutron separation energy S_{1n} and, eliminating the effect of pairing, also by the two-neutron separation energy S_{2n} , which are defined by

$$S_{1n} = B(Z, N-1) - B(Z, N), \quad (1.5)$$

$$S_{2n} = B(Z, N-2) - B(Z, N), \quad (1.6)$$

in terms of the binding energy $B(Z, N)$. When $S_{1n} = 0$, the nucleus becomes unstable against neutron emission. That is where the neutron drip line is reached. The same holds in the case of the proton drip line.

The neutron drip line is due to the asymmetry term in the nuclear binding energy, while the proton drip line appears additionally due to the Coulomb repulsion. While many proton-rich nuclei, between the valley of stability and the proton drip line, have been investigated experimentally and the proton drip line has been mapped out, many neutron-rich nuclei as well as the position of the neutron drip line are still unknown.

Another interesting effect connected to drip lines is the pairing term of Eq. (1.4). This term increases the binding energy for nuclei with even numbers of protons and neutrons and leads to odd-even staggering of the neutron and proton drip line. This can be observed, e.g., in the helium isotopes, where ^4He , ^6He and ^8He are bound while ^3He , ^5He , and ^7He are not.

A lot of experimental effort is put into measuring neutron-rich nuclei and recent highlights include precision measurements of neutron-rich calcium isotopes, see Refs. [34, 114]. More studies will be possible in the next-generation ion-beam facilities, like FAIR and FRIB.

Improving the knowledge of these nuclei is especially important because they are key for the understanding of the r-process, one of the main processes for the nucleosynthesis of the elements [29, 30]. This process runs through the neutron-rich side of the nuclear chart and will be explained in Sec. 1.2.2.1 in more detail.

Given the lack of experimental data for neutron-rich nuclei, these nuclei are ideal to test predictions of theories of the strong interaction. In the following Sections, we will give details on nucleosynthesis, explain the symmetry energy and its density dependence, and the connection of the neutron-matter EoS with neutron-rich nuclei.

1.2.2.1 Neutron-rich nuclei and nucleosynthesis

As discussed previously, the understanding of neutron-rich nuclei and the correct position of the neutron drip line is tightly connected to the understanding of the origin of the elements in the universe. In the region of these nuclei, along the neutron drip line, works the so-called rapid neutron capture process or r-process [29, 30]. The astrophysical r-process is one of the two dominant processes responsible for the creation of elements heavier than iron. The other major process is the slow neutron-capture process or s-process [29, 30]. The structure and properties of the very neutron-rich nuclei, thus, directly affect the creation of elements.

A major goal in nuclear astrophysics is to describe nuclear reactions and processes in stellar environments as well as to explain the abundance pattern of elements in the solar system, see Fig. 1.12. Different nucleosynthesis processes work in different mass regions. The most abundant element is hydrogen which builds the fuel for the creation of heavier elements. Starting from hydrogen, elements up to ^{56}Fe are synthesized in different stellar burning processes which have been explained before. Stellar burning ends at the elements of the iron region, leading to the iron-peak in the solar abundance patterns, see Fig. 1.12. Heavier elements cannot be created in stellar burning and are made in the s-process, the r-process as well as the p-process [115]. The p-process runs along the proton drip line creating the proton-rich nuclei. However, the s- and r-processes are predominant in nucleosynthesis and we will only focus on these.

The s-process takes place mostly at relatively low neutron densities and temperatures in Asymptotic Giant Branch (AGB) stars, which are low- to medium mass stars in the red-giant phase. This site was supported by the finding of technetium, which has a half life of only ≈ 4 million years,

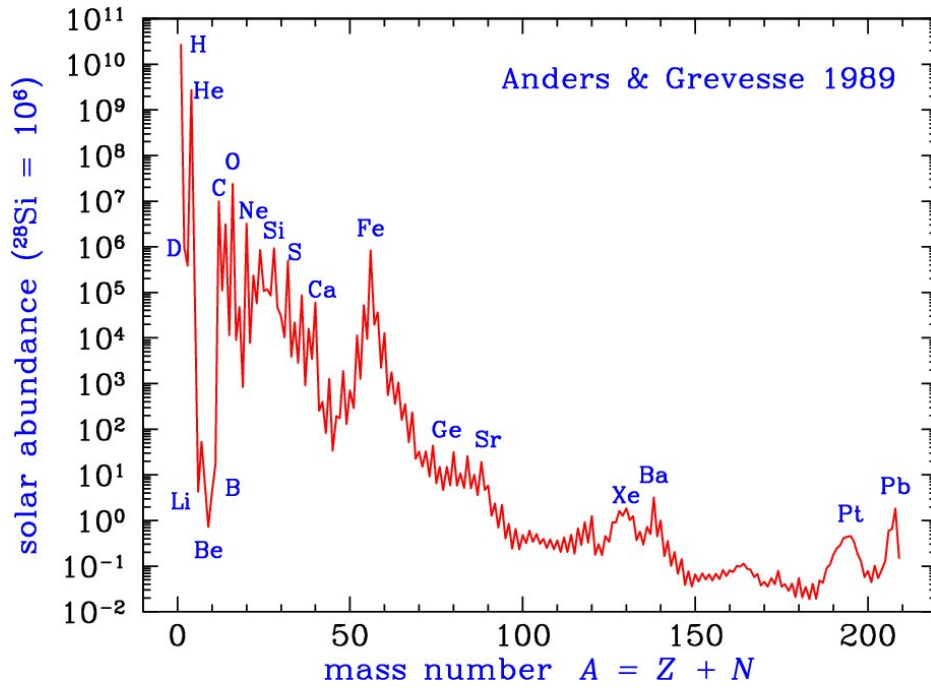


Figure 1.12: Abundances of elements in the solar system from Ref. [32].

in stars which were billion of years old, showing that this element, which cannot be created in stellar fusion processes, had to be recently created in a different process in the star [116].

In an AGB star, free neutrons from stellar burning reactions can be captured by a stable nucleus ${}^AX^Z$ to produce the daughter nucleus ${}^{A+1}X^Z$. This process continues until the daughter nucleus is unstable against β decay. For an unstable daughter, at low neutron densities, the capture time for an additional neutron is smaller than the β decay half life, and the nucleus will most likely decay to ${}^{A+1}Y^{Z+1}$. Then, another neutron will be captured, continuing this process following the valley of stability up to bismuth. Thus, the s-process is in general a sequence of neutron-captures and β decays and occurs over timescales of thousands of years. The abundances of the created elements are highest, when the neutron-capture cross sections are small, which is the case for closed neutron shells or subshells. The s-process, thus, creates abundance peaks for Sr, Ba, and Pb, see Fig. 1.12.

In addition to the s-process, there has to be a second nucleosynthesis process acting on the neutron-rich side to create certain isotopes outside the s-process path. This process is the r-process, which takes place in explosive scenarios with high temperatures and high neutron densities on very short timescales of the order of seconds. The r-process site is not identified, but possible scenarios include supernovae or neutron-star mergers [117].

In this scenario, because of the very high neutron density, neutron capture is a lot faster than β decay and a stable nucleus can capture many neutrons consecutively, creating very neutron-rich nuclei close to the neutron drip line. The neutron capture stops, when photo disintegration and neutron capture are in equilibrium, i.e., for nuclei with neutron separation energies of the order of 2 MeV. After a β decay of such a nuclei, the rapid neutron capture continues up to the next stopping point, and so on. Thus, many neutron-rich nuclei along the drip line will be created in the r-process. After the neutron exposure ends, the created elements will decay back to the valley of stability. The abundances of nuclei created in the r-process are influenced by the neutron-capture cross sections. Nuclei with small cross sections will be created in larger

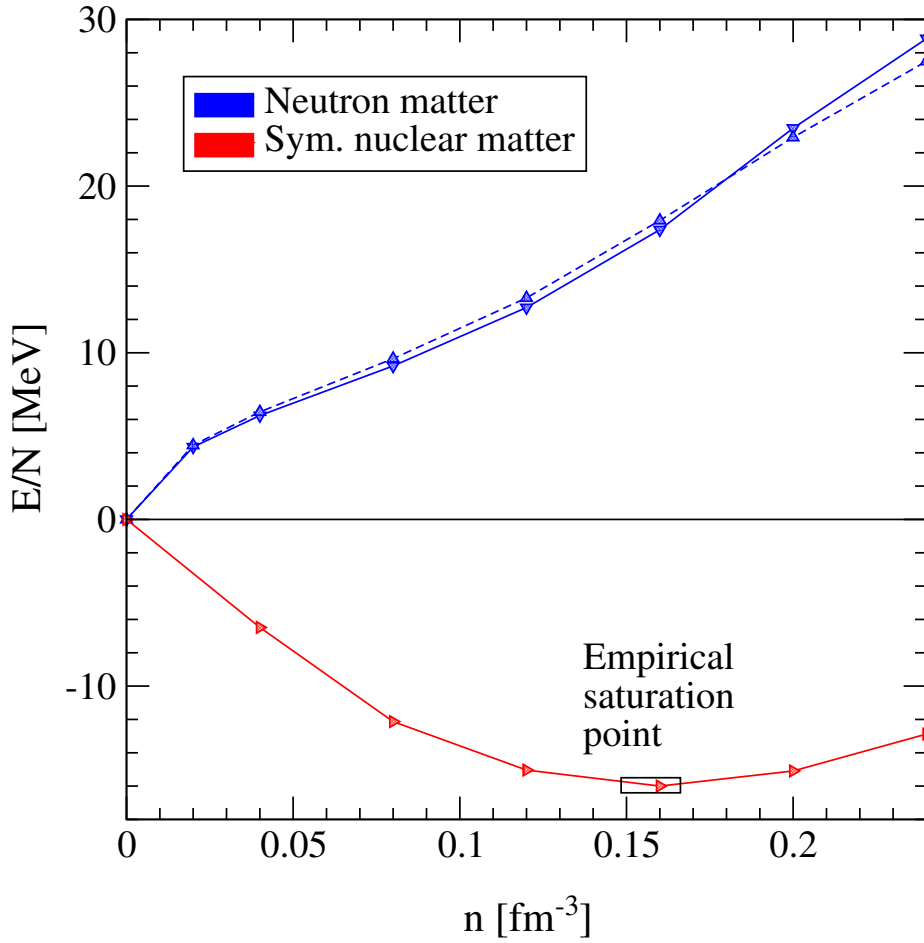


Figure 1.13: Energy per particle in neutron matter (blue curves) and symmetric matter (red curve) versus the density from Ref. [118]. The curves are obtained using phenomenological potentials with and without boost corrections for neutron matter. The symmetric matter results have been fitted to the empirical saturation point.

abundances, as the r-process slows down there. These nuclei are mostly the ones with shell- or subshell closures like Sr, Ba, and Pb. Because of the β decays to the valley of stability, the r-process leads to abundance peaks at Ge, Xe, and Pt, see Fig. 1.12.

The s- and r-process can explain a major part of the isotope abundances for elements heavier than iron, with the r-process contributing to the abundances of most isotopes on the neutron-rich side except the ones shielded by stable nuclei. To calculate the solar abundances, complex network calculations are done, which need as an input properties of the involved nuclei, like masses etc. Thus, calculations of neutron-rich nuclei and their properties are crucial to improve the understanding of nucleosynthesis and to reproduce the solar abundance pattern.

In this work we will build the basis for improved studies of neutron-rich nuclei with QMC methods using chiral EFT interactions.

1.2.2.2 Nuclear matter and symmetry energy

Nuclear matter is an idealized system of infinite extent that uniformly contains neutrons and protons in arbitrary fractions. The system is characterized by the density n , which is finite, and the proton fraction

$$x = \frac{n_p}{n_p + n_n}, \quad (1.7)$$

where n_p and n_n are the proton and neutron densities, respectively. Electromagnetic interactions are ignored, and only the strong interaction is taken into account. Thus, pure neutron matter is one extreme case for nuclear matter with proton fraction $x = 0$. Another interesting case is symmetric nuclear matter with the same amount of protons and neutrons, $x = 0.5$. These two cases are depicted in Fig. 1.13. Nuclear matter with arbitrary proton fractions is usually called asymmetric nuclear matter.

While neutron matter is the simplest approximation to neutron-star matter, symmetric nuclear matter is the simplest approximation to larger nuclei. This can also be seen from the semi-empirical mass formula of Eq. (1.4). In the case of infinite nuclear matter, we can ignore the Coulomb and surface terms. We also do not take into account pairing and for symmetric nuclear matter, also the asymmetry term vanishes. Thus, the only term contributing is the volume term a_V .

This term reflects the binding energy per nucleon at nuclear saturation density n_0 and is empirically ~ 16 MeV. A second property, that a theory of the strong interaction has to reproduce, is saturation at n_0 . Saturation means that the pressure of the system has to vanish, which is equivalent to an energy minimum at n_0 . In contrast, neutron matter has positive energies per particle, leading to a positive pressure in neutron matter. This stabilizes neutron stars against gravitational collapse and has as a result that there are no self-bound systems containing only neutrons.

An important parameter for nuclear matter is the symmetry energy parameter S_V . The symmetry energy can be defined in two ways: first, via the energy difference S per nucleon between pure neutron matter and symmetric nuclear matter:

$$S(n) = \frac{E}{A}(n, x = 0) - \frac{E}{A}(n, x = 1/2), \quad (1.8)$$

where $\frac{E}{A}(n, x)$ is the energy per particle at the density n with proton fraction x . The symmetry energy is given as $S(n_0)$, and this parameter is of the order of 30 MeV, see Fig. 1.13.

A different definition can be given via an expansion of the energy per particle in the proton fraction around neutron matter [56, 119, 120]

$$\frac{E}{A}(n, x) = \frac{E}{A}(n, x = 0) - 4x(1 - x)S_V(n) + \dots, \quad (1.9)$$

where higher terms in the expansion can be neglected to a good approximation. Given this expansion, the parameter S_V is defined as

$$S_V(n) = \frac{1}{8} \frac{\partial^2}{\partial x^2} \frac{E}{A}(n, x) \Big|_{x=1/2}. \quad (1.10)$$

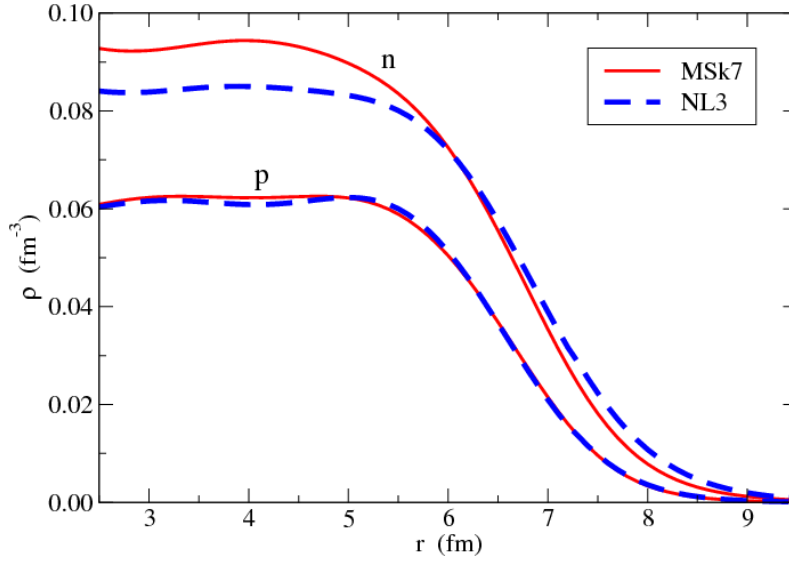


Figure 1.14: Neutron and proton density profiles in ^{208}Pb using two mean-field models from Ref. [122].

and the symmetry energy is $S_V(n_0)$. Usually, $S(n_0) \approx S_V(n_0)$ but these two definitions can also differ due to quartic and higher terms in the expansion (1.9) [121].

Another important parameter is the density dependence of the symmetry energy $L(n_0)$ which is defined as

$$L(n_0) = 3n_0 \left. \frac{\partial S_V(n)}{\partial n} \right|_{n_0}. \quad (1.11)$$

The L parameter is proportional to the pressure of neutron matter at saturation density and is, thus, positive. Both the symmetry energy parameter S_V and L are important as they impact astrophysical calculations. For example the expected neutrino signals of galactic core-collapse supernovae depend on the symmetry energy, and the radius of neutron stars is connected to the L parameter [121].

1.2.2.3 Neutron-matter equation of state and neutron skins

In this Thesis, we want to develop nonperturbative benchmarks for neutron matter and the basis for improved calculations of neutron-rich nuclei. In addition to the explicit calculation of neutron-rich nuclei and their properties, we can also infer information about them directly from the neutron-matter equation of state.

As we have stated above, the EoS of neutron matter can be connected to several physical systems through the important S_V and L parameters. The latter is a measure for the pressure of neutron matter at saturation density, and clearly affects, for instance, the neutron-star radius, because higher pressure between neutrons will lead to more repulsion and, thus, increase radii.

In a neutron-rich nucleus, the density profiles of protons and neutrons differ, which can be seen in Fig. 1.14 in the case of ^{208}Pb . Due to the large excess of neutrons and a reduction of the proton density due to the Coulomb barrier, the neutron density falls off at larger radii, leading to a larger neutron than proton radius. The difference between neutron and proton rms radius is called neutron skin, $R_{\text{skin}} = R_n - R_p$, and is directly influenced by the pressure among neutrons.

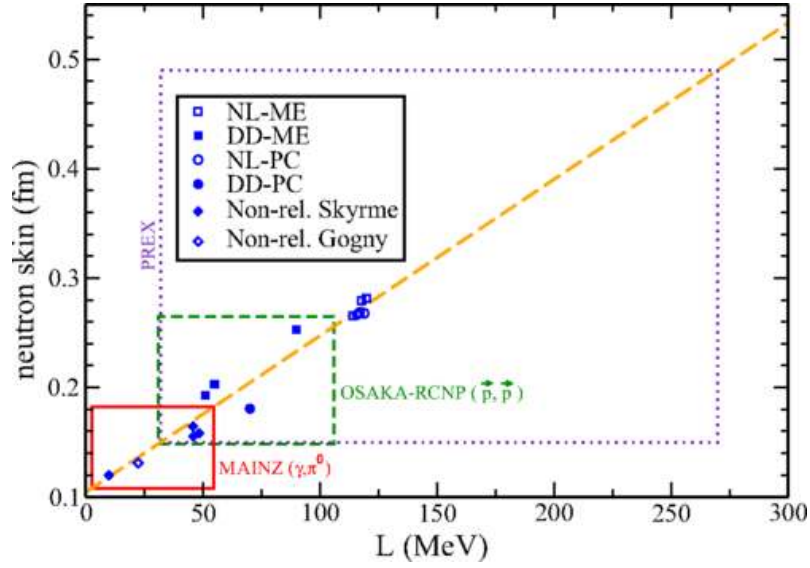


Figure 1.15: Neutron skin of ^{208}Pb vs. L parameter from Ref. [123]. For different models (blue points) one finds a linear correlation (orange line). Shown are also different experimental constraints [124, 125, 126].

A higher pressure (a larger L parameter) leads to a larger neutron skin of neutron-rich nuclei because neutrons are pushed out, similar to what happens in a neutron star. This is depicted in Fig. 1.15, where the neutron skin thickness of ^{208}Pb is plotted vs. the L parameter for different model EoS. One finds a linear correlation between these two parameters. Every neutron-matter EoS constrains the value of the L parameter and, thus, also the neutron-skin thickness of lead. On the other hand, by measuring the neutron skin of lead, one puts constraints also on the neutron-matter EoS. In the picture, experimental constraints are shown from the PREX experiment [124], from the Osaka polarized proton elastic scattering experiment [125], and from the Mainz pion-photoproduction experiments [126]. For neutron-skin measurements in other neutron-rich nuclei see, e.g., Refs. [127, 128].

The experimental constraints on the neutron skins still have large uncertainties. The reason is that, although the charge radius or proton radius can be accurately measured with uncertainties of $\approx 1\%$ in electron scattering experiments, the determination of the neutron radius is less precise. It is usually measured with hadronic probes leading to a model dependency of the results [123]. A direct determination of the neutron radius is parity-violating electron scattering which has been done by the PREX collaboration [124], leading to $R_{\text{skin}} = 0.33^{+0.16}_{-0.18}$ fm for ^{208}Pb with a very large uncertainty. However, in the future PREX II experiment the uncertainty is expected to reduce to ± 0.06 fm [129]. Nevertheless, the three experiments overlap for L values of 30 – 50 MeV.

As we have shown, complementary to direct *ab initio* calculations of nuclei, also the neutron-matter EoS will give insight into the physics of neutron-rich nuclei and puts constraints on their modeling.

1.2.3 Ultracold atoms

The last physics case we discuss is neutron matter at very low densities. The strong interaction between neutrons at these densities is characterized by a large scattering length,

$a_{nn} = -18.9 \text{ fm}$, which is an order of magnitude larger than the interparticle distance at low densities. At low densities or small momenta, other parameters like the effective range can be neglected, and the system is solely described only by one parameter, the density. In this regime neutron matter shows universality, see Sec. 1.2.3.1.

In experiments with ultracold fermionic atoms, the strength of the atomic interaction can be tuned using so-called Feshbach resonances [20]. With these resonances, the two-body interaction can be adjusted to an infinite scattering length, which allows to probe pure neutron matter and study constraints on the equation of state.

In the following Sections, we explain universality and show the connections of neutron matter with ultracold atom experiments.

1.2.3.1 Universality

For short-range interactions at low densities, the scattering amplitude can be expanded in the effective-range expansion [130]. If the particles interact only via S-wave interactions, this expansion is given by

$$k \cot(\delta_0) = -\frac{1}{a_S} + \frac{1}{2}r_e k^2 - Pr_e^3 k^4 + \dots, \quad (1.12)$$

where the S wave scattering length a_S , the effective range r_e , and the shape parameter P are constants. The scattering is described by the T-matrix given by

$$T^{(+)} = \frac{4\pi}{m} \frac{1}{\frac{1}{a} - \frac{1}{2}r_e k^2 - Pr_e^3 k^4 + \dots + ik}. \quad (1.13)$$

At low energies, like in low-density neutron matter, we can neglect high terms in k and find for the T-matrix

$$T^{(+)} = \frac{4\pi}{m} \frac{1}{ik \left(1 + \frac{1}{ika}\right) - \frac{1}{2i}r_e k}, \quad (1.14)$$

where we only include the scattering length and effective-range terms. For neutron matter at low densities, $r_e \approx 2.7 \text{ fm} \ll k_F^{-1} \ll a_S$, which means that the interparticle spacing is much larger than the effective range of the interaction. The system is therefore fully described by k_F and a_S and effectively interacts via contact interactions. This means we can ignore the effective-range term, finding $k \cot(\delta_0) \approx -\frac{1}{a_S}$. In this case, the T-matrix only includes the first bracket in the denominator, and the system is solely described by the scattering length a_S . Systems with the same scattering length a_S and the same Fermi momentum k_F then show the same physics. If additionally the scattering length is very large, as it is for neutrons, all length scales drop out, and the system is completely described by the density, given by the Fermi momentum k_F . This regime is called universal regime. Neutron matter at low densities can be approximated as such a system, which interacts via S-wave, large scattering length contact interactions. Since the system's properties only depend on the density, the system's energy has to be a fraction of the energy of a free Fermi gas,

$$E(n) = \xi E_{\text{FG}}(n). \quad (1.15)$$

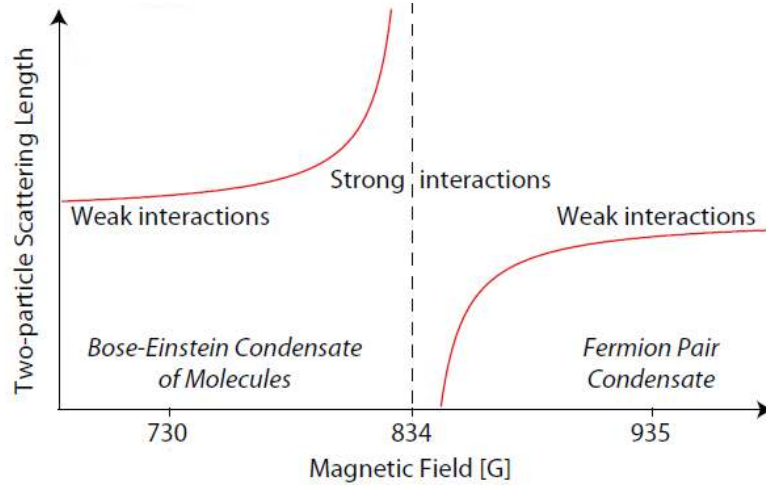


Figure 1.16: Scattering length vs. magnetic field for ${}^6\text{Li}$ from [133]. At a certain magnetic field strength, here 834G , the scattering length shows a resonance, the Feshbach resonance. By varying the magnetic field, the scattering length can be tuned over a wide range, and can be used to probe also the universal limit for infinite scattering lengths.

The parameter ξ is called Bertsch parameter after George Bertsch, who posed the many-body challenge of determining this parameter in 1999 [131]. Theoretical determinations lead to a value for ξ of $\xi \approx 0.37$ [64], and agree very well with the most precise measurement with ${}^6\text{Li}$ atoms of Ref. [24], obtained with a precise determination of the Feshbach resonance in Ref. [132].

This system is called unitary Fermi gas, and will arise for any dilute Fermionic system with a short range interaction with $r_e \ll k_F^{-1} \ll a$. Since low-density neutron matter is close to a unitary Fermi gas, it is possible to study the unitary limit in experiments to constrain the low-density neutron matter EoS.

1.2.3.2 Neutron-matter equation of state and ultracold atoms

In case of nuclear interactions, and especially neutron matter, the scattering length is very large compared to the effective range of the nuclear interaction, $|a_{nn}| = 18.9\text{fm} \gg 2.7\text{fm} \approx r_e$. This regime can be accessed in experiments with ultracold atoms using so-called Feshbach resonances. These Feshbach resonances occur, when a magnetic field is applied to a system of ultracold atoms. By varying the magnetic field strength, the scattering length can be tuned over a wide range, and can be used to probe also the universal limit for infinite scattering lengths. In Fig. 1.16 we show the scattering length vs. magnetic field strength for ${}^6\text{Li}$. For these atoms, the interaction shows a nearly zero effective range, making them ideal for these experiments [23]. For smaller magnetic fields and positive scattering lengths, the interaction is attractive and atoms are bound together to a molecular state. By increasing the magnetic field, the energy of this state increases towards the point, where the atoms become free. For these slightly bound systems, the scattering length is infinitely large. Increasing the magnetic field further, the scattering length changes its sign while the system becomes slightly unbound. A further increase of the magnetic field leads to unbound atoms.

In case of fermionic atoms one can probe systems like neutron matter. Left of the Feshbach resonance, in the molecular phase, fermionic atoms can pair and form bosons, which for low-enough temperatures will form a Bose-Einstein condensate. Right of the resonance, in the unbound phase, one can probe pairing of the fermions to Cooper pairs in the BCS phase. By changing the magnetic field to a value close to the Feshbach resonance, a system of ultracold fermionic atoms can be used to probe neutron matter in the unitary limit at very low densities. Thus, properties of the low-density neutron matter EoS can be both probed experimentally and studied theoretically [23].

2 Chiral effective field theory for nuclear forces

As outlined in the previous Chapter, neutron matter is a fascinating physical system to study over a wide range of densities, from low densities which can be probed on Earth, up to very high densities in astronomical objects. To describe neutron matter, an important requirement is a reliable theory for nuclear forces. Many approaches to nuclear forces have been introduced [134], e.g., sophisticated meson exchange models or phenomenological interactions.

With the formulation of quantum chromodynamics (QCD), the fundamental theory of the strong interactions was found. Nuclear interactions can be described as the residual interaction of the strong force between the quark and gluon constituents of the nucleons. This is similar to the Van-der-Waals force between molecules, which is the residual force of the Coulomb interaction between atoms.

At low densities, which are relevant in nuclear physics, QCD is nonperturbative and nuclear forces cannot be derived from QCD directly with sufficient precision. A solution is the use of effective field theories (EFT) of QCD in the low-energy regime [135]. In an EFT, the interactions in a certain energy regime are expanded in a series of operators which are ordered according to a power counting scheme.

For very low energies, nuclear forces can be described in pionless EFT. Pionless EFT treats nuclear interactions in terms of nucleon contact interactions with momentum-, spin-, and isospin-dependencies.

At higher energies, pion exchanges are explicitly resolved, and by including these, one arrives at chiral EFT. Chiral EFT is a modern approach to nuclear forces because it provides a systematically improvable way of describing nuclear interactions and allows to estimate the theoretical uncertainty of the calculations. Chiral EFT has been very successfully applied to calculations of few- and many-body systems. In the following Sections, we will give a theoretical basis of chiral EFT. More details can be found in Refs. [136, 137, 138].

2.1 Quantum chromodynamics

Among the four fundamental interactions in nature, the strong interaction binds nucleons together to nuclei. It is based on the theory of QCD which describes the interactions between quarks and gluons, the main building blocks of all hadrons. There are six quark flavors: up ($m_u \approx 2\text{ MeV}$), down ($m_d \approx 5\text{ MeV}$), strange ($m_s \approx 100\text{ MeV}$), charm ($m_c \approx 1\text{ GeV}$), bottom ($m_b \approx 4\text{ GeV}$), and top ($m_t \approx 180\text{ GeV}$) [139]. In addition to mass and electric charge, QCD introduces an additional property for quarks and gluons which is color charge. There are three types of color charges namely red (r), green (g) and blue (b). Furthermore, anti-quarks carry the anti-colors anti-red (\bar{r}), anti-green (\bar{g}) and anti-blue (\bar{b}). The strong interaction is mediated by gluons, which are gauge bosons for the strong interaction.

All particles built out of quarks are called hadrons and have to be color neutral. Thus, quarks cannot exist freely, and are confined to hadrons (confinement). There are two possibilities to

form color neutral systems: a pair of a quark and an anti-quark which carry color and the corresponding anticolor, e.g., $u_r \bar{d}_{\bar{r}}$. These bosonic systems are called mesons, e.g., the pion. Systems consisting of three quarks with different colors, e.g., $u_r d_g d_b$, are called baryons and are fermionic states, e.g., the neutron.

Another characteristic property of QCD is "asymptotic freedom", which describes the fact that the strong coupling constant α_s becomes weaker at high momenta, making the theory perturbative at high momenta. At low momenta, however, the strength of the coupling constant increases and the theory becomes nonperturbative. This low-energy region is of particular interest for nuclear matter calculations, and the nonperturbativeness makes direct calculations of nuclear interactions from QCD very hard.

For calculations of nuclear matter and nuclei, only the three lightest quarks u , d and s need to be considered while the other quarks can be treated as heavy and integrated out. The QCD Lagrangian with only the three lightest quarks is given by [140]

$$\mathcal{L} = \sum_{i=1}^3 (\bar{q}_i i \not{D} q_i - m_i \bar{q}_i q_i) - \frac{1}{2} \text{Tr} G_{\mu\nu} G^{\mu\nu}, \quad (2.1)$$

where the q_i are the quark fields, m_i are the quark masses, $\not{D} = \gamma^\mu D_\mu = \gamma^\mu (\partial_\mu + ig A_\mu)$ is the covariant derivative, A_μ are the gluon fields and $G_{\mu\nu}$ is the gluon field strength.

One can draw a phase diagram for QCD where different phases of matter for temperature vs. baryon density are given. At low baryon chemical potentials and temperatures, below 170 MeV [141], matter exists in the hadronic phase, where quarks are confined to hadrons. Increasing temperature and/or baryon chemical potential, the system undergoes a transition to quark matter, where quarks and gluons are deconfined. At high temperatures, this phase is called quark-gluon plasma.

2.1.1 Chiral symmetry

The kinetic term of the QCD Lagrangian can be decomposed into terms for right-handed and left-handed quarks [140],

$$\sum_{i=1}^3 \bar{q}_i i \not{D} q_i = \sum_{i=1}^3 (\bar{q}_{Li} i \not{D} q_{Li} + \bar{q}_{Ri} i \not{D} q_{Ri}). \quad (2.2)$$

Thus, the kinetic term is symmetric under independent rotations of left-handed and right-handed quarks $q_{Li} \rightarrow L_{ij} q_{Lj}$ and $q_{Ri} \rightarrow R_{ij} q_{Rj}$. This $SU(3)_L \times SU(3)_R$ symmetry is called chiral symmetry. Chiral symmetry is broken twofold: it is broken explicitly in the QCD Lagrangian due to the quark mass term. This term can be written as

$$\sum_{i=1}^3 m_i \bar{q}_i q_i = \sum_{i,j} \bar{q}_{Ri} M_{ij} q_{Lj} + h.c., \quad (2.3)$$

where $M = \text{diag}(m_u, m_d, m_s)$ is the quark mass matrix. For non-zero quark masses this term couples left-handed and right-handed quarks and breaks chiral symmetry explicitly.

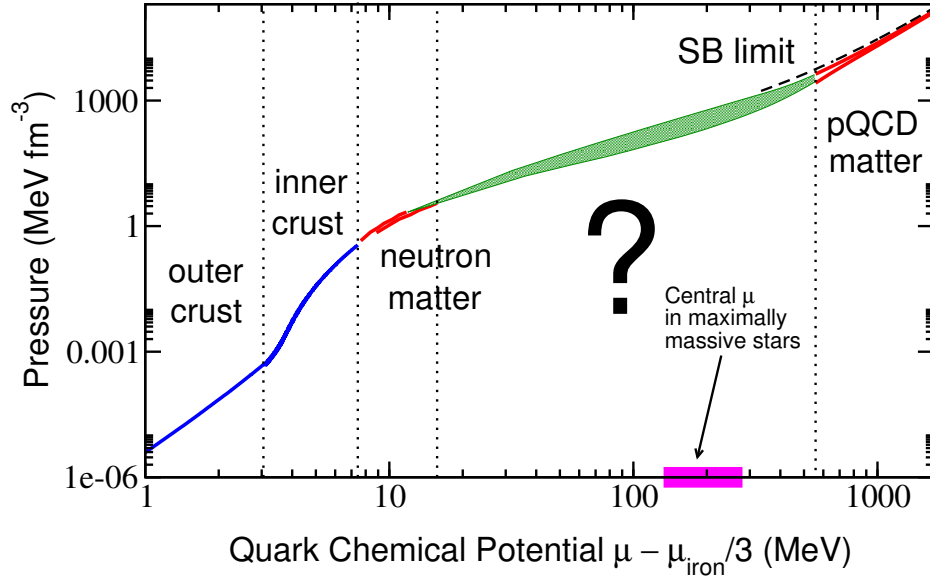


Figure 2.1: The neutron-star EoS in several density regions [142]. The EoS at low densities, which corresponds to low quark chemical potentials, is given by the crust EoS. At nuclear densities, one can infer the EoS from neutron-matter calculations. The higher density part cannot be calculated reliably so far. At very high chemical potentials, perturbative QCD can be used to constrain the EoS.

Chiral symmetry is furthermore also spontaneously broken. If this would not be the case, particles whose quantum numbers only differ in parity would appear in parity doublets. However, these particles differ in mass. The spontaneous chiral symmetry breaking leads to the formation of the chiral condensate $\langle \bar{q}q \rangle$, which is an order parameter for the chiral symmetry-breaking transition. The chiral condensate is the expectation value of a quark-antiquark pair in a system and is non-zero when chiral symmetry is spontaneously broken in the hadronic phase. It vanishes in the quark-gluon plasma, where quarks and gluons are deconfined.

Furthermore, according to Goldstone's theorem, spontaneous symmetry breaking leads to Goldstone bosons, which are massless excitations of the vacuum. The Goldstone bosons of spontaneously broken chiral symmetry are the pions. Due to the explicit breaking of chiral symmetry, pions acquire small masses, and are called Pseudo-Goldstone bosons.

The Pseudo-Goldstone bosons of spontaneously broken chiral symmetry play an important role for nuclear forces because the long-range parts of the nuclear interaction are described by pion-exchange interactions.

2.1.2 QCD calculations for neutron matter

It is not possible at the moment to infer properties of neutron matter from QCD directly due to the nonperturbativeness and complexity of QCD at the relevant low energies of interest. However, there are possibilities to obtain information directly from QCD at very high densities. Due to asymptotic freedom, at high energy scales, the strong coupling constant α_s becomes small and QCD can be solved perturbatively. Perturbative QCD can be used to constrain the high-density, high energy part of the equation of state [144, 145]. This has been used together with

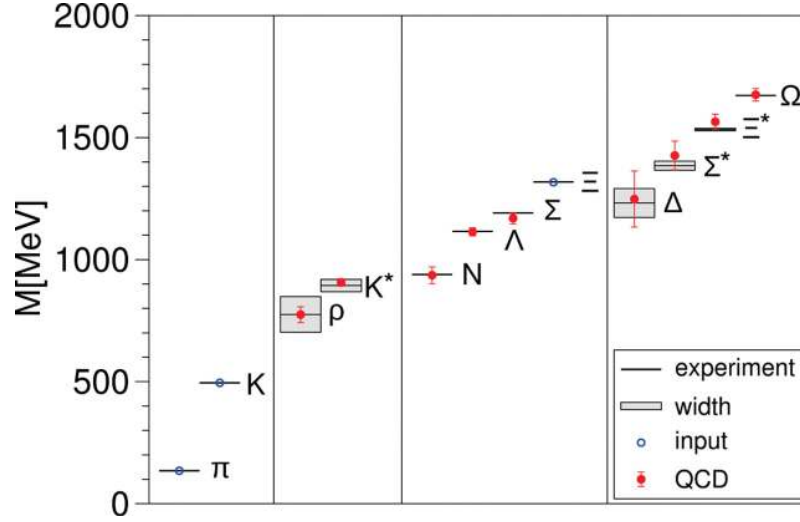


Figure 2.2: The spectrum of light hadrons calculated in LQCD [143]. The horizontal bars correspond to the experimental values with their width, the red crosses correspond to the LQCD results and their uncertainties. The blue dots are input parameters. See Ref. [143] for more details.

neutron-matter calculations at nuclear densities [57] to constrain the neutron-star EoS [142], as depicted in Fig. 2.1.

The only method available at the moment to obtain low-energy properties of nuclear systems directly from QCD is Lattice QCD (LQCD) [146]. In LQCD, quark and gluon fields are defined in hypercubic space-time lattice with a discretized space-time grid. Path integrals are evaluated numerically. The results of LQCD calculations are, among other values, characterized by the lattice size L , defining the volume, and the lattice spacing a , characterizing the coarseness of the grid. Although the results deviate from QCD results, these effects can be studied and systematically eliminated by extrapolating $a \rightarrow 0$ to the continuum and $L \rightarrow \infty$ to infinite volume.

A remarkable example of LQCD calculations is given in Ref. [143] and depicted in Fig. 2.2, where the light-hadron spectrum was calculated directly from LQCD at the physical pion mass. Many interesting results have been obtained in lattice QCD and nuclear physics observables become accessible in LQCD [147]. As examples we mention the calculation of nuclei and hyper-nuclei with $A \leq 4$ from Ref. [148], nucleon-nucleon scattering parameters [149], and magnetic moments of light nuclei [150]. There are many more interesting results in the given references and references therein.

However, LQCD is computationally very costly and LQCD results für $A \geq 2$ at the moment are only obtained at non-physical quark or, respectively, pion masses. The $A \geq 2$ results above were obtained at quark masses of $m_\pi \approx 800 \text{ MeV}$. To obtain valid results at physical quark masses, controlled extrapolations both to physical quark masses as well as to the continuum are needed. Furthermore, finite-lattice-size effects have to be eliminated. In order to do so one requires computationally expensive calculations as input.

It is to be expected, that light $A \leq 4$ nuclei at physical quark masses will become available in lattice QCD in the future. For heavier nuclei, however, many-body approaches based on lattice QCD input will be needed.

2.2 Chiral effective field theory for QCD at low energies

As stated before, at the energy region of interest for nuclear physics, QCD is non-perturbative, and, at the moment, only accessible in lattice QCD calculations, which are computationally very challenging. However, at low energies one can make use of effective field theories for QCD. These will be explained in the following Sections.

2.2.1 Basic principles

Effective field theories employ the idea of choosing the relevant degrees of freedom of the physical system of interest while leaving the symmetry properties of the system unchanged. In the theory of strong interactions, the basic degrees of freedom are quarks. However, at low energies and low momenta, which means large resolution scales, these are not resolved, and the degrees of freedom of interest are low-energy or low-momenta (long-distance) degrees of freedom, like external nucleon momenta. Only at higher energies, substructures can be resolved and new degrees of freedom will start to contribute. This is called separation of scales. At these high-energy scales, the effective field theory will break down. The dividing scale between these two energy regimes is called breakdown scale Λ_B and is characteristic for the EFT.

The effective field theory employs an expansion of the most general Lagrangian of the system, which is consistent with all the system's symmetries, in the typical low-momentum scale of the system q with respect to this breakdown scale q/Λ_B :

$$\mathcal{L} = \sum_v \left(\frac{q}{\Lambda_B} \right)^v \mathcal{F}_v(q, g_i). \quad (2.4)$$

Here, \mathcal{F}_v is a function of order 1 and the g_i are low-energy constants (LECs) which have to be determined. This expansion works better for lower energies of the system and for higher breakdown scales.

The different terms in the effective expansion are ordered according to the power v of q/Λ_B , using a power-counting scheme, which measures the importance of different expansion terms. There is a lowest order, or leading order (LO), $v = 0$, which includes the most important contributions and infinitely many higher orders, starting from next-to-leading order (NLO), $v = 2$, $N^2\text{LO}$, $v = 3$, etc., including contributions with decreasing importance. Due to the existence of a lowest order, only a limited number of interaction terms contribute at every order. For chiral effective field theory, which we will use in this work, precise results can be obtained already at $N^2\text{LO}$. Going to higher-order involves the determination of more LECs which limits the predictive power of the theory. However, the inclusion of higher-order terms decreases the theoretical uncertainty of the calculations, leading to a systematic improveability of the theory.

High-momentum degrees of freedom can only exist for short times or short distances, respectively. These length scales are not resolved in a low-energy EFT. As a consequence these degrees of freedom can be treated as heavy and can be integrated out. Interactions involving these high-momentum degrees of freedom are treated as contact interactions which are accompanied by low-energy couplings (LECs), g_i in Eq. (2.4). The LECs absorb high-momentum degrees of freedom, which is depicted in Fig. 2.3. For a natural EFT expansion, these LECs are of order ~ 1 and will not enlarge or diminish individual terms, which could lead to a delay in the EFT convergence. For NN interactions, the LECs are fitted to experimental data of the two-body

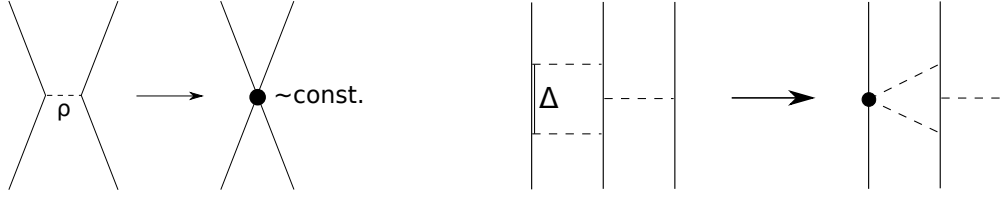


Figure 2.3: High-momentum degrees of freedom are treated as heavy and get absorbed into low-energy constants. Left: a rho-meson exchange between two nucleons is unresolved in pionless or chiral EFT and absorbed into a two-nucleon contact interaction accompanied by an LEC which includes the ρ meson. Right: in Δ -less EFT a Δ -excitation is not resolved explicitly and absorbed into a higher order vertex.

system, which contains information of all physics for all momentum scales. In principle, LECs can be calculated from QCD [151, 152].

Effective field theories of QCD incorporate not only nucleon-nucleon (NN) interactions but also many-body interactions such as three-nucleon (3N) and four-nucleon (4N) forces. These many-body interactions and their operator structure arise naturally in the EFT Lagrangian and are a result of the fact, that nucleons are composite particles and have a substructure of quarks and gluons, which is unresolved.

In EFTs for QCD, NN and many-body interactions are consistent and the same vertices in the two-body and many-body sectors are accompanied by the same LECs. Additional new LECs, which accompany only many-body interactions, may also appear and have to be fitted in few-body systems. Many-body forces involving four or more nucleons, however, seem to be less important and the main focus in nuclear physics at the moment lies on the better description of 3N interactions. It was shown that 3N forces have an important contributions to several physical systems, e.g., neutron matter [56, 57], neutron-rich nuclei [43, 153], and light nuclei [154]. The dominant uncertainties of these calculations are caused by the 3N forces.

2.2.2 Pionless effective field theory

As an example, we want to briefly introduce pionless effective field theory. For more details on this topic, see Ref. [135]. Pions, as the pseudo-Goldstone bosons of spontaneously broken chiral symmetry, are very light. However, at very low momenta, well below the pion mass of only $m_\pi \approx 140 \text{ MeV}$, the only relevant degrees of freedom are the nucleon momenta. The corresponding EFT is called pionless EFT. The breakdown scale of this theory is of the order of the pion mass.

In this regime, nuclear interactions are given by a set of different contact interactions with different momentum dependencies or derivatives, respectively. For example, the most general Lagrangian at lowest order has two independent interactions, because nucleons with $L=0$ can exist in an $S=0$ and $S=1$ state. It is given by

$$\mathcal{L} = N^\dagger \left(i\partial_0 + \frac{\nabla^2}{2m} + \dots \right) N - C_{0t}(N^\dagger P_t N)^2 - C_{0s}(N^\dagger P_s N)^2 + \dots, \quad (2.5)$$

where P_s and P_t are projectors on the $S=0$ and $S=1$ states, respectively.

Calculating the scattering T-matrix in one of these channels, we find that the intermediate state integrals in the scattering series are linearly divergent and have to be regularized introducing a regularization scheme with a certain cutoff Λ . This leads to a renormalization of the contact LECs to keep observables Λ -independent. It can be shown, that the renormalized contact LECs at LO are given by

$$C_0(\Lambda) = \frac{4\pi}{m} \frac{1}{\frac{1}{a_0} - c\Lambda}, \quad (2.6)$$

where $C_0(\Lambda)$ by construction gives cutoff independent results. The constant c depends on the regularization scheme. For a sharp cutoff, it is $c = 2/\pi$. Thus, the two momentum-independent LO contact interactions can reproduce the scattering lengths for the two possible $L = 0$ NN states in the effective-range expansion. Including also higher-order terms leads to the reproduction of the effective range and the shape parameters, and improves the predictions at higher energies. However, more LECs are needed to be fixed. In pionless EFT, in addition to NN forces, also 3N forces start contributing at LO. They are also given by a set of 3N contact interactions. Pionless EFT has been used to calculate low-energy systems, e.g., the deuteron [155].

2.2.3 Chiral effective field theory

Typical nucleon momenta in nuclei and in nuclear matter are of the order of the pion mass, which makes this momentum regime the regime of interest. At these momenta, pion interactions are explicitly resolved and pionless EFT will break down. To get an reliable description of nuclear systems, pions have to be included as degrees of freedom into the EFT. This EFT is called chiral EFT and makes use of the separation of scales between pion mass and the ρ meson mass, where new physics will enter. The Lagrangian is then expanded in terms of pion and nucleon degrees of freedom (Chiral perturbation theory, ChPT). The breakdown scale for chiral EFT is of the order of the ρ meson mass, $\Lambda_B \approx 500 \text{ MeV}$. Chiral EFT is founded in the seminal work of Weinberg [156, 157, 158, 159].

Chiral EFT includes short-range contact interactions similar to the ones in pionless EFT, but additionally explicitly includes also long-range pion exchange interactions. In chiral EFT, the expansion parameter is roughly

$$\frac{q}{\Lambda_B} \approx \frac{m_\pi}{\Lambda_B} \approx \frac{140 \text{ MeV}}{500 \text{ MeV}} \simeq \frac{1}{3}. \quad (2.7)$$

The power counting scheme in this work is Weinberg power counting, which is based on dimensional analysis, see Refs. [36, 37] and references therein for more details. In Weinberg power counting, every interaction term is characterized by the number of nucleon fields n_i , the number of pion fields p_i and the number of derivatives or insertions of the pion mass d_i . Derivatives contribute one power of q , meson fields $-1/2$ powers of q and each intermediate state contributes -1 power of q . Every loop adds 3 powers of q due to the integral over the loop momentum. For each interaction term the resulting power of q/Λ_B is then given by [157]

$$v = \sum_i V_i \left(d_i - \frac{1}{2} p_i \right) - D + 3L. \quad (2.8)$$




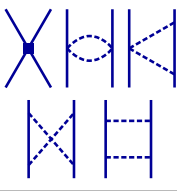



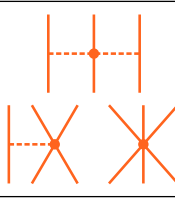


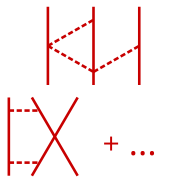
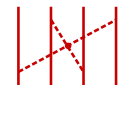
		NN	3N	4N
LO	$\mathcal{O}\left(\frac{Q^0}{\Lambda^0}\right)$			
NLO	$\mathcal{O}\left(\frac{Q^2}{\Lambda^2}\right)$			
N ² LO	$\mathcal{O}\left(\frac{Q^3}{\Lambda^3}\right)$			
N ³ LO	$\mathcal{O}\left(\frac{Q^4}{\Lambda^4}\right)$	 + ...	 + ...	 + ...

Figure 2.4: Hierarchy of nuclear forces in chiral EFT up to N³LO. 3N forces start to contribute at N²LO and 4N forces at N³LO.

Here, D is the number of intermediate states, L is the number of pion loops and V_i is the number of vertices of type i . Using the topological identities [157]

$$D = \sum_i V_i - 1, \quad I = L + D, \quad 2I + 2N = \sum_i V_i(p_i + n_i), \quad (2.9)$$

with the number of nucleons N and the number of internal lines I , and a modification to account for the proper normalization of N -nucleon states [151], one arrives at the power ν of the expansion in Weinberg power counting [136, 158]

$$\nu = -4 + 2N + 2L + \sum_i V_i \Delta_i, \quad \Delta_i = d_i + \frac{1}{2}n_i - 2. \quad (2.10)$$

From this equation one sees that diagrams with loops or vertices with a larger number of derivatives or pion mass insertions are suppressed by powers of q/Λ_B . Furthermore, this equation establishes a natural hierarchy of nuclear forces. Two-body interactions start at LO and dominate over many-body forces. At NLO, 3N interactions start to contribute, and at next-to-next-to-next-to-leading order (N³LO), 4N interactions have to be considered. The hierarchy of nuclear forces and different interaction topologies are depicted in Fig. 2.4 up to N³LO. The 3N forces vanish at NLO [136, 160], and the first non-vanishing 3N contribution appears at N²LO. An improved understanding of these leading 3N forces, which means an improved determination of their LECs, is a current frontier in nuclear physics and essential to produce reliable theoretical results.

Furthermore, the excitation of the Δ isobar can be included as an explicit degree of freedom because the Δ -nucleon mass difference is about 300 MeV and, thus, of the order of the pion mass and below the breakdown scale of chiral EFT. Intermediate Δ -baryon states can be excited in pion-nucleon and nucleon-nucleon vertices. Their contribution is absorbed in the higher-order vertices for the TPE, enhancing the corresponding LECs. This is depicted in the right part of Fig. 2.3. Chiral EFT with explicit Δ excitations is called Δ -full chiral EFT and research along these lines is in progress [161].

In this work we use Δ -less chiral EFT in QMC simulations, but in principle also Δ -full EFT can be included in QMC. In the following, we introduce the NN and 3N contributions to the Δ -less chiral interactions up to N^3 LO. We will ignore the 4N interactions as they have been found to be only small corrections [17, 57, 162].

2.2.4 Two-nucleon interactions up to N^3 LO

In chiral EFT, employing Weinberg power counting, the NN potential up to N^3 LO is given as a series of terms

$$V_{\text{chiral}} = V^{(0)} + V^{(2)} + V^{(3)} + V^{(4)} + \dots, \quad (2.11)$$

where the superscript denotes the power in the expansion parameter q/Λ_B . Two-nucleon interactions start at LO and are the dominant contributions to nuclear interactions.

In general, there are long- and intermediate-range contributions due to the exchange of one or more pions as well as short-range contact interactions parametrizing the short-range, or high-momentum, physics. As stated above, the latter are characterized by a set of LECs which have to be fit to experiment, while the first are completely determined by the chiral symmetry of QCD and low-energy experimental data for the pion-nucleon system.

The Weinberg counting scheme has been used in the derivation of nuclear forces [59, 163, 161, 164] and electromagnetic currents [165, 166] and has as a consequence that the leading relativistic corrections to the one-pion-exchange (OPE) potential enter at N^3 LO.

In the following, we discuss the chiral NN interactions up to N^3 LO, which are the current state-of-the-art chiral NN potentials. We will follow Ref. [59]. At LO, the NN interaction has no loops and only lowest-dimension vertices, $\Delta_i = 0$. There are two topologies: a two-nucleon-contact interaction and a one-pion exchange interaction. The contact interaction is parametrized as a set of operator structures, which in general contain momentum operators of the two particles, spin as well as isospin operators. The NN interactions depend on two momentum scales, usually chosen as the momentum transfer $\mathbf{q} = \mathbf{p}' - \mathbf{p}$ with the incoming and outgoing relative momenta $\mathbf{p} = (\mathbf{p}_1 - \mathbf{p}_2)/2$ and $\mathbf{p}' = (\mathbf{p}'_1 - \mathbf{p}'_2)/2$, respectively, and the momentum transfer in the exchange channel $\mathbf{k} = \frac{1}{2}(\mathbf{p}' + \mathbf{p})$. Here, the \mathbf{p}_i and \mathbf{p}'_i correspond to incoming and outgoing momenta of the nucleon i .

At LO, the NN forces are momentum independent, and the most general set of contact interactions is given by the operators $\mathbb{1}$, $\boldsymbol{\sigma}_1 \cdot \boldsymbol{\sigma}_2$, $\boldsymbol{\tau}_1 \cdot \boldsymbol{\tau}_2$, and $\boldsymbol{\sigma}_1 \cdot \boldsymbol{\sigma}_2 \boldsymbol{\tau}_1 \cdot \boldsymbol{\tau}_2$, leading to

$$V_{\text{cont}}^{(0)} = \alpha_1 + \alpha_2 \boldsymbol{\sigma}_1 \cdot \boldsymbol{\sigma}_2 + \alpha_3 \boldsymbol{\tau}_1 \cdot \boldsymbol{\tau}_2 + \alpha_4 \boldsymbol{\sigma}_1 \cdot \boldsymbol{\sigma}_2 \boldsymbol{\tau}_1 \cdot \boldsymbol{\tau}_2. \quad (2.12)$$

Out of these four terms only two are linearly independent. As nucleons are fermions, they obey the Pauli principle, and after antisymmetrization the potential V_{as} is given by:

$$V_{\text{as}} = \frac{1}{2}(V - \mathcal{A}[V]), \quad (2.13)$$

with the antisymmetrizer \mathcal{A} defined via

$$\begin{aligned}\mathcal{A}[V(\mathbf{q}, \mathbf{k})] &= \frac{1}{4}(1 + \boldsymbol{\sigma}_1 \cdot \boldsymbol{\sigma}_2)(1 + \boldsymbol{\tau}_1 \cdot \boldsymbol{\tau}_2) \\ &\times V\left(\mathbf{q} \rightarrow -2\mathbf{k}, \mathbf{k} \rightarrow -\frac{1}{2}\mathbf{q}\right).\end{aligned}\quad (2.14)$$

The momentum part of the antisymmetrizer can be easily derived for $\mathbf{q} = \mathbf{p}' - \mathbf{p} = \mathbf{p}'_2 - \mathbf{p}'_1 - \mathbf{p}_2 + \mathbf{p}_1$ and $\mathbf{k} = \frac{1}{2}(\mathbf{p} + \mathbf{p}') = \frac{1}{2}(\mathbf{p}'_2 - \mathbf{p}'_1 + \mathbf{p}_2 - \mathbf{p}_1)$ with the momentum-exchange operator \mathcal{P}_{12} :

$$\begin{aligned}\langle 1'2' | \mathcal{P}_{12} V(\mathbf{q}, \mathbf{k}) | 12 \rangle &= \langle 2'1' | V(\mathbf{q}, \mathbf{k}) | 12 \rangle \\ &= V\left(\mathbf{p}'_1 - \mathbf{p}'_2 - \mathbf{p}_2 + \mathbf{p}_1, \frac{1}{2}(\mathbf{p}'_1 - \mathbf{p}'_2 + \mathbf{p}_2 - \mathbf{p}_1)\right) \\ &= V\left(-2\mathbf{k}, -\frac{1}{2}\mathbf{q}\right).\end{aligned}\quad (2.15)$$

For the LO contact potential, we have

$$\begin{aligned}V_{\text{cont,as}}^{(0)} &= \frac{1}{2} \left(1 - \frac{1}{4}(1 + \boldsymbol{\sigma}_1 \cdot \boldsymbol{\sigma}_2)(1 + \boldsymbol{\tau}_1 \cdot \boldsymbol{\tau}_2) \right) V_{\text{cont}}^{(0)} \\ &= \left(\frac{3}{8}\alpha_1 - \frac{3}{8}\alpha_2 - \frac{3}{8}\alpha_3 - \frac{9}{8}\alpha_4 \right) \\ &\quad + \left(-\frac{1}{8}\alpha_1 + \frac{5}{8}\alpha_2 - \frac{3}{8}\alpha_3 + \frac{3}{8}\alpha_4 \right) \boldsymbol{\sigma}_1 \cdot \boldsymbol{\sigma}_2 \\ &\quad + \left(-\frac{1}{8}\alpha_1 - \frac{3}{8}\alpha_2 + \frac{5}{8}\alpha_3 + \frac{3}{8}\alpha_4 \right) \boldsymbol{\tau}_1 \cdot \boldsymbol{\tau}_2 \\ &\quad + \left(-\frac{1}{8}\alpha_1 + \frac{1}{8}\alpha_2 + \frac{1}{8}\alpha_3 + \frac{3}{8}\alpha_4 \right) \boldsymbol{\sigma}_1 \cdot \boldsymbol{\sigma}_2 \boldsymbol{\tau}_1 \cdot \boldsymbol{\tau}_2 \\ &= \tilde{C}_S + \tilde{C}_T \boldsymbol{\sigma}_1 \cdot \boldsymbol{\sigma}_2 + \left(-\frac{2}{3}\tilde{C}_S - \tilde{C}_T \right) \boldsymbol{\tau}_1 \cdot \boldsymbol{\tau}_2 \\ &\quad + \left(-\frac{1}{3}\tilde{C}_S \right) \boldsymbol{\sigma}_1 \cdot \boldsymbol{\sigma}_2 \boldsymbol{\tau}_1 \cdot \boldsymbol{\tau}_2.\end{aligned}\quad (2.16)$$

Obviously, there are only two independent couplings at leading order after antisymmetrization. This is similar to pionless EFT, and these two couplings describe the two possible S wave channels. Following Weinberg [167], the two commonly chosen LO contact operators are

$$V_{\text{cont}}^{(0)} = C_S + C_T \boldsymbol{\sigma}_1 \cdot \boldsymbol{\sigma}_2, \quad (2.17)$$

but in principle any different two of the four contact interactions can be chosen, and all operator structures are obtained after antisymmetrization. This is analogous to Fierz ambiguities. The chosen contact operators depend on the spin-independent contact coupling C_S and the spin-dependent contact coupling C_T , where C_S usually has to be large and negative while C_T is much smaller [157]. This can be inferred from the nuclear S wave phase shifts.

In addition to contact operators, the one-pion-exchange (OPE) interaction appears at LO, given by

$$V_{\text{OPE}}^{(0)} = -\frac{g_A^2}{4f_\pi^2} \frac{\boldsymbol{\sigma}_1 \cdot \mathbf{q} \boldsymbol{\sigma}_2 \cdot \mathbf{q}}{q^2 + m_\pi^2} \boldsymbol{\tau}_1 \cdot \boldsymbol{\tau}_2 \quad (2.18)$$

in momentum space. Here, g_A , f_π , and m_π denote the axial-vector coupling constant of the nucleon, the pion decay constant, and the pion mass, respectively. In general, we can write all pion-exchange contributions in the form

$$\begin{aligned} V_\pi = & V_C + \boldsymbol{\tau}_1 \cdot \boldsymbol{\tau}_2 W_C \\ & + (V_S + \boldsymbol{\tau}_1 \cdot \boldsymbol{\tau}_2 W_S) \boldsymbol{\sigma}_1 \cdot \boldsymbol{\sigma}_2 \\ & + (V_T + \boldsymbol{\tau}_1 \cdot \boldsymbol{\tau}_2 W_T) \boldsymbol{\sigma}_1 \cdot \mathbf{q} \boldsymbol{\sigma}_2 \cdot \mathbf{q} \\ & + (V_{LS} + \boldsymbol{\tau}_1 \cdot \boldsymbol{\tau}_2 W_{LS}) i(\boldsymbol{\sigma}_1 + \boldsymbol{\sigma}_2) \cdot \mathbf{q} \times \mathbf{k} \\ & + (V_{\sigma L} + \boldsymbol{\tau}_1 \cdot \boldsymbol{\tau}_2 W_{\sigma L}) \boldsymbol{\sigma}_1 \cdot \mathbf{q} \times \mathbf{k} \boldsymbol{\sigma}_2 \cdot \mathbf{q} \times \mathbf{k}, \end{aligned} \quad (2.19)$$

with central, spin, tensor, spin-orbit and quadratic spin-orbit components, respectively. The OPE interaction adds to the isospin-dependent tensor channel, W_T . It describes the longest-range contributions to nuclear forces.

At NLO ($\nu = 2$), 14 different contact interactions are allowed by symmetries:

$$\begin{aligned} V_{\text{cont}}^{(2)} = & \gamma_1 q^2 + \gamma_2 q^2 \boldsymbol{\sigma}_1 \cdot \boldsymbol{\sigma}_2 + \gamma_3 q^2 \boldsymbol{\tau}_1 \cdot \boldsymbol{\tau}_2 \\ & + \gamma_4 q^2 \boldsymbol{\sigma}_1 \cdot \boldsymbol{\sigma}_2 \boldsymbol{\tau}_1 \cdot \boldsymbol{\tau}_2 \\ & + \gamma_5 k^2 + \gamma_6 k^2 \boldsymbol{\sigma}_1 \cdot \boldsymbol{\sigma}_2 + \gamma_7 k^2 \boldsymbol{\tau}_1 \cdot \boldsymbol{\tau}_2 \\ & + \gamma_8 k^2 \boldsymbol{\sigma}_1 \cdot \boldsymbol{\sigma}_2 \boldsymbol{\tau}_1 \cdot \boldsymbol{\tau}_2 \\ & + \gamma_9 (\boldsymbol{\sigma}_1 + \boldsymbol{\sigma}_2) (\mathbf{q} \times \mathbf{k}) \\ & + \gamma_{10} (\boldsymbol{\sigma}_1 + \boldsymbol{\sigma}_2) (\mathbf{q} \times \mathbf{k}) \boldsymbol{\tau}_1 \cdot \boldsymbol{\tau}_2 \\ & + \gamma_{11} (\boldsymbol{\sigma}_1 \cdot \mathbf{q}) (\boldsymbol{\sigma}_2 \cdot \mathbf{q}) \\ & + \gamma_{12} (\boldsymbol{\sigma}_1 \cdot \mathbf{q}) (\boldsymbol{\sigma}_2 \cdot \mathbf{q}) \boldsymbol{\tau}_1 \cdot \boldsymbol{\tau}_2 \\ & + \gamma_{13} (\boldsymbol{\sigma}_1 \cdot \mathbf{k}) (\boldsymbol{\sigma}_2 \cdot \mathbf{k}) \\ & + \gamma_{14} (\boldsymbol{\sigma}_1 \cdot \mathbf{k}) (\boldsymbol{\sigma}_2 \cdot \mathbf{k}) \boldsymbol{\tau}_1 \cdot \boldsymbol{\tau}_2. \end{aligned} \quad (2.20)$$

In analogy to the LO case, only seven couplings are independent and one has the freedom to choose an appropriate basis. Many currently available versions of chiral potentials [59, 60] use the 7 isospin-independent operators

$$\begin{aligned} V_{\text{cont}}^{(2)} = & \bar{C}_1 q^2 + \bar{C}_2 q^2 \boldsymbol{\sigma}_1 \cdot \boldsymbol{\sigma}_2 + \bar{C}_3 k^2 + \bar{C}_4 k^2 \boldsymbol{\sigma}_1 \cdot \boldsymbol{\sigma}_2 \\ & + \bar{C}_5 (\boldsymbol{\sigma}_1 + \boldsymbol{\sigma}_2) (\mathbf{q} \times \mathbf{k}) + \bar{C}_6 (\boldsymbol{\sigma}_1 \cdot \mathbf{q}) (\boldsymbol{\sigma}_2 \cdot \mathbf{q}) + \bar{C}_7 (\boldsymbol{\sigma}_1 \cdot \mathbf{k}) (\boldsymbol{\sigma}_2 \cdot \mathbf{k}). \end{aligned} \quad (2.21)$$

Later we will make use of the possibility to choose different 7 out of these 14 operators. Furthermore, the strength of the OPE potential is slightly shifted due to the Goldberger-Treiman discrepancy (GTD) [168],

$$g_{\pi N} = \frac{g_A m_N}{F_\pi} \left(1 - \frac{2M_\pi^2 \bar{d}_{18}}{g_A} \right), \quad (2.22)$$

where $g_{\pi N}$ is the pion-nucleon coupling constant and \bar{d}_{18} is a LEC from the third-order pion-nucleon effective Lagrangian, which is of the same order in the chiral expansion as $V_{NN}^{(2)}$. This leads to a replacement of g_A by $g_A - 2\bar{d}_{18}M_\pi^2$ in the OPE potential. For further corrections which lead to a renormalization of the LECs g_A, f_π , and M_π see Ref. [169].

In addition, at NLO two-pion-exchange (TPE) interactions appear, which include pion loops that have to be regularized. We use the spectral-function-regularization (SFR). In the framework of the SFR, the loop integrals in the spectral representation of the TPE potential go from $2M_\pi$ to the ultraviolet cutoff $\tilde{\Lambda}$ rather than to ∞ corresponding to the case of dimensional regularization [170]. Taking $\tilde{\Lambda}$ of the order of Λ_b ensures that no unnaturally large short-range terms are induced by the subleading TPE potential [171]. The momentum-space expressions for the NLO TPE potential in the spectral-function representation with spectral function cutoff $\tilde{\Lambda}$ are given by

$$W_C^{\text{NLO}}(q) = -\frac{1}{384\pi^2 f_\pi^2} L^{\tilde{\Lambda}}(q) \left(4m_\pi^2(5g_A^4 - 4g_A^2 - 1) + q^2(23g_A^4 - 10g_A^2 - 1) + \frac{48g_A^4 m_\pi^4}{4m_\pi^2 + q^2} \right), \quad (2.23)$$

$$V_T^{\text{NLO}}(q) = -\frac{1}{q^2} V_S^{\text{NLO}}(q) = -\frac{3g_A^4}{64\pi^2 f_\pi^4} L^{\tilde{\Lambda}}(q), \quad (2.24)$$

where the loop function $L^{\tilde{\Lambda}}(q)$ is given by

$$L^{\tilde{\Lambda}}(q) = \Theta(\tilde{\Lambda} - 2m_\pi) \frac{\omega}{2q} \ln \frac{\tilde{\Lambda}^2 \omega^2 + q^2 s^2 + 2\tilde{\Lambda} q \omega s}{4m_\pi^2 (\tilde{\Lambda}^2 + q^2)}, \quad (2.25)$$

with

$$\omega = \sqrt{q^2 + 4m_\pi^2}, \quad s = \sqrt{\tilde{\Lambda}^2 - 4m_\pi^2}. \quad (2.26)$$

At N^2LO there are no additional contact interactions but corrections to the lower-order pion exchanges. Corrections to the OPE potential lead to a renormalization of g_A . Additional subleading TPE contributions appear. They are given by

$$V_C^{\text{N}^2\text{LO}}(q) = -\frac{3g_A^2}{16\pi f_\pi^4} \left(2m_\pi^2(2c_1 - c_3) - c_3 q^2 \right) (2m_\pi^2 + q^2) A^{\tilde{\Lambda}}(q), \quad (2.27)$$

$$W_T^{\text{N}^2\text{LO}}(q) = -\frac{1}{q^2} W_S^{\text{N}^2\text{LO}}(q) = -\frac{g_A^2}{32\pi f_\pi^4} c_4 (4m_\pi^2 + q^2) A^{\tilde{\Lambda}}(q), \quad (2.28)$$

where c_i denote the LECs of the subleading pion-nucleon vertices [172]. These LECs absorb Δ excitation effects in the TPE interaction and, hence, are enlarged. The loop function $A^{\tilde{\Lambda}}(q)$ is defined via

$$A^{\tilde{\Lambda}}(q) = \Theta(\tilde{\Lambda} - 2m_\pi) \frac{1}{2q} \arctan \frac{q(\tilde{\Lambda} - 2m_\pi)}{q^2 + 2\tilde{\Lambda}m_\pi}. \quad (2.29)$$

At N³LO additional contact operators $\sim q^4$ add to the potential. There are in total 30 different operator structures

$$\begin{aligned}
V_{\text{cont}}^{(4)} = & \delta_1 \mathbf{q}^4 + \delta_2 \mathbf{q}^4 \boldsymbol{\tau}_1 \cdot \boldsymbol{\tau}_2 + \delta_3 \mathbf{k}^4 + \delta_4 \mathbf{k}^4 \boldsymbol{\tau}_1 \cdot \boldsymbol{\tau}_2 \\
& + \delta_5 \mathbf{q}^2 \mathbf{k}^2 + \delta_6 \mathbf{q}^2 \mathbf{k}^2 \boldsymbol{\tau}_1 \cdot \boldsymbol{\tau}_2 + \delta_7 (\mathbf{q} \times \mathbf{k})^2 \\
& + \delta_8 (\mathbf{q} \times \mathbf{k})^2 \boldsymbol{\tau}_1 \cdot \boldsymbol{\tau}_2 \\
& + \delta_9 \mathbf{q}^4 \boldsymbol{\sigma}_1 \cdot \boldsymbol{\sigma}_2 + \delta_{10} \mathbf{q}^4 \boldsymbol{\sigma}_1 \cdot \boldsymbol{\sigma}_2 \boldsymbol{\tau}_1 \cdot \boldsymbol{\tau}_2 \\
& + \delta_{11} \mathbf{k}^4 \boldsymbol{\sigma}_1 \cdot \boldsymbol{\sigma}_2 + \delta_{12} \mathbf{k}^4 \boldsymbol{\sigma}_1 \cdot \boldsymbol{\sigma}_2 \boldsymbol{\tau}_1 \cdot \boldsymbol{\tau}_2 \\
& + \delta_{13} \mathbf{q}^2 \mathbf{k}^2 \boldsymbol{\sigma}_1 \cdot \boldsymbol{\sigma}_2 + \delta_{14} \mathbf{q}^2 \mathbf{k}^2 \boldsymbol{\sigma}_1 \cdot \boldsymbol{\sigma}_2 \boldsymbol{\tau}_1 \cdot \boldsymbol{\tau}_2 \\
& + \delta_{15} (\mathbf{q} \times \mathbf{k})^2 \boldsymbol{\sigma}_1 \cdot \boldsymbol{\sigma}_2 + \delta_{16} (\mathbf{q} \times \mathbf{k})^2 \boldsymbol{\sigma}_1 \cdot \boldsymbol{\sigma}_2 \boldsymbol{\tau}_1 \cdot \boldsymbol{\tau}_2 \\
& + i \frac{1}{2} \delta_{17} \mathbf{q}^2 (\boldsymbol{\sigma}_1 + \boldsymbol{\sigma}_2) \cdot (\mathbf{q} \times \mathbf{k}) \\
& + i \frac{1}{2} \delta_{18} \mathbf{q}^2 (\boldsymbol{\sigma}_1 + \boldsymbol{\sigma}_2) \cdot (\mathbf{q} \times \mathbf{k}) \boldsymbol{\tau}_1 \cdot \boldsymbol{\tau}_2 \\
& + i \frac{1}{2} \delta_{19} \mathbf{k}^2 (\boldsymbol{\sigma}_1 + \boldsymbol{\sigma}_2) \cdot (\mathbf{q} \times \mathbf{k}) \\
& + i \frac{1}{2} \delta_{20} \mathbf{k}^2 (\boldsymbol{\sigma}_1 + \boldsymbol{\sigma}_2) \cdot (\mathbf{q} \times \mathbf{k}) \boldsymbol{\tau}_1 \cdot \boldsymbol{\tau}_2 \\
& + \delta_{21} \mathbf{q}^2 \boldsymbol{\sigma}_1 \cdot \mathbf{q} \boldsymbol{\sigma}_2 \cdot \mathbf{q} + \delta_{22} \mathbf{q}^2 \boldsymbol{\sigma}_1 \cdot \mathbf{q} \boldsymbol{\sigma}_2 \cdot \mathbf{q} \boldsymbol{\tau}_1 \cdot \boldsymbol{\tau}_2 \\
& + \delta_{23} \mathbf{k}^2 \boldsymbol{\sigma}_1 \cdot \mathbf{q} \boldsymbol{\sigma}_2 \cdot \mathbf{q} + \delta_{24} \mathbf{k}^2 \boldsymbol{\sigma}_1 \cdot \mathbf{q} \boldsymbol{\sigma}_2 \cdot \mathbf{q} \boldsymbol{\tau}_1 \cdot \boldsymbol{\tau}_2 \\
& + \delta_{25} \mathbf{q}^2 \boldsymbol{\sigma}_1 \cdot \mathbf{k} \boldsymbol{\sigma}_2 \cdot \mathbf{k} + \delta_{26} \mathbf{q}^2 \boldsymbol{\sigma}_1 \cdot \mathbf{k} \boldsymbol{\sigma}_2 \cdot \mathbf{k} \boldsymbol{\tau}_1 \cdot \boldsymbol{\tau}_2 \\
& + \delta_{27} \mathbf{k}^2 \boldsymbol{\sigma}_1 \cdot \mathbf{k} \boldsymbol{\sigma}_2 \cdot \mathbf{k} + \delta_{28} \mathbf{k}^2 \boldsymbol{\sigma}_1 \cdot \mathbf{k} \boldsymbol{\sigma}_2 \cdot \mathbf{k} \boldsymbol{\tau}_1 \cdot \boldsymbol{\tau}_2 \\
& + \delta_{29} ((\boldsymbol{\sigma}_1 + \boldsymbol{\sigma}_2) \cdot (\mathbf{q} \times \mathbf{k}))^2 \\
& + \delta_{30} ((\boldsymbol{\sigma}_1 + \boldsymbol{\sigma}_2) \cdot (\mathbf{q} \times \mathbf{k}))^2 \boldsymbol{\tau}_1 \cdot \boldsymbol{\tau}_2,
\end{aligned} \tag{2.30}$$

from which usually the 15 isospin-independent operators are chosen [59, 60].

Additionally, at N³LO, further corrections to the OPE potential arise leading to a renormalization of the OPE potential as well as the contact interactions [59]. Additionally, relativistic $1/m^2$ corrections will appear at this order and the OPE potential then takes the form

$$V_{\text{OPE}}(q) = - \left(\frac{g_A}{2f_\pi} \right)^2 \left(1 - \frac{p^2 + p'^2}{2m^2} \right) \boldsymbol{\tau}_1 \cdot \boldsymbol{\tau}_2 \frac{\boldsymbol{\sigma}_1 \cdot \mathbf{q} \boldsymbol{\sigma}_2 \cdot \mathbf{q}}{q^2 + m_\pi^2}. \tag{2.31}$$

For the N³LO loop corrections to the TPE potential, no closed expressions can be given and we refer to Ref. [59] for the corresponding expressions. Also, relativistic $1/m$ corrections to the TPE arise, introducing spin-orbit interactions into the TPE potential.

At N³LO additional three-pion-exchange interactions appear. The three-pion-exchange is much weaker than the TPE potentials [59] at long distances and only enhances the total potential at small r , where chiral EFT is anyways unreliable.

In addition to these forces, isospin-breaking corrections have to be included in chiral potentials. They are due to the difference in charged and neutral pion masses in pion exchanges in the nn, np, and pp systems and due to electromagnetic forces between nucleons. We will not give these expressions here and refer the reader to Ref. [59] for more details.

The above potential introduces ultraviolet divergences into the scattering equation because the potential grows with q . To overcome this problem, the potentials are regularized with typical momentum space regulators of the form $f_\Lambda(p) = \exp(-(p/\Lambda)^{2n})$ with a positive number n and $f(p')$. With this regulator function, the potential in the Lippmann-Schwinger equation becomes $V(\mathbf{p}, \mathbf{p}') \rightarrow f_\Lambda(p)V(\mathbf{p}, \mathbf{p}')f_\Lambda(p')$.

2.2.5 Three-nucleon interactions up to N³LO

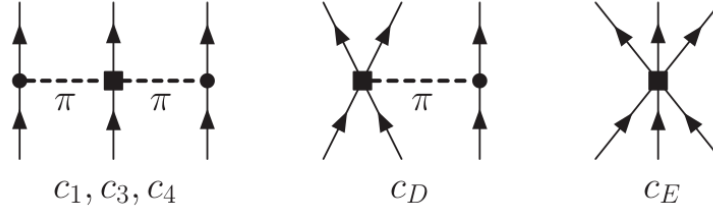


Figure 2.5: 3N force topologies at N²LO. The long-range two-pion-exchange depends on the LECs c_1 , c_3 and c_4 , the intermediate-range one-pion-exchange-contact part on c_D and the short-range three-nucleon-contact interaction on c_E .

The leading 3N forces start to contribute at N²LO [160, 173] and consist of three topologies: a two-pion-exchange part V_C , a one-pion-exchange-contact part V_D and a three-nucleon-contact interaction V_E , see Fig. 2.5.

The two-pion exchange part V_C depends on the LECs c_1 , c_3 and c_4 and is given by

$$V_C = \frac{1}{2} \left(\frac{g_A}{2f_\pi} \right)^2 \sum_{i \neq j \neq k} \frac{(\boldsymbol{\sigma}_i \cdot \mathbf{q}_i)(\boldsymbol{\sigma}_j \cdot \mathbf{q}_j)}{(q_i^2 + m_\pi^2)(q_j^2 + m_\pi^2)} F_{ijk}^{\alpha\beta} \tau_i^\alpha \tau_j^\beta. \quad (2.32)$$

The function $F_{ijk}^{\alpha\beta}$ is defined as

$$F_{ijk}^{\alpha\beta} = \delta^{\alpha\beta} \left[-\frac{4c_1 m_\pi^2}{f_\pi^2} + \frac{2c_3}{f_\pi^2} \mathbf{q}_i \cdot \mathbf{q}_j \right] + \sum_\gamma \frac{c_4}{f_\pi^2} \epsilon^{\alpha\beta\gamma} \tau_k^\gamma \boldsymbol{\sigma}_k \cdot (\mathbf{q}_i \times \mathbf{q}_j), \quad (2.33)$$

and contains different two-pion exchange structures, whose strength is determined by the LECs c_i , which already appear in the NN sector in the subleading TPE interactions at N²LO, see Eqs. (2.27) and (2.28).

The one-pion-exchange contact interaction V_D is given by

$$V_D = -\frac{g_A}{8f_\pi^2} \frac{c_D}{f_\pi^2 \Lambda_\chi} \sum_{i \neq j \neq k} \frac{\boldsymbol{\sigma}_j \cdot \mathbf{q}_j}{q_j^2 + m_\pi^2} (\boldsymbol{\tau}_i \cdot \boldsymbol{\tau}_j) (\boldsymbol{\sigma}_i \cdot \mathbf{q}_j), \quad (2.34)$$

where c_D is the corresponding LEC and $\Lambda_\chi = 700$ MeV.

The third contribution is the three-nucleon-contact interaction V_E which is given by

$$V_E = \frac{1}{2} \frac{c_E}{f_\pi^4 \Lambda_\chi} \sum_{j \neq k} (\boldsymbol{\tau}_j \cdot \boldsymbol{\tau}_k). \quad (2.35)$$

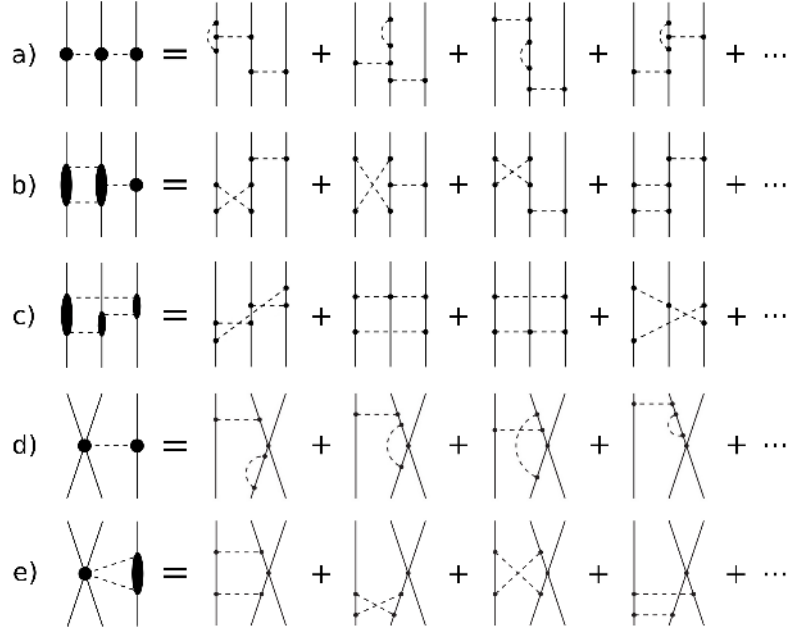


Figure 2.6: Sample of different diagrams for the 3N force topologies at $N^3\text{LO}$ introduced in Refs. [174] and [175]. There are five topologies: a) two-pion-exchange topology, b) two-pion-one-pion-exchange topology, c) pion-ring topology, d) one-pion-exchange-contact topology, e) two-pion-exchange-contact topology. In addition, there are contributions due to relativistic corrections. All of these contributions are completely predicted from the NN sector and no new LECs appear.

It is determined by the LEC c_E .

The LECs c_D and c_E are new many-body parameters appearing in the leading 3N forces and have to be adjusted to reproduce few-body observables, commonly chosen among the ^3H and ^4He binding energies or radii. We will go into detail about the fitting of these constants in Sec. 6.3.

The 3N forces at $N^3\text{LO}$ have been derived in Refs. [174, 175]. They contain no new parameters and are completely predicted from the LO NN sector. They depend only on C_S and C_T and consist of five topologies with diagrams with one loop or tree diagrams with dimension-two vertices. Additionally, there appear relativistic $1/m$ corrections to the NLO 3N forces:

$$V_{3N} = V_{2\pi} + V_{2\pi-1\pi} + V_{\text{ring}} + V_{1\pi\text{-cont}} + V_{2\pi\text{-cont}} + V_{1/m}.$$

Here, $V^{2\pi}$, $V^{2\pi-1\pi}$ and V^{ring} are the long-range two-pion exchange, the two-pion-one-pion exchange and the pion-ring contributions, respectively [174], and $V^{1\pi\text{-cont}}$, $V^{2\pi\text{-cont}}$ and $V^{1/m}$ are the the short-range one-pion-exchange-contact, the two-pion-exchange-contact contributions, and the relativistic corrections [175]. The topologies are depicted in Fig. 2.6.

The two-pion-exchange topology is show in Fig. 2.6 and only leads to shifts in the values of the LECs c_1 , c_3 and c_4 [174],

$$c_1 \rightarrow \bar{c}_1 = c_1 - \frac{g_A^2 m_\pi}{64\pi f_\pi^2}, \quad c_3 \rightarrow \bar{c}_3 = c_3 + \frac{g_A^4 m_\pi}{16\pi f_\pi^2}, \quad c_4 \rightarrow \bar{c}_4 = c_4 - \frac{g_A^4 m_\pi}{16\pi f_\pi^2}. \quad (2.36)$$

Furthermore, the N³LO TPE topology has another contribution,

$$V_{2\pi}^{(4)} = \frac{g_A^4}{256\pi f_\pi^6} \sum_{i \neq j \neq k} \frac{(\boldsymbol{\sigma}_i \cdot \mathbf{q}_i)(\boldsymbol{\sigma}_j \cdot \mathbf{q}_j)}{(q_i^2 + m_\pi^2)(q_j^2 + m_\pi^2)} \left[\boldsymbol{\tau}_i \cdot \boldsymbol{\tau}_j \left(m_\pi(m_\pi^2 + 3q_i^2 + 3q_j^2 + 4\mathbf{q}_i \cdot \mathbf{q}_j) \right. \right. \\ \left. \left. + (2m_\pi^2 + q_i^2 + q_j^2 + 2\mathbf{q}_i \cdot \mathbf{q}_j)(3m_\pi^2 + 3q_i^2 + 3q_j^2 + 4\mathbf{q}_i \cdot \mathbf{q}_j)A(q_k) \right) \right. \\ \left. - (\boldsymbol{\tau}_i \times \boldsymbol{\tau}_j) \cdot \boldsymbol{\tau}_k (\mathbf{q}_i \times \mathbf{q}_j) \cdot \boldsymbol{\sigma}_k \left(m_\pi + (4m_\pi^2 + q_i^2 + q_j^2 + 2\mathbf{q}_i \cdot \mathbf{q}_j)A(q_k) \right) \right], \quad (2.37)$$

with the loop function $A(q)$

$$A(q) = \frac{1}{2q} \arctan\left(\frac{q}{2m_\pi}\right). \quad (2.38)$$

The two-pion-one-pion-exchange topology can be written as

$$V_{2\pi-1\pi} = \sum_{i \neq j \neq k} \frac{\boldsymbol{\sigma}_j \cdot \mathbf{q}_j}{q_j^2 + m_\pi^2} \left[\boldsymbol{\tau}_i \cdot \boldsymbol{\tau}_j \left(\boldsymbol{\sigma}_k \cdot \mathbf{q}_i \mathbf{q}_i \cdot \mathbf{q}_j F_1(q_i) + \boldsymbol{\sigma}_k \cdot \mathbf{q}_i F_2(q_i) + \boldsymbol{\sigma}_k \cdot \mathbf{q}_j F_3(q_1) \right) \right. \\ \left. + \boldsymbol{\tau}_k \cdot \boldsymbol{\tau}_j \left(\boldsymbol{\sigma}_i \cdot \mathbf{q}_i \mathbf{q}_i \cdot \mathbf{q}_j F_4(q_i) + \boldsymbol{\sigma}_i \cdot \mathbf{q}_j F_5(q_i) + \boldsymbol{\sigma}_k \cdot \mathbf{q}_i F_6(q_i) + \boldsymbol{\sigma}_k \cdot \mathbf{q}_j F_7(q_i) \right) \right. \\ \left. + (\boldsymbol{\tau}_i \times \boldsymbol{\tau}_k) \cdot \boldsymbol{\tau}_j (\boldsymbol{\sigma}_i \times \boldsymbol{\sigma}_k) \cdot \mathbf{q}_i F_8(q_i) \right], \quad (2.39)$$

with the structure functions $F_1(q)$ to $F_8(q)$ defined as

$$F_1(q) = -\frac{g_A^6}{256\pi f_\pi^6} \left[\frac{m_\pi}{4m_\pi^2 + q^2} + \frac{2m_\pi}{q^2} - \frac{8m_\pi^2 + q^2}{q^2} A(q) \right] \\ + \frac{g_A^4}{256\pi f_\pi^6} \left[\frac{m_\pi}{q^2} + \frac{q^2 - 4m_\pi^2}{q^2} A(q) \right], \quad (2.40)$$

$$F_2(q) = \frac{1}{2} F_6(q) = F_7(q) = -4F_8(q) = \frac{g_A^4}{128\pi f_\pi^6} \left[m_\pi + (q^2 + 2m_\pi^2)A(q) \right], \quad (2.41)$$

$$F_3(q) = -\frac{g_A^6}{256\pi f_\pi^6} \left[3m_\pi + (8m_\pi^2 + 3q^2)A(q) \right] + \frac{g_A^4}{256\pi f_\pi^6} \left[m_\pi + (q^2 + 4m_\pi^2)A(q) \right], \quad (2.42)$$

$$F_4(q) = -\frac{1}{q^2} F_5(q) = -\frac{g_A^6}{128\pi f_\pi^6} A(q). \quad (2.43)$$

The pion-ring topology at N³LO contains very involved structure functions and is given by

$$V_{\text{ring}} = \sum_{i \neq j \neq k} \boldsymbol{\sigma}_i \cdot \boldsymbol{\sigma}_k \boldsymbol{\tau}_k \cdot \boldsymbol{\tau}_j R_1 + \boldsymbol{\sigma}_i \cdot \mathbf{q}_i \boldsymbol{\sigma}_k \cdot \mathbf{q}_i \boldsymbol{\tau}_k \cdot \boldsymbol{\tau}_j R_2 + \boldsymbol{\sigma}_i \cdot \mathbf{q}_i \boldsymbol{\sigma}_k \cdot \mathbf{q}_j \boldsymbol{\tau}_k \cdot \boldsymbol{\tau}_j R_3 \\ + \boldsymbol{\sigma}_i \cdot \mathbf{q}_j \boldsymbol{\sigma}_k \cdot \mathbf{q}_i \boldsymbol{\tau}_k \cdot \boldsymbol{\tau}_j R_4 + \boldsymbol{\sigma}_i \cdot \mathbf{q}_j \boldsymbol{\sigma}_k \cdot \mathbf{q}_j \boldsymbol{\tau}_k \cdot \boldsymbol{\tau}_j R_5 + \boldsymbol{\tau}_i \cdot \boldsymbol{\tau}_j R_6 + \boldsymbol{\sigma}_i \cdot \mathbf{q}_i \boldsymbol{\sigma}_j \cdot \mathbf{q}_i R_7 \\ + \boldsymbol{\sigma}_i \cdot \mathbf{q}_i \boldsymbol{\sigma}_j \cdot \mathbf{q}_j R_8 + \boldsymbol{\sigma}_i \cdot \mathbf{q}_j \boldsymbol{\sigma}_j \cdot \mathbf{q}_i R_9 + \boldsymbol{\sigma}_i \cdot \boldsymbol{\sigma}_j R_{10} + \mathbf{q}_i \cdot (\mathbf{q}_j \times \boldsymbol{\sigma}_k) \boldsymbol{\tau}_i \cdot (\boldsymbol{\tau}_k \times \boldsymbol{\tau}_j) R_{11} \\ + \boldsymbol{\tau}_i \cdot \boldsymbol{\tau}_k S_1 + \boldsymbol{\sigma}_i \cdot \mathbf{q}_i \boldsymbol{\sigma}_j \cdot \mathbf{q}_i \boldsymbol{\tau}_i \cdot \boldsymbol{\tau}_k S_2 + \boldsymbol{\sigma}_i \cdot \mathbf{q}_j \boldsymbol{\sigma}_j \cdot \mathbf{q}_i \boldsymbol{\tau}_i \cdot \boldsymbol{\tau}_k S_3 + \boldsymbol{\sigma}_i \cdot \mathbf{q}_i \boldsymbol{\sigma}_j \cdot \mathbf{q}_j \boldsymbol{\tau}_i \cdot \boldsymbol{\tau}_k S_4 \\ + \boldsymbol{\sigma}_i \cdot \mathbf{q}_j \boldsymbol{\sigma}_j \cdot \mathbf{q}_j \boldsymbol{\tau}_i \cdot \boldsymbol{\tau}_k S_5 + \boldsymbol{\sigma}_i \cdot \boldsymbol{\sigma}_j \boldsymbol{\tau}_i \cdot \boldsymbol{\tau}_k S_6 + \mathbf{q}_i \cdot (\mathbf{q}_j \times \boldsymbol{\sigma}_i) \boldsymbol{\tau}_i \cdot (\boldsymbol{\tau}_k \times \boldsymbol{\tau}_j) S_7. \quad (2.44)$$

The structure functions R_i and S_i defined in Eqs. (A2) and (A7) of Ref. [174]. Note that there is a factor of 1/2 missing in the structure functions R_6 , R_8 , R_9 , R_{10} , and R_{11} [17, 57]. The one-pion-exchange-contact topology vanishes at N³LO [175]. The two-pion-exchange-contact topology is given by

$$V_{2\pi\text{-cont}} = \frac{g_A^4 C_T}{48\pi f_\pi^4} \sum_{i \neq j \neq k} \left[2\boldsymbol{\tau}_i \cdot \boldsymbol{\tau}_k \boldsymbol{\sigma}_k \cdot \boldsymbol{\sigma}_j \left(3m_\pi - \frac{m_\pi^3}{4m_\pi^2 + q_i^2} + 2(2m_\pi^2 + q_i^2)A(q_i) \right) + 9(\mathbf{q}_i \cdot \boldsymbol{\sigma}_i \mathbf{q}_i \cdot \boldsymbol{\sigma}_k - q_i^2 \boldsymbol{\sigma}_i \cdot \boldsymbol{\sigma}_k) A(q_i) \right] - \frac{g_A^2 C_T}{24\pi f_\pi^4} \sum_{i \neq j \neq k} \boldsymbol{\tau}_i \cdot \boldsymbol{\tau}_k \boldsymbol{\sigma}_k \cdot \boldsymbol{\sigma}_j (m_\pi + (2m_\pi^2 + q_i^2)A(q_i)). \quad (2.45)$$

The interaction depends on the spin-dependent two-body LO contact coupling C_T . The last contribution to the 3N forces at N³LO stems from relativistic corrections to the NLO 3N TPE and OPE-contact topologies, and is given by

$$V_{1/m} = \frac{g_A^2}{32m_N f_\pi^4} \sum_{i \neq j \neq k} \frac{1}{(q_i^2 + m_\pi^2)(q_j^2 + m_\pi^2)} \left[\boldsymbol{\tau}_i \cdot \boldsymbol{\tau}_j (\boldsymbol{\sigma}_i \cdot \mathbf{q}_i \boldsymbol{\sigma}_j \cdot \mathbf{q}_j a_{ikj} + \boldsymbol{\sigma}_i \cdot \mathbf{q}_i \boldsymbol{\sigma}_j \cdot \mathbf{k}_j c_{ikj}) + (\boldsymbol{\tau}_i \times \boldsymbol{\tau}_k) \cdot \boldsymbol{\tau}_j (\boldsymbol{\sigma}_i \cdot \mathbf{q}_i \boldsymbol{\sigma}_j \cdot \mathbf{q}_j b_{ikj} + \boldsymbol{\sigma}_i \cdot \mathbf{q}_i \boldsymbol{\sigma}_j \cdot \mathbf{k}_j d_{ikj}) \right] + \frac{g_A^2}{8m_N f_\pi^2} \sum_{i \neq j \neq k} \frac{1}{q_i^2 + m_\pi^2} \boldsymbol{\tau}_i \cdot \boldsymbol{\tau}_k (\boldsymbol{\sigma}_i \cdot \mathbf{q}_i f_{ikj} + \boldsymbol{\sigma}_i \cdot \mathbf{k}_i g_{ikj}). \quad (2.46)$$

Here, a_{ikj} , b_{ikj} , c_{ikj} , d_{ikj} , f_{ikj} , and g_{ikj} are functions defined in Eqs. (4.11) and (4.13) of Ref. [175]. In addition to C_T , they depend on the spin-independent LO two-body contact coupling C_S and on the constants $\bar{\beta}_8$ and $\bar{\beta}_9$ [175].

For the regularization of the 3N forces, several regulators can be chosen. In our infinite matter calculations, we usually employ a regulator of the form

$$f_R(p, q) = \exp[-((k_1^2 + k_2^2 + k_3^2 - \mathbf{k}_1 \cdot \mathbf{k}_2 - \mathbf{k}_1 \cdot \mathbf{k}_3 - \mathbf{k}_2 \cdot \mathbf{k}_3)/(3\Lambda_{3N}^2))^{n_{\text{exp}}}], \quad (2.47)$$

with the single-particle momenta \mathbf{k}_i and $n_{\text{exp}} = 4$. In contrast, also regulators on the momentum exchanges can be chosen, like in Ref. [176]. We will give more details on 3N regularization in Sec. 6.5.

2.3 Results with chiral EFT interactions

The systematics of chiral EFT makes it a powerful tool for nuclear physics and enables calculations with controlled theoretical uncertainties. Especially the consistent description of many-body forces, and in particular 3N forces, leads to remarkable results for neutron-rich nuclei and the evolution of shell structure for these, as well as for the neutron-matter EoS. It was shown, that the 3N forces are a necessary ingredient for the correct reproduction and prediction of nuclear observables and that they constitute the dominant uncertainty in current chiral EFT calculations.

In the following, we present current state-of-the art calculations employing chiral EFT Hamiltonians for nuclei and nuclear matter.

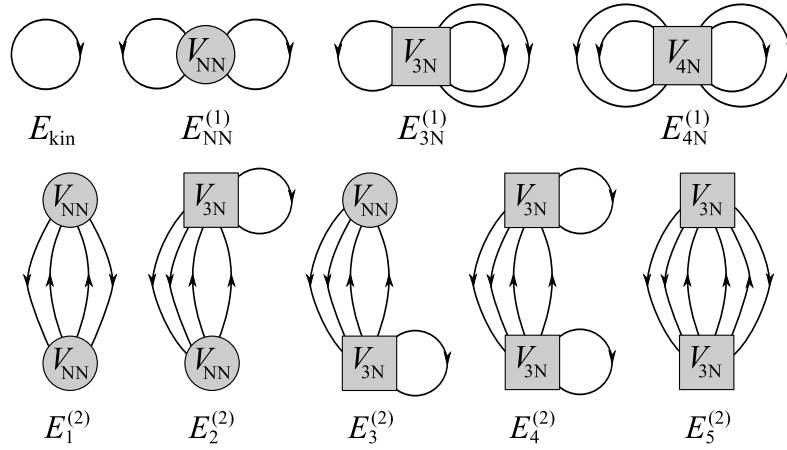


Figure 2.7: Diagrams up to second order in many-body perturbation theory. The diagrams in the first row contribute to the Hartree-Fock energy. These are the kinetic energy E_{kin} and the first order NN, 3N, and 4N interaction energies $E_{\text{NN}}^{(1)}$, $E_{3\text{N}}^{(1)}$, and $E_{4\text{N}}^{(1)}$. The other diagrams are second-order contributions to the energy due to NN-NN interactions ($E_1^{(2)}$), NN-3N interactions ($E_2^{(2)}$ and $E_3^{(2)}$), and 3N-3N interactions ($E_4^{(2)}$ and $E_5^{(2)}$). We left out diagrams for 2nd-order contributions involving 4N forces.

2.3.1 Many-body perturbation theory

Many-body perturbation theory (MBPT) is a systematically improvable many-body method and was used to calculate current state-of-the-art theoretical results for nuclear matter and neutron-rich nuclei using chiral EFT. In the following we will focus on MBPT calculations for nuclear matter because we will use these calculations later in this work.

In general, a system's Hamiltonian has contributions of NN and many-body forces and is given by

$$H = T + V_{\text{NN}} + V_{3\text{N}} + V_{4\text{N}} + \dots \quad (2.48)$$

with the kinetic energy T , the NN interactions V_{NN} , 3N interactions $V_{3\text{N}}$, and 4N interactions $V_{4\text{N}}$. In MBPT, the interaction is treated as a perturbation, thus, giving the kinetic energy as the zeroth-order contribution to the energy. The first-order corrections due to NN ($E_{\text{NN}}^{(1)}$), 3N ($E_{3\text{N}}^{(1)}$), and 4N ($E_{4\text{N}}^{(1)}$) interactions are given by

$$\begin{aligned} E^{(1)} &= \sum_{\alpha} \langle \alpha | V | \alpha \rangle \\ &= \sum_{\alpha_{\text{NN}}} \langle \alpha_{\text{NN}} | V_{\text{NN}} | \alpha_{\text{NN}} \rangle + \sum_{\alpha_{3\text{N}}} \langle \alpha_{3\text{N}} | V_{3\text{N}} | \alpha_{3\text{N}} \rangle + \sum_{\alpha_{4\text{N}}} \langle \alpha_{4\text{N}} | V_{4\text{N}} | \alpha_{4\text{N}} \rangle \\ &= E_{\text{NN}}^{(1)} + E_{3\text{N}}^{(1)} + E_{4\text{N}}^{(1)}, \end{aligned} \quad (2.49)$$

where we sum over different states α of the system, in detail NN, 3N and 4N states. These different contributions, together with the kinetic energy, are depicted in the first row of Fig. 2.7.

For infinite nuclear matter, the Hartree-Fock (HF) states of the system can be labeled by the momenta, spins and isospins of the particles. Summing over all these quantum numbers, for an a -particle HF contribution to the energy per particle E/A one finds

$$\frac{E^{(1)}}{A} = \frac{1}{a! \cdot n} \left(\prod_{i=1}^a \text{tr}_{\tau_i} \text{tr}_{\sigma_i} \int \frac{d^3 k_i}{(2\pi)^3} n_{\mathbf{k}_i} \right) f_R^2(p, q) \langle 1 \cdots a | \mathcal{A}_{1 \cdots a} V_a | 1 \cdots a \rangle, \quad (2.50)$$

with the spin and isospin Pauli matrices of the i -th particle σ_i and τ_i , the particle momentum distribution $n_{\mathbf{k}_i}$, the regulator function $f_R(p, q)$, the a -body antisymmetrizer $\mathcal{A}_{1 \cdots a}$, and the momentum states $|1 \cdots a\rangle$ for the a particles.

The second-order energy contribution to the energy in MBPT is given by

$$E^{(2)} = \sum_{\alpha \neq \beta} \frac{\langle \alpha | V | \beta \rangle \langle \beta | V | \alpha \rangle}{E_{\alpha}^{(0)} - E_{\beta}^{(0)}}, \quad (2.51)$$

with the many-body states α and β . Since $4N$ forces are small, we will ignore all higher-order contributions including them. The $3N$ forces usually enter as antisymmetrized density-dependent two-body interactions, which are constructed by summing the third particle over occupied states in the Fermi sea [54]

$$\bar{V}_{3N} = \text{tr}_{\tau_3} \text{tr}_{\sigma_3} \int \frac{d^3 k_3}{(2\pi)^3} n_{\mathbf{k}_3} \mathcal{A}_{123} V_{3N}. \quad (2.52)$$

We obtain then for the second-order energy contributions

$$\begin{aligned} E^{(2)} &= \sum_{\alpha_{NN} \neq \beta_{NN}} \frac{\langle \alpha_{NN} | V_{NN} | \beta_{NN} \rangle \langle \beta_{NN} | V_{NN} | \alpha_{NN} \rangle}{E_{\alpha_{NN}}^{(0)} - E_{\beta_{NN}}^{(0)}} \\ &+ \sum_{\alpha_{NN} \neq \beta_{NN}} \frac{\langle \alpha_{NN} | V_{NN} | \beta_{NN} \rangle \langle \beta_{NN} | \bar{V}_{3N} | \alpha_{NN} \rangle}{E_{\alpha_{NN}}^{(0)} - E_{\beta_{NN}}^{(0)}} \\ &+ \sum_{\alpha_{NN} \neq \beta_{NN}} \frac{\langle \alpha_{NN} | \bar{V}_{3N} | \beta_{NN} \rangle \langle \beta_{NN} | V_{NN} | \alpha_{NN} \rangle}{E_{\alpha_{NN}}^{(0)} - E_{\beta_{NN}}^{(0)}} \\ &+ \sum_{\alpha_{NN} \neq \beta_{NN}} \frac{\langle \alpha_{NN} | \bar{V}_{3N} | \beta_{NN} \rangle \langle \beta_{NN} | \bar{V}_{3N} | \alpha_{NN} \rangle}{E_{\alpha_{NN}}^{(0)} - E_{\beta_{NN}}^{(0)}} \\ &+ \sum_{\alpha_{3N} \neq \beta_{3N}} \frac{\langle \alpha_{3N} | V_{3N} | \beta_{3N} \rangle \langle \beta_{3N} | V_{3N} | \alpha_{3N} \rangle}{E_{\alpha_{3N}}^{(0)} - E_{\beta_{3N}}^{(0)}} \\ &= E_1^{(2)} + E_2^{(2)} + E_3^{(2)} + E_4^{(2)} + E_5^{(2)}. \end{aligned} \quad (2.53)$$

These five contributions are NN-NN correlations ($E_1^{(2)}$), NN-3N correlations ($E_2^{(2)}$ and $E_3^{(2)}$) and 3N-3N correlations ($E_4^{(2)}$ and $E_5^{(2)}$). These contributions are depicted in the middle and bottom row of Fig. 2.7.

In infinite homogeneous matter, we can again integrate over all states and find for the 2nd order correction terms $E_1^{(2)} - E_4^{(2)}$

$$E_{1-4}^{(2)} = \frac{1}{4} \left(\prod_{i=1}^4 \text{tr}_{\tau_i} \text{tr}_{\sigma_i} \int \frac{d^3 k_i}{(2\pi)^3} \right) |\langle 12 | V_{NN/3N} | 34 \rangle|^2 \frac{n_{\mathbf{k}_1} n_{\mathbf{k}_2} (1 - n_{\mathbf{k}_3})(1 - n_{\mathbf{k}_4})}{\epsilon_{\mathbf{k}_1} + \epsilon_{\mathbf{k}_2} - \epsilon_{\mathbf{k}_3} - \epsilon_{\mathbf{k}_4}} \quad (2.54)$$

$$\times (2\pi)^3 \delta(\mathbf{k}_1 + \mathbf{k}_2 - \mathbf{k}_3 - \mathbf{k}_4),$$

with $V_{NN/3N}$ being the antisymmetrized NN or density-dependent 3N interaction and $\epsilon_{\mathbf{k}_i}$ the single-particle energies. The term $E_5^{(2)}$ is given by

$$E_5^{(2)} = \frac{1}{36} \left(\prod_{i=1}^6 \text{tr}_{\tau_i} \text{tr}_{\sigma_i} \int \frac{d^3 k_i}{(2\pi)^3} \right) |\langle 123 | \mathcal{A}_{123} V_{3N} | 456 \rangle|^2 \frac{n_{\mathbf{k}_1} n_{\mathbf{k}_2} n_{\mathbf{k}_3} (1 - n_{\mathbf{k}_4})(1 - n_{\mathbf{k}_5})(1 - n_{\mathbf{k}_6})}{\epsilon_{\mathbf{k}_1} + \epsilon_{\mathbf{k}_2} + \epsilon_{\mathbf{k}_3} - \epsilon_{\mathbf{k}_4} - \epsilon_{\mathbf{k}_5} - \epsilon_{\mathbf{k}_6}} \quad (2.55)$$

$$\times (2\pi)^3 \delta(\mathbf{k}_1 + \mathbf{k}_2 + \mathbf{k}_3 - \mathbf{k}_4 - \mathbf{k}_5 - \mathbf{k}_6).$$

We will not discuss corrections beyond second order here, although we also include particle-particle contributions from third order in our calculations, see Ref. [55]. Their size provides an estimate of the convergence of the MBPT calculation.

In addition to nuclear matter, MBPT is also used in the framework of the nuclear shell model to derive Hamiltonians for the valence space [177]. It is used in a diagrammatic approach to calculate the single-particle energies and two-body matrix elements necessary for the shell model calculations and includes further corrections, e.g., contributions from outside the valence space, perturbatively. In state-of-the-art calculations, NN and 3N interactions are included up to third order.

Pioneering MBPT results of neutron matter with chiral NN and many-body forces at $N^3\text{LO}$ have been obtained, where the subleading 3N forces have been included in first order [17, 57]. We show these results in Fig. 2.8. The results include uncertainties in the many-body forces, in the many-body calculation, as well as due to cutoff variation. We show bands for different NN potentials, and for each band the uncertainty is dominated by the many-body forces and in particular by the uncertainties in the 3N LECs c_i . However, the many-body method also adds a sizeable contribution to the uncertainty. The final result at n_0 , including all uncertainties, is $14.1 - 21.0 \text{ MeV}$ per particle. The neutron-matter energy of Fig. 2.8 agrees very well with NLO lattice results [53] and QMC simulations [178] at very low densities, and with variational calculations [118] and AFDMC calculations (GCR) [16] based on phenomenological potentials, where the latter is adjusted to an energy difference of 32 MeV between neutron matter and the empirical saturation point.

In Fig. 2.8 we also show newer $N^3\text{LO}$ neutron-matter results, which in addition to the previous results also include second-order corrections to the $N^3\text{LO}$ 3N forces [179]. The two bands show excellent agreement and the inclusion of the second-order contributions reduces the theoretical uncertainty of the calculation by $\sim 1 \text{ MeV}$ at n_0 .

For infinite-matter results with finite proton fraction, current state-of-the-art calculations with arbitrary proton fractions are presented in Ref. [120]. However, these results do not yet include $N^3\text{LO}$ many-body forces.

Remarkable results using MBPT in shell model calculations have been obtained for neutron-rich oxygen [153] and calcium isotopes [34, 180, 181]. The calcium chain is optimally suited for computations of the shell evolution in neutron-rich nuclei because it contains two doubly magic

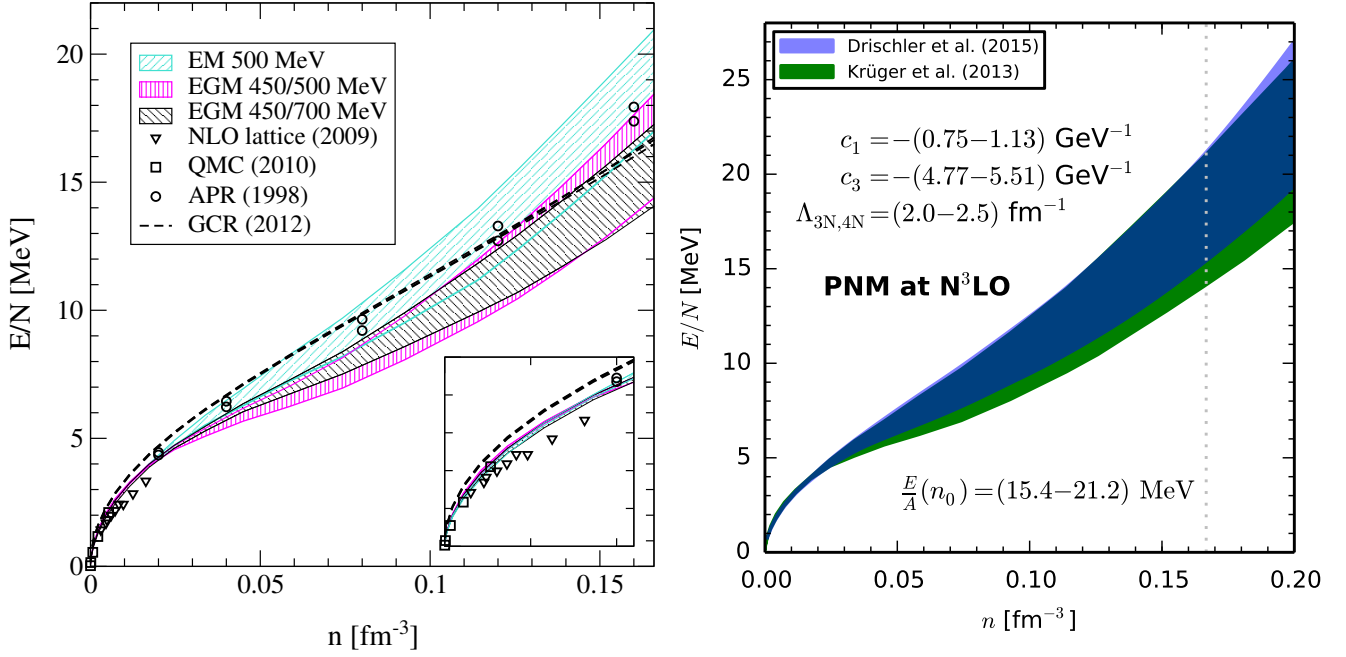


Figure 2.8: Left: Neutron-matter energy per particle as a function of density including NN, and first-order 3N and 4N forces at $N^3\text{LO}$ [57, 17]. The three overlapping bands are labeled by the different NN potentials and include uncertainty estimates due to the many-body calculation, the low-energy c_i constants and by varying the 3N/4N cut-offs. For comparison, results are shown at low densities (see also the inset) from NLO lattice [53] and Quantum Monte Carlo (QMC) simulations [178], and at nuclear densities from variational (APR) [118] and AFDMC calculations (GCR) [16] based on adjusted nuclear force models. Right: Neutron matter energy per particle when also including 2nd-order corrections for the $N^3\text{LO}$ 3N forces [179] (blue) in comparison with the calculation without these corrections from the left panel (green).

nuclei (^{40}Ca , ^{48}Ca). Furthermore, there is a lot of experimental data in the calcium chain and recent high-precision experiments found new shell closures in ^{52}Ca and ^{54}Ca [34, 114]. MBPT calculations are in very good agreement with experimental findings [34, 181], see also Fig. 2.9. In oxygen, the neutron drip line is anomalously close to the valley of stability. This so-called oxygen anomaly cannot be explained by only considering NN forces in the nuclear Hamiltonian and is only described when 3N forces are considered. This has been shown in MBPT shell-model calculations with chiral interactions [43] and was confirmed using different *ab initio* methods, which we will describe in the next Section.

2.3.2 Ab initio results

To derive properties of nuclear systems from first principles, two ingredients are needed: 1) a reliable Hamiltonian derived within a systematic theory bases on QCD and 2) an *ab initio* many-body method without further approximations. Chiral EFT Hamiltonians are connected to QCD by construction and have been successfully used in several *ab initio* many-body methods. In the following we briefly want to present these methods. For more details, we refer the reader to Ref. [35].

In the coupled-cluster (CC) method [61], one starts from a closed-shell reference state and similarity transforms a normal-ordered Hamiltonian H , $\tilde{H} = e^{-T} H e^T$, where T is the so-called cluster operator. The cluster operator includes particle-hole excitations for up to A particles, $T = T_1 + T_2 + \dots T_A$, to all orders. Usually, only single and double excitations are included (CCSD), $T = T_1 + T_2$. The operators T_1 and T_2 are obtained by solving the coupled-cluster equations. CC methods are limited in the regard that they can only access nuclei which are one or two particles away from closed shells.

Another method is the self-consistent Green's function (SCGF) approach [182, 183], where the single-particle Green's function is calculated to infer information about the propagation of single-particle and single-hole excitations in the system to find the system's ground state. In Gorkov SCGF [184, 185], also open-shell nuclei can be accessed.

Another method is the in-medium similarity renormalization group (IM-SRG) approach [186, 187], where the system's Hamiltonian is unitarily transformed to a band- or block-diagonal form. This leads to a decoupling of the ground and excited states. Recent progress allows to access open-shell nuclei (MR-IM-SRG) [188].

In the no-core shell model (NCSM) [39] the Hamiltonian is exactly diagonalized to solve the many-body problem. Using importance truncation (IT-NCSM) [189, 40], larger model spaces can be accessed.

Further methods include nuclear lattice EFT [41, 42], which defines the nuclear many-body problem on a space-time lattice similar to lattice QCD, and the hyperspherical harmonics (HH) approach [190], using hyperspherical harmonic basis functions.

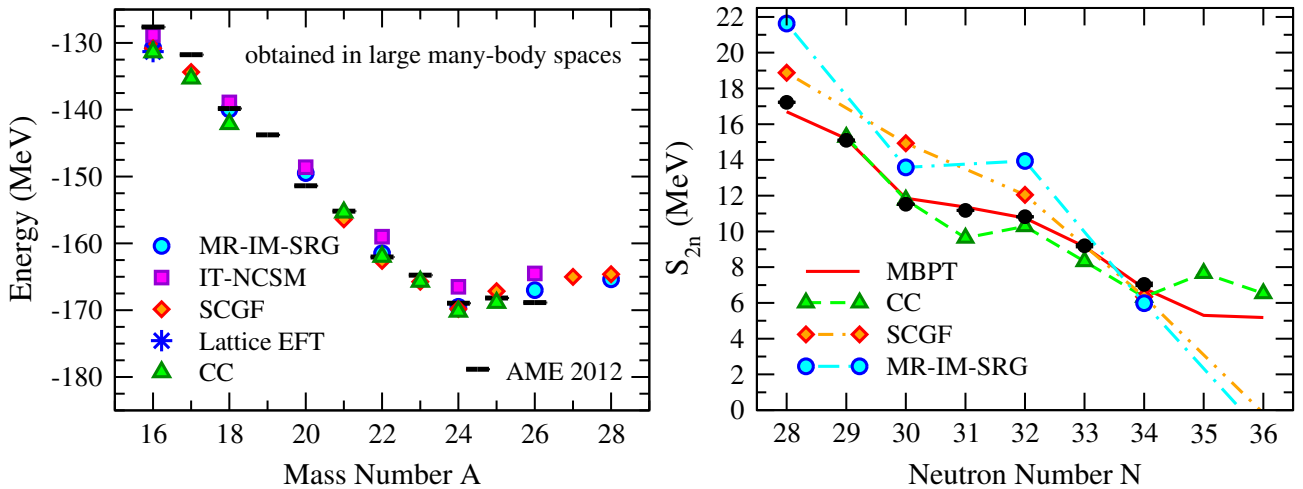


Figure 2.9: Left: Ground state energies of the oxygen isotopes for different many-body methods using chiral NN and 3N forces compared to experiment. Right: Two-neutron separation energies S_{2n} in the neutron-rich side of the Calcium chain for different methods compared to experiment. The pictures are taken from Ref. [35].

These methods have been used to calculate both nuclei and infinite nuclear matter. In Fig. 2.9 we show the ground state energies of the neutron-rich oxygen isotopes for different many-body methods using chiral NN and 3N forces as well as two-neutron separation energies S_{2n} in the neutron-rich side of the Calcium chain for different methods, compared to experimental values, see Ref. [35] and references therein. In the oxygen chain, the different many-body methods show remarkable agreement and all predict the neutron drip line at ^{24}O .

For the calcium chain, different methods lead to a spread in the predictions of the S_{2n} energies but the MBPT results agree with the experimental results [34, 114]. Furthermore, for larger neutron numbers, different methods predict different trends and it will be interesting to obtain more experimental data on these nuclei.

The CC approach as well as the SCGF method have also been used to calculate infinite nuclear matter [191, 192, 193, 194]. We will compare with these results later in this thesis.

2.3.3 Motivation for nonperturbative benchmarks

Remarkable results have been obtained with chiral interactions in a multitude of different many-body methods for both nuclear matter and nuclei. The current state-of-the-art results for infinite matter up to $N^3\text{LO}$ are obtained in the framework of MBPT. These calculations suffer from several problems.

The successful MBPT method can only be used for interactions which converge sufficiently fast. For these perturbative interactions, reliable results can already be obtained at second order in perturbation theory. However, chiral EFT has a freedom to choose a regularization scheme and cutoffs over a certain range in momentum-space, leading to different possible potential properties. For low-momentum cutoffs, one obtains soft interactions, which are usually perturbative. For higher cutoffs, the potentials become less perturbative, which makes them unsuitable for MBPT and several other many-body methods. Thus, all these harder interactions cannot be explored.

Second, in MBPT calculations, no definite answer can be given on the question if results are already converged or not. As the calculation of higher orders is very cumbersome, many calculations stop at second or third order in MBPT. It is not clear if the results at this orders are already converged. In addition to the uncertainty of nuclear Hamiltonians this introduces additional uncertainties due to the many-body method, as stated in Ref. [57]. For MBPT in shell model, the estimation of uncertainties is work in progress.

It would be desirable to minimize the theoretical uncertainties due to the many-body method to reduce the overall uncertainty. Furthermore, it would be worthwhile to being able to clearly investigate different chiral interactions. To achieve this, one needs a nonperturbative and precise *ab initio* method, to calculate nonperturbative benchmarks for neutron matter for, e.g., neutron stars, for ultracold atoms, and for nuclei based on chiral EFT interactions. While some of the *ab initio* methods presented above provide the possibility of nonperturbative benchmarks in certain regions of the nuclear chart and for infinite matter, the very powerful family of quantum Monte Carlo (QMC) methods has so far not been used with chiral EFT interactions due to nonlocalities in the momentum-space formulation of chiral interactions.

QMC simulations provide the possibility of solving the many-body Schrödinger equation stochastically, using Monte Carlo integration methods. The accuracy of these simulations is mainly determined by the number of Monte Carlo runs and, thus, can be improved to a certain level with increasing number of computations. QMC methods have been found to be one of the most reliable many-body methods and have been used to obtain high-precision results of light nuclei [195] and nuclear matter [16] with phenomenological interactions. We introduce the family of these methods in Chap. 3.

In this work, we develop QMC calculations with chiral EFT interactions to combine systematic nuclear interactions with a reliable many-body method. This will allow us to provide nonperturbative benchmarks for all the systems discussed above, to test the perturbativeness of chiral

interactions, to benchmark current state-of-the-art results, and also to provide the possibility to match chiral EFT to lattice QCD simulations, for example for few-neutron systems in a box, and also varying the pion mass in chiral EFT.

3 Quantum Monte Carlo

A very powerful family of *ab initio* many-body methods are Quantum Monte Carlo methods. In this Chapter, we explain the basic ideas of QMC approaches and present the two QMC methods we will use throughout this work: Green's function Monte Carlo (GFMC) [196, 74] and auxiliary-field diffusion Monte Carlo (AFDMC) [77]. These methods have been used in the past with phenomenological interactions of the Argonne type [197, 198] and 3N interactions of the Urbana [199] and Illinois [200] form to calculate light nuclei and neutron-matter properties with high precision. We will present some of these results at the end of this Chapter.

3.1 Basic principles

The QMC family of methods is an *ab initio* method aimed at solving the many-body Schrödinger equation exactly using stochastic algorithms. The GFMC method as well as the AFDMC method are very close to Diffusion Monte Carlo (DMC) where the Schrödinger equation is regarded as a diffusion equation in imaginary time, acting on a trial wave function $|\psi_T\rangle$. By evolving the trial wave function to large imaginary times, the true ground state of the system can be projected out, if trial wave function and ground state wave function overlap. Otherwise, the lowest energy eigenstate which has an overlap with the trial wave function will be obtained.

Starting from the trial wave function $|\psi_T\rangle$, which can be developed in the eigenfunctions $|\phi_i\rangle$ of the system's Hamiltonian, $|\psi_T\rangle = \sum_i a_i |\phi_i\rangle$, we find for the system's wave function $|\psi(t)\rangle$ at time t

$$\begin{aligned} |\psi(t)\rangle &= e^{-\frac{i\hat{H}t}{\hbar}} |\psi_T\rangle = e^{-\frac{\hat{H}\tau}{\hbar}} |\psi_T\rangle = \sum_i e^{-\frac{E_i\tau}{\hbar}} a_i |\phi_i\rangle \\ &= e^{-\frac{E_0\tau}{\hbar}} a_0 |\phi_0\rangle + e^{-\frac{E_1\tau}{\hbar}} a_1 |\phi_1\rangle + e^{-\frac{E_2\tau}{\hbar}} a_2 |\phi_2\rangle + \dots \\ &\xrightarrow{\tau \rightarrow \infty} a_0 |\phi_0\rangle, \end{aligned} \quad (3.1)$$

where we assume $E_0 = 0$ for better illustration. Thus, for large τ , only the ground state has a nonvanishing contribution.

We start from the many-body Schrödinger equation in imaginary time $\tau = i \cdot t$ for N particles,

$$H |\Psi(\mathbf{R}, \tau)\rangle = -\frac{\partial}{\partial \tau} |\Psi(\mathbf{R}, \tau)\rangle, \quad (3.2)$$

where $\mathbf{R} = \{\mathbf{r}_1, \dots, \mathbf{r}_N, \mathbf{s}_1, \dots, \mathbf{s}_N\}$ contains the configurations of all N particles with all degrees of freedom. While the \mathbf{r}_i are the Cartesian coordinates of the particles, the \mathbf{s}_i contain all spin and isospin coordinates of the system and are four-spinors with complex amplitudes for the base $|p \uparrow\rangle, |p \downarrow\rangle, |n \uparrow\rangle$, and $|n \downarrow\rangle$.

From this follows that the wave function at imaginary time τ , $|\Psi(\mathbf{R}, \tau)\rangle$, is obtained from a wave function at a starting time τ_0 due to time evolution,

$$|\Psi(\mathbf{R}, \tau)\rangle = e^{-\frac{\hat{H}}{\hbar}(\tau - \tau_0)} |\Psi(\mathbf{R}, \tau_0)\rangle. \quad (3.3)$$

In the following we set $\hbar = 1$ and use the general solution for the Schrödinger equation,

$$\Psi(\mathbf{R}, \tau) = \int d^3R' G(\mathbf{R}, \mathbf{R}', \tau) \Psi(\mathbf{R}', \tau_0), \quad (3.4)$$

with the Green's function or propagator

$$G(\mathbf{R}, \mathbf{R}', \tau) = \langle \mathbf{R} | e^{-H(\tau-\tau_0)} | \mathbf{R}' \rangle. \quad (3.5)$$

We set the starting time $\tau_0 = 0$ to simplify the expressions and compute the propagator for a small time step $\Delta\tau$:

$$e^{-\hat{H}\Delta\tau} = e^{-(\hat{T}+\hat{V})\Delta\tau} = e^{-\left(\hat{T}+\frac{\hat{V}}{2}+\frac{\hat{V}}{2}\right)\Delta\tau} = e^{-\frac{\hat{V}}{2}\Delta\tau} e^{-\hat{T}\Delta\tau} e^{-\frac{\hat{V}}{2}\Delta\tau} + \mathcal{O}(\Delta\tau^3), \quad (3.6)$$

using the Trotter-Suzuki formula [201]. The smaller the imaginary time step, the smaller is the error of this approximation. Thus, to propagate the initial wave function to very large imaginary times, we separate the propagator into n small time steps $\Delta\tau$ and apply it consecutively:

$$\begin{aligned} G(\mathbf{R}, \mathbf{R}', \tau) &= \langle \mathbf{R} | e^{-H\tau} | \mathbf{R}' \rangle = \langle \mathbf{R} | e^{-Hn\Delta\tau} | \mathbf{R}' \rangle = \langle \mathbf{R} | (e^{-H\Delta\tau})^n | \mathbf{R}' \rangle \\ &= \int d^3R'' \int d^3R''' \dots \int d^3R^{(N)} G(\mathbf{R}, \mathbf{R}'', \Delta\tau) G(\mathbf{R}'', \mathbf{R}', \Delta\tau) \dots G(\mathbf{R}^{(N)}, \mathbf{R}', \Delta\tau). \end{aligned} \quad (3.7)$$

We first study the propagator of the free system, so $V(R) = 0$. The free propagator $G_0(\mathbf{R}, \mathbf{R}', \Delta\tau)$ is given by a Gaussian integral and can be solved analytically:

$$G_0(\mathbf{R}, \mathbf{R}', \Delta\tau) = \langle \mathbf{R} | e^{-\hat{T}\Delta\tau} | \mathbf{R}' \rangle \quad (3.8)$$

$$\begin{aligned} &= \langle \mathbf{R} | e^{-\sum \frac{p_i^2}{2m} \Delta\tau} | \mathbf{R}' \rangle \\ &= \left(\frac{m}{2\pi\Delta\tau} \right)^{\frac{3N}{2}} e^{-\frac{m}{2\Delta\tau} \sum_i^N (\mathbf{r}_i - \mathbf{r}'_i)^2}. \end{aligned} \quad (3.9)$$

If we calculate the propagator with interaction, it is necessary, that the interaction is local. Locality means $\langle r' | \hat{V} | r \rangle = V(r) \delta(r - r')$, and thus, the potential is only a function of particle separations. The difficulty of handling nonlocal interactions in QMC methods results from how interactions enter, see also Ref. [202]. The implementation of continuum QMC methods relies on being able to separate all momentum dependencies as a quadratic $\sum_{i=1}^N p_i^2$ term like above. This is the case for local interactions, but not for general momentum-dependent, nonlocal interactions. In the local case, the momentum-dependent part is the free propagator, and the effects of interactions concern only the separations of the particles. In this case,

$$\begin{aligned} G(\mathbf{R}, \mathbf{R}', \Delta\tau) &= \langle \mathbf{R} | e^{-\frac{\hat{V}}{2}\Delta\tau} e^{-\hat{T}\Delta\tau} e^{-\frac{\hat{V}}{2}\Delta\tau} | \mathbf{R}' \rangle \\ &= G_0(\mathbf{R}, \mathbf{R}', \Delta\tau) e^{-\frac{V(\mathbf{R})+V(\mathbf{R}')}{2}\Delta\tau}. \end{aligned} \quad (3.10)$$

For nonlocal potentials, the evaluation of the propagator would involve the numerical calculation of derivatives, which is computationally too expensive. Thus, the QMC methods which we will use in this work need local interactions as input.

The Green's function is then inserted into Eq. (3.4) and we find for one time step

$$\Psi(\mathbf{R}, \tau + \Delta\tau) = \int d^3R' G_0(\mathbf{R}, \mathbf{R}', \Delta\tau) e^{-\frac{V(\mathbf{R})+V(\mathbf{R}')}{2}\Delta\tau} \Psi(\mathbf{R}', \tau_0). \quad (3.11)$$

This integral is solved by means of stochastic Monte Carlo integration by propagating the particle coordinates using a path sampled according to the Gaussian factor in the integral for many different initial configurations, or walkers. The final result will be averaged over the different walkers. In addition, this efficiency of this algorithm can be improved by importance sampling methods [203].

The QMC methods we use in this work need the trial wave function to have a definite sign. For Fermions this is not true due to the antisymmetry of the wave function. To circumvent this sign problem, the space is split into regions of positive and negative wave functions. This defines the nodal surface, where the trial wave function is zero, and walkers which cross this surface will be dropped. This is called fixed-node approximation [204, 205]. A generalization of this approximation to complex wave functions, which we use here, is the constrained-path method [206, 207, 208]. It constrains the path of walkers to regions of space where the overlap of walker and the trial wave function has a positive real part.

The trial wave function in QMC methods is usually chosen of the form

$$\psi_T(\mathbf{R}) = \left[\prod_{i < j} f_J(r_{ij}) \right] \Phi_A(\mathbf{R}), \quad (3.12)$$

where the first part is the Jastrow factor which includes inter-particle correlations into the trial wave function. For a nodeless Jastrow term, most QMC methods are independent of the choice one makes for $f(r)$: the Jastrow function impacts the statistical error by emphasizing the “appropriate” regions of phase space, but not the value itself. The part Φ_A is usually given by the ground state of non-interacting particles. It has to be chosen individually for each system, e.g., it can be chosen as a Slater determinant,

$$\Phi_A(\mathbf{R}) = \mathcal{A} \left[\prod_i \phi_\alpha(\mathbf{r}_i, s_i) \right], \quad (3.13)$$

where the α labels the single-particle states which depend on the system studied.

Summarizing, the basic QMC strategy is to choose a trial wave function $|\psi_T\rangle$ which is not orthogonal to the ground state, construct the propagator for the system and a small imaginary time step, and evolve the trial wave function. This is repeated consecutively for a large number of times, until the system's wave function will converge to the ground state wave function of the system.

3.1.1 Green's function Monte Carlo

During this work we will use two different QMC methods: GFMC and AFDMC. The starting wave function for a GFMC simulation is usually obtained in a Variational Monte Carlo (VMC)

calculation. In VMC, starting from a variational trial wave function, which is a good approximation to the true ground-state wave function, one calculates an upper bound to the true ground state energy E_0 of a system:

$$E_{\text{VMC}} = \frac{\int d\mathbf{R} \psi_T(\mathbf{R}) H \psi_T(\mathbf{R})}{\int d\mathbf{R} |\psi_T(\mathbf{R})|^2} \geq E_0. \quad (3.14)$$

This integral is sampled N_S times according to the probability density

$$W(\mathbf{R}) = \frac{|\psi_T(\mathbf{R})|^2}{\int d\mathbf{R} |\psi_T(\mathbf{R})|^2} \quad (3.15)$$

using the Metropolis algorithm [209]. For each configuration \mathbf{R}_n , we calculate the local energy

$$E_L(\mathbf{R}) = \frac{H \psi_T(\mathbf{R})}{\psi_T(\mathbf{R})}. \quad (3.16)$$

The VMC energy is then given by

$$E_{\text{VMC}} \approx \frac{1}{N_S} \sum_{n=1}^{N_S} E_L(\mathbf{R}_n). \quad (3.17)$$

The parameters in the VMC wave function are then varied to find the lowest energy. The result of a VMC simulation is very much dependent on the choice of the initial wave function.

The final output configuration of the VMC simulation is then used as starting configuration for a GFMC simulation. GFMC works as described in the previous Section by projecting out the lowest-energy state from the trial wave function ψ_T . If this wave function overlaps with the ground state wave function of the system GFMC will project out this state.

GFMC performs, in addition to a stochastic integration over the particle coordinates as described above, explicit summations in spin-isospin space. Since nuclear forces contain quadratic spin, isospin, and tensor operators (of the form $\sigma_i^\alpha A_{ij}^{\alpha\beta} \sigma_j^\beta$), the many-body wave function cannot be expressed as a product of single-particle spin-isospin states. As an example, to evaluate the quadratic spin operator $\sigma_i \cdot \sigma_j$, the wave function has to contain the singlet and triplet components for each particle pair. All possible spin-isospin nucleon-pair states need to be explicitly accounted for. The number of states grows exponentially with particle number, and as a result, limits the particle number in GFMC simulations. Green's Function Monte Carlo calculations are computationally very costly and presently limited to 12 nucleons or 16 neutrons [70].

The computational effort can be reduced if a good trial wave function is chosen which converges faster to the ground state. Furthermore, the trial wave function influences the importance sampling, and a good wave function will improve the efficiency of the GFMC simulation.

3.1.2 Auxiliary-field diffusion Monte Carlo

In contrast to GFMC, the second method, AFDMC [77], also stochastically evaluates summations in spin-isospin space, and shows a better scaling behavior at the cost of less accuracy. To achieve

this, AFDMC rewrites the Green's function by applying a Hubbard-Stratonovich transformation using auxiliary-fields to change the quadratic spin-isospin operator dependencies to linear at the cost of with additional integrations over auxiliary-fields.

To explain this, we follow Ref. [203]. Considering only quadratic spin, isospin and tensor operators, we can rewrite the potential in the form

$$V = V_{SI} + \frac{1}{2} \sum_{i\alpha, j\beta} \sigma_{i\alpha} A_{i\alpha, j\beta}^{(\sigma)} \sigma_{j\beta} + \frac{1}{2} \sum_{i\alpha, j\beta} \sigma_{i\alpha} A_{i\alpha, j\beta}^{(\sigma\tau)} \sigma_{j\beta} \boldsymbol{\tau}_i \cdot \boldsymbol{\tau}_j + \frac{1}{2} \sum_{i,j} A_{i,j}^{(\tau)} \boldsymbol{\tau}_i \cdot \boldsymbol{\tau}_j, \quad (3.18)$$

where the first term absorbs spin-isospin-independent parts of the interaction, the second term absorbs the isospin-independent but spin-dependent parts, the third term absorbs spin-isospin-dependent parts, and the last term the spin-independent but isospin-dependent parts. Here, Latin indices label nucleons and Greek indices label Cartesian components.

These matrices have real eigenvectors and eigenvalues

$$\sum_{j\beta} A_{i\alpha, j\beta}^{(\sigma)} \psi_{n, j\beta}^{(\sigma)} = \lambda_n^{(\sigma)} \psi_{n, i\alpha}^{(\sigma)}, \quad (3.19)$$

$$\sum_{j\beta} A_{i\alpha, j\beta}^{(\sigma\tau)} \psi_{n, j\beta}^{(\sigma\tau)} = \lambda_n^{(\sigma\tau)} \psi_{n, i\alpha}^{(\sigma\tau)}, \quad (3.20)$$

$$\sum_j A_{i,j}^{(\tau)} \psi_{n,j}^{(\tau)} = \lambda_n^{(\tau)} \psi_{n,i}^{(\tau)}. \quad (3.21)$$

Using these eigenvectors, one can use the eigendecomposition of the A matrices and rewrite the potential as

$$V = V_{SI} + \frac{1}{2} \sum_n O_n^{(\sigma)2} \lambda_n^{(\sigma)} + \frac{1}{2} \sum_{n\alpha} O_{n\alpha}^{(\sigma\tau)2} \lambda_n^{(\sigma\tau)} + \frac{1}{2} \sum_{n\alpha} O_{n\alpha}^{(\tau)2} \lambda_n^{(\tau)}, \quad (3.22)$$

with the operators

$$O_n^{(\sigma)} = \sum_{j\beta} \sigma_{j\beta} \psi_{n, j\beta}^{(\sigma)}, \quad (3.23)$$

$$O_{n\alpha}^{(\sigma\tau)} = \sum_{j\beta} \tau_{j\alpha} \sigma_{j\beta} \psi_{n, j\beta}^{(\sigma\tau)}, \quad (3.24)$$

$$O_{n\alpha}^{(\tau)} = \sum_j \tau_{j\alpha} \psi_{n,j}^{(\tau)}. \quad (3.25)$$

The spin-dependent A matrices have each 3N eigenvalues and eigenvectors while the spin-independent matrix $A_{i,j}^{(\tau)}$ has N eigenvalues and eigenvectors. This results in 3N $O_n^{(\sigma)}$ matrices, 9N $O_{n\alpha}^{(\sigma\tau)}$ matrices, and 3N $O_{n\alpha}^{(\tau)}$ matrices, leading to a total of 15N O matrices.

We can now use a Hubbard-Stratonovich transformation for an operator O,

$$e^{-\frac{1}{2}\lambda\hat{O}^2} = \frac{1}{\sqrt{2\pi}} \int dx e^{-\frac{x^2}{2} + \sqrt{-\lambda}x\hat{O}}, \quad (3.26)$$

and use this to rewrite the Green's function

$$G(\mathbf{R}, \mathbf{R}', \Delta\tau) = G_0(\mathbf{R}, \mathbf{R}', \Delta\tau) e^{-\frac{V_{SI}(\mathbf{R}) + V_{SI}(\mathbf{R}')}{2} \Delta\tau} \prod_{i=1}^{15N} \frac{1}{\sqrt{2\pi}} \int dx_i e^{-\frac{x_i^2}{2} + \sqrt{-\lambda_i \Delta\tau} x_i \hat{O}_i}. \quad (3.27)$$

With this transformation the dependence on spin-isospin operators changes from quadratic to linear, with $15N$ additional integrations over the variables x_i . The x_i are called auxiliary-fields and give this QMC method its name. Using this transformation it is possible to write the wave function as a product of single-particle spin-isospin states. As a result, the new propagator independently rotates the spin of every single nucleon.

The reduction of the operator dependence from quadratic to linear reduces the number of states in the trial wave function from exponential to linear at the cost of $15N$ additional Monte Carlo integrations over the auxiliary-fields and the necessary computation of the O matrices.

In addition to the operators described above, in the case of neutrons it has also been possible to include fully in AFDMC spin-orbit interactions and three-body forces [210, 211]. Following Ref. [203], we can write the spin-orbit potential as

$$v_{LS,ij} = v_{LS}(r_{ij}) \mathbf{L}_{ij} \cdot \mathbf{S}_{ij}, \quad (3.28)$$

where $\mathbf{L}_{ij} = \frac{1}{2i} \mathbf{r}_{ij} \times \nabla_{ij}$ is the angular momentum operator, and $\mathbf{S} = \frac{1}{2}(\boldsymbol{\sigma}_i + \boldsymbol{\sigma}_j)$ is the total spin operator. This contribution is non-local and complicates the evaluation of the Green's function. To implement this term, the exponential term will be expanded in $\Delta\tau$ to first order,

$$e^{-\frac{1}{2} v_{LS}(r_{ij}) \mathbf{L}_{ij} \cdot \mathbf{S}_{ij} \Delta\tau} = 1 - \frac{1}{2} v_{LS}(r_{ij}) \mathbf{L}_{ij} \cdot \mathbf{S}_{ij} \Delta\tau + \mathcal{O}(\Delta\tau^2). \quad (3.29)$$

The dominant contribution stems from $\mathbf{L}_{ij} \cdot \mathbf{S}_{ij}$ acting on the free propagator G_0 ,

$$\begin{aligned} \mathbf{L}_{ij} \cdot \mathbf{S}_{ij} G_0(\mathbf{R}, \mathbf{R}', \Delta\tau) &= -\frac{1}{4i} \frac{m}{\Delta\tau} \mathbf{r}_{ij} \times (\mathbf{r}_{ij} - \mathbf{r}'_{ij}) \cdot (\boldsymbol{\sigma}_i + \boldsymbol{\sigma}_j) G_0(\mathbf{R}, \mathbf{R}', \Delta\tau) \\ &= \frac{1}{4i} \frac{m}{\Delta\tau} \mathbf{r}_{ij} \times \mathbf{r}'_{ij} \cdot (\boldsymbol{\sigma}_i + \boldsymbol{\sigma}_j) G_0(\mathbf{R}, \mathbf{R}', \Delta\tau), \end{aligned} \quad (3.30)$$

and one arrives at

$$e^{-\frac{1}{2} v_{LS}(r_{ij}) \mathbf{L}_{ij} \cdot \mathbf{S}_{ij} \Delta\tau} G_0(\mathbf{R}, \mathbf{R}', \Delta\tau) \approx \left(1 - \frac{m}{8i} v_{LS}(r_{ij}) \mathbf{r}_{ij} \times \mathbf{r}'_{ij} \cdot (\boldsymbol{\sigma}_i + \boldsymbol{\sigma}_j) \right) G_0(\mathbf{R}, \mathbf{R}', \Delta\tau). \quad (3.31)$$

Although the explicit $\Delta\tau$ dependence drops out of the spin-orbit propagator since $\mathbf{r}_{ij} \times \mathbf{r}'_{ij} = \mathbf{r}_{ij} \times (\mathbf{r}_{ij} + \Delta\mathbf{r}_{ij}) = \mathbf{r}_{ij} \times \Delta\mathbf{r}_{ij} \sim \sqrt{\Delta\tau}$ due to the sampling of $\Delta\mathbf{r}_{ij}$ from the Green's function. This propagator has to be corrected for counter terms from the first-order expansion of the original exponential, see Ref. [203] for more details. In the case of neutron matter, the isospin operator $\boldsymbol{\tau}_i \cdot \boldsymbol{\tau}_j$ evaluates to a constant. For isospin-dependent spin-orbit interactions in neutron matter the above scheme can be applied. In general, however, the inclusion of isospin-dependent spin-orbit interactions is very difficult and the counter terms become cubic in the spin-isospin operator structure. This makes them very difficult to include into AFDMC simulations. Additionally, the inclusion of protons into AFDMC calculations lead to small accuracy of the results [212]. The used trial wave functions include no tensor or other spin- or isospin-dependent

correlations. Due to the fixed-node or constrained-path approximations the correlations in the trial wave function are important to finding the true ground state energy of a system with both protons and neutrons, because the tensor component in the np system is significant. However, the expectation value of the NN tensor component almost vanishes if the tensor correlations are neglected in the trial wave function [212]. Furthermore, there are numerical issues arising from time-step errors. These issues have been recently tackled, and AFDMC calculations with both neutrons and protons become possible [212].

The inclusion of 3N forces of the Urbana and Illinois form is shown in Ref. [203]. For pure neutron matter it is possible to rewrite these interactions as two-body terms which simplifies their inclusion. We will follow this strategy and show how to include 3N forces in Sec. 6.2 for chiral 3N interactions.

In our AFDMC simulations we use trial wave functions of the Jastrow-Slater form, see Eq. (3.12). Although the Jastrow factor should not influence the results, due to the complicated spin-dependence of nuclear interactions, it has been found that AFDMC has a small dependence on the Jastrow function as reported in Ref. [213]. This has to be studied in our simulations.

For nuclear matter calculations, we simulate N particles in a cubic box with size L . The particle number has to be chosen large enough to probe the thermodynamic limit. The Φ_A is given by the ground state of a free Fermi gas in this box, constructed from plane waves with momenta $\mathbf{k}_\alpha = \frac{2\pi}{L}(n_x, n_y, n_z)$. The numbers n_x, n_y , and n_z are integer numbers and the single-particle states are given by

$$\Phi_\alpha(\mathbf{R}) = e^{i\mathbf{k}_\alpha \cdot \mathbf{r}_i} \chi_{s, m_s}(\mathbf{s}_i), \quad (3.32)$$

with the spin functions $\chi_{s, m_s}(\mathbf{s}_i)$. Using these wave functions, the system acquires a shell structure, with the shell number $I = n_x^2 + n_y^2 + n_z^2$. For a homogenic and isotropic system, these shells must be closed. For $I = 0$, there is one combination, for $I = 1$ there are six, for $I = 2$ there are 12, and so on. This leads to shell closures at 1, 7, 19, 27, 33, etc. particles in a certain spin-isospin configuration. Thus, in spin-symmetric neutron matter, the shell closures are at particle numbers 2, 14, 38, 54, 66, etc. Using AFDMC, we can treat $\mathcal{O}(100)$ nucleons. In our neutron matter simulation, we typically simulate 66 fermions to access the thermodynamic limit.

3.2 Quantum Monte Carlo results with phenomenological interactions

3.2.1 Phenomenological interactions

Up to now, nuclear QMC calculations have used phenomenological NN interactions as input, typically of the Argonne type [197, 198]. These potentials are accurate for NN scattering, but are not connected to QCD, and the two-pion-exchange interaction is modeled purely phenomenologically, which makes it difficult to construct consistent 3N forces. The generic non-relativistic nuclear Hamiltonian is given by

$$H = -\frac{\hbar^2}{2m} \sum_i \nabla_i^2 + \sum_{i<j} v_{ij} + \sum_{i<j<k} V_{ijk} + \dots \quad (3.33)$$

where the first term is the kinetic term, the term v_{ij} the NN force and V_{ijk} the 3N interaction. The basic idea of phenomenological interactions is to choose a general operator basis, which is dependent on spin, isospin and momentum operators. The radial functions and couplings for each operator are then adjusted to reproduce experimental data.

3.2.1.1 Two-nucleon interactions

The typical phenomenological NN interactions used in QMC simulations are of the Argonne type. They consist of several parts: the long-range part is given by the one-pion-exchange interaction,

$$v_{ij}^{\pi} = \frac{f_{\pi NN}^2}{4\pi} \frac{m_{\pi}}{3} X_{ij}(\mathbf{r}_{ij}) \boldsymbol{\tau}_i \cdot \boldsymbol{\tau}_j, \quad (3.34)$$

with the pion-nucleon coupling constant $f_{\pi NN}/4\pi = 0.075(2)$ [214], and the function

$$X_{ij}(\mathbf{r}_{ij}) = Y(m_{\pi} r_{ij}) \boldsymbol{\sigma}_i \cdot \boldsymbol{\sigma}_j + T(m_{\pi} r_{ij}) S_{ij}(\mathbf{r}_{ij}), \quad (3.35)$$

which contains the tensor operator S_{ij} and radial functions $Y(x)$ and $T(x)$ given by

$$S_{ij}(\mathbf{r}) = 3\boldsymbol{\sigma}_i \cdot \hat{\mathbf{r}} \boldsymbol{\sigma}_j \cdot \hat{\mathbf{r}} - \boldsymbol{\sigma}_i \cdot \boldsymbol{\sigma}_j, \quad (3.36)$$

$$Y(x) = \frac{e^{-x}}{x} \xi_Y(x), \quad (3.37)$$

$$T(x) = \left(1 + \frac{3}{x} + \frac{3}{x^2}\right) Y(x) \xi_T(x). \quad (3.38)$$

The ξ functions are the cutoff functions, which are usually of the form $1 - e^{-cx^2}$.

The intermediate- and short-range parts of the interaction are modeled in a general operator basis. The current state-of-the-art potential is AV18 which uses 18 general structures. The AV18 interaction can be written as

$$v_{ij} = \sum_{k=1}^{18} v_k(r_{ij}) O_{ij}^k, \quad (3.39)$$

where the $v_k(r_{ij})$ are the radial functions for the operators O_{ij}^k . The first eight terms are the spin-independent, spin, tensor, and spin-orbit operators. Each of these can be isospin-dependent or independent. They are given by

$$O_{ij}^{k=1,8} = \{\mathbb{1}, \boldsymbol{\sigma}_i \cdot \boldsymbol{\sigma}_j, S_{ij}, \mathbf{L}_{ij} \cdot \mathbf{S}_{ij}\} \times \{\mathbb{1}, \boldsymbol{\tau}_i \cdot \boldsymbol{\tau}_j\}. \quad (3.40)$$

These operators are also appearing in the NLO chiral interactions. The other operators are given by

$$O_{ij}^{k=9,14} = \{\mathbf{L}_{ij}^2, \mathbf{L}_{ij}^2 \boldsymbol{\sigma}_i \cdot \boldsymbol{\sigma}_j, (\mathbf{L}_{ij} \cdot \mathbf{S}_{ij})^2\} \times \{\mathbb{1}, \boldsymbol{\tau}_i \cdot \boldsymbol{\tau}_j\}, \quad (3.41)$$

$$O_{ij}^{k=15,18} = \{T_{ij}, T_{ij} \boldsymbol{\sigma}_i \cdot \boldsymbol{\sigma}_j, S_{ij} T_{ij}, \tau_i^z + \tau_j^z\}, \quad (3.42)$$

where $T_{ij} = 3\tau_i^z \tau_j^z - \boldsymbol{\tau}_i \cdot \boldsymbol{\tau}_j$ is the isotensor operator. The first set of these operators improves the description of different partial-wave phase shifts. The latter four operators are charge-independence breaking (CIB) corrections, which describe the difference between protons and neutrons. The potential is fitted to the Nijmegen scattering database.

3.2.1.2 Three-nucleon interactions

The 3N interactions most commonly used with Argonne NN forces are the Illinois [200] and Urbana [199] form, given by

$$V_{ijk} = A_{2\pi}^{PW} O_{ijk}^{2\pi, PW} + A_{2\pi}^{SW} O_{ijk}^{2\pi, SW} + A_{3\pi}^{\Delta R} O_{ijk}^{3\pi, \Delta R} + A_R^{PW} O_{ijk}^R, \quad (3.43)$$

where the first two structures are the P - and S -wave part of the TPE interaction, the third term is a three-pion-exchange term and the last term is a spin and isospin-independent term. These operators are all contained in the Illinois 3N forces, while the Urbana 3N forces only include the first and the last term.

The first term is given by

$$A_{2\pi}^{PW} O_{ijk}^{2\pi, PW} = A_{2\pi}^{PW} \sum_{\text{cyc}} \left(\{X_{ij}, X_{jk}\} \{\boldsymbol{\tau}_i \cdot \boldsymbol{\tau}_j, \boldsymbol{\tau}_j \cdot \boldsymbol{\tau}_k\} + \frac{1}{4} [X_{ij}, X_{jk}] [\boldsymbol{\tau}_i \cdot \boldsymbol{\tau}_j, \boldsymbol{\tau}_j \cdot \boldsymbol{\tau}_k] \right), \quad (3.44)$$

where the brackets denote the anticommutator and commutator of X_{ij} and X_{jk} . The Urbana and Illinois TPE interaction models the process, where nucleons exchange two pions with an intermediate Δ resonance.

The S -wave part of the TPE is given by

$$A_{2\pi}^{SW} O_{ijk}^{2\pi, SW} = A_{2\pi}^{SW} \sum_{\text{cyc}} Z(m_\pi r_{ij}) Z(m_\pi r_{jk}) \boldsymbol{\sigma}_i \cdot \hat{\mathbf{r}}_{ij} \boldsymbol{\sigma}_k \cdot \hat{\mathbf{r}}_{kj} \boldsymbol{\tau}_i \cdot \boldsymbol{\tau}_k, \quad (3.45)$$

with the function $Z(x) = \frac{x}{3} (Y(x) - T(x))$. These first two terms are also included in the leading 3N interaction in the chiral forces at $N^2\text{LO}$, which will be shown later in Chap. 6.

The third interaction term stems from pion-ring diagrams with one or two Δ excitations. They are included in chiral EFT interactions beyond $N^3\text{LO}$ and are, thus, not important for this work. Their expressions are rather complicated, see Ref. [200] for more details.

The last term of the 3N forces was empirically introduced to compensate the overbinding by other parts of the Urbana and Illinois 3N forces. It is given by

$$A_R O_{ijk}^R = A_R \sum_{\text{cyc}} T^2(m_\pi r_{ij}) T^2(m_\pi r_{jk}). \quad (3.46)$$

This spin- and isospin-independent term is not included in chiral EFT 3N forces up to $N^3\text{LO}$ and is purely phenomenological.

The interaction strengths for the various 3N contributions are fitted to reproduce the ground states of light nuclei.

3.2.1.3 Problems of phenomenological interactions

Although calculations with the phenomenological AV18 NN and Urbana and Illinois 3N forces give very good results for nuclei and nuclear matter, see below, there are several conceptual disadvantages in using these interactions.

First, these interactions are not connected to the fundamental theory of QCD. Indeed in the NN sector, operators of one-boson-exchange (OBE) potentials are used and have a theoretical motivation. This is reflected in the fact that the first eight operators of AV18 are also appearing in the NLO chiral EFT interactions. However, there are other operators which are introduced purely phenomenological. This arbitrary choice of operators is especially clear in the 3N sector. Although the TPE is theoretically motivated by the Weinberg-Tomozawa interaction, which also appears in the leading chiral 3N forces, the other leading 3N force contributions V_D and V_E are missing, while additional higher-order contributions appear. There is no strategy of systematically writing down the many-body operator structures due to their more complicated nature. Additionally, the NN and many-body sectors are not consistent with each other. Similar vertices, which appear in NN and 3N forces, have different coupling constants.

The second disadvantage is that there is no way to estimate the importance of individual contributions. This can especially be seen in the 3N sector, which includes terms similar to chiral interactions at N²LO and from higher orders, leaving out other important contributions. Thus, phenomenological interactions cannot be constructed in a systematic way with a power counting scheme, and it is not possible to estimate the theoretical uncertainties of the interactions.

3.2.2 Light nuclei

The current state-of-the art GFMC calculations and benchmarks for light nuclei are presented in Fig. 3.1. It shows a calculation of the ground states and first excited states of nuclei up to ¹²C from Ref. [195], which was updated in 2012. The results were obtained using the AV18 NN interaction, and with the additional inclusion of the Illinois-7 3N forces, and are compared to experiment. For all the light nuclei, the GFMC calculations with phenomenological interactions show remarkable agreement with experimental results after 3N forces are included, which are, however, fit to nuclear binding energies. The results suffer from the disadvantages mentioned above: they lack reliable error estimates and a way of systematical improveability.

In addition to the energy states of light nuclei, other properties of light nuclei have been computed using QMC methods, like charge form factors [76] or electromagnetic matrix elements [215].

3.2.3 Neutron matter and neutron stars

QMC methods with phenomenological interactions have also been used to calculate neutron matter. It has been found that 3N interactions provide a sizable contribution to the neutron matter energy [211]. In Fig. 3.2, we show a calculation of the neutron-matter energy per particle as a function of density using the AFDMC algorithm [16]. Results with different colors are tuned to reproduce different symmetry energies.

The red line shows the results for NN forces only, and the 3N forces add sizable contributions. The green and blue band are obtained by varying the range of A_R , see Eq. (3.43). This shows that different choices for the phenomenological 3N forces have sizable effects. However, there is no possibility of estimating a reliable theoretical uncertainty using phenomenological 3N interactions because both operator structure and radial functions can be varied.

We also show the neutron star mass-radius relation for these neutron matter calculations. Only the inclusion of 3N forces adds enough repulsion to reproduce the observed two-solar-mass neutron stars in this model.

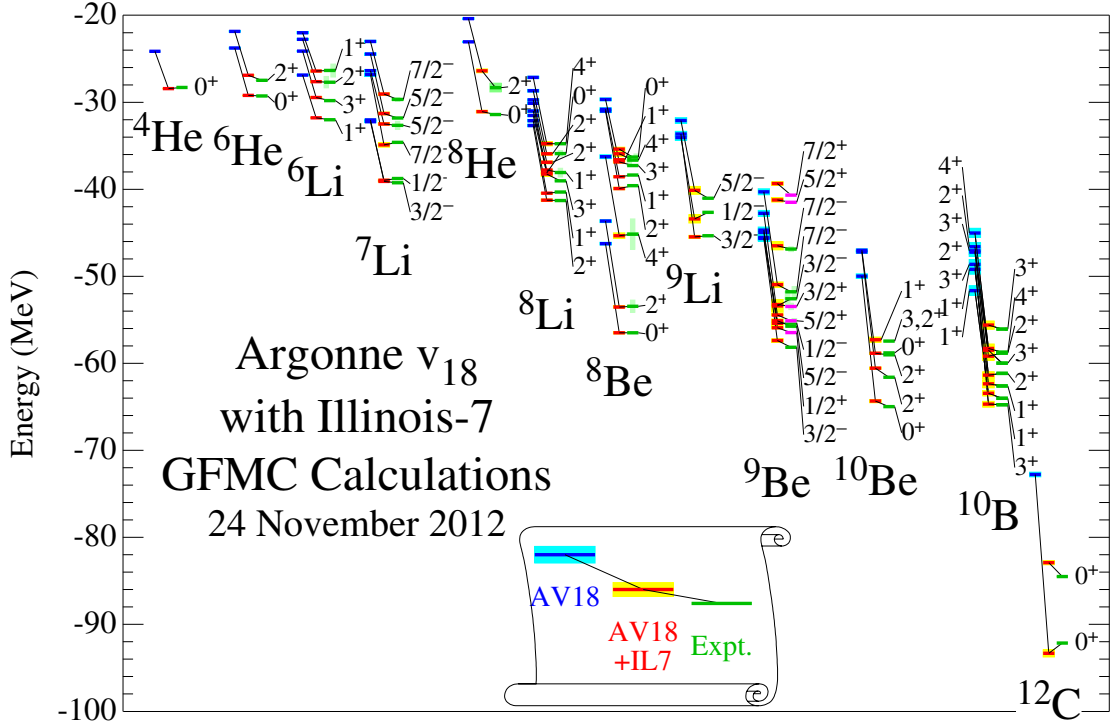


Figure 3.1: Ground-state energies and energies of excited states for light nuclei up to ^{12}C using GFMF with the Argonne AV18 NN interaction and the Illinois-7 3N forces from Ref. [195]. The results are compared to experimental data.

3.2.4 Ultracold atoms

The $T = 0$ equation of state for cold atoms and low density neutron matter has been calculated using QMC methods with Jastrow-BCS wave functions in Ref. [23]. The interaction between cold atoms was chosen to be of the Poeschl-Teller form,

$$v(r) = -v_0 \frac{2\hbar^2}{m} \frac{\mu^2}{\cosh^2(\mu r)} \quad (3.47)$$

where $\mu = 24/r_0$ and r_0 is defined via $1/\rho = 4/3\pi r_0^3$. The neutron-neutron interaction was chosen as the S wave part of AV18.

The result for the EoS is shown in Fig. 3.3. Depicted is the energy relative to the energy of a free Fermi gas at the same density vs. $-k_F a$, which is the product of Fermi momentum and scattering length. For neutron matter, a is fixed and a variation of k_F represents a variation of the density. For cold atoms, $k_F a$ is varied in a Feshbach resonance by varying a . At very high a the cold atom result at unitarity is shown. The curve at low densities shows the analytical expansion for a normal Fermi gas [23]. The results show that cold atom and neutron matter EoS behave similar at low densities and that one can probe neutron matter in experiments with cold atoms. This can be also useful to probe the pairing gap, see Ref. [23, 216] for more details.

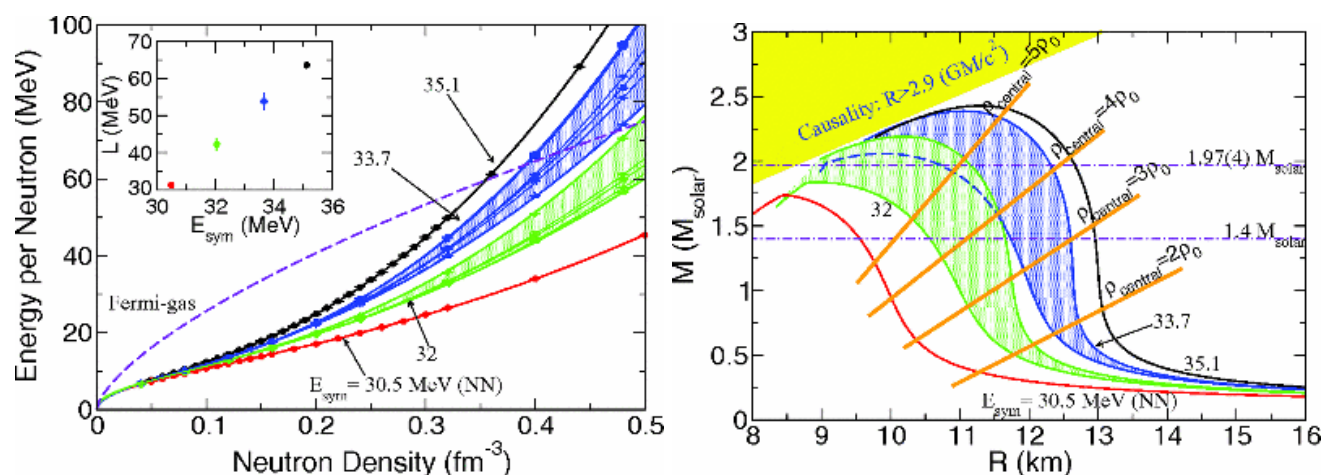


Figure 3.2: Left: Energy per particle of neutron matter from AFDMC simulations [16]. Different colors correspond to different symmetry energies. For the blue and green bands, 3N forces are included. The bands show the effect of different 3N structures. Right: Mass-radius relation of neutron stars corresponding to these neutron-matter EoS [16].

3.3 Motivation for Quantum Monte Carlo with chiral EFT interactions

QMC methods have been used to obtain precise results for strongly interacting systems. However, the current state-of-the-art calculations suffer from the above mentioned disadvantages of phenomenological interactions. Using chiral EFT interactions as input for QMC algorithms would combine these precise *ab initio* many-body methods with systematic nuclear Hamiltonians. This would allow the computation of nonperturbative benchmarks for nuclear matter for astrophysics, nuclei, and neutron drops, which are rooted in QCD, include all contributions consistently, and with controlled theoretical uncertainty estimates.

Regarding nuclear matter, a perturbative approach has been able to predict realistic saturation properties using parameters fit only to few-body systems [55]. QMC calculations with chiral interactions would be key to validating this. QMC calculations of systems in external potentials with local chiral N²LO NN and 3N forces would also provide *ab initio* constraints for nuclear density functionals.

Furthermore, due to the precision of QMC methods, especially in light systems, QMC with chiral EFT interactions will allow direct matching to lattice QCD results [148]. For example, for few-nucleon systems in a box, lattice QCD results can be compared to QMC simulations with chiral interactions, which can also vary the pion mass to unphysical values accessible in lattice QCD methods. As a final goal, this could be used to match the LECs in the chiral potentials to lattice QCD computations, and would enable predictions from first principles.

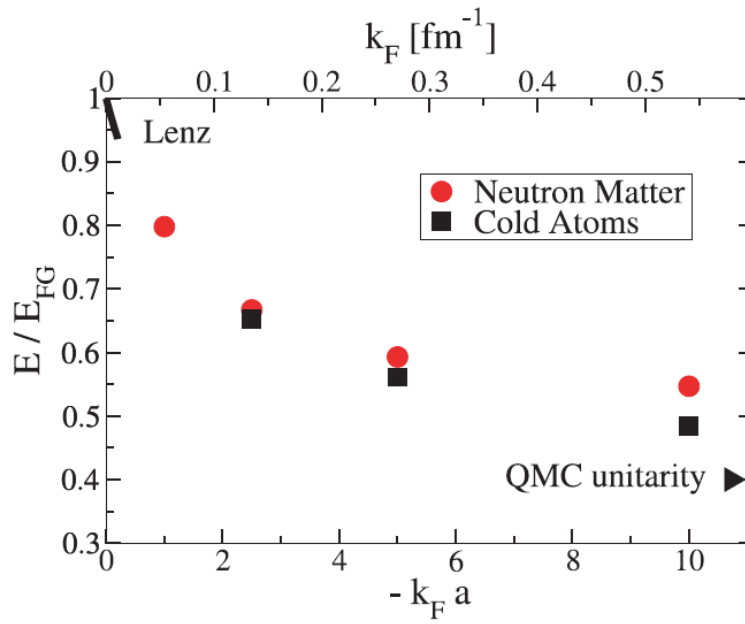


Figure 3.3: Equation of state for neutron matter and cold atoms at $T = 0$ from Ref. [23]. Shown is the energy normalized to the Fermi energy of the system vs. the product of Fermi momentum k_F and scattering length a for QMC simulations of cold atoms and neutron matter. The systems are very similar, even for higher Fermi momenta.



4 Local chiral NN interactions

Chiral EFT interactions are based on a momentum expansion and are therefore naturally formulated in momentum space [36, 37]. In their current formulation, they are nonlocal and therefore not suitable for Quantum Monte Carlo simulations. There have been several attempts to solve this problem, e.g., finding ways of treating nonlocal interactions in QMC simulations directly [202, 217] or using local projections of chiral EFT potentials [218] with non-local residual interactions. These strategies, however, require soft interactions as input and are not very much developed.

In this work, we use a different idea first outlined in Ref. [78] and show, how to create local chiral NN potentials up to $N^2\text{LO}$ in coordinate space, based on Ref. [213, 219]. These local interactions enable us to combine accurate chiral interactions with precise QMC many-body methods and, thus, enable QMC simulations with improvable Hamiltonians rooted in QCD, where we do not constrain the interactions further. In this Chapter we present details of the construction of local chiral NN potentials. In the next Chapter, we show results of QMC simulations for pure neutron matter with these local chiral NN potentials, study the order-by-order convergence of chiral interactions, and test the perturbativeness of chiral potentials to benchmark MBPT calculations with the same interactions.

4.1 Nonlocalities in chiral interactions and strategies for their removal

There are two sources of nonlocalities in chiral EFT interactions: one usually employs regulator functions of the form $f(p) = e^{-(p/\Lambda)^{2n}}$ and $f(p')$, as stated in Sec. 2.2.4. Upon Fourier transformation, this leads to nonlocal interactions $V(\mathbf{r}, \mathbf{r}')$ already due to the choice of the regulator. Further sources of nonlocality in chiral EFT are due to contact interactions that depend on the momentum transfer in the exchange channel $\mathbf{k} = (\mathbf{p}' + \mathbf{p})/2$ and to \mathbf{k} -dependent parts in pion-exchange contributions beyond $N^2\text{LO}$. In contrast, dependencies on the momentum transfer $\mathbf{q} = \mathbf{p}' - \mathbf{p}$ are local, and lead to nonlocalities only because of the regulator functions used. The \mathbf{k} -dependent contact interactions start to appear at NLO, see Sec. 2.2.4.

To avoid regulator-generated nonlocalities for the long-range pion-exchange parts of chiral EFT interactions, we will use local coordinate-space expressions for the LO one-pion-exchange and NLO and $N^2\text{LO}$ two-pion-exchange interactions [170, 171] and regulate them directly in coordinate space using the function $f_{\text{long}}(r) = 1 - e^{-(r/R_0)^4}$, which smoothly cuts off interactions at short distances $r < R_0$ while leaving the long-range parts unchanged. Thus, R_0 takes over the role of the cutoff Λ in momentum space. To regularize the pion loop integrals of the two-pion-exchange contributions, we use a spectral-function regularization [171].

Local regulators have also been used in a new version of semi-local chiral potentials up to fifth order ($N^4\text{LO}$), where contact interactions are regularized in a non-local way while long-range pion physics is regularized locally [220, 221]. The advantage of local regulators for long-range interactions is that short-range singularities $\sim r^{-3n}$ from tensor forces are cut more effectively while keeping nonlocal short-range interactions has advantages for the fitting of the couplings. This will be discussed later throughout this work.

To remove the \mathbf{k} -dependent contact interactions to $N^2\text{LO}$, we make use of the freedom to choose a basis of short-range operators in chiral EFT interactions, as described in Sec. 2.2.4. Our approach follows Weinberg's power counting with typical cutoffs of order the breakdown scale $\sim 500\text{MeV}$ [36, 222], but the same local rearrangement can be applied to modified power counting [223, 224], to pionless EFT [225], to power counting that includes k_F as an explicit scale [226], and when making use of off-shell ambiguities [227].

4.2 Derivation of local chiral NN interaction

4.2.1 Leading order

At LO, as stated in Sec. 2.2.4, there appear the leading momentum-independent NN contact interactions as well as the OPE interaction. One usually considers the two momentum-independent contact interactions $C_S + C_T \boldsymbol{\sigma}_1 \cdot \boldsymbol{\sigma}_2$. However, it is equivalent to choose any two of the four operators $\mathbb{1}$, $\boldsymbol{\sigma}_1 \cdot \boldsymbol{\sigma}_2$, $\boldsymbol{\tau}_1 \cdot \boldsymbol{\tau}_2$, and $\boldsymbol{\sigma}_1 \cdot \boldsymbol{\sigma}_2 \boldsymbol{\tau}_1 \cdot \boldsymbol{\tau}_2$, with spin and isospin operators $\boldsymbol{\sigma}_i, \boldsymbol{\tau}_i$, because there are only two S-wave channels due to the Pauli principle. It is a convention in present chiral EFT interactions to neglect the isospin dependence, which is then generated from the exchange terms, as shown in Sec. 2.2.4. As this contact interaction is momentum-independent, it is local and we can directly use it in the local chiral potentials. Fourier transformation of the LO contact interaction leads to a simple δ function interaction

$$V_{\text{cont}}^{(0)}(\mathbf{r}) = (C_S + C_T \boldsymbol{\sigma}_1 \cdot \boldsymbol{\sigma}_2) \delta(\mathbf{r}), \quad (4.1)$$

see App. A for details.

In addition to the short-range contact interactions, at LO there appears the long-range OPE. Given that the long-range potentials in chiral EFT depend only on the momentum transfer, the corresponding coordinate-space potentials are local. Analogue as in Sec. 2.2.4, we employ the decomposition for the long- and intermediate-range pion-exchange potentials up to $N^2\text{LO}$ in coordinate space as

$$\begin{aligned} V_{\text{long}}(r) = & V_C(r) + W_C(r) \boldsymbol{\tau}_1 \cdot \boldsymbol{\tau}_2 \\ & + (V_S(r) + W_S(r) \boldsymbol{\tau}_1 \cdot \boldsymbol{\tau}_2) \boldsymbol{\sigma}_1 \cdot \boldsymbol{\sigma}_2 \\ & + (V_T(r) + W_T(r) \boldsymbol{\tau}_1 \cdot \boldsymbol{\tau}_2) S_{12}, \end{aligned} \quad (4.2)$$

where $\mathbf{r} = \mathbf{r}_1 - \mathbf{r}_2$ denotes the separation between the nucleons and $S_{12} = (3\boldsymbol{\sigma}_1 \cdot \hat{\mathbf{r}} \boldsymbol{\sigma}_2 \cdot \hat{\mathbf{r}} - \boldsymbol{\sigma}_1 \cdot \boldsymbol{\sigma}_2)$ is the tensor operator. The expression for the OPE potential at LO takes the well-known form

$$W_S^{(0)}(r) = \frac{M_\pi^3}{12\pi} \left(\frac{g_A}{2F_\pi} \right)^2 \frac{e^{-M_\pi r}}{M_\pi r}, \quad (4.3)$$

$$W_T^{(0)}(r) = \frac{M_\pi^3}{12\pi} \left(\frac{g_A}{2F_\pi} \right)^2 \frac{e^{-M_\pi r}}{M_\pi r} \left(1 + \frac{3}{M_\pi r} + \frac{3}{(M_\pi r)^2} \right). \quad (4.4)$$

In addition to these long-range contributions, the OPE potential also involves a short-range piece proportional to a δ function. This short-range δ piece is important to maintain the Goldstone boson nature of the pion and is absorbed into the leading contact interaction.

In addition to the isospin-symmetric contributions to the potential, there also appear isospin-symmetry-breaking corrections [228] in chiral interactions. We take into account isospin-symmetry-breaking corrections in the pion exchanges as well as the leading momentum-independent CIB and charge-symmetry-breaking (CSB) contact terms at all orders and include these corrections already in the LO local chiral interactions to be able to reproduce the correct scattering lengths in the nn, np and pp channel already at LO. Furthermore, already at LO we account for the Goldberger-Treiman discrepancy which slightly shifts the strength of the OPE potential.

The main corrections are from long-range CIB terms due to the pion mass splitting in the OPE potential,

$$V_{\text{OPE, full}} = V_{\text{OPE}}(M_{\pi^\pm}) \boldsymbol{\tau}_1 \cdot \boldsymbol{\tau}_2 + 4 \left[V_{\text{OPE}}(M_{\pi^0}) - V_{\text{OPE}}(M_{\pi^\pm}) \right] \tau_1^3 \tau_2^3, \quad (4.5)$$

where V_{OPE} is the isospin independent part of the OPE interaction

$$V_{\text{OPE}}(M) = \frac{M^3}{12\pi} \left(\frac{g_A}{2F_\pi} \right)^2 \frac{e^{-Mr}}{Mr} \left[\boldsymbol{\sigma}_1 \cdot \boldsymbol{\sigma}_2 + \left(1 + \frac{3}{Mr} + \frac{3}{(Mr)^2} \right) S_{12} \right]. \quad (4.6)$$

For the contact interactions, the leading momentum-independent CIB and CSB terms have the form

$$V_{\text{cont, CIB}}(\mathbf{r}) = C_{\text{CIB}} \frac{1 + 4\tau_1^3 \tau_2^3}{2} \frac{1 - \boldsymbol{\sigma}_1 \cdot \boldsymbol{\sigma}_2}{4}, \quad (4.7)$$

$$V_{\text{cont, CSB}}(\mathbf{r}) = C_{\text{CSB}} (\tau_1^3 + \tau_2^3) \frac{1 - \boldsymbol{\sigma}_1 \cdot \boldsymbol{\sigma}_2}{4}. \quad (4.8)$$

These contact interactions are defined in such a way that they do not affect neutron-proton observables and only appear in the nn or pp channel. Furthermore, in coordinate space, due to regularization, we need to ensure that spin-triplet partial waves are not affected by the above terms and have to take into account a factor $(1 - \boldsymbol{\sigma}_1 \cdot \boldsymbol{\sigma}_2)/4$, which is a projection operator on spin-0 states. This factor is redundant for non-regularized expressions.

4.2.2 Next-to-leading order

At NLO, there are 14 different momentum-dependent contact interactions as well as two-pion-exchange interactions. We have the freedom to choose 7 linearly independent contact interactions. Since we want to construct a local chiral potential, we have to eliminate contact interactions that depend on the momentum transfer in the exchange channel \mathbf{k} . We use this freedom to choose the contact operators to keep isospin-dependent q^2 contact interactions and an isospin-dependent $(\boldsymbol{\sigma}_1 \cdot \mathbf{q})(\boldsymbol{\sigma}_2 \cdot \mathbf{q})$ tensor part in favor of nonlocal k^2 contact interactions and a nonlocal $(\boldsymbol{\sigma}_1 \cdot \mathbf{k})(\boldsymbol{\sigma}_2 \cdot \mathbf{k})$ tensor part.

This leads to the following seven linearly independent contact interactions at NLO that are local,

$$\begin{aligned} V_{\text{cont}}^{(2)} = & C_1 q^2 + C_2 q^2 \boldsymbol{\tau}_1 \cdot \boldsymbol{\tau}_2 \\ & + (C_3 q^2 + C_4 q^2 \boldsymbol{\tau}_1 \cdot \boldsymbol{\tau}_2) \boldsymbol{\sigma}_1 \cdot \boldsymbol{\sigma}_2 \\ & + i \frac{C_5}{2} (\boldsymbol{\sigma}_1 + \boldsymbol{\sigma}_2) \cdot (\mathbf{q} \times \mathbf{k}) \\ & + C_6 (\boldsymbol{\sigma}_1 \cdot \mathbf{q})(\boldsymbol{\sigma}_2 \cdot \mathbf{q}) \\ & + C_7 (\boldsymbol{\sigma}_1 \cdot \mathbf{q})(\boldsymbol{\sigma}_2 \cdot \mathbf{q}) \boldsymbol{\tau}_1 \cdot \boldsymbol{\tau}_2, \end{aligned} \quad (4.9)$$

except for the \mathbf{k} -dependent spin-orbit interaction (C_5), which can, however, be treated in QMC as discussed before. Without regulators, the expressions for the contact interactions in coordinate space are of the form

$$\begin{aligned}
V_{\text{cont}}^{(2)}(\mathbf{r}) = & -(C_1 + C_2 \boldsymbol{\tau}_1 \cdot \boldsymbol{\tau}_2) \Delta \delta(\mathbf{r}) \\
& - (C_3 + C_4 \boldsymbol{\tau}_1 \cdot \boldsymbol{\tau}_2) \boldsymbol{\sigma}_1 \cdot \boldsymbol{\sigma}_2 \Delta \delta(\mathbf{r}) \\
& + \frac{C_5}{2} \frac{\partial_r \delta(\mathbf{r})}{r} \mathbf{L} \cdot \mathbf{S} + (C_6 + C_7 \boldsymbol{\tau}_1 \cdot \boldsymbol{\tau}_2) \\
& \times \left[(\boldsymbol{\sigma}_1 \cdot \hat{\mathbf{r}})(\boldsymbol{\sigma}_2 \cdot \hat{\mathbf{r}}) \left(\frac{\partial_r \delta(\mathbf{r})}{r} - \partial_r^2 \delta(\mathbf{r}) \right) \right. \\
& \left. - \boldsymbol{\sigma}_1 \cdot \boldsymbol{\sigma}_2 \frac{\partial_r \delta(\mathbf{r})}{r} \right]. \tag{4.10}
\end{aligned}$$

The derivation of these expressions is given in Appendix A. Since at NLO the only two possible momentum operators allowed by symmetries are q^2 and k^2 (or equivalently $p^2 + p'^2$ and $\mathbf{p} \cdot \mathbf{p}'$), and similarly for the tensor parts, it is thus possible to remove all sources of nonlocality in chiral EFT in the NLO contact interactions.

We now turn to the long-range contributions at NLO. For the two-pion exchange (TPE) we use the SFR expressions as detailed in Ref. [171]. The coordinate-space expressions for the TPE potential can be most easily obtained utilizing the spectral-function representation with spectral functions ρ_i and η_i :

$$V_C(r) = \frac{1}{2\pi^2 r} \int_{2M_\pi}^{\tilde{\Lambda}} d\mu \mu e^{-\mu r} \rho_C(\mu), \tag{4.11}$$

$$V_S(r) = -\frac{1}{6\pi^2 r} \int_{2M_\pi}^{\tilde{\Lambda}} d\mu \mu e^{-\mu r} \left(\mu^2 \rho_T(\mu) - 3\rho_S(\mu) \right), \tag{4.12}$$

$$V_T(r) = -\frac{1}{6\pi^2 r^3} \int_{2M_\pi}^{\tilde{\Lambda}} d\mu \mu e^{-\mu r} \rho_T(\mu) (3 + 3\mu r + \mu^2 r^2), \tag{4.13}$$

and similarly for W_C , W_S , and W_T in terms of η_C , η_S , and η_T (instead of ρ_C , ρ_S , and ρ_T). The TPE spectral functions at NLO are given by [170]

$$\rho_T^{(2)}(\mu) = \frac{1}{\mu^2} \rho_S^{(2)}(\mu) = \frac{3g_A^4}{128\pi F_\pi^4} \frac{\sqrt{\mu^2 - 4M_\pi^2}}{\mu}, \tag{4.14}$$

$$\begin{aligned}
\eta_C^{(2)}(\mu) = & \frac{1}{768\pi F_\pi^4} \frac{\sqrt{\mu^2 - 4M_\pi^2}}{\mu} \left(4M_\pi^2 (5g_A^4 - 4g_A^2 - 1) \right. \\
& \left. - \mu^2 (23g_A^4 - 10g_A^2 - 1) + \frac{48g_A^4 M_\pi^4}{4M_\pi^2 - \mu^2} \right). \tag{4.15}
\end{aligned}$$

4.2.3 Next-to-next-to-leading order

At N²LO, there are no additional contact interactions but the subleading TPE interactions appear. The spectral functions for these at N²LO read

$$\rho_C^{(3)}(\mu) = -\frac{3g_A^2}{64\mu F_\pi^4} (2M_\pi^2 - \mu^2) \left(2M_\pi^2(2c_1 - c_3) + c_3\mu^2 \right), \quad (4.16)$$

$$\eta_T^{(3)}(\mu) = \frac{1}{\mu^2} \eta_S^{(3)}(\mu) = -\frac{g_A^2}{128\mu F_\pi^4} c_4(4M_\pi^2 - \mu^2), \quad (4.17)$$

where the c_i denote the LECs of the subleading pion-nucleon vertices [172]. For the subleading TPE potential, the integrals in Eqs. (4.11)–(4.13) can be carried out analytically leading to

$$\begin{aligned} V_C^{(3)}(r) = & \frac{3g_A^2}{32\pi^2 F_\pi^4} \frac{e^{-2x}}{r^6} \left[2c_1 x^2(1+x)^2 + c_3(6 + 12x + 10x^2 + 4x^3 + x^4) \right] \\ & - \frac{3g_A^2}{128\pi^2 F_\pi^4} \frac{e^{-y}}{r^6} \left[4c_1 x^2 \left(2 + y(2+y) - 2x^2 \right) + c_3 \left(24 + y(24 + 12y + 4y^2 + y^3) \right. \right. \\ & \left. \left. - 4x^2(2 + 2y + y^2) + 4x^4 \right) \right], \end{aligned} \quad (4.18)$$

$$\begin{aligned} W_S^{(3)}(r) = & \frac{g_A^2}{48\pi^2 F_\pi^4} \frac{e^{-2x}}{r^6} c_4(1+x)(3+3x+2x^2) \\ & - \frac{g_A^2}{384\pi^2 F_\pi^4} \frac{e^{-y}}{r^6} c_4 \left(24 + 24y + 12y^2 + 4y^3 + y^4 - 4x^2(2 + 2y + y^2) \right), \end{aligned} \quad (4.19)$$

$$\begin{aligned} W_T^{(3)}(r) = & -\frac{g_A^2}{48\pi^2 F_\pi^4} \frac{e^{-2x}}{r^6} c_4(1+x)(3+3x+x^2) \\ & + \frac{g_A^2}{768\pi^2 F_\pi^4} \frac{e^{-y}}{r^6} c_4 \left(48 + 48y + 24y^2 + 7y^3 + y^4 - 4x^2(8 + 5y + y^2) \right), \end{aligned} \quad (4.20)$$

where we have introduced dimensionless variables $x \equiv M_\pi r$ and $y \equiv \tilde{\Lambda} r$. Analytic expressions for the leading TPE potentials for the case of $\tilde{\Lambda} = \infty$ are given in Ref. [170].

4.2.4 Next-to-next-to-next-to-leading order

At N³LO, additional contact operators as well as TPE diagrams and also three-pion exchange diagrams contribute. In addition, relativistic corrections have to be included.

The N³LO chiral interaction cannot be written down in a local way. To highlight this, we remind the reader of the N³LO contact interactions defined in Eq. (2.30). There are 30 different operators, 15 of which are linearly independent. However, they are $\sim Q^4$ with momentum operators like q^4 , k^4 and $q^2 k^2$ and only 8 operators at this order are local. Additional nonlocalities arise in the relativistic corrections to the OPE potential, see Ref. [59] for more details.

Possible solutions to this problem are the definition of a "maximally local" N³LO potential, where as many local contact operators as possible are chosen. From the remaining operators, a suitable set of operators is chosen which can be treated perturbatively, like it is done for the nonlocal parts of the Argonne V18 potential [69]. For Δ -full chiral EFT, work along those lines has been done [229]. We plan to investigate these "maximally local" Δ -less chiral N³LO potentials in our future work.

4.2.5 Regularization and fits of low-energy couplings

We are now in the position to specify the regularization scheme for the NN potential. We multiply the coordinate-space expressions for the long-range potential in Eqs. (4.3), (4.4), (4.11)–(4.13), and (4.18)–(4.20) with the regulator function

$$V_{\text{long}}(r) \rightarrow V_{\text{long}}(r) \left(1 - e^{-(r/R_0)^4}\right). \quad (4.21)$$

This ensures that short-distance parts $\sim r^{-n}$ of the long-range potentials at r smaller than R_0 are smoothly cut off while the long-distance physics stays unchanged.

Upon Fourier transformation, the LO and NLO contact interactions lead to local δ functions. The regularization is achieved by employing a local regulator $f_{\text{local}}(q^2)$, leading to the replacement of the δ function by a smeared one with the same exponential smearing factor as for the long-range regulator,

$$\delta(\mathbf{r}) \rightarrow \delta_{R_0}(\mathbf{r}) = \alpha e^{-(r/R_0)^4}, \quad (4.22)$$

where the normalization constant,

$$\alpha = \frac{1}{\pi \Gamma(3/4) R_0^3}, \quad (4.23)$$

ensures that

$$\int d^3r \delta_{R_0}(\mathbf{r}) = 1. \quad (4.24)$$

We, thus, have for the LO contact interactions in coordinate space

$$\int \frac{d\mathbf{q}}{(2\pi)^3} C_{S,T} f_{\text{local}}(q^2) e^{i\mathbf{q}\cdot\mathbf{r}} = C_{S,T} \frac{e^{-(r/R_0)^4}}{\pi \Gamma(\frac{3}{4}) R_0^3}. \quad (4.25)$$

The analogous local expressions involving the NLO contact interactions are obtained by replacing $C_{S,T}$ with the seven different operators of Eq. (4.9) and are given in App. A. We use the same scale R_0 similarly in the short- and long-range parts.

The choice of the coordinate-space cutoff R_0 is dictated by the following considerations. On the one hand, one would like to take R_0 as small as possible to ensure that one keeps most of the long-range physics associated with the pion-exchange potentials. On the other hand, it is shown in Ref. [230] that at least for the particular class of pion-exchange diagrams corresponding to the multiple-scattering series, the chiral expansion for the NN potential breaks down at distances of the order of $r \sim 0.8$ fm but converges fast for $r \gtrsim 1$ fm. This suggests that a useful choice of the

cutoff R_0 is $R_0 \sim 1$ fm, which corresponds to momentum-space cutoffs of the order of ~ 500 MeV. This follows from Fourier transforming the regulator function, integrating it from 0 to infinity, and comparing to a sharp cutoff. This value is similar to the ones adopted in the already existing, nonlocal implementations of the chiral potential [59, 60], see also Ref. [231, 232] for a related discussion.

In view of the arguments provided in Refs. [222, 233, 234], we will not use significantly lower values of R_0 in applications. In Ref. [213], we varied the cutoff from $R_0 = 0.8$ fm to $R_0 = 1.2$ fm, based on the work of Ref. [78]. We found an error in the tensor channel of the pion-exchange interactions which, however, only has a small effect on pure neutron matter. We corrected this error, refitted the local chiral potentials and were able to obtain fits to NN phase shifts using the lowest cutoff $R_0 = 0.9$ fm. However, the LECs start to become unnatural for this cutoff.

On the other hand, choosing considerably larger values of R_0 results in cutting off the long-range physics we want to preserve and, thus, introduces an unnecessary limitation in the breakdown momentum of the approach. Therefore, here and in the following, we will allow for a variation of the cutoff R_0 in the range of $R_0 = 1.0 - 1.2$ fm.

Since the local regulator eliminates a considerable part of short-distance components of the TPE potential, we are much less sensitive to the choice of the SFR cutoff $\tilde{\Lambda}$ as compared to Refs. [59, 235] and can safely increase it up to $\tilde{\Lambda} = 1.4$ GeV without producing spurious deeply bound states. In this work, we will vary $\tilde{\Lambda}$ in the range $\tilde{\Lambda} = 1.0 - 1.4$ GeV. In future work, we will explore removing the SFR cutoff $\tilde{\Lambda} \rightarrow \infty$.

We would like to underline that there is no conceptual difference between the local regularization and the nonlocal regularization currently used in widely employed versions of chiral interactions in momentum space. The local chiral potentials include the same physics as the momentum-space versions. This is especially clear when antisymmetrizing. The local regulator by construction preserves the long-range parts of the interaction. When Fourier transformed, it generates higher-order q^2 -dependent terms when applied to short-range operators, like those already present at NLO and N^2 LO. Note that antisymmetrization and local regularization do not commute, but the commutator is given by higher-order terms. At NLO and N^2 LO, the $2 + 7$ contact interactions provide a most general representation consistent with all symmetries.

It remains to specify the values of the LECs and masses that enter the NN potentials at N^2 LO. In the following, we use $m_p = 938.272$ MeV, $m_n = 939.565$ MeV, the average pion mass $m_\pi = 138.03$ MeV, the neutral pion mass $m_\pi^0 = 134.98$ MeV, the charged pion mass $m_\pi^\pm = 139.57$ MeV, the pion decay constant $F_\pi = 92.4$ MeV, and the axial coupling $g_A = 1.267$. For the pion-nucleon coupling, we adopt the value of $g_{\pi N}^2/(4\pi) = 13.54$ which is consistent with Ref. [236], which also agrees with the recent determination in Ref. [237] based on the Goldberger-Miyazawa-Oehme sum rule and utilizing the most accurate available data on the pion-nucleon scattering lengths. In order to account for the GTD as described above, we use the value $g_A = 1.29$ in the expressions for the OPE potential. For the LECs c_i in the N^2 LO TPE potential, we use the same values as in Ref. [59], namely $c_1 = -0.81$ GeV $^{-1}$, $c_3 = -3.4$ GeV $^{-1}$, and $c_4 = 3.4$ GeV $^{-1}$.

We emphasize that we use the same expression for the OPE potential that includes isospin-symmetry-breaking corrections and accounts for the GTD as well as the same isospin-symmetry-breaking contact interactions at all orders in the chiral expansion to allow for a more meaningful comparison between LO, NLO and N^2 LO.

With the NN potential specified as above, we have performed χ^2 -fits to neutron-proton phase shifts from the Nijmegen PWA [238] for $R_0 = 0.9, 1.0, 1.1$ and 1.2 fm and $\tilde{\Lambda} = 0.8, 1.0, 1.2$ and 1.4 GeV. We used the separation of spin-singlet and spin-triplet channels, and, at LO,

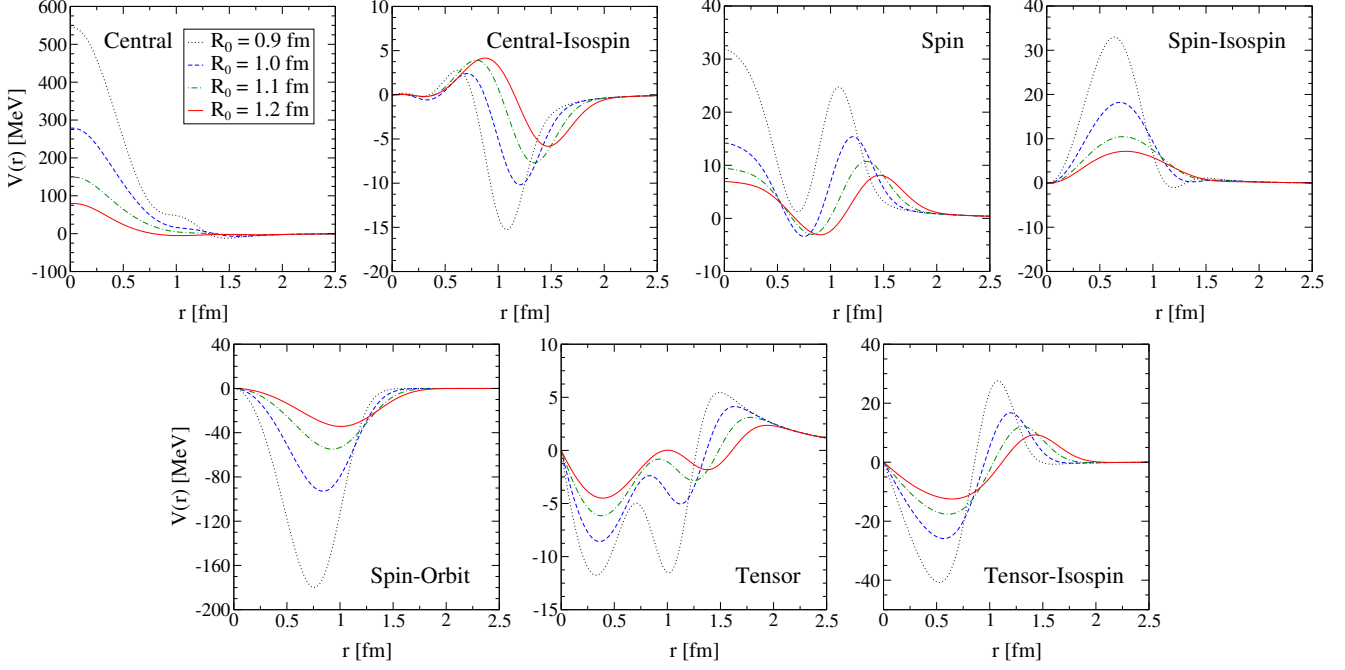


Figure 4.1: Local chiral NN potentials $V(r)$ at $N^2\text{LO}$ for an SFR cutoff $\tilde{\Lambda} = 1000$ MeV, decomposed into the central, central-isospin, spin, spin-isospin, spin-orbit, tensor, and tensor-isospin components, for cutoffs $R_0 = 0.9 - 1.2$ fm. For all components, we observe a softening of the potential going from a cutoff $R_0 = 0.9$ fm to $R_0 = 1.2$ fm. We include the $R_0 = 0.9$ fm potential for illustration, but as discussed in the text, will not use it in many-body calculations.

fit the 1S_0 and 3S_1 partial waves separately while at NLO and $N^2\text{LO}$ we fit the $\{^1S_0, ^1P_1\}$ and $\{^3S_1, \epsilon_1, ^3P_0, ^3P_1, ^3P_2\}$ partial waves. The partial-wave-decomposed matrix elements of the contact interactions can be found in App. B.

At NLO and $N^2\text{LO}$, we used the same energies of $E_{\text{lab}} = 1, 5, 10, 25, 50, 100$ and 150 MeV for $R_0 = 1.0$ and $R_0 = 1.1$ fm as in the Nijmegen PWA and the errors in the phase shifts provided in Ref. [238]. For $R_0 = 1.2$ fm, the fits are performed up to $E_{\text{lab}} = 100$ MeV. At LO, the fits are performed up to $E_{\text{lab}} = 50$ MeV. Finally, the values of the LECs C_{CIB} and C_{CSB} are adjusted to reproduce the proton-proton 1S_0 scattering length $a_{pp} = -7.81$ fm and the recommended value of the neutron-neutron scattering length $a_{nn} = -18.9$ fm. Note that we only take into account the point-like Coulomb force for the electromagnetic interaction as appropriate to $N^2\text{LO}$, see Ref. [59] for more details. The resulting LECs for $R_0 = 1.0, 1.1, 1.2$ fm and $\tilde{\Lambda} = 1000$ MeV are shown in Table 4.1 and for $\tilde{\Lambda} = 1400$ MeV in Table 4.2.

It would be useful to have a quantitative comparison of different fits, e.g., comparing the local chiral potentials presented here with the nonlocal optimized $N^2\text{LO}$ potentials of Refs. [239, 240] or with the analyses of Refs. [241, 242]. One possibility would be to calculate the χ^2/datum , but unfortunately we presently do not have the machinery to do this. We also emphasize that our fitting strategy is different to the nonlocal optimized $N^2\text{LO}$ potentials. As discussed, we only fit at low energies and take the c_i 's from pion-nucleon scattering, whereas the optimized $N^2\text{LO}$ potentials fit these over the full energy range considered.

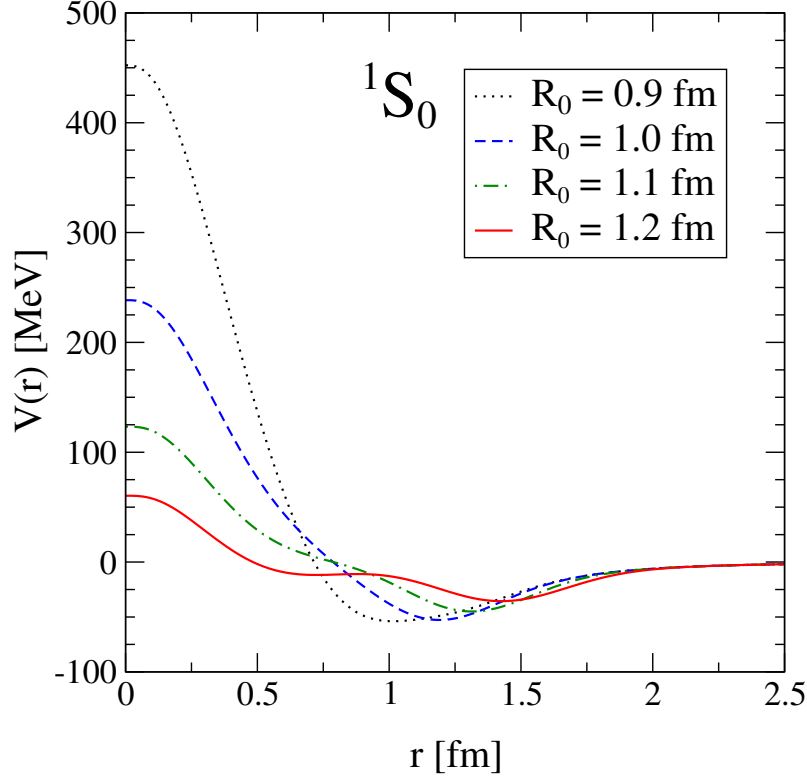


Figure 4.2: Local chiral NN potentials $V(r)$ at N^2LO for an SFR cutoff $\tilde{\Lambda} = 1000 \text{ MeV}$ in the 1S_0 partial wave in the neutron-neutron system for various cutoffs R_0 .

In Fig. 4.1, we show the local chiral potentials $V(r)$ at N^2LO for a SFR cutoff $\tilde{\Lambda} = 1000 \text{ MeV}$, decomposed into the central, central-isospin, spin, spin-isospin, spin-orbit, tensor, and tensor-isospin components

$$\begin{aligned}
 V(r) = & V^{\text{central}}(r) + V^{\text{central-isospin}}(r) \boldsymbol{\tau}_1 \cdot \boldsymbol{\tau}_2 \\
 & + \left[V^{\text{spin}}(r) + V^{\text{spin-isospin}}(r) \boldsymbol{\tau}_1 \cdot \boldsymbol{\tau}_2 \right] \boldsymbol{\sigma}_1 \cdot \boldsymbol{\sigma}_2 \\
 & + V^{\text{LS}}(r) \mathbf{L} \cdot \mathbf{S} \\
 & + \left[V^{\text{tensor}}(r) + V^{\text{tensor-isospin}}(r) \boldsymbol{\tau}_1 \cdot \boldsymbol{\tau}_2 \right] S_{12}(\mathbf{r}), \quad (4.26)
 \end{aligned}$$

for cutoffs $R_0 = 0.9 - 1.2 \text{ fm}$. We include the 0.9 fm potential for illustration, but we do not recommend it for many-body calculations and therefore do not include it in our own calculations or in the tables. For all components we see a softening of the potential going from $R_0 = 0.9 \text{ fm}$ to $R_0 = 1.2 \text{ fm}$, as expected, because short-range parts of the potentials are strongly scheme dependent. The structures in the individual channels are due to adding up different contributions with different r -dependencies to those channels.

In addition, we show the local chiral potentials $V(r)$ at N^2LO for a SFR cutoff $\tilde{\Lambda} = 1000 \text{ MeV}$ in the 1S_0 channel in Fig. 4.2 in the neutron-neutron system. Again, we observe a softening of the potential when increasing the coordinate space cutoff from $R_0 = 0.9 \text{ fm}$ to $R_0 = 1.2 \text{ fm}$.

4.2.6 Phase shifts

Next, we present the neutron-proton phase shifts in partial waves up to $J = 4$ for the local chiral potentials at LO, NLO, and N^2LO for laboratory energies up to 250 MeV in comparison with the

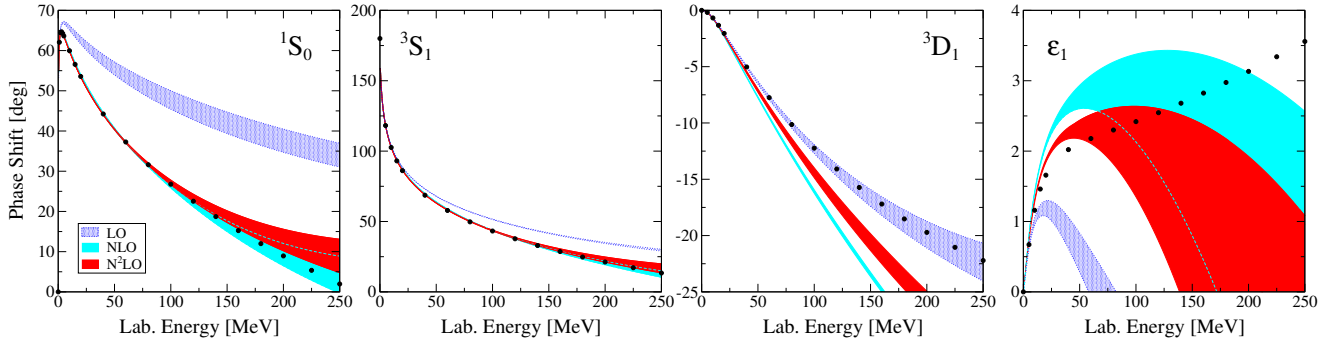


Figure 4.3: Phase shifts for the 1S_0 and $^3S_1 - ^3D_1$ partial waves at LO, NLO, and N^2 LO in comparison with the Nijmegen partial wave analysis (PWA) [238]. The bands at each order correspond to the cutoff variation of $R_0 = 1.0 - 1.2$ fm. At NLO and N^2 LO, we also vary the SFR cutoff from $\tilde{\Lambda} = 1.0 - 1.4$ GeV.

Nijmegen PWA [238]. We vary the cutoff between $R_0 = 1.0 - 1.2$ fm and, at NLO and N^2 LO, the SFR cutoff between $\tilde{\Lambda} = 1.0 - 1.4$ GeV.

In Fig. 4.3, we show the 1S_0 phase shifts as well as the $^3S_1 - ^3D_1$ coupled channel. The description of the 1S_0 channel at LO is only good at very low energies and improves when going to NLO and the effective range physics is included. When going from NLO to N^2 LO, the cutoff bands overlap. In the 3S_1 channel the situation is similar but the cutoff bands are narrower. In both S-wave channels the width of the bands at NLO and N^2 LO are of similar size. This is due to the truncation of the short-range contact interactions and the large c_i couplings entering at N^2 LO, and is visible in all phase shifts.

In the 3D_1 channel the description worsens when going from LO to NLO and improves only slightly from NLO to N^2 LO. At N^2 LO the description of the 3D_1 channel is poor for energies larger than 50 MeV. In addition, also the description of the $J = 1$ mixing angle is poor at all orders, a fact which is clearly reflected in the size of the cutoff bands.

In Fig. 4.4 we show the phase shifts for the P waves and the $J = 2$ coupled channel. In the 1P_1 channel the LO band starts to deviate from the data already at low energies. Including additional spin-orbit and tensor contributions at NLO improves the description of the 1P_1 channel only little. However, the situation highly improves when going to N^2 LO.

In the 3P waves the phase shifts improve considerably going from LO to higher orders and the description of the 3P waves at N^2 LO is substantially better than in our previous fits [213]. Furthermore, the description of the $J = 2$ coupled channel is considerably better than for the $J = 1$ coupled channel and improves when going from LO to N^2 LO.

In Fig. 4.5 we show the phase shifts for the remaining uncoupled partial waves up to $J = 4$. The description of the individual channels is good even at high energies except for the D waves. This can also be seen in Fig. 4.6 where we show the $J = 3$ and $J = 4$ coupled channels.

In general, the description of all D wave channels is poor up to N^2 LO and does not improve when going from NLO to N^2 LO. This is due to the truncation of the contact interactions at N^2 LO because in partial waves with orbital angular momentum $L > 1$ no contact interactions contribute at this order except for regulator effects. Thus, the D wave phase shifts are described almost solely by pion-exchange interactions and are parameter free. This can be improved by going to N^3 LO. The higher $L > 2$ partial waves instead are mostly described by long-range

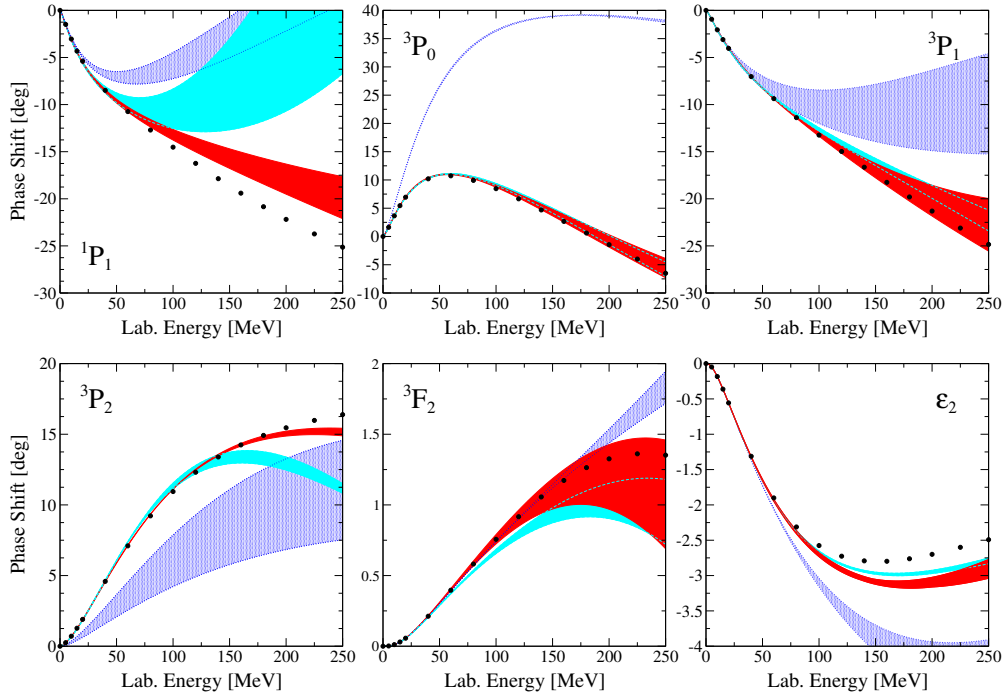


Figure 4.4: Phase shifts for the 1P_1 , 3P_0 , 3P_1 and 3P_2 – 3F_2 partial waves at LO, NLO, and N²LO in comparison with the Nijmegen PWA [238]. The bands are obtained as in Fig. 4.3.

pion-exchange interactions and already the OPE interaction at LO describes the data well at low energies. Thus, the higher partial waves can be well described already at N²LO.

Comparing our phase shift results to the results obtained with the nonlocal N²LO momentum space potential of Ref. [59], we find that the local potentials describe all partial waves up to $J = 4$ better except for the D waves. In addition, the cutoff variation is smaller for the local chiral potentials.

We want to mention that the effect of the spin projection operator in the CIB and CSB contacts on the NN phase shifts is very small, typically between 1 – 2%. This is smaller than the deviation from the phase shifts of the Nijmegen partial wave analysis (PWA) and smaller than the theoretical uncertainty of the results. Thus, in the following we will neglect the spin-0 projection factor.

4.2.7 Deuteron properties

In this Section, we calculate deuteron properties using the local chiral potentials presented in the previous Sections at LO, NLO, and N²LO. We calculate the deuteron binding energy E_d , the quadrupole moment Q_d , the magnetic moment μ_d , the asymptotic D/S ratio η , the root-mean-square (rms) radius r_d , the asymptotic S -wave factor A_s , and the D -state probability P_D . We vary the cutoff $R_0 = 1.0 - 1.2$ fm and, at NLO and N²LO, the SFR cutoff $\tilde{\Lambda} = 1.0 - 1.4$ GeV. The deuteron properties are calculated as described in Ref. [59]. The results are shown in Table 4.3 and are compared with experimental results of Refs. [243, 244, 245, 246, 247, 248] and the N²LO Epelbaum, Glöckle, and Meißner (EGM) results of Ref. [59], where the cutoff variation is $\Lambda = 450 - 650$ MeV and $\tilde{\Lambda} = 500 - 700$ MeV.

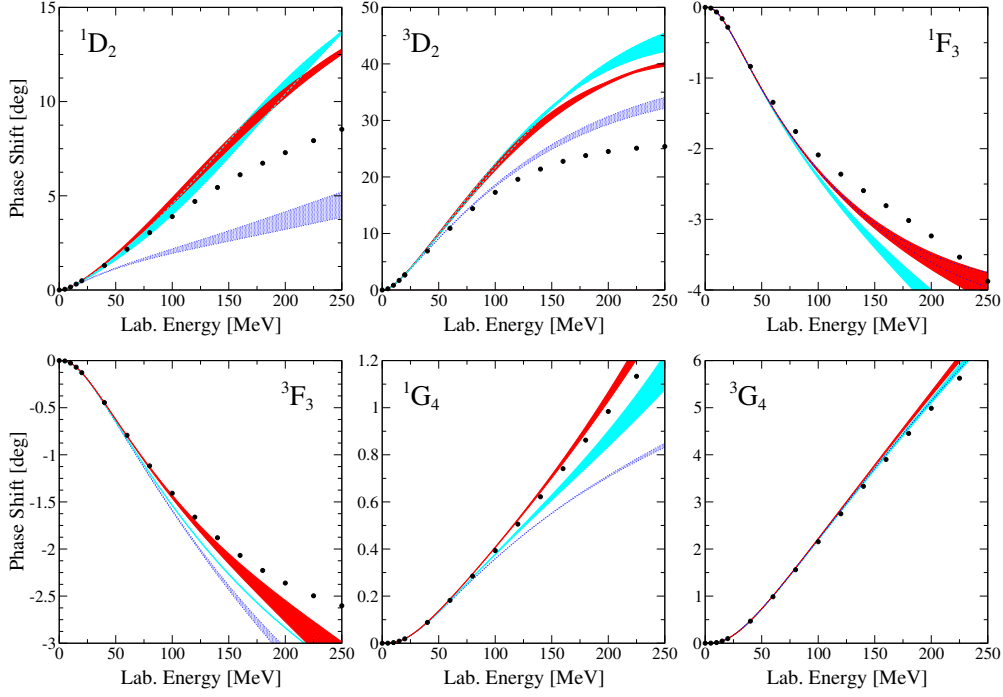


Figure 4.5: Phase shifts for the 1D_2 , 3D_2 , 1F_3 , 3F_3 , 1G_4 , and 3G_4 partial waves at LO, NLO, and N^2 LO in comparison with the Nijmegen PWA [238]. The bands are obtained as in Fig. 4.3.

At N^2 LO we find a deuteron binding energy of -2.208 ± 0.010 MeV, which has to be compared with the experimental value of -2.225 MeV. Thus, the N^2 LO result deviates from the experimental result by less than 1%, which is better than 2.196 ± 0.007 for the nonlocal, momentum-space N^2 LO EGM potentials of Ref. [59]. However, for those potentials the range of the cutoff variation is different, which affects the results and theoretical error estimates.

The description of the deuteron quadrupole moment is surprisingly good for the local chiral potentials and the experimental result lies within the N^2 LO uncertainty band. Note that electromagnetic two-body currents are not included. The results for the N^2 LO momentum space potentials instead deviate by 4 – 5%. Also for the other observables the result of the local N^2 LO potentials deviates less than 1% from the experimental values.

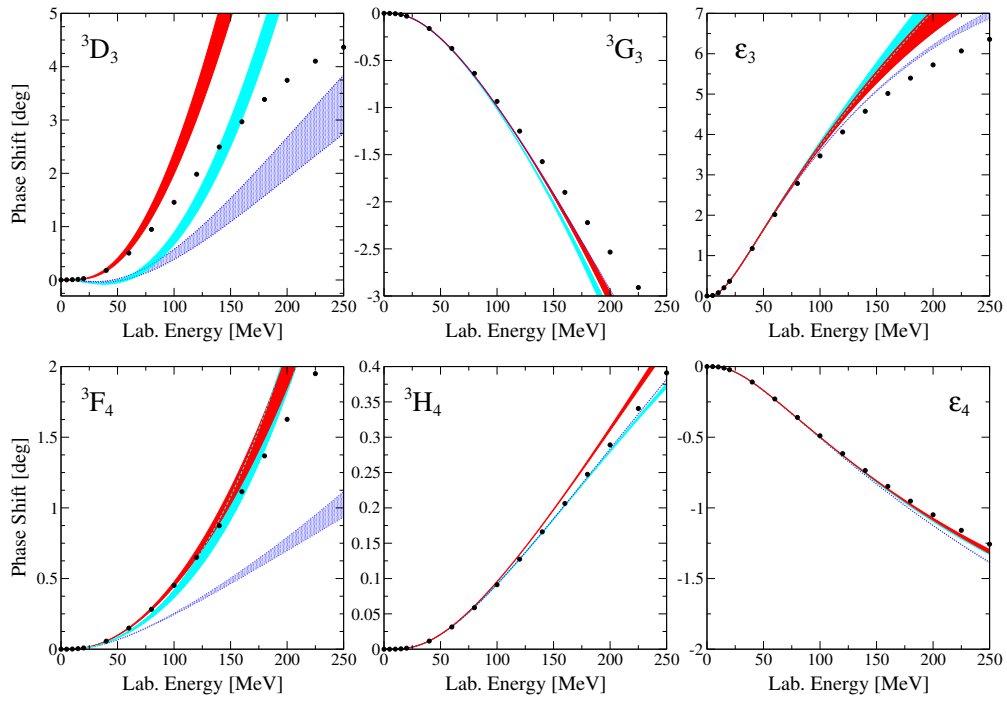


Figure 4.6: Phase shifts for the 3D_3 – 3G_3 and 3F_4 – 3H_4 partial waves at LO, NLO, and N²LO in comparison with the Nijmegen PWA [238]. The bands are obtained in the same way as in Fig. 4.3.

Table 4.1: Low-energy constants for $R_0 = 1.0, 1.1, 1.2 \text{ fm}$ at LO, NLO, and N²LO (with a spectral-function cutoff $\tilde{\Lambda} = 1000 \text{ MeV}$). The couplings C_{1-7} are given in fm^4 while the rest are in fm^2 .

R_0	1.0 fm			1.1 fm			1.2 fm		
	LO	NLO	N ² LO	LO	NLO	N ² LO	LO	NLO	N ² LO
C_S	-0.75112	3.16803	5.43850	-1.29631	1.03075	3.88699	-1.79693	0.03551	2.68765
C_T	0.37409	1.41396	0.27672	0.25648	0.90699	0.24416	0.15442	0.71729	0.23382
C_1		0.31420	-0.14084		0.27239	-0.09650		0.22288	-0.07951
C_2		0.25786	0.04243		0.22032	0.05947		0.22878	0.07610
C_3		-0.13134	-0.12338		-0.13641	-0.14183		-0.15043	-0.16926
C_4		0.11861	0.11018		0.09420	0.11146		0.08929	0.12359
C_5		2.38552	2.11254		2.16238	2.0082		2.02932	1.94280
C_6		0.37319	0.15898		0.33065	0.18318		0.34011	0.21421
C_7		-0.35668	-0.26994		-0.33570	-0.30105		-0.36248	-0.34193
C_{CB}	-0.02361	0.05094	0.05320	-0.01922	0.05153	0.05538	-0.01335	0.05477	0.05648
C_{CSB}	-0.01988	0.00823	0.00976	-0.02001	0.00704	0.00902	-0.01959	0.00660	0.00771

Table 4.2: Low-energy constants for $R_0 = 1.0, 1.1, 1.2$ fm at LO, NLO, and N²LO (with a spectral-function cutoff $\tilde{\Lambda} = 1400$ MeV). The couplings C_{1-7} are given in fm⁴ while the rest are in fm².

R_0	1.0 fm			1.1 fm			1.2 fm		
	LO	NLO	N ² LO	LO	NLO	N ² LO	LO	NLO	N ² LO
C_S	-0.75112	3.32404	8.16454	-1.29631	1.13903	5.89685	-1.79693	0.10909	4.19629
C_T	0.37409	1.30221	-0.14809	0.25648	0.81867	-0.08689	0.15442	0.64646	-0.02820
C_1		0.30649	-0.12250		0.25830	-0.04061		0.21280	0.00211
C_2		0.26558	0.00843		0.23565	0.02161		0.24032	0.03805
C_3		-0.14378	-0.12964		-0.14535	-0.15446		-0.16477	-0.18525
C_4		0.13434	0.12390		0.10401	0.12110		0.10228	0.12819
C_5		2.39094	2.13434		2.16525	2.02482		2.02827	1.95804
C_6		0.38680	0.12495		0.34394	0.14992		0.35219	0.18335
C_7		-0.37920	-0.27533		-0.35731	-0.30346		-0.38191	-0.34227
C_{CIB}	-0.02361	0.05088	0.05290	-0.01922	0.05151	0.05538	-0.01335	0.05468	0.05592
C_{CSB}	-0.01988	0.00821	0.00961	-0.02001	0.00701	0.00883	-0.01959	0.00652	0.00714

Table 4.3: Deuteron properties for the local chiral potentials at LO, NLO, and N²LO. We tabulate the deuteron binding energy E_d , the D -state probability P_D , the magnetic moment μ_d , the quadrupole moment Q_d , the asymptotic D/S ratio η , the asymptotic S -wave factor A_s , and the rms radius r_d . The ranges include a cutoff variation $R_0 = 1.0 - 1.2$ fm and, at NLO and N²LO, a variation of the SFR cutoff $\tilde{\Lambda} = 1.0 - 1.4$ GeV. The experimental results are taken from Refs. [243, 244, 245, 246, 247, 248]. We compare our results with the N²LO EGM results of Ref. [59], where the cutoff variation is $\Lambda = 450 - 650$ MeV and $\tilde{\Lambda} = 500 - 700$ MeV.

	LO	NLO	N ² LO	N ² LO EGM	Exp.
E_d [MeV]	-2.0243... - 2.0161	-2.1597... - 2.1446	-2.2177... - 2.1981	-2.202... - 2.189	-2.225
P_D [%]	4.2761... 5.3356	6.9249... 8.1702	5.5059... 6.1356	3.53... 4.93	0.857
μ_d [μ_N]	0.8494... 0.8554	0.8332... 0.8403	0.8438... 0.8484	0.271... 0.275	0.286
Q_d [fm ²]	0.2580... 0.2691	0.3013... 0.3039	0.2828... 0.2890	0.0255... 0.0256	0.0256
η	0.0232... 0.0240	0.0275... 0.0278	0.0256... 0.0267	0.0255... 0.0256	0.0256
A_s [fm ^{-1/2}]	0.8299... 0.8321	0.8605... 0.8648	0.8765... 0.8818	0.874... 0.879	0.885
r_d [fm]	1.9897... 1.9919	1.9737... 1.9758	1.9677... 1.9698	1.970... 1.972	1.966

5 Quantum Monte Carlo calculations with chiral EFT NN interactions

In this Chapter we present results of QMC simulations of neutron matter and light nuclei using the chiral NN interactions derived in the previous Chapter. Results also including chiral 3N forces are discussed in the next Chapters.

5.1 Neutron matter

We apply the developed local LO, NLO, and N^2 LO chiral EFT interactions in systematic QMC calculations for neutron matter, see also Refs. [213, 219]. To simulate $O(100)$ neutrons in order to access the thermodynamic limit in neutron matter we turn to the AFDMC method, which is capable of efficiently handling spin-dependent Hamiltonians. For pure neutron matter, either in the homogeneous case or in a confining potential, the AFDMC method has been carefully benchmarked with nuclear GFMC, which can handle beyond-central correlations as well as release the nodal or phase constraint after convergence to the ground state. Both have been found to have minimal effects on the equation of state of neutrons [79, 211, 249].

First, we studied finite-size effects and the dependence on the Jastrow correlations in the trial Jastrow-Slater wave function (in continuum QMC calculations there are no discretization effects). By comparing AFDMC results for 14 particles using the Argonne family of potentials with a GFMC calculation for the same potentials and neutron number (the largest neutron number for which GFMC results exist), we found that the Jastrow dependence disappears in AFDMC when using a softened Jastrow function.

Since no GFMC results exist for 66 particles, we have carried out separate computations at $n = 0.16 \text{ fm}^{-3}$. We studied Jastrow terms from solving the Schrödinger equation for the Argonne v'_8 potential, a typical QMC potential of reference, and from the consistent local chiral potentials. In addition, we have examined the effect of artificially softening the Jastrow term by multiplying the input potential (only when producing the Jastrow function) by a fixed coefficient, in order to see the effect of removing the Jastrow. The highest energies always result from using a largely unmodified Argonne v'_8 potential, as this is the potential that is most different from the new chiral interactions. In the case of $R_0 = 1.0 \text{ fm}$ the different Jastrow terms lead to an energy per particle that varies by at most 0.1 MeV at 0.16 fm^{-3} , while for the $R_0 = 1.2 \text{ fm}$ potentials the variation is 0.15 MeV. Both these results are much smaller than the 0.6 MeV quoted in Ref. [213] for the $R_0 = 0.8 \text{ fm}$ potential. This is a reflection of the softer local potentials used here.

Furthermore, we have probed in detail the finite-size effects for the local chiral potentials. As we are interested in describing the thermodynamic limit of neutron matter, it is important that we use sufficiently many particles in our AFDMC simulations. In order to avoid issues related to preferred directions in momentum-space, we have performed calculations for closed shells $N = 14, 38, 54, 66, 114$, see Sec. 3.1.2. We chose the SFR cutoff $\tilde{\Lambda} = 1000 \text{ MeV}$ and performed simulations at N^2 LO for both the $R_0 = 1.0 \text{ fm}$ and $R_0 = 1.2 \text{ fm}$ potentials at the highest density $n = 0.16 \text{ fm}^{-3}$. The results are shown in Fig. 5.1. We observe that the two potentials exhibit

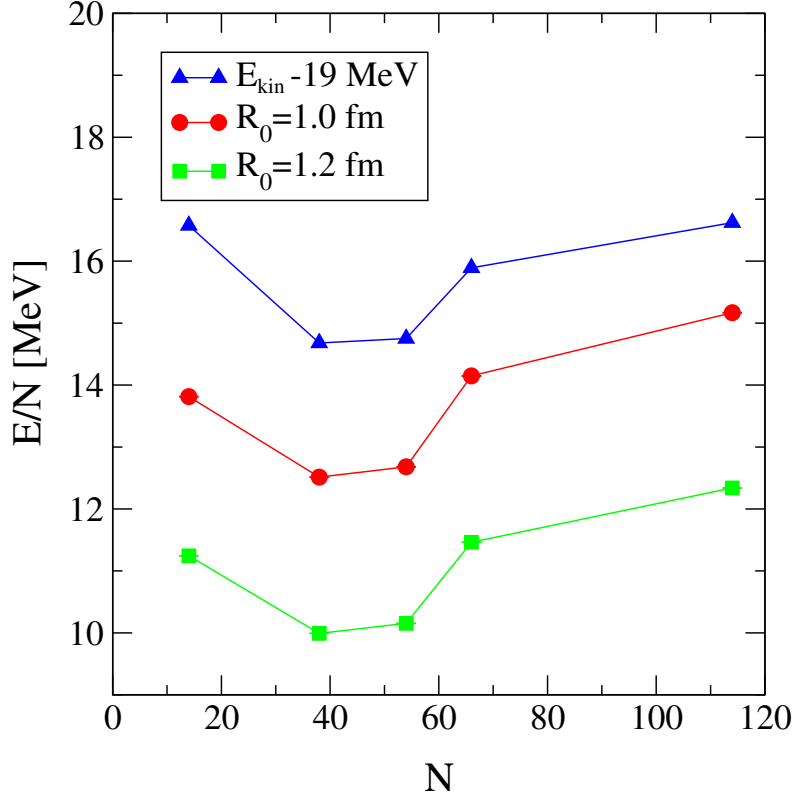


Figure 5.1: Finite-size effects for the ground-state energy of neutron matter for a SFR cutoff $\tilde{\Lambda} = 1000 \text{ MeV}$ at $N^2\text{LO}$. Results are shown for different particle numbers for the $R_0 = 1.0 \text{ fm}$ and the $R_0 = 1.2 \text{ fm}$ potentials. We also show the kinetic energy, shifted down by 19 MeV. The finite-size effects for the local chiral potentials follow the shell effects of the kinetic energy operator.

essentially identical shell structure, as was expected because the ranges involved in the two potentials are basically the same. These results show a dependence on N that is very similar to that in Table III of Ref. [211] for the values of N used in that reference, namely 14, 38, and 66. The shell structure is very similar to that of the free Fermi gas in a periodic box, which we also show in Fig. 5.1. From the free Fermi gas we expect that the thermodynamic limit value is below the $N = 114$ result and very close to the $N = 66$ value. This explains our choice of using 66 particles to simulate the thermodynamic limit. The only qualitative difference between the free Fermi-gas shell structure and our AFDMC results appears at $N = 14$. For the free gas $N = 14$ leads to an energy that is higher than that at $N = 66$. This results from the very small periodic box needed to produce the same density for $N = 14$. In that case the interaction length scales also start to be important. In contrast, for larger N , shell effects come almost completely from the kinetic energy behavior. Therefore, we have performed calculations for an optimal number of 66 particles, while also including contributions from the 26 cells, neighboring the primary simulation box.

We have also explored the dependence of the results on different values of the SFR cutoff. As discussed, the effect of the SFR cutoff $\tilde{\Lambda}$ is expected to be smaller than that of R_0 . We show the results of varying the SFR cutoff from $\tilde{\Lambda} = 1000 \text{ MeV}$ to $\tilde{\Lambda} = 1400 \text{ MeV}$ for $R_0 = 1.0 \text{ fm}$ and $R_0 = 1.2 \text{ fm}$ in Fig. 5.2. There is essentially no effect at low densities, while at higher densities

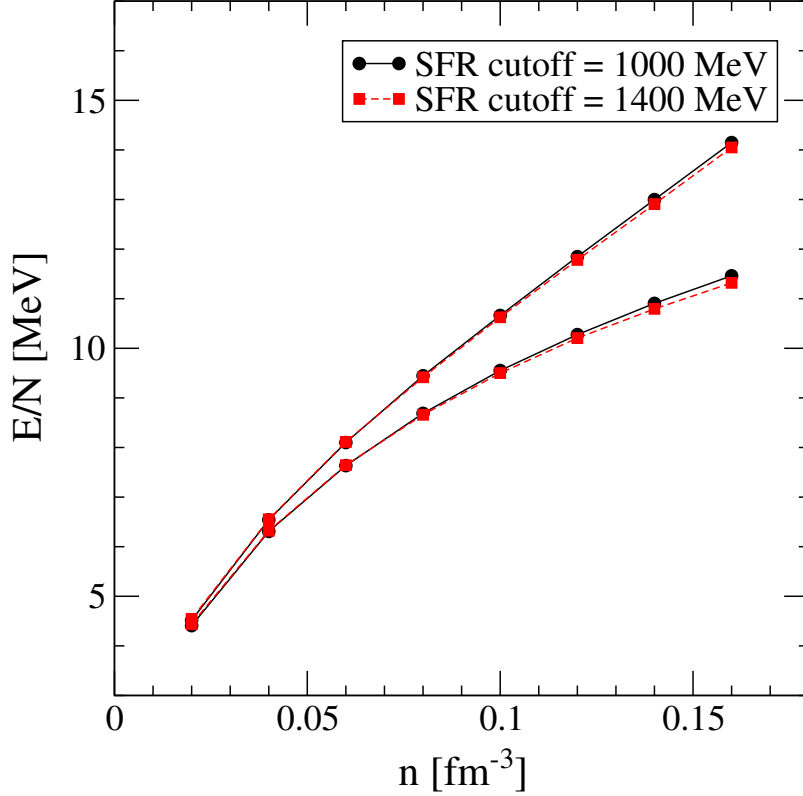


Figure 5.2: Ground-state energy of 66 neutrons at $N^2\text{LO}$. Shown are results for two SFR cutoffs, $\tilde{\Lambda} = 1000\text{ MeV}$ and $\tilde{\Lambda} = 1400\text{ MeV}$, and two different cutoffs $R_0 = 1.0\text{ fm}$ (upper lines) and $R_0 = 1.2\text{ fm}$ (lower lines). The results exhibit a very weak $\tilde{\Lambda}$ dependence.

the difference for $R_0 = 1.0\text{ fm}$ never exceeds 0.1 MeV and for $R_0 = 1.2\text{ fm}$ it is always less than 0.15 MeV. This shows that the SFR cutoff has a negligible impact on the many-body results.

In Fig. 5.3 we present first AFDMC calculations for the neutron matter energy with chiral EFT NN interactions at LO, NLO, and $N^2\text{LO}$. Our results represent nonperturbative energies for neutron matter based on chiral EFT beyond low densities.

At each chiral order, the full interaction is used both in the propagator and when evaluating observables. The bands in Fig. 5.3 give the range of the energy obtained by varying R_0 between 1.0–1.2 fm, where the softer $R_0 = 1.2\text{ fm}$ interactions yield the lower energies. At low densities, or low Fermi momenta, as expected, the energy is well constrained at LO. The LO results at higher densities lead to a broad band, the lower part of which ($R_0 = 1.2\text{ fm}$) even changes slope as the density is increased. This reflects the fact that the LO potential does not describe the phase shifts at the relevant energies as there are only two LECs at this order.

The overlap of the bands at different orders in Fig. 5.3 is excellent. In addition, the comparable size of the NLO and $N^2\text{LO}$ bands is expected due to the large c_i entering at $N^2\text{LO}$ and the same truncation of the contact interactions at both orders. The width of these bands is similar to that of the phase shifts discussed in Sec. 4.2.6. At the highest density studied, the size of the $N^2\text{LO}$ band is approximately 10% of the potential energy, which may be improved by including 3N forces [54] or going to $N^3\text{LO}$.

These QMC results for neutron matter exhibit a systematic order-by-order convergence in chiral EFT. Although we present results up to saturation density, we emphasize that the contributions of 3N forces will become important for densities $n \gtrsim 0.05\text{ fm}^{-3}$ [54]. Our results present a

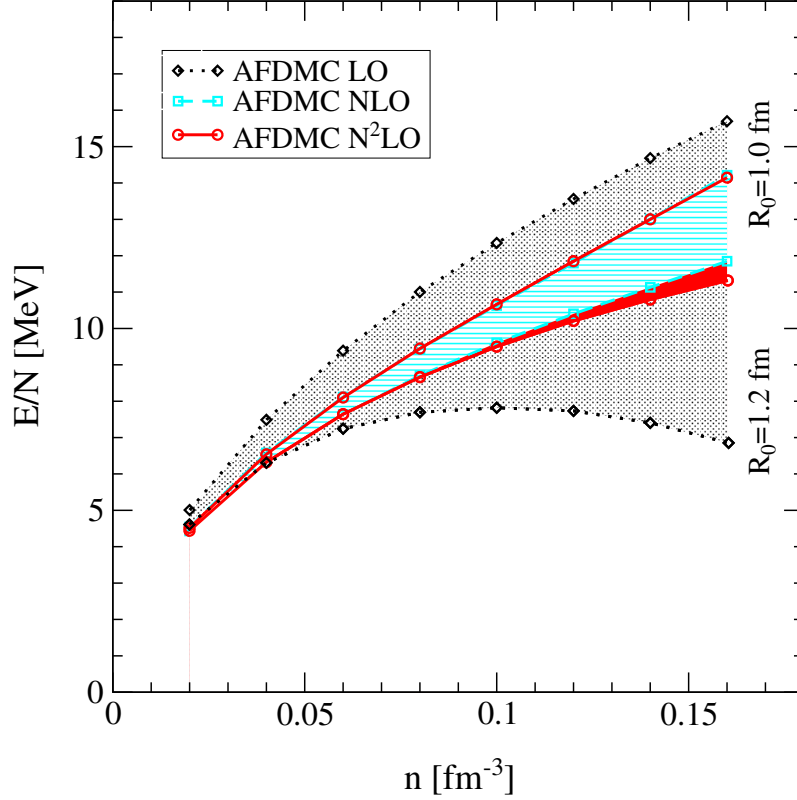


Figure 5.3: Neutron matter energy per particle E/N as a function of density n using AFDMC with the local chiral NN potentials at LO, NLO, and N^2 LO. The bands are obtained by varying the cutoff $R_0 = 1.0 - 1.2$ fm and the SFR cutoff $\tilde{\Lambda} = 1000 - 1400$ MeV.

nonperturbative benchmark that can lead to further predictions at higher density, when 3N forces are consistently included. They will be discussed in the following Chapters.

Finally, in the low-density regime, the results in Fig. 5.3 match the QMC calculations of Ref. [68, 178] based on central interactions that reproduce the large neutron-neutron scattering length and the effective range physics.

In Fig. 5.4 we compare our AFDMC N^2 LO results for neutron matter with the MBPT N^2 LO calculation of Ref. [57] based on the momentum-space potentials of Ref. [59], the coupled-cluster results of Ref. [192] using the optimized N^2 LO potential of Ref. [239], the MBPT results of Ref. [250], and the configuration-interaction Monte Carlo (CIMC) calculation of Ref. [217], both using the same optimized N^2 LO potential. The bands for the MBPT results are obtained as described in Ref. [57].

The different many-body results for the optimized N^2 LO potential are in very good agreement. These results are also consistent with recent self-consistent Green's function results [194]. In addition, the optimized N^2 LO results agree very well with the N^2 LO band of Ref. [57] which includes also a NN cutoff variation and is therefore rather broad. Comparing with the AFDMC results of this work, we find that at saturation density the resulting energies per particle agree very well. However, the general density dependence of the AFDMC results is more flat, leading to higher energies at intermediate densities and a different density dependence at saturation density. These differences could be due to the differences in the phase shift predictions, and we expect both results to come closer when going to N^3 LO.

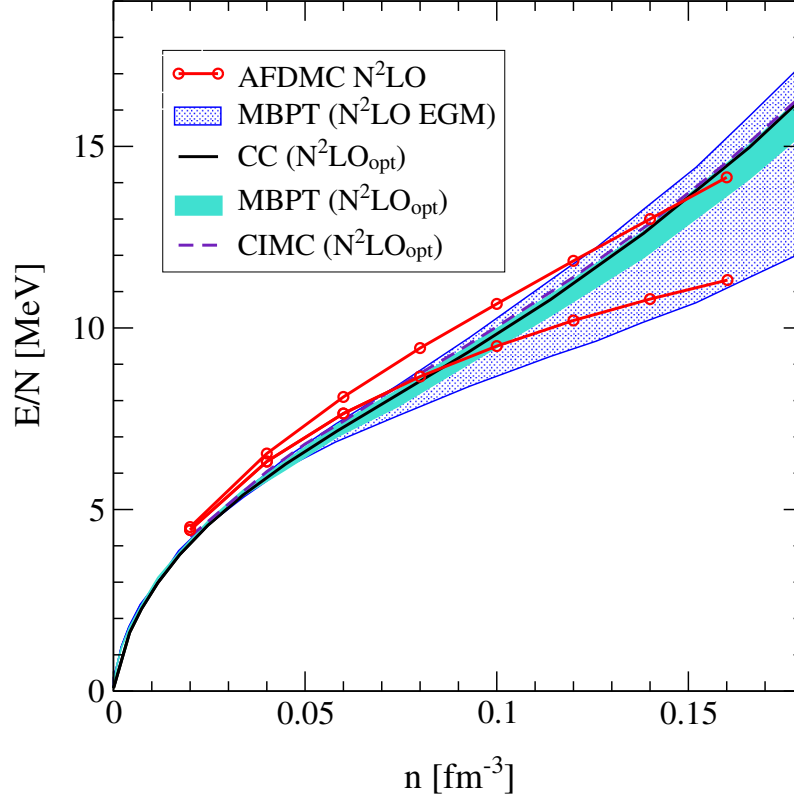


Figure 5.4: Neutron matter energy per particle E/N as a function of density n . We compare the AFDMC $N^2\text{LO}$ results of this work with the MBPT $N^2\text{LO}$ results of Ref. [57] using the momentum-space potentials of Ref. [59], the coupled-cluster results of Ref. [192] using the optimized $N^2\text{LO}$ potential of Ref. [239], the MBPT results of Ref. [250], and the QMC results of Ref. [217], both using the same optimized $N^2\text{LO}$ potential.

5.2 Nonperturbative validation of MBPT calculations for soft chiral interactions

Our AFDMC results provide first nonperturbative benchmarks for chiral EFT interactions at nuclear densities. We have performed neutron matter calculations using MBPT following Refs. [17, 54, 55, 57] for the same local chiral potentials and the same regulators as in the previous Sections. Details on the derivation of the NN matrix elements necessary for the MBPT calculation are given in Appendix C. We show the results in Fig. 5.5 together with the AFDMC results at LO, NLO, and $N^2\text{LO}$ for the three different cutoffs $R_0 = 1.0, 1.1$, and 1.2 fm, and varying the SFR cutoff $\tilde{\Lambda} = 1000 - 1400$ MeV.

At every order in the chiral expansion and for every cutoff we show the results at the Hartree-Fock level as a dashed line, including second-order contributions as a shaded band, and including also third-order particle-particle and hole-hole corrections as solid bands. The bands are obtained by employing a free or Hartree-Fock single-particle spectrum and by varying the SFR cutoff as stated above. Again, we observe that the $R_0 = 1.1$ fm results at all three chiral orders lie between the $R_0 = 1.0$ fm and $R_0 = 1.2$ fm ones.

At LO, the local chiral potentials, in general, follow the trend of the AFDMC results for all three cutoffs. The width of the individual bands is very small and the energy changes from first to second and from second to third order are small. As discussed in Ref. [17], this energy difference, combined with the weak dependence on the different single-particle spectra, is a

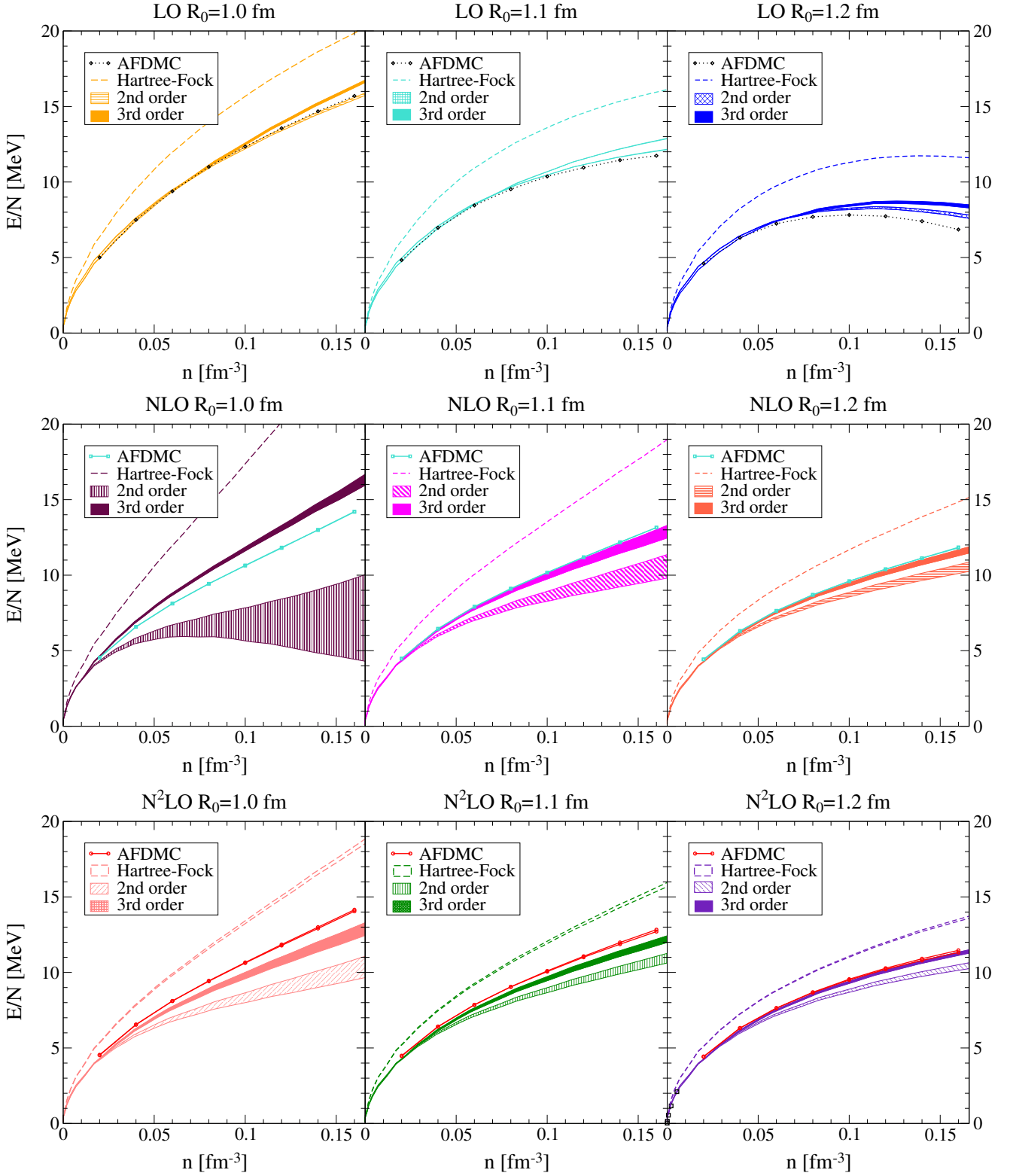


Figure 5.5: Results for MBPT and AFDMC calculations at LO, NLO, and N^2 LO for $R_0 = 1.0\text{--}1.2$ fm. For the MBPT results, we show the Hartree-Fock energies as well as the energy at second order and including third-order particle-particle and hole-hole corrections. The width of the bands includes a variation of the single-particle spectrum from a free to a Hartree-Fock spectrum. In addition, for both the MBPT and AFDMC results we also vary the SFR cutoff $\tilde{\Lambda} = 1000\text{--}1400$ MeV. For the LO 1.1 fm results, the lower band corresponds to the second-order results.

measure of the perturbative convergence for the individual potentials. All potentials at this chiral order seem to be perturbative. We find a good agreement between the AFDMC and the MBPT results, especially at lower densities, although at higher densities the trend is that the second-order results compare better with AFDMC than third-order results.

At NLO, we find the $R_0 = 1.0$ fm potential to have the slowest, if any, perturbative convergence. The second-order band is very broad and the third-order contributions are large: at saturation density they are 6 – 10 MeV. Going to higher coordinate-space cutoffs, meaning lower momentum cutoffs, we find that the potential becomes more perturbative. At $R_0 = 1.2$ fm both the second- and third-order bands are narrow and the third-order contributions are ≈ 1.5 MeV.

At N²LO the results are very similar to NLO. We find that the $R_0 = 1.0$ fm potential shows the slowest perturbative convergence, with an energy difference from second to third order of about 3 MeV at saturation density. However, the perturbativeness for this cutoff at N²LO is better than at NLO. Going to higher coordinate-space cutoffs again improves the perturbativeness and for $R_0 = 1.2$ fm the energy difference is ≈ 1.0 MeV at this density. This behavior is similar to the nonlocal potentials used in Ref. [17] where it was shown that soft (low momentum cutoff) potentials have a better convergence.

For the perturbative $R_0 = 1.2$ fm potentials, the agreement between the third-order perturbative results and the AFDMC results is excellent. For $R_0 = 1.2$ fm, at N²LO, the perturbative results lie almost on top of the AFDMC values. The difference between the third-order result with Hartree-Fock single-particle spectrum and the AFDMC results is 0.2 MeV at 0.16 fm^{-3} for $\tilde{\Lambda} = 1400 \text{ MeV}$ and only 20 keV for $\tilde{\Lambda} = 1000 \text{ MeV}$. In comparison, at NLO the difference is 0.2 MeV at 0.16 fm^{-3} for $\tilde{\Lambda} = 1400 \text{ MeV}$ and 0.1 MeV for $\tilde{\Lambda} = 1000 \text{ MeV}$, while at LO it is 1.6 MeV.

These results constitute the first direct validation of MBPT for neutron matter based on low momentum potentials, in this case $R_0 = 1.1$ fm and $R_0 = 1.2$ fm, and highlight the need for nonperturbative benchmarks for infinite matter calculations to assess the quality of different many-body methods.

5.3 Light nuclei

In Ref. [251] the local chiral NN potentials at LO, NLO and N²LO have been used in GFMC calculations of light nuclei for the first time. Binding energies and radii of the $A = 3, 4$ systems were calculated. The authors varied the cutoff in the range $R_0 = 1.0 - 1.2$ fm. The results for the ${}^4\text{He}$ binding energies at different chiral orders are shown in Fig. 5.6, and the results for the $A = 3$ systems are qualitatively similar.

It was shown that at LO the nuclei are overbound and the corresponding radii are too small. Going to NLO, the binding energy decreases and the nuclei are underbound with radii that are larger than the experimental result. At N²LO the binding energies are still too small but improve compared to NLO. However, at N²LO, the leading 3N forces start to contribute and give important contributions necessary to reproduce correct binding energies and radii. With increasing chiral order, the theoretical uncertainty of the results due to the cutoff variation reduces from ~ 4 MeV at LO to ~ 1 MeV at N²LO. A negligible dependence on the SFR cutoff has been found as well.

The result with the phenomenological AV8' potential is shown compared to the results at different chiral orders. This potential is a truncated version of the AV18 potential with similar contact operators as in the chiral interactions. The results in Fig. 5.6 highlight the deficiencies in the

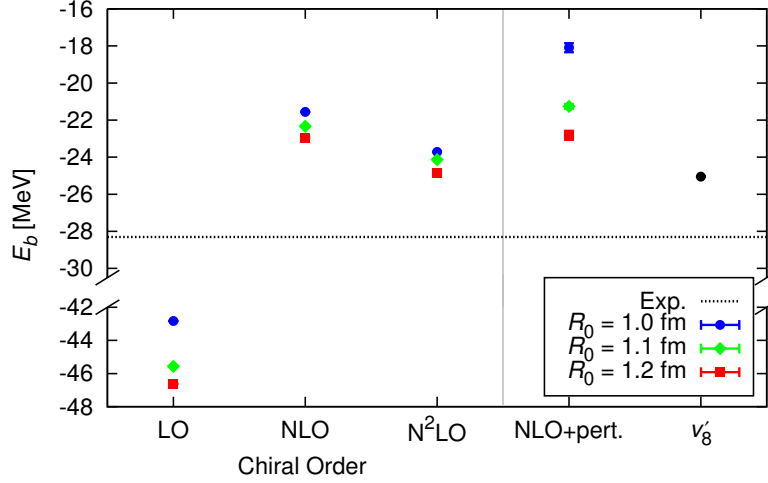


Figure 5.6: Binding energies of ${}^4\text{He}$ using local chiral NN forces at LO, NLO and $N^2\text{LO}$ in comparison with the experimental result and the result for the Argonne V8' potential from Ref. [251]. Furthermore, the results for the $N^2\text{LO}$ binding energy with the NLO wave function are shown. The statistical errors are smaller than the points.

phenomenological interactions and the improvement due to chiral interactions. Chiral potentials allow for systematic improvement by increasing the chiral order, they provide theoretical uncertainties, and they allow for consistent many-body interactions, see the next Chapters. The GFMC calculations with chiral EFT interactions, thus, are the initial step towards GFMC and AFDMC calculations of heavier nuclei.

5.4 Summary of main results

In summary, we have presented QMC calculations with chiral NN interactions. This was achieved by using a freedom in chiral EFT to remove all sources of nonlocality to $N^2\text{LO}$. We have presented details of the derivation of local chiral EFT potentials at LO, NLO, and $N^2\text{LO}$. We performed improved fits of the LECs to low-energy NN phase shifts. The reproduction of the NN phase shifts is very good compared to the momentum-space $N^2\text{LO}$ NN potentials of Ref. [59].

We have applied the new local chiral potentials to neutron matter using AFDMC and MBPT and obtained first nonperturbative benchmarks for the neutron-matter equation of state at nuclear densities. Our results show systematic order-by-order convergence with theoretical uncertainties and validate perturbative calculations for the softer local NN interactions. The excellent agreement of the results for the softer $R_0 = 1.1$ fm and $R_0 = 1.2$ fm potentials within the two many-body frameworks represents a direct validation of MBPT for neutron matter.

In particular, we have investigated the sensitivity of the results to the local regulator and to the SFR cutoff, to the influence of the Jastrow term, and also to finite size effects in AFDMC.

Since for densities higher than $0.5 n_0$ 3N forces become important, we have to include these into the AFDMC calculations to obtain *ab initio* constraints for nuclear density functionals and for dense matter in astrophysics. In the next Chapters we will show how to include the 3N forces into our calculations and present first results.

6 Chiral three-body forces for Quantum Monte Carlo calculations

The leading 3N forces in chiral EFT enter at N²LO in the chiral expansion and contain three contributions: a two-pion-exchange interaction V_C , which consists of three parts proportional to the low-energy constants c_1 , c_3 , and c_4 with different momentum, spin and isospin structures. Furthermore, they contain a one-pion-exchange–contact interaction V_D given by c_D , and a 3N contact interaction V_E given by c_E , see Sec. 2.2.5. We show the N²LO 3N contributions diagrammatically in Fig. 2.5. The couplings c_i already appear in the subleading NN two-pion exchange while the couplings c_D and c_E are free parameters and have to be fitted to properties of $A \geq 3$ systems. Since we want to include the N²LO 3N forces in an AFDMC calculation in coordinate space we have to find local coordinate space expressions for these leading 3N forces, as similarly done in Ref. [176, 252].

6.1 Derivation of local chiral 3N forces

We perform the Fourier transformation of the momentum-space expressions of the N²LO 3N forces. In momentum space, the N²LO 3N interactions are given by [173], see Sec. 2.2.5,

$$V_C = \frac{1}{2} \left(\frac{g_A}{2f_\pi} \right)^2 \sum_{\pi(ijk)} \frac{\boldsymbol{\sigma}_i \cdot \mathbf{q}_i \boldsymbol{\sigma}_k \cdot \mathbf{q}_k}{(q_i^2 + m_\pi^2)(q_k^2 + m_\pi^2)} F_{ijk}^{\alpha\beta} \tau_i^\alpha \tau_k^\beta, \quad (6.1)$$

$$V_D = -\frac{g_A}{8f_\pi^2} \frac{c_D}{f_\pi^2 \Lambda_\chi} \sum_{\pi(ijk)} \frac{\boldsymbol{\sigma}_k \cdot \mathbf{q}_k}{q_k^2 + m_\pi^2} \boldsymbol{\sigma}_i \cdot \mathbf{q}_k \boldsymbol{\tau}_i \cdot \boldsymbol{\tau}_k, \quad (6.2)$$

$$V_E = \frac{c_E}{2f_\pi^4 \Lambda_\chi} \sum_{\pi(ijk)} \boldsymbol{\tau}_i \cdot \boldsymbol{\tau}_k, \quad (6.3)$$

where $F_{ijk}^{\alpha\beta}$ includes the different contributions from the c_i 's

$$F_{ijk}^{\alpha\beta} = \delta^{\alpha\beta} \left[-\frac{4c_1 m_\pi^2}{f_\pi^2} + \frac{2c_3}{f_\pi^2} \mathbf{q}_i \cdot \mathbf{q}_k \right] + \sum_\gamma \frac{c_4}{f_\pi^2} \varepsilon^{\alpha\beta\gamma} \tau_j^\gamma \boldsymbol{\sigma}_j \cdot (\mathbf{q}_i \times \mathbf{q}_k). \quad (6.4)$$

Similarly to the NN sector, 3N pion exchanges are local and generate nonlocalities only due to nonlocal regulator functions chosen. Furthermore, the leading 3N contact interactions are momentum-independent and, thus, local. Because of this, the N²LO 3N forces can be constructed in a local way, if local regulators are chosen.

We Fourier transform the 3N interactions with respect to the momentum transfers of particle i and k , which yields the coordinate-space expression V^{ijk} as a function of \mathbf{r}_{ij} and \mathbf{r}_{kj} . These expressions will then be regularized directly in coordinate space, as done in the NN sector. Because the 3N interactions include a sum over all permutations, taking a different choice for

the momentum transfers would lead to the same result. However, this will not be the case when a regulator in momentum space is included before Fourier transforming.

In the following, we show how to do the Fourier transformation of the three 3N topologies. We give the definitions of some general functions in coordinate space:

$$Y(r) = \frac{\exp(-m_\pi \cdot r)}{r}, \quad (6.5)$$

$$U(r) = 1 + \frac{1}{m_\pi r}, \quad (6.6)$$

$$T(r) = 1 + \frac{3}{m_\pi r} + \frac{3}{(m_\pi r)^2}, \quad (6.7)$$

$$S_{ij}(\mathbf{r}) = 3\boldsymbol{\sigma}_i \cdot \hat{\mathbf{r}} \boldsymbol{\sigma}_j \cdot \hat{\mathbf{r}} - \boldsymbol{\sigma}_i \cdot \boldsymbol{\sigma}_j, \quad (6.8)$$

$$X_{ij}(\mathbf{r}) = (S_{ij}(\mathbf{r})T(r) + \boldsymbol{\sigma}_i \cdot \boldsymbol{\sigma}_j) Y(r). \quad (6.9)$$

Here, $Y(r)$ is the well-known Yukawa function, $U(r)$ and $T(r)$ are scalar functions depending on the radius r , $S_{ij}(\mathbf{r})$ is the tensor force operator and $X_{ij}(\mathbf{r})$ denotes the one-pion-exchange interaction in coordinate space.

More details on the Fourier transformations are given in Appendix D.

6.1.1 Two-pion-exchange interaction V_C

We first turn to the two-pion-exchange contribution V_C in neutron matter:

$$V_{C,c_1}^{ijk} = -\frac{c_1 m_\pi^2 g_A^2}{2f_\pi^4} \sum_{\pi(ijk)} \boldsymbol{\tau}_i \cdot \boldsymbol{\tau}_k \int \frac{d^3 q_i}{(2\pi)^3} \frac{\boldsymbol{\sigma}_i \cdot \mathbf{q}_i}{q_i^2 + m_\pi^2} e^{i\mathbf{q}_i \cdot \mathbf{r}_{ij}} \int \frac{d^3 q_k}{(2\pi)^3} \frac{\boldsymbol{\sigma}_k \cdot \mathbf{q}_k}{q_k^2 + m_\pi^2} e^{i\mathbf{q}_k \cdot \mathbf{r}_{kj}}. \quad (6.10)$$

The integrals are readily evaluated using

$$\int \frac{d^3 q_i}{(2\pi)^3} \frac{\boldsymbol{\sigma}_i \cdot \mathbf{q}_i}{q_i^2 + m_\pi^2} e^{i\mathbf{q}_i \cdot \mathbf{r}_{ij}} = -i \sigma_i^\alpha \partial^\alpha \frac{e^{-m_\pi r_{ij}}}{4\pi r_{ij}} = i \frac{m_\pi}{4\pi} \sigma_i^\alpha \hat{r}_{ij}^\alpha U(r_{ij}) Y(r_{ij}). \quad (6.11)$$

This leads to

$$V_{C,c_1}^{ijk} = \frac{c_1 m_\pi^4 g_A^2}{2f_\pi^4 (4\pi)^2} \sum_{\pi(ijk)} \boldsymbol{\tau}_i \cdot \boldsymbol{\tau}_k \boldsymbol{\sigma}_i \cdot \hat{\mathbf{r}}_{ij} \boldsymbol{\sigma}_k \cdot \hat{\mathbf{r}}_{kj} U(r_{ij}) Y(r_{ij}) U(r_{kj}) Y(r_{kj}). \quad (6.12)$$

This contribution is similar to the long-range (LR) S wave TPE part of the phenomenological Illinois or Urbana forces [200]. Its implementation into quantum Monte Carlo codes, thus, is straightforward.

For the Fourier transformation of the more complicated c_3 part of the 3N two-pion-exchange interaction, we find

$$V_{C,c_3}^{ijk} = \frac{c_3 g_A^2}{4f_\pi^4} \sum_{\pi(ijk)} \boldsymbol{\tau}_i \cdot \boldsymbol{\tau}_k \int \frac{d^3 q_i}{(2\pi)^3} \frac{\boldsymbol{\sigma}_i \cdot \mathbf{q}_i}{q_i^2 + m_\pi^2} q_i^\alpha e^{i\mathbf{q}_i \cdot \mathbf{r}_{ij}} \int \frac{d^3 q_k}{(2\pi)^3} \frac{\boldsymbol{\sigma}_k \cdot \mathbf{q}_k}{q_k^2 + m_\pi^2} q_k^\alpha e^{i\mathbf{q}_k \cdot \mathbf{r}_{kj}}. \quad (6.13)$$

Similar to the Fourier transformation for the one-pion exchange in Eq. (6.17) one gets

$$\begin{aligned} & \int \frac{d^3 q_i}{(2\pi)^3} \frac{\boldsymbol{\sigma}_i \cdot \mathbf{q}_i}{q_i^2 + m_\pi^2} q_i^\alpha e^{i\mathbf{q}_i \cdot \mathbf{r}_{ij}} \\ &= -\frac{m_\pi^2}{4\pi} \sigma_i^\beta \left[\left(\hat{r}_{ij}^\alpha \hat{r}_{ij}^\beta - \frac{1}{3} \delta^{\alpha\beta} \right) T(r_{ij}) Y(r_{ij}) + \frac{1}{3} \delta^{\alpha\beta} Y(r_{ij}) - \frac{1}{3} \frac{4\pi}{m_\pi^2} \delta^{\alpha\beta} \delta(\mathbf{r}_{ij}) \right]. \end{aligned} \quad (6.14)$$

Thus, the Fourier transformation is given by

$$\begin{aligned} V_{C,c_3}^{ijk} &= \sum_{\pi(ijk)} \frac{1}{2} \left(\frac{g_A}{2f_\pi} \right)^2 \left(\frac{2c_3}{f_\pi^2} \right) \boldsymbol{\tau}_i \cdot \boldsymbol{\tau}_k \left(\frac{m_\pi^2}{4\pi} \right)^2 \frac{1}{9} \left[\left(\frac{4\pi}{m_\pi^2} \right)^2 \boldsymbol{\sigma}_i \cdot \boldsymbol{\sigma}_k \delta(\mathbf{r}_{ij}) \delta(\mathbf{r}_{kj}) \right. \\ &\quad \left. - \frac{4\pi}{m_\pi^2} X_{ik}(\mathbf{r}_{ij}) \delta(\mathbf{r}_{kj}) - \frac{4\pi}{m_\pi^2} X_{ik}(\mathbf{r}_{kj}) \delta(\mathbf{r}_{ij}) + X_{ij}(\mathbf{r}_{ij}) X_{kj}(\mathbf{r}_{kj}) \right]. \end{aligned}$$

In coordinate space, for the two-pion exchange there are four terms that are proportional to c_3 , due to a long-range and short-range spin-dependent piece in every pion exchange, indicated by $X_{ab}(\mathbf{r}_{ij})$ and the δ function after Fourier transformation. The first term $\sim X_{ij}(\mathbf{r}_{ij}) X_{kj}(\mathbf{r}_{kj})$ is a long-range two-pion-exchange contribution similar to the anticommutator part of the P wave two-pion-exchange interaction of Ref. [200]. In addition, there is also a short-range (SR) spin-dependent three-nucleon contact term $\sim \delta(\mathbf{r}_{ij}) \delta(\mathbf{r}_{kj})$ and two intermediate-range (IR) terms $\sim X_{ik}(\mathbf{r}_{ij}) \delta(\mathbf{r}_{kj}) + X_{ik}(\mathbf{r}_{kj}) \delta(\mathbf{r}_{ij})$ similar to a one-pion-exchange–contact interaction. We note that, although the spin/isospin structure is similar to the Urbana IX force and in general to the two pion-exchange of the Illinois forces, the spatial functions are quite different, as shorter-range terms emerge.

Finally, we transform the c_4 part of the two-pion-exchange interaction V_C . We find the final result

$$\begin{aligned} V_{C,c_4}^{ijk} &= \frac{c_4 g_A^2}{72 f_\pi^4} \sum_{\pi(ijk)} \boldsymbol{\tau}_i \cdot (\boldsymbol{\tau}_k \times \boldsymbol{\tau}_j) \left[\frac{m_\pi^4}{2i(4\pi)^2} [X_{ij}(\mathbf{r}_{ij}), X_{kj}(\mathbf{r}_{kj})] \right. \\ &\quad - \frac{m_\pi^2}{4\pi} \boldsymbol{\sigma}_i \cdot (\boldsymbol{\sigma}_k \times \boldsymbol{\sigma}_j) (1 - T(r_{ij})) Y(r_{ij}) \delta(\mathbf{r}_{kj}) \\ &\quad - \frac{m_\pi^2}{4\pi} \boldsymbol{\sigma}_i \cdot (\boldsymbol{\sigma}_k \times \boldsymbol{\sigma}_j) (1 - T(r_{kj})) Y(r_{kj}) \delta(\mathbf{r}_{ij}) \\ &\quad - \frac{3m_\pi^2}{4\pi} \boldsymbol{\sigma}_i \cdot \hat{\mathbf{r}}_{ij} \hat{\mathbf{r}}_{ij} \cdot (\boldsymbol{\sigma}_k \times \boldsymbol{\sigma}_j) T(r_{ij}) Y(r_{ij}) \delta(\mathbf{r}_{kj}) \\ &\quad - \frac{3m_\pi^2}{4\pi} \boldsymbol{\sigma}_k \cdot \hat{\mathbf{r}}_{kj} \hat{\mathbf{r}}_{kj} \cdot (\boldsymbol{\sigma}_j \times \boldsymbol{\sigma}_i) T(r_{kj}) Y(r_{kj}) \delta(\mathbf{r}_{ij}) \\ &\quad \left. + \boldsymbol{\sigma}_i \cdot (\boldsymbol{\sigma}_k \times \boldsymbol{\sigma}_j) \delta(\mathbf{r}_{ij}) \delta(\mathbf{r}_{kj}) \right]. \end{aligned} \quad (6.15)$$

The c_4 part of the two-pion exchange also consists of several terms: a long-range term $\sim [X_{ij}(\mathbf{r}_{ij}), X_{kj}(\mathbf{r}_{kj})]$, which is similar to the commutator part of the P wave two-pion exchange of the Urbana and Illinois 3N forces, see Ref. [200]. In addition, there is a three-nucleon contact part $\sim \delta(\mathbf{r}_{ij}) \delta(\mathbf{r}_{kj})$ and medium-range mixed terms $\sim Y(r_{ij}) \delta(\mathbf{r}_{kj})$.

6.1.2 One-pion-exchange–contact interaction V_D

For the Fourier transformation of the V_D contribution we start from

$$\begin{aligned} V_D^{ijk} &= \int \frac{d^3 q_i}{(2\pi)^3} \frac{d^3 q_k}{(2\pi)^3} e^{i\mathbf{q}_i \cdot \mathbf{r}_{ij}} e^{i\mathbf{q}_k \cdot \mathbf{r}_{kj}} V_D, \\ &= -\frac{g_A}{8f_\pi^2} \frac{c_D}{f_\pi^2 \Lambda_\chi} \sum_{\pi(ijk)} \boldsymbol{\tau}_i \cdot \boldsymbol{\tau}_k \int \frac{d^3 q_i}{(2\pi)^3} e^{i\mathbf{q}_i \cdot \mathbf{r}_{ij}} \int \frac{d^3 q_k}{(2\pi)^3} \frac{\boldsymbol{\sigma}_k \cdot \mathbf{q}_k \boldsymbol{\sigma}_i \cdot \mathbf{q}_k}{q_k^2 + m_\pi^2} e^{i\mathbf{q}_k \cdot \mathbf{r}_{kj}}. \end{aligned} \quad (6.16)$$

The second integral gives an expression similar to the one-pion exchange:

$$\int \frac{d^3 q_k}{(2\pi)^3} \frac{\boldsymbol{\sigma}_k \cdot \mathbf{q}_k \boldsymbol{\sigma}_i \cdot \mathbf{q}_k}{q_k^2 + m_\pi^2} e^{i\mathbf{q}_k \cdot \mathbf{r}_{kj}} = -\frac{m_\pi^2}{12\pi} X_{ik}(\mathbf{r}_{kj}) + \frac{1}{3} \boldsymbol{\sigma}_i \cdot \boldsymbol{\sigma}_k \delta(\mathbf{r}_{kj}). \quad (6.17)$$

As a result, in addition to the one-pion-exchange–contact part, the Fourier transformation also leads to a 3N contact contribution in V_D^{ijk} :

$$V_D^{ijk} = \frac{g_A}{24f_\pi^2} \frac{c_D}{f_\pi^2 \Lambda_\chi} \sum_{\pi(ijk)} \boldsymbol{\tau}_i \cdot \boldsymbol{\tau}_k \left[\frac{m_\pi^2}{4\pi} \delta(\mathbf{r}_{ij}) X_{ik}(\mathbf{r}_{kj}) - \boldsymbol{\sigma}_i \cdot \boldsymbol{\sigma}_k \delta(\mathbf{r}_{ij}) \delta(\mathbf{r}_{kj}) \right]. \quad (6.18)$$

There is no similar interaction in the phenomenological Argonne or Urbana three-nucleon models.

We want to emphasize that there is an ambiguity in performing the Fourier transformation for the V_D term, depending on the choice of the initial spin-isospin structure. This leads either to terms $\delta(\mathbf{r}_{ij}) X_{ik}(\mathbf{r}_{kj})$ or $\delta(\mathbf{r}_{ij}) X_{ik}(\mathbf{r}_{ik})$ with different spin indices in the X function. The two expressions are analogous due to the δ functions but lead to different results after regularization. Thus, the differences from choosing different structures are only a regulator effect and higher-order corrections, as mentioned in Ref. [176]. They will vanish in the limit of infinite cutoff. In the following, we will distinguish between the two versions:

$$\begin{aligned} V_{D,1}^{ijk} &= \frac{g_A}{24f_\pi^2} \frac{c_D}{f_\pi^2 \Lambda_\chi} \sum_{\pi(ijk)} \boldsymbol{\tau}_i \cdot \boldsymbol{\tau}_k \left[\frac{m_\pi^2}{4\pi} \delta(\mathbf{r}_{ij}) X_{ik}(\mathbf{r}_{kj}) - \boldsymbol{\sigma}_i \cdot \boldsymbol{\sigma}_k \delta(\mathbf{r}_{ij}) \delta(\mathbf{r}_{kj}) \right], \\ V_{D,2}^{ijk} &= \frac{g_A}{24f_\pi^2} \frac{c_D}{f_\pi^2 \Lambda_\chi} \sum_{\pi(ijk)} \boldsymbol{\tau}_i \cdot \boldsymbol{\tau}_k \left[\frac{m_\pi^2}{4\pi} \delta(\mathbf{r}_{ij}) X_{ik}(\mathbf{r}_{ik}) - \boldsymbol{\sigma}_i \cdot \boldsymbol{\sigma}_k \delta(\mathbf{r}_{ij}) \delta(\mathbf{r}_{ik}) \right]. \end{aligned} \quad (6.19)$$

6.1.3 Three-body contact interaction V_E

As the three-nucleon contact interaction is momentum-independent, the Fourier transformation is simply given by

$$\begin{aligned} V_E(\mathbf{r}_{ij}, \mathbf{r}_{kj}) &= \int \frac{d^3 \mathbf{q}_i}{(2\pi)^3} \frac{d^3 \mathbf{q}_k}{(2\pi)^3} \exp(i\mathbf{q}_i \cdot \mathbf{r}_{ij}) \exp(i\mathbf{q}_k \cdot \mathbf{r}_{kj}) V_E(\mathbf{q}_i, \mathbf{q}_k) \\ &= \frac{c_E}{2f_\pi^4 \Lambda_\chi} \boldsymbol{\tau}_i \cdot \boldsymbol{\tau}_k \int \frac{d^3 \mathbf{q}_i}{(2\pi)^3} \exp(i\mathbf{q}_i \cdot \mathbf{r}_{ij}) \int \frac{d^3 \mathbf{q}_k}{(2\pi)^3} \exp(i\mathbf{q}_k \cdot \mathbf{r}_{kj}) \\ &= \frac{c_E}{2f_\pi^4 \Lambda_\chi} \boldsymbol{\tau}_i \cdot \boldsymbol{\tau}_k \delta(\mathbf{r}_{ij}) \delta(\mathbf{r}_{kj}). \end{aligned} \quad (6.20)$$

This contribution is a product of two δ functions. It is similar to the spin-independent interaction V^R of the Urbana and Illinois three-nucleon potentials [200] and, thus, can easily be implemented in existing quantum Monte Carlo codes using Urbana and Illinois three-body forces.

6.1.4 Regularization of coordinate space 3N interactions

We regularize the local 3N forces after the Fourier transformation in a consistent way compared to the NN force and replace δ functions by smeared ones of the form

$$\delta(\mathbf{r}) \rightarrow \delta_{R_{3N}}(\mathbf{r}) = \frac{1}{\pi\Gamma(3/4)R_{3N}^3} e^{-(r/R_{3N})^4}, \quad (6.21)$$

where R_{3N} is the three-body cutoff. To regularize the long-range pion contributions, we multiply all the appearing Yukawa functions with the long-range regulator f_{long} , given by

$$Y(r) \rightarrow Y(r) \left(1 - e^{-(r/R_{3N})^4}\right). \quad (6.22)$$

To be consistent with the NN cutoff $R_0 = 1.0 - 1.2$ fm, which was used before, we will in the following also vary the 3N cutoff in this range, $R_{3N} = 1.0 - 1.2$ fm. This will be justified later. Furthermore, we adopt the same c_i values as in the NN sector.

The one-pion-exchange–contact interactions vanish in momentum space for neutron matter due to the spin-isospin structure if a regulator which is symmetric in the particle labels is used, see Ref. [54]. The same is true for the 3N contact contributions. They vanish in momentum-space in neutron matter due to the Pauli principle. Because a local regulator does not fulfill this requirement and the δ functions acquire a finite range, these terms will contribute to neutron matter if a local regulator is employed.

We want to stress that the contributions of the IR and SR parts of the two-pion exchange as well as V_E and V_D in neutron matter are solely regulator effects and vanish for $R_{3N} \rightarrow 0$, i.e., infinite momentum cutoffs.

6.2 Implementation in Quantum Monte Carlo

In the following we show how to include the local 3N forces into quantum Monte Carlo simulations. We begin with the inclusion into AFDMC, which we use to calculate pure neutron matter, and follow the strategy of Ref. [203] to rewrite the 3N interactions in form of two-body operators.

In AFDMC, the NN potential can be recast into the following form, when the spin-orbit part is neglected:

$$V = V_{\text{Spin-indep.}} + \frac{1}{2} \sum_{i\alpha,j\beta} \sigma_{i\alpha} A_{i\alpha,j\beta}^{(\sigma)} \sigma_{j\beta} + \frac{1}{2} \sum_{i\alpha,j\beta} \sigma_{i\alpha} A_{i\alpha,j\beta}^{(\sigma\tau)} \sigma_{j\beta} \tau_i \cdot \tau_j + \frac{1}{2} \sum_{i,j} A_{i,j}^{(\tau)} \tau_i \cdot \tau_j. \quad (6.23)$$

Here, i and j are particle indices and α and β are Cartesian coordinates.

As we use AFDMC only to calculate pure neutron matter, the isospin structure can be evaluated explicitly, with all $\boldsymbol{\tau}_i \cdot \boldsymbol{\tau}_j = 1$ and the c_4 part vanishes due to $\boldsymbol{\tau}_i \times \boldsymbol{\tau}_k \cdot \boldsymbol{\tau}_j = 0$ [54], leading to

$$V = V_{\text{Spin-indep.}} + \frac{1}{2} \sum_{i\alpha, j\beta} \sigma_{i\alpha} A_{i\alpha, j\beta}^{(\sigma)} \sigma_{j\beta}. \quad (6.24)$$

Our goal is it to recast the three-body interaction into a similar form and to find a matrix $A_{i\alpha, j\beta}^{(\sigma)}$ for the 3N forces, which is then added to the NN matrix.

In the AFDMC code, the three-body forces are included as a sum $V_3 = \sum_{i<j<k} V^{ijk}$, with the particles i, j and k . The 3N forces between these particles, V^{ijk} , contain a cyclic summation $V^{ijk} = \sum_{\text{cyc}} V(i, j, k) = V(i, j, k) + V(j, k, i) + V(k, i, j)$. As chiral 3N forces in their original form contain a sum over all permutations of the particle indices, $\sum_{\pi(ijk)} V(i, j, k)$, we have to carefully rewrite the chiral 3N interactions using sums over cyclic permutations.

For neutron matter, the two-pion exchange V_C contributes and has several terms, which have been derived before:

$$V_{C, c_1}^{ijk} = - \sum_{\pi(ijk)} \frac{1}{2} \left(\frac{g_A}{2f_\pi} \right)^2 \left(\frac{m_\pi}{4\pi} \right)^2 \left(-\frac{4c_1 m_\pi^2}{f_\pi^2} \right) \frac{\boldsymbol{\sigma}_i \cdot \mathbf{r}_{ij}}{r_{ij}} \frac{\boldsymbol{\sigma}_k \cdot \mathbf{r}_{kj}}{r_{kj}} U(r_{ij}) Y(r_{ij}) U(r_{kj}) Y(r_{kj}) \quad (6.25)$$

$$V_{C, c_3}^{ijk} = \sum_{\pi(ijk)} \frac{1}{2} \left(\frac{g_A}{2f_\pi} \right)^2 \left(\frac{1}{4\pi} \right)^2 \left(\frac{2c_3}{f_\pi^2} \right) \left[\frac{m_\pi^4}{9} X_{ij}(\mathbf{r}_{ij}) X_{kj}(\mathbf{r}_{kj}) - \frac{4\pi m_\pi^2}{9} X_{ik}(\mathbf{r}_{ij}) \delta(\mathbf{r}_{kj}) \right. \\ \left. - \frac{4\pi m_\pi^2}{9} X_{ik}(\mathbf{r}_{kj}) \delta(\mathbf{r}_{ij}) + \frac{(4\pi)^2}{9} \boldsymbol{\sigma}_i \cdot \boldsymbol{\sigma}_k \delta(\mathbf{r}_{ij}) \delta(\mathbf{r}_{kj}) \right]. \quad (6.26)$$

We will start with the c_3 part, in particular with the long-range two-pion-exchange:

$$V_{C, c_3, \text{LR}}^{ijk} = \sum_{\pi(ijk)} \frac{1}{2} \left(\frac{g_A}{2f_\pi} \right)^2 \left(\frac{1}{4\pi} \right)^2 \left(\frac{2c_3}{f_\pi^2} \right) \frac{m_\pi^4}{9} X_{ij}(\mathbf{r}_{ij}) X_{kj}(\mathbf{r}_{kj}) \quad (6.27) \\ = \sum_{\text{cyc}} \frac{1}{2} \left(\frac{g_A}{2f_\pi} \right)^2 \left(\frac{1}{4\pi} \right)^2 \left(\frac{2c_3}{f_\pi^2} \right) \frac{m_\pi^4}{9} [X_{ij}(\mathbf{r}_{ij}) X_{kj}(\mathbf{r}_{kj}) + X_{kj}(\mathbf{r}_{ij}) X_{ij}(\mathbf{r}_{kj})] \\ = \sum_{\text{cyc}} \frac{1}{2} \left(\frac{g_A}{2f_\pi} \right)^2 \left(\frac{1}{4\pi} \right)^2 \left(\frac{2c_3}{f_\pi^2} \right) \frac{m_\pi^4}{9} \{X_{ij}(\mathbf{r}_{ij}), X_{kj}(\mathbf{r}_{kj})\} \\ = \sum_{\text{cyc}} a_{c_3}^{\text{TPE}} \{X_{ij}(\mathbf{r}_{ij}), X_{kj}(\mathbf{r}_{kj})\},$$

with the prefactor

$$a_{c_3}^{\text{TPE}} = \frac{1}{2} \left(\frac{g_A}{2f_\pi} \right)^2 \left(\frac{1}{4\pi} \right)^2 \left(\frac{2c_3}{f_\pi^2} \right) \frac{m_\pi^4}{9}. \quad (6.28)$$

This is analogue to the P wave Illinois TPE interaction, which is already implemented in the AFDMC code. For reasons of completeness, we give the strategy for the implementation of this part into AFDMC. To begin, we rewrite $X_{ij}(\mathbf{r}_{ij})$:

$$\begin{aligned}
X_{ab}(\mathbf{r}_{ij}) &= \left((3\sigma_a \cdot \hat{\mathbf{r}}_{ij} \sigma_b \cdot \hat{\mathbf{r}}_{ij} - \sigma_a \cdot \sigma_b) T(r_{ij}) + \sigma_a \cdot \sigma_b \right) Y(r_{ij}) \\
&= \left((3\sigma_a^\alpha \hat{r}_{ij}^\alpha \sigma_b^\beta \hat{r}_{ij}^\beta - \sigma_a^\alpha \sigma_b^\beta \delta^{\alpha\beta}) T(r_{ij}) + \sigma_a^\alpha \sigma_b^\beta \delta^{\alpha\beta} \right) Y(r_{ij}) \\
&= \sigma_a^\alpha \left[3\hat{r}_{ij}^\alpha \hat{r}_{ij}^\beta Y(r_{ij}) T(r_{ij}) + \delta^{\alpha\beta} (Y(r_{ij}) - T(r_{ij}) Y(r_{ij})) \right] \sigma_b^\beta \\
&= \sigma_a^\alpha X_{i\alpha,j\beta} \sigma_b^\beta.
\end{aligned} \tag{6.29}$$

The matrix $X_{i\alpha,j\beta}$ is symmetric under transposition in $i \leftrightarrow j$ and $\alpha \leftrightarrow \beta$. The diagonal elements $X_{i\alpha,i\beta} = 0$ due to the regulator. Using this, we can rewrite Eq. (6.27) and find

$$\begin{aligned}
V_{C,c_3,LR} &= \sum_{i<j<k} \sum_{\text{cyc}} a_{c_3}^{\text{TPE}} \{X_{ij}(\mathbf{r}_{ij}), X_{kj}(\mathbf{r}_{kj})\} \\
&= \sum_{i<j<k} \sum_{\text{cyc}} a_{c_3}^{\text{TPE}} \left[\sigma_i^\alpha X_{i\alpha,j\beta} \sigma_j^\beta \sigma_k^\gamma X_{k\gamma,j\delta} \sigma_j^\delta + \sigma_k^\gamma X_{k\gamma,j\delta} \sigma_j^\delta \sigma_i^\alpha X_{i\alpha,j\beta} \sigma_j^\beta \right] \\
&= \sum_{i<j<k} \sum_{\text{cyc}} a_{c_3}^{\text{TPE}} \left[\sigma_i^\alpha X_{i\alpha,j\beta} \sigma_k^\gamma X_{k\gamma,j\delta} (\delta^{\beta\delta} + i\epsilon^{\beta\delta\kappa} \sigma_j^\kappa) + \sigma_k^\gamma X_{k\gamma,j\delta} \sigma_i^\alpha X_{i\alpha,j\beta} (\delta^{\beta\delta} + i\epsilon^{\delta\beta\kappa} \sigma_j^\kappa) \right] \\
&= \sum_{i<j<k} \sum_{\text{cyc}} 2a_{c_3}^{\text{TPE}} \sigma_i^\alpha X_{i\alpha,j\beta} X_{j\beta,k\gamma} \sigma_k^\gamma.
\end{aligned}$$

We can replace the summation $\sum_{i<j<k} \sum_{\text{cyc}}$ with $\sum_{i<k} \sum_{j \neq i,k}$. Both sums lead to the same number of terms, but the latter expression also includes non-cyclic permutations of i and k . As the forces are, however, symmetric under transposition of particles i and k , these non-cyclic permutations are similar to the corresponding cyclic ones, and we get finally

$$\begin{aligned}
V_{C,c_3,LR} &= \sum_{i<j<k} \sum_{\text{cyc}} 2a_{c_3}^{\text{TPE}} \sigma_{i,\alpha} X_{i\alpha,j\beta} X_{j\beta,k\gamma} \sigma_{k,\gamma} \\
&= \sum_{i<k} \sum_{j \neq i,k} 2a_{c_3}^{\text{TPE}} \sigma_{i,\alpha} X_{i\alpha,j\beta} X_{j\beta,k\gamma} \sigma_{k,\gamma} \\
&= \sum_{i<k} \left(\sum_j 2a_{c_3}^{\text{TPE}} \sigma_{i,\alpha} X_{i\alpha,j\beta} X_{j\beta,k\gamma} \sigma_{k,\gamma} - 2a_{c_3}^{\text{TPE}} \sigma_{i,\alpha} X_{i\alpha,i\beta} X_{i\beta,k\gamma} \sigma_{k,\gamma} - 2a_{c_3}^{\text{TPE}} \sigma_{i,\alpha} X_{i\alpha,k\beta} X_{k\beta,k\gamma} \sigma_{k,\gamma} \right) \\
&= \sum_{i<k} \sum_j 2a_{c_3}^{\text{TPE}} \sigma_{i,\alpha} X_{i\alpha,j\beta} X_{j\beta,k\gamma} \sigma_{k,\gamma} \\
&= \sum_{i<k} 2a_{c_3}^{\text{TPE}} \sigma_{i,\alpha} X_{i\alpha,k\gamma}^2 \sigma_{k,\gamma}.
\end{aligned}$$

This form is similar to a two-body interaction and can be easily added to the corresponding NN matrix $A_{i\alpha,k\gamma}$.

Now we turn to the V_E -like structure of the TPE interaction:

$$\begin{aligned}
V_{C,c_3,V_E}^{ijk} &= \sum_{\pi(ijk)} \frac{1}{2} \left(\frac{g_A}{2f_\pi} \right)^2 \left(\frac{1}{4\pi} \right)^2 \left(\frac{2c_3}{f_\pi^2} \right) \frac{(4\pi)^2}{9} \boldsymbol{\sigma}_i \cdot \boldsymbol{\sigma}_k \delta(\mathbf{r}_{ij}) \delta(\mathbf{r}_{kj}) \\
&= \sum_{\text{cyc}} \frac{1}{9} \left(\frac{g_A}{2f_\pi} \right)^2 \left(\frac{2c_3}{f_\pi^2} \right) \boldsymbol{\sigma}_i \cdot \boldsymbol{\sigma}_k \delta(\mathbf{r}_{ij}) \delta(\mathbf{r}_{kj}) \\
&= \sum_{\text{cyc}} a_{c_3}^{V_E} \boldsymbol{\sigma}_i \cdot \boldsymbol{\sigma}_k \delta(\mathbf{r}_{ij}) \delta(\mathbf{r}_{kj}).
\end{aligned} \tag{6.30}$$

We want to recast this contribution into a matrix form like before. For this, we will use the matrix $X_{i,j}^\delta = \delta(r_{ij})$. The diagonal elements of this matrix correspond to the normalization of the smeared-out δ function. We get

$$\begin{aligned}
V_{3N,c_3,V_E} &= a_{c_3}^{V_E} \sum_{i<j<k} \sum_{\text{cyc}} \sigma_i^\alpha \delta^{\alpha\gamma} \delta(\mathbf{r}_{ij}) \delta(\mathbf{r}_{kj}) \sigma_k^\gamma \\
&= a_{c_3}^{V_E} \sum_{i<k} \sum_{j \neq i,k} \sigma_i^\alpha \delta^{\alpha\gamma} X_{i,j}^\delta X_{k,j}^\delta \sigma_k^\gamma \\
&= a_{c_3}^{V_E} \sum_{i<k} \sum_j \sigma_i^\alpha \delta^{\alpha\gamma} X_{i,j}^\delta X_{k,j}^\delta \sigma_k^\gamma - a_{c_3}^{V_E} \sum_{i<k} \sigma_i^\alpha \delta^{\alpha\gamma} X_{i,i}^\delta X_{k,i}^\delta \sigma_k^\gamma - a_{c_3}^{V_E} \sum_{i<k} \sigma_i^\alpha \delta^{\alpha\gamma} X_{i,k}^\delta X_{k,k}^\delta \sigma_k^\gamma \\
&= a_{c_3}^{V_E} \sum_{i<k} \sigma_i^\alpha \delta^{\alpha\gamma} \left[\sum_j X_{i,j}^\delta X_{k,j}^\delta - X_{i,i}^\delta X_{k,i}^\delta - X_{i,k}^\delta X_{k,k}^\delta \right] \sigma_k^\gamma.
\end{aligned} \tag{6.31}$$

All contributions containing diagonal elements cancel each other, and we can simply define the diagonal elements of the matrix as 0. This leads to the same result in an easier notation:

$$\begin{aligned}
V_{3N,c_3,V_E} &= a_{c_3}^{V_E} \sum_{i<k} \sigma_i^\alpha \delta^{\alpha\gamma} \sum_j X_{i,j}^\delta X_{k,j}^\delta \sigma_k^\gamma \\
&= a_{c_3}^{V_E} \sum_{i<k} \sigma_i^\alpha \sum_j X_{ia,ka}^\delta \sigma_k^\alpha.
\end{aligned} \tag{6.32}$$

For the last c_3 contribution, which looks similar to V_D , we find

$$\begin{aligned}
V_{C,c_3,V_D}^{ijk} &= \sum_{\pi(ijk)} \frac{1}{2} \left(\frac{g_A}{2f_\pi} \right)^2 \left(\frac{1}{4\pi} \right)^2 \left(\frac{2c_3}{f_\pi^2} \right) \left[-\frac{4\pi m_\pi^2}{9} X_{ik}(\mathbf{r}_{ij}) \delta(\mathbf{r}_{kj}) - \frac{4\pi m_\pi^2}{9} X_{ik}(\mathbf{r}_{kj}) \delta(\mathbf{r}_{ij}) \right] \\
&= 2 \sum_{\text{cyc}} a_{\text{ind}}^{V_D} [X_{ik}(\mathbf{r}_{ij}) \delta(\mathbf{r}_{kj}) + X_{ik}(\mathbf{r}_{kj}) \delta(\mathbf{r}_{ij})] \\
&= 2 \sum_{\text{cyc}} a_{\text{ind}}^{V_D} \left[\left(3\boldsymbol{\sigma}_i \cdot \hat{\mathbf{r}}_{ij} \boldsymbol{\sigma}_k \cdot \hat{\mathbf{r}}_{ij} T(r_{ij}) Y(r_{ij}) + \boldsymbol{\sigma}_i \cdot \boldsymbol{\sigma}_k (Y(r_{ij}) - T(r_{ij}) Y(r_{ij})) \right) \delta(\mathbf{r}_{kj}) \right. \\
&\quad \left. + \left(3\boldsymbol{\sigma}_i \cdot \hat{\mathbf{r}}_{kj} \boldsymbol{\sigma}_k \cdot \hat{\mathbf{r}}_{kj} T(r_{kj}) Y(r_{kj}) + \boldsymbol{\sigma}_i \cdot \boldsymbol{\sigma}_k (Y(r_{kj}) - T(r_{kj}) Y(r_{kj})) \right) \delta(\mathbf{r}_{ij}) \right] \\
&= 2 \sum_{\text{cyc}} a_{\text{ind}}^{V_D} \left[\boldsymbol{\sigma}_i \cdot \boldsymbol{\sigma}_k (Y(r_{ij}) - T(r_{ij}) Y(r_{ij})) \delta(\mathbf{r}_{kj}) + \boldsymbol{\sigma}_i \cdot \boldsymbol{\sigma}_k (Y(r_{kj}) - T(r_{kj}) Y(r_{kj})) \delta(\mathbf{r}_{ij}) \right. \\
&\quad \left. + 3\boldsymbol{\sigma}_i \cdot \hat{\mathbf{r}}_{ij} \boldsymbol{\sigma}_k \cdot \hat{\mathbf{r}}_{ij} T(r_{ij}) Y(r_{ij}) \delta(\mathbf{r}_{kj}) + 3\boldsymbol{\sigma}_i \cdot \hat{\mathbf{r}}_{kj} \boldsymbol{\sigma}_k \cdot \hat{\mathbf{r}}_{kj} T(r_{kj}) Y(r_{kj}) \delta(\mathbf{r}_{ij}) \right] \\
&= 2 \sum_{\text{cyc}} a_{\text{ind}}^{V_D} \left[\sigma_i^\alpha \delta^{\alpha\beta} \left(X_{i,j}^{V_D,Y} X_{k,j}^\delta + X_{k,j}^{V_D,Y} X_{i,j}^\delta \right) \sigma_k^\beta + \sigma_i^\alpha \left(X_{ia,j\beta}^{V_D,T} X_{k,j}^\delta + X_{ka,j\beta}^{V_D,T} X_{i,j}^\delta \right) \sigma_k^\beta \right].
\end{aligned} \tag{6.33}$$

where we have used

$$X_{i,j}^{V_D,Y} = Y(r_{ij}) (1 - T(r_{ij})) , \quad (6.34)$$

$$X_{i\alpha,j\beta}^{V_D,T} = 3\hat{r}_{ij}^\alpha \hat{r}_{ij}^\beta T(r_{ij}) Y(r_{ij}) . \quad (6.35)$$

For the total contribution of this 3N interaction, we find

$$\begin{aligned} V_{C,c_3,V_D} &= \sum_{i<j<k} V_{C,c_3,V_D}^{ijk} \\ &= 2 \sum_{i<j<k} \sum_{\text{cyc}} a_{\text{ind}}^{V_D} \left[\sigma_i^\alpha \delta^{\alpha\beta} \left(X_{i,j}^{V_D,Y} X_{k,j}^\delta + X_{k,j}^{V_D,Y} X_{i,j}^\delta \right) \sigma_k^\beta + \sigma_i^\alpha \left(X_{i\alpha,j\beta}^{V_D,T} X_{k,j}^\delta + X_{k\alpha,j\beta}^{V_D,T} X_{i,j}^\delta \right) \sigma_k^\beta \right] \\ &= 2 \sum_{i<k} a_{\text{ind}}^{V_D} \sigma_i^\alpha \left[\delta^{\alpha\beta} \left(\sum_j X_{i,j}^{V_D,Y} X_{k,j}^\delta + \sum_j X_{k,j}^{V_D,Y} X_{i,j}^\delta \right) + \left(\sum_j X_{i\alpha,j\beta}^{V_D,T} X_{k,j}^\delta + \sum_j X_{k\alpha,j\beta}^{V_D,T} X_{i,j}^\delta \right) \right] \sigma_k^\beta , \end{aligned} \quad (6.36)$$

which again can be added to the two-body matrix $A_{i\alpha,k\gamma}$.

We turn finally to the last contribution $\sim c_1$,

$$\begin{aligned} V_{C,c_1}^{ijk} &= - \sum_{\pi(ijk)} \frac{1}{2} \left(\frac{g_A}{2f_\pi} \right)^2 \left(\frac{m_\pi}{4\pi} \right)^2 \left(-\frac{4c_1 m_\pi^2}{f_\pi^2} \right) \frac{\boldsymbol{\sigma}_i \cdot \mathbf{r}_{ij}}{r_{ij}} \frac{\boldsymbol{\sigma}_k \cdot \mathbf{r}_{kj}}{r_{kj}} U(r_{ij}) Y(r_{ij}) U(r_{kj}) Y(r_{kj}) \\ &= 2 \sum_{\text{cyc}} a_{c_1}^{\text{TPE}} \frac{\boldsymbol{\sigma}_i \cdot \mathbf{r}_{ij}}{r_{ij}} \frac{\boldsymbol{\sigma}_k \cdot \mathbf{r}_{kj}}{r_{kj}} U(r_{ij}) Y(r_{ij}) U(r_{kj}) Y(r_{kj}) . \end{aligned} \quad (6.37)$$

For the total c_1 contribution we obtain

$$\begin{aligned} V_{C,c_1} &= 2 \sum_{i<j<k} \sum_{\text{cyc}} a_{c_1}^{\text{TPE}} \sigma_i^\alpha \sigma_k^\gamma \hat{\mathbf{r}}_{ij}^\alpha \hat{\mathbf{r}}_{kj}^\gamma U(r_{ij}) Y(r_{ij}) U(r_{kj}) Y(r_{kj}) \\ &= 2 \sum_{i<k} \sum_{j \neq i,k} a_{c_1}^{\text{TPE}} \sigma_i^\alpha \nu_\alpha^{c_1}(\mathbf{r}_{ij}) \nu_\gamma^{c_1}(\mathbf{r}_{kj}) \sigma_k^\gamma \\ &= 2 \sum_{i<k} \left(\sum_j a_{c_1}^{\text{TPE}} \sigma_i^\alpha \nu_\alpha^{c_1}(\mathbf{r}_{ij}) \nu_\gamma^{c_1}(\mathbf{r}_{kj}) \sigma_k^\gamma - a_{c_1}^{\text{TPE}} \sigma_i^\alpha \nu_\alpha^{c_1}(\mathbf{r}_{ii}) \nu_\gamma^{c_1}(\mathbf{r}_{ki}) \sigma_k^\gamma - a_{c_1}^{\text{TPE}} \sigma_i^\alpha \nu_\alpha^{c_1}(\mathbf{r}_{ik}) \nu_\gamma^{c_1}(\mathbf{r}_{kk}) \sigma_k^\gamma \right) \\ &= 2 \sum_{i<k} a_{c_1}^{\text{TPE}} \sigma_i^\alpha \sum_j \nu_\alpha^{c_1}(\mathbf{r}_{ij}) \nu_\gamma^{c_1}(\mathbf{r}_{kj}) \sigma_k^\gamma , \end{aligned} \quad (6.38)$$

where we have defined $\nu_\alpha^{c_1}(\mathbf{r}_{ij}) = \hat{\mathbf{r}}_{ij}^\alpha U(r_{ij}) Y(r_{ij})$.

The term V_D consists of two contributions after Fourier transformation:

$$V_{D,1}^{ijk} = \sum_{\pi(ijk)} \frac{m_\pi^2}{12\pi} \frac{g_A}{8f_\pi^2} \frac{c_D}{f_\pi^2 \Lambda_\chi} \delta(\mathbf{r}_{ij}) X_{ik}(\mathbf{r}_{kj}) , \quad (6.39)$$

$$V_{D,2}^{ijk} = - \sum_{\pi(ijk)} \frac{1}{3} \frac{g_A}{8f_\pi^2} \frac{c_D}{f_\pi^2 \Lambda_\chi} (\boldsymbol{\sigma}_i \cdot \boldsymbol{\sigma}_k) \delta(\mathbf{r}_{ij}) \delta(\mathbf{r}_{kj}) . \quad (6.40)$$

The first term can be brought into a different form:

$$V_{D,1}^{ijk} = \sum_{\pi(ijk)} \frac{m_\pi^2}{12\pi} \frac{g_A}{8f_\pi^2} \frac{c_D}{f_\pi^2 \Lambda_\chi} \delta(\mathbf{r}_{ij}) X_{ik}(\mathbf{r}_{kj}) \quad (6.41)$$

$$= \sum_{\text{cyc}} \frac{m_\pi^2}{12\pi} \frac{g_A}{8f_\pi^2} \frac{c_D}{f_\pi^2 \Lambda_\chi} [X_{ik}(\mathbf{r}_{kj}) \delta(\mathbf{r}_{ij}) + X_{ik}(\mathbf{r}_{ij}) \delta(\mathbf{r}_{kj})] \quad (6.42)$$

$$= 2 \sum_{\text{cyc}} \frac{1}{2} \frac{m_\pi^2}{12\pi} \frac{g_A}{8f_\pi^2} \frac{c_D}{f_\pi^2 \Lambda_\chi} [X_{ik}(\mathbf{r}_{kj}) \delta(\mathbf{r}_{ij}) + X_{ik}(\mathbf{r}_{ij}) \delta(\mathbf{r}_{kj})] \quad (6.43)$$

$$= 2 \sum_{\text{cyc}} a_{V_D} [X_{ik}(\mathbf{r}_{kj}) \delta(\mathbf{r}_{ij}) + X_{ik}(\mathbf{r}_{ij}) \delta(\mathbf{r}_{kj})] . \quad (6.44)$$

This form is similar to the V_D -like IR part of V_C of Eq. (6.33) and can be easily included into the code by adding the factor a_{V_D} to $a_{\text{ind}}^{V_D}$. For the second contribution we find

$$V_{D,2}^{ijk} = - \sum_{\pi(ijk)} \frac{1}{3} \frac{g_A}{8f_\pi^2} \frac{c_D}{f_\pi^2 \Lambda_\chi} (\boldsymbol{\sigma}_i \cdot \boldsymbol{\sigma}_k) \delta(\mathbf{r}_{ij}) \delta(\mathbf{r}_{kj}) \quad (6.45)$$

$$= -2 \sum_{\text{cyc}} \frac{1}{3} \frac{g_A}{8f_\pi^2} \frac{c_D}{f_\pi^2 \Lambda_\chi} \sigma_{i,\alpha} \delta^{\alpha\gamma} \delta(\mathbf{r}_{ij}) \delta(\mathbf{r}_{kj}) \sigma_{k,\gamma}$$

$$= a_{V_D,2} \sum_{\text{cyc}} \sigma_{i,\alpha} \delta^{\alpha\gamma} \delta(\mathbf{r}_{ij}) \delta(\mathbf{r}_{kj}) \sigma_{k,\gamma} . \quad (6.46)$$

This V_E -like part of V_D is similar to the V_E -like part of V_C and, thus, easy to include into the code by adding $a_{V_D,2}$ to $a_{c_3}^{V_E}$.

We now turn to the last piece of the N²LO 3N forces. The 3N contact interaction V_E is spin-independent and similar to the R-part of the Illinois three-nucleon forces:

$$V_E^{ijk} = \frac{c_E}{2f_\pi^4 \Lambda_\chi} \sum_{\pi(ijk)} \delta(\mathbf{r}_{ij}) \delta(\mathbf{r}_{kj}) = \frac{c_E}{f_\pi^4 \Lambda_\chi} \sum_{\text{cyc}} \delta(\mathbf{r}_{ij}) \delta(\mathbf{r}_{kj}) . \quad (6.47)$$

For the total contribution we find

$$V_E = \sum_{i < j < k} \sum_{\text{cyc}} \frac{c_E}{f_\pi^4 \Lambda_\chi} \delta(\mathbf{r}_{ij}) \delta(\mathbf{r}_{kj}) \quad (6.48)$$

$$= \sum_{i < k} \sum_{j \neq i, k} a_{V_E} \delta(\mathbf{r}_{ij}) \delta(\mathbf{r}_{kj})$$

$$= \sum_{i < k} a_{V_E} \sum_j \delta(\mathbf{r}_{ij}) \delta(\mathbf{r}_{kj})$$

$$= \frac{1}{2} \sum_{i \neq k} a_{V_E} \sum_j \delta(\mathbf{r}_{ij}) \delta(\mathbf{r}_{kj}) ,$$

where we again set the diagonal matrix elements to 0 as their contribution cancels each other.

To implement the chiral forces in GFMC we use operator structures which are already implemented in the code. To achieve this we rewrite the spin and isospin operators in form of commutators and anticommutators, using the following expressions:

$$\{\boldsymbol{\tau}_i \cdot \boldsymbol{\tau}_j, \boldsymbol{\tau}_j \cdot \boldsymbol{\tau}_k\} = 2\boldsymbol{\tau}_i \cdot \boldsymbol{\tau}_k, \quad (6.49)$$

$$[\boldsymbol{\tau}_i \cdot \boldsymbol{\tau}_j, \boldsymbol{\tau}_j \cdot \boldsymbol{\tau}_k] = 2i\boldsymbol{\tau}_i \cdot \boldsymbol{\tau}_k \times \boldsymbol{\tau}_j, \quad (6.50)$$

and similarly for the spin operators. Arbitrary products of these operators with arbitrary radial functions can be directly implemented in the GFMC algorithm. Furthermore, we have to rewrite the sums in the 3N interaction as cyclic sums as before. With this, it is straightforward to implement the chiral 3N contributions.

Furthermore, some contributions can be recast into terms similar to the Urbana or Illinois 3N interactions, which are already implemented in GFMC algorithms. As an example we show the LR two-pion exchange c_3 and c_4 parts with two X operators:

$$\begin{aligned} V_{C,LR,c_3}^{ijk} &= \sum_{\pi(ijk)} \frac{1}{2} \left(\frac{g_A}{2f_\pi} \right)^2 \left(\frac{1}{4\pi} \right)^2 \left(\frac{2c_3}{f_\pi^2} \right) \boldsymbol{\tau}_i \cdot \boldsymbol{\tau}_k \frac{m_\pi^4}{9} X_{ij}(\mathbf{r}_{ij}) X_{kj}(\mathbf{r}_{kj}) \\ &= a_{\text{TPE}}^{\text{PW}} c_3 \sum_{\text{cyc}} \{ \boldsymbol{\tau}_i \cdot \boldsymbol{\tau}_j, \boldsymbol{\tau}_j \cdot \boldsymbol{\tau}_k \} \{ X_{ij}(\mathbf{r}_{ij}) X_{kj}(\mathbf{r}_{kj}) \}, \end{aligned} \quad (6.51)$$

$$\begin{aligned} V_{C,LR,c_4}^{ijk} &= \sum_{\pi(ijk)} \frac{1}{9} \frac{1}{2} \left(\frac{g_A}{2f_\pi} \right)^2 \frac{c_4}{f_\pi^2} \boldsymbol{\tau}_i \cdot (\boldsymbol{\tau}_k \times \boldsymbol{\tau}_j) \left(\frac{m_\pi^2}{4\pi} \right)^2 \frac{1}{2i} [X_{ij}(r_{ij}), X_{kj}(r_{kj})] \\ &= -a_{\text{TPE}}^{\text{PW}} \frac{c_4}{2} \sum_{\text{cyc}} [\boldsymbol{\tau}_i \cdot \boldsymbol{\tau}_j, \boldsymbol{\tau}_j \cdot \boldsymbol{\tau}_k] [X_{ij}(r_{ij}), X_{kj}(r_{kj})]. \end{aligned} \quad (6.52)$$

For the sum we find

$$\begin{aligned} &V_{C,LR,c_3}^{ijk} + V_{C,LR,c_4}^{ijk} \\ &= a_{\text{TPE}}^{\text{PW}} c_3 \sum_{\text{cyc}} \left[\{ \boldsymbol{\tau}_i \cdot \boldsymbol{\tau}_j, \boldsymbol{\tau}_j \cdot \boldsymbol{\tau}_k \} \{ X_{ij}(\mathbf{r}_{ij}) X_{kj}(\mathbf{r}_{kj}) \} - \frac{c_4}{2c_3} [\boldsymbol{\tau}_i \cdot \boldsymbol{\tau}_j, \boldsymbol{\tau}_j \cdot \boldsymbol{\tau}_k] [X_{ij}(r_{ij}), X_{kj}(r_{kj})] \right]. \end{aligned} \quad (6.53)$$

These forces are similar to the phenomenological Urbana and Illinois P wave TPE interaction. In chiral EFT, if only considering the Δ excitation absorbed into the c_i , $c_3 = -2c_4$, and we find exactly the Urbana 3N expression.

For more details on the inclusion of the local chiral 3N forces into the GFMC algorithm, we refer the reader to Ref. [253].

6.3 Fits of c_D and c_E

To determine the couplings c_D and c_E in the $N^2\text{LO}$ 3N forces, we use the GFMC method to fit these couplings to properties in the $A \geq 3$ systems. More specifically, we choose to fit the two couplings to the ^4He binding energy and, to probe spin-orbit physics, neutron- α P wave scattering phase shifts, see Ref. [253] for more details.

In Fig. 6.1 we show the couplings c_E vs. c_D obtained by fitting the ^4He binding energy, where blue (red) lines correspond to $R_0 = 1.0\text{fm}$ (1.2fm), while open (closed) symbols represent

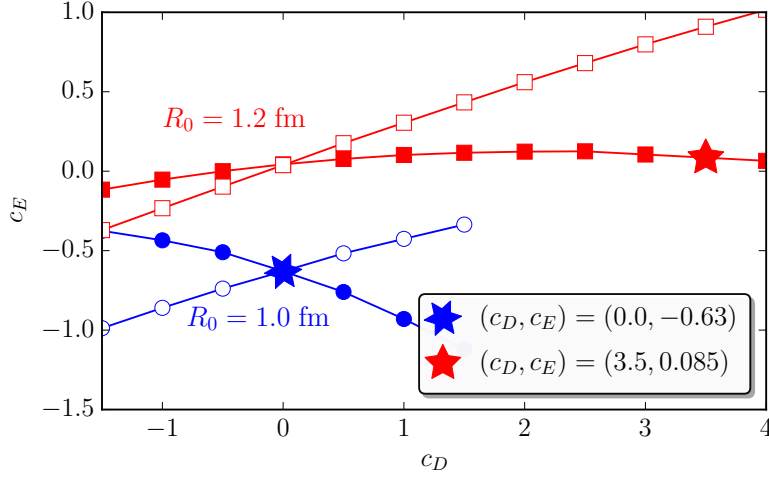


Figure 6.1: The couplings c_E vs. c_D obtained by fitting the ${}^4\text{He}$ binding energy. Blue (red) lines correspond to $R_0 = 1.0$ fm (1.2 fm), while open (closed) symbols represent $V_{D,1}$ ($V_{D,2}$). The stars represent the values which also fit the n - α P wave phase shifts.

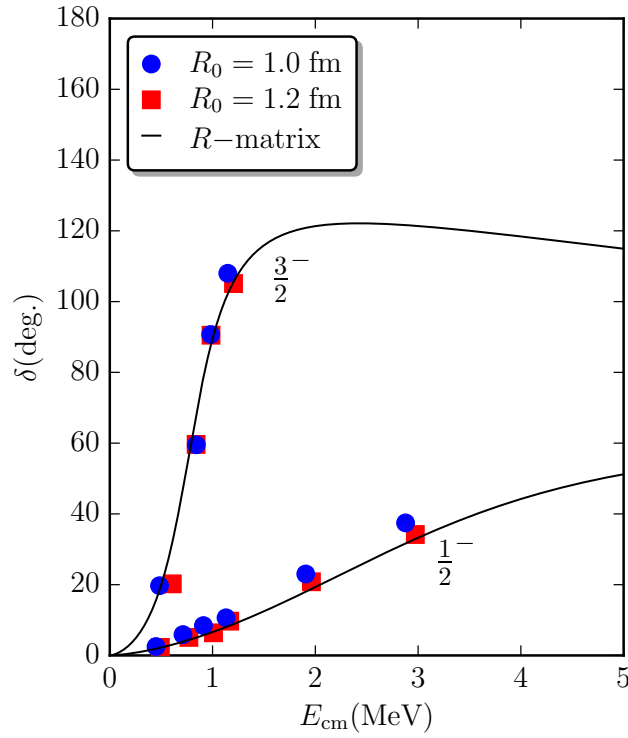


Figure 6.2: The P wave n - α elastic scattering phase shifts for $V_{D,2}$ and the couplings from Fig. 6.1. The points are compared to an R-matrix analysis of experimental data, see Ref. [253] for more details.

$V_{D,1}$ ($V_{D,2}$). The 3N cutoff R_{3N} is chosen similar to R_0 . The stars represent the values which also fit the n - α P wave phase shifts, see Fig. 6.2, where the choice is made to use the operator structure of $V_{D,2}$.

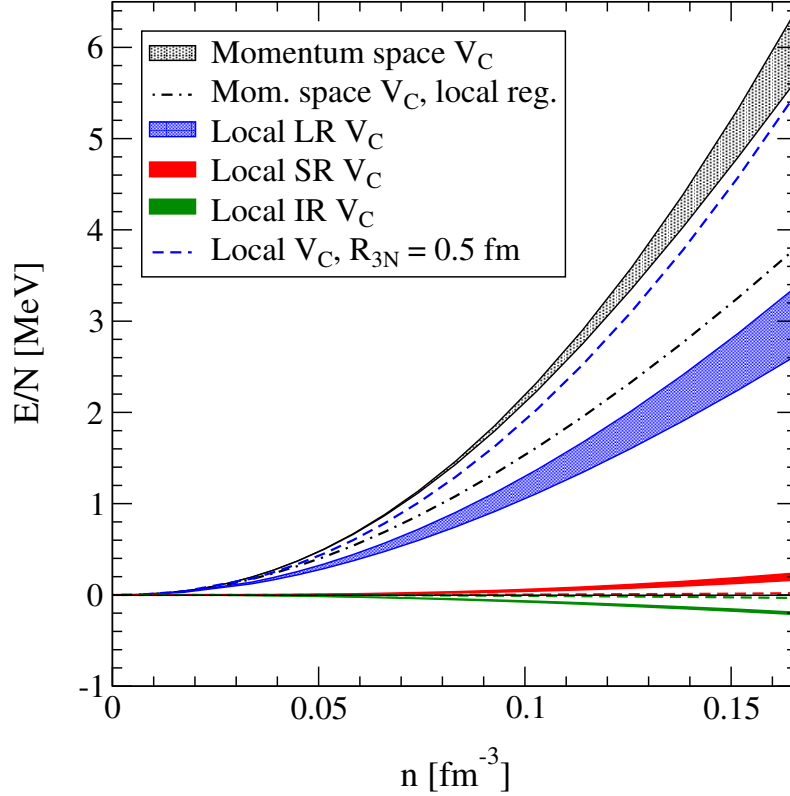


Figure 6.3: Contributions to the neutron-matter energy per particle E/N as a function of density n at the Hartree-Fock level. The black band shows the energy obtained using a nonlocal regulator, as in Ref. [17], with a cutoff $2.0 - 2.5 \text{ fm}^{-1}$. The blue band corresponds to the LR part of the two-pion-exchange interaction V_C with the local regulator used here, the red band to the SR part of V_C , and the green band to the IR of V_C . For these bands, the cutoff in the local regulator is varied between $R_{3N} = 1.0 - 1.2 \text{ fm}$. The dashed-dotted line corresponds to the results for V_C using the local momentum-space regulator of Ref. [176] with a cutoff $\Lambda_{3N} = 500 \text{ MeV}$. This shows that local 3N forces provide less repulsion at the Hartree-Fock level than with nonlocal regulators. The dashed lines show the results for V_C with the local regulator and $R_{3N} = 0.5 \text{ fm}$.

For the $R_0 = 1.0 \text{ fm}$ NN potential, we find $c_E = -0.63$ and $c_D = 0.0$. The different operator structures for V_D , thus, have no effect for this potential. For $R_0 = 1.2 \text{ fm}$ we find $c_E = 0.085$ and $c_D = 3.5$ for $V_{D,2}$, while for $V_{D,1}$ no good fit could so far be obtained.

These are the first c_D and c_E fits and they have only been calculated very recently. It is necessary to obtain improved fits as well as the dependence of the couplings c_E and c_D on the two different V_D structures. In the following AFDMC calculations of neutron matter we will, therefore, only consider the LR two-pion-exchange term V_C and neglect the contributions of V_D and V_E .

6.4 Local chiral 3N forces in neutron matter

In this Section we discuss the results of the local $N^2\text{LO}$ 3N forces in neutron matter at the Hartree-Fock (HF) level and using AFDMC. We begin with HF calculations similarly to Refs. [17, 57], using our MBPT machinery. Details on the Fourier transformation of the regularized local 3N forces from coordinate space to momentum space are given in Appendix E.

In Fig. 6.3 we show the contributions to the neutron-matter energy per particle E/N as a function of density n for all terms of the two-pion exchange V_C at the Hartree-Fock level. The black band shows the energy obtained using a nonlocal regulator, as in Ref. [17], with a cutoff $2.0 - 2.5 \text{ fm}^{-1}$. In momentum space, this is the only contribution to pure neutron matter stemming from the $N^2\text{LO}$ 3N forces, if the nonlocal regulator of Ref. [17] is used. The blue band corresponds to the LR part of the two-pion-exchange interaction V_C with the local regulator used here, the red band to the SR part of V_C , and the green band to the IR of V_C . For these bands, the cutoff in the local regulator is varied between $R_{3N} = 1.0 - 1.2 \text{ fm}$. The dashed-dotted line corresponds to the results for V_C using the local momentum-space regulator of Ref. [176] with a cutoff $\Lambda_{3N} = 500 \text{ MeV}$. The dashed lines show the results for V_C with the local regulator and $R_{3N} = 0.5 \text{ fm}$.

The HF energies in neutron matter for the local V_C of this work are in total $\approx 3 \text{ MeV}$ at saturation density $n_0 = 0.16 \text{ fm}^{-3}$ for our cutoff range $1.0 - 1.2 \text{ fm}$, which is only half the magnitude of V_C using a non-local regulator for the cutoff range $400 - 500 \text{ MeV}$. The shorter-range contributions, which are pure regulator effects, are very small and with opposite sign. If we lower the coordinate-space cutoff, $R_{3N} = 0.5 \text{ fm}$ (dashed lines), we find that the IR and SR parts almost vanish, as expected, and that the total HF energy is 5.5 MeV for the local V_C , which agrees very well with the momentum-space determination. Thus, the smaller 3N energies for the local 3N forces seem to be due to the locality of these regulator functions and our chosen cutoff range.

To check this assumption, we performed a HF calculation of V_C using the local momentum-space regulator of Ref. [176] with a cutoff of $\Lambda_{3N} = 500 \text{ MeV}$. At saturation density, we find an energy per particle of 3.8 MeV , which is comparable to the result of the local 3N forces of this paper. This supports the above conclusion, that the smaller 3N energies are due to local regulators and that local 3N forces provide less repulsion at the Hartree-Fock level than with nonlocal regulators. We will study local regulators in more detail in the next Section.

In Ref. [54] it was shown that the three-nucleon contact interaction V_E vanishes in pure neutron matter due to the Pauli principle and that the one-pion-exchange–contact interacting V_D vanishes due to the spin-isospin structure, if non-local Jacobi-momentum regulators are chosen. This statement is true as long as the regulator is symmetric under exchange of all particle labels. For the local 3N forces, however, this does not hold, and these two contributions also add to pure neutron matter. Although these contributions are pure regulator effects and vanish for $R_{3N} \rightarrow 0$, they add sizeable contributions to pure neutron matter, which we show in Fig. 6.4. The couplings c_E and c_D are chosen as the maximal values from the fitting procedure, so $c_E = -0.63$ and $c_D = 3.5$, and the plot, thus, shows only the maximal HF results.

The term V_D , where the IR and SR part have different sign and almost cancel each other, has a magnitude of only several hundred keV. For other cutoffs, the value of the coupling c_D decreases, and the contribution becomes even smaller. Thus, V_D can easily be neglected in a neutron matter calculation. The V_E contribution, however, can be sizeable, and for $c_E = -0.63$ for the hard NN potential with $R_0 = 1.0 \text{ fm}$ we find a HF energy of $\approx -(3 - 4) \text{ MeV}$. This contribution is larger than the energy of V_C and has the opposite sign. For the softer potential with $R_0 = 1.2 \text{ fm}$, the HF energy is $\approx 0.5 \text{ MeV}$.

Preliminary results show, that by choosing the $\mathbb{1}$ operator instead of the $\boldsymbol{\tau}_i \cdot \boldsymbol{\tau}_k$ operator for the V_E contact interaction, similar to what has been done in the NN sector, V_E takes the opposite sign but with a similar magnitude. The local regulator, thus, does not preserve the freedom to choose the contact operator in the 3N system. Furthermore, these results indicate that the local SR 3N

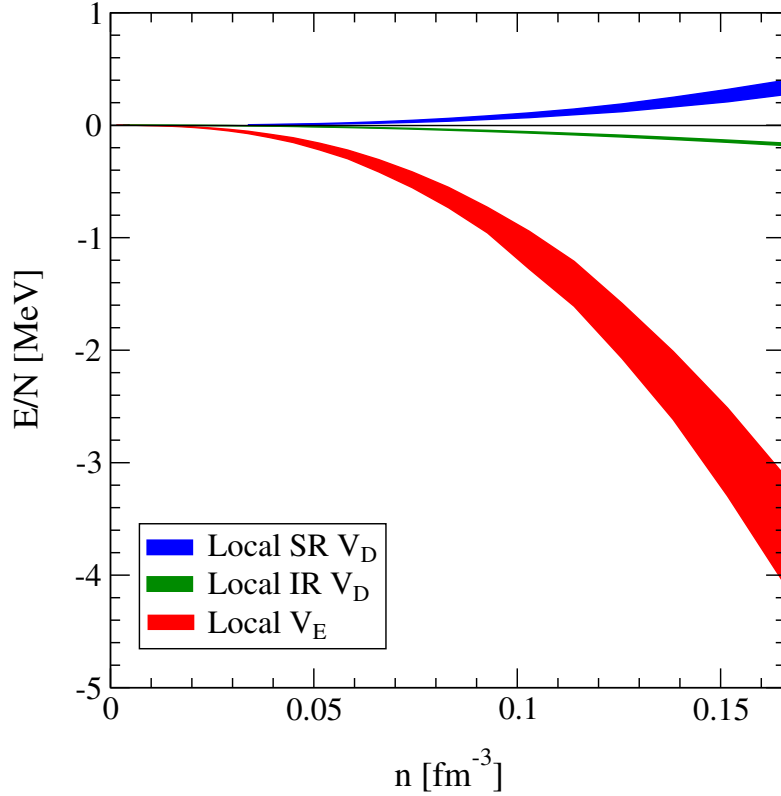


Figure 6.4: Contributions to the neutron-matter energy per particle E/N as a function of density n at the Hartree-Fock level for the local V_E (red band), the local IR part of V_D (blue band) and the local SR part of V_D (blue dotted band). The couplings c_E and c_D are chosen as $c_E = -0.63$ and $c_D = 3.5$.

contact interaction V_E adds a sizeable uncertainty to the neutron-matter equation of state. This has to be investigated further.

In Fig. 6.5, we show the contributions to the energy per particle E/N at saturation density as a function of the cutoff R_{3N} . The lines show the LR, SR, and IR parts of the two-pion-exchange interaction V_C with the local regulator used here, calculated at the Hartree-Fock level. For all 3N cutoffs, the SR and IR parts are very small and of opposite sign while the major contribution to the many-body forces comes from the long-range parts. The SR and IR parts vanish for small coordinate-space (high momentum-space) cutoffs, as expected. The LR part increases up to the infinite-momentum-cutoff limit. For our cutoff range, $R_{3N} = 1.0 - 1.2$ fm, the total magnitude of V_C is about 3.0 MeV. Reducing the cutoff to 0.5 fm leads to an energy of ~ 5.5 MeV per neutron at the HF level. This is what we found before.

We also investigated the N^2 LO 3N forces V_C in neutron matter employing the AFDMC method. In Fig. 6.5, in addition to the HF results, we show the contributions of the LR, IR and SR parts of V_C to the AFDMC energy for a variation of the NN cutoff $R_0 = 1.0 - 1.2$ fm as bands. These results are also shown in Fig. 6.6, where we plot the variation of the AFDMC energy per particle at saturation density as a function of the 3N cutoff R_{3N} for an NN cutoff 1.0 fm (black lines in the upper part) and 1.2 fm (red lines in the lower part). The horizontal lines correspond to the NN-only energy. The squares are obtained by including the LR c_1 and c_3 part of V_C , the crosses include also the SR c_3 part of V_C , and the circles include all parts of V_C .

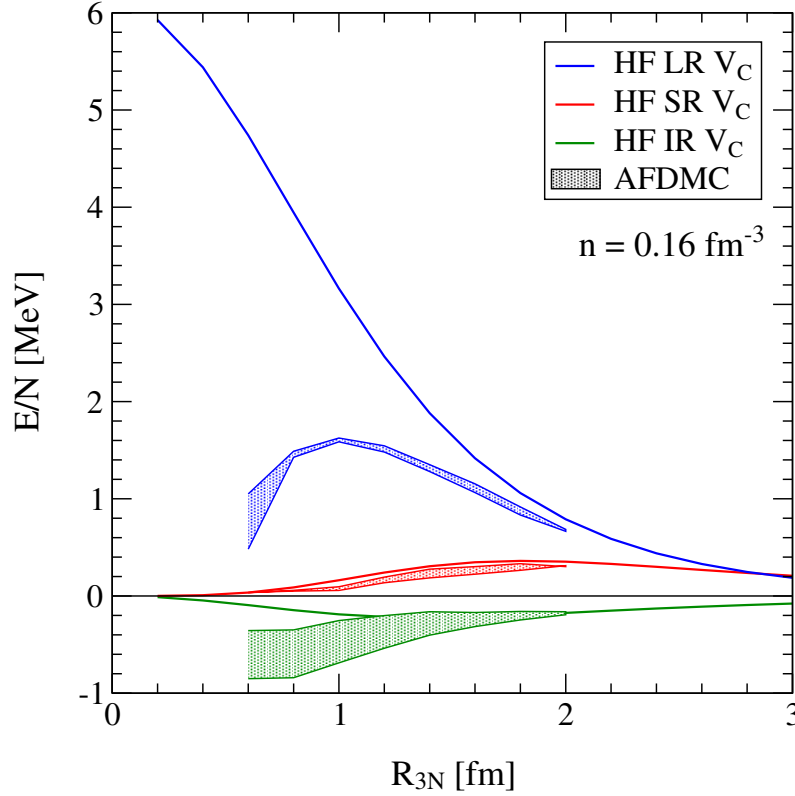


Figure 6.5: Contributions to the energy per particle E/N at saturation density as a function of the cutoff R_{3N} . The lines show the LR, SR, and IR parts of the two-pion-exchange interaction V_C with the local regulator used here, calculated at the Hartree-Fock level. The bands are the contributions of the corresponding 3N parts to the AFDMC energies for a variation of the NN cutoff $R_0 = 1.0 - 1.2$ fm, see also Fig. 6.6.

In Fig. 6.5, for the SR part, the AFDMC energies agree very well with the HF energies so HF is a very good approximation for its magnitude. For the IR range part, for high coordinate-space cutoffs, the agreement between HF and AFDMC results is good but worsens for lower cutoffs. The uncertainty grows and the energies increase by an order of magnitude compared to the HF result. For the LR parts, the AFDMC energies are about 70 – 80% of the HF energies for high cutoffs, which suggests that for the N^2 LO 3N forces contributions beyond Hartree-Fock are important. Lowering the 3N cutoff, the energy increases to a plateau structure and then rapidly decreases for smaller cutoffs due to a collapse of the system. In addition, also the uncertainty increases.

These collapses in the LR and IR parts of V_C can also be seen in Fig. 6.6. Although they do not appear in the HF calculation, they are not an artifact of the AFDMC method. The collapses are due to the function $X_{ij}(\mathbf{r})$, which includes terms $\sim 1/r^3$. If three particles are in a small volume then this function diverges, unless it gets regulated with a large enough R_{3N} . These cutoff values correspond to the position of the plateaus. In the HF formalism we do not see this collapse because it is encoded in higher-order contributions at higher momenta.

For the soft NN potential, $R_0 = 1.2$ fm, we find the plateau to be at $R_{3N} = 1.2 - 1.4$ fm. If the cutoff is lowered, the energy drops fast and for $R_{3N} = 0.6$ fm we find an attractive 3N contribution. For the harder NN potential, $R_0 = 1.0$ fm, the plateau is found for smaller 3N cutoffs, $R_{3N} = 1.0 - 1.2$ fm. In general, the plateau is reached when $R_{3N} \sim R_0$.

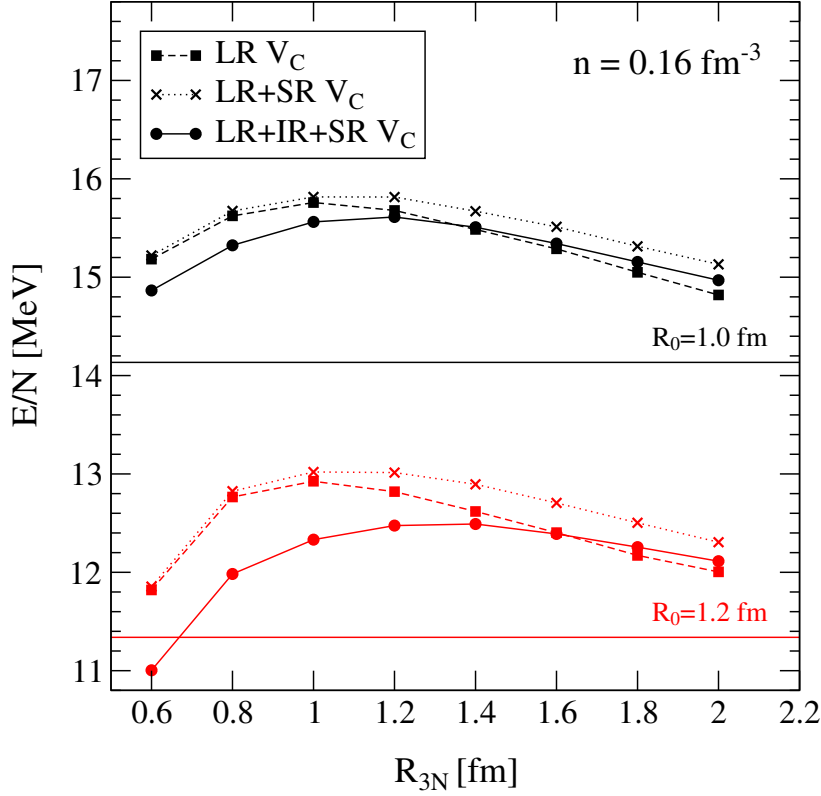


Figure 6.6: Variation of the AFDMC energy per particle at saturation density as a function of the 3N cutoff R_{3N} for an NN cutoff 1.0 fm (black lines in the upper part) and 1.2 fm (red lines in the lower part). The horizontal lines correspond to the NN-only energy. The squares are for the c_1 and LR c_3 part of V_C , the crosses include also the SR c_3 part of V_C , and the circles include all parts of V_C .

This can be understood because harder NN potentials do not favor particles to be close and smaller 3N cutoffs are needed to overcome this repulsion. We find that the collapse happens for $R_{3N} < R_0$, i.e., when R_{3N} is significantly smaller than R_0 . If we want to decrease R_{3N} , we also have to decrease R_0 , which will lead to a harder core in the NN potential. Thus, R_{3N} has to be chosen consistently with R_0 which justifies the 3N cutoff range we chose: too high cutoffs cannot be chosen as important physics would be cut away, while too low cutoffs lead to a collapse in neutron matter. Because the NN cutoff R_0 cannot be decreased below 1.0 fm, we also cannot decrease the 3N cutoff below that limit.

This behavior is qualitatively similar to the overbinding given by the Illinois 3N forces in pure neutron systems [210]. It would be interesting to see if using a similar cutoff would avoid the overbinding of neutron matter using Illinois forces.

6.5 Local regulators

In the previous Section we found that local regulators in the 3N sector seem to systematically lead to less repulsion from 3N forces, already at the Hartree-Fock level. In the following, we present first explorations of the dependence of the local chiral 3N forces on the local long-range regulator to gain a better understanding of the energy difference between local vs. nonlocal forces and possible deficiencies of local regulators. This is necessary for the development of

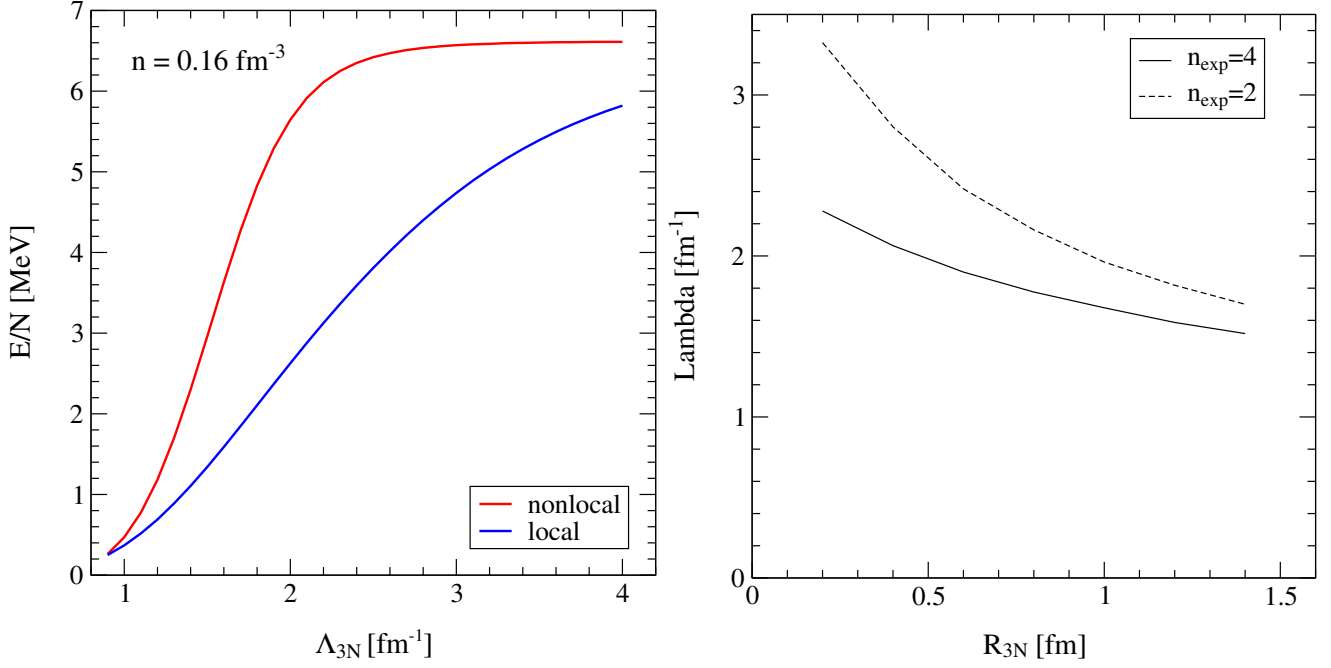


Figure 6.7: Left: $N^2\text{LO}$ 3N contribution V_C in momentum space at saturation density obtained with the nonlocal regulator of Ref. [17] compared to a calculation obtained with the local regulator of Ref. [176] in the HF approximation in neutron matter as a function of the 3N cutoff Λ_{3N} . Right: Translation from the local regulator scale R_{3N} to the momentum space cutoff Λ_{3N} in the momentum space regulator of Ref. [17] for the LR part of V_C for $n_{\text{exp}} = 2, 4$.

improved local regulators. In this Section, we only consider the LR V_C contribution in neutron matter to 1) eliminate the influence of the SR V_E contribution and 2) to have a better comparison with nonlocal chiral 3N forces.

In the left panel of Fig. 6.7 we compare the $N^2\text{LO}$ 3N contribution V_C to neutron matter in momentum space at saturation density obtained at the HF level with the nonlocal regulator of Ref. [17] compared to a calculation obtained with the local regulator of Ref. [176] as a function of the 3N cutoff Λ_{3N} . For a typical cutoff of 2.5 fm^{-1} , for nonlocal regulators the result is $\approx 97\%$ of the infinite cutoff result, while the local result is around 60 % of the infinite cutoff result. These results elaborate on the results in Fig. 6.3.

We determined the translation from the coordinate-space cutoff R_{3N} to the momentum-space cutoff Λ_{3N} in nonlocal regulators by matching the HF contribution of the LR part of V_C . We show this in the right panel of Fig. 6.7 for $n_{\text{exp}} = 2, 4$ in the momentum space regulator of Ref. [17]. For the usual choice $n_{\text{exp}} = 4$, the cutoff in the local regulator has to be reduced to values $R_{3N} \ll 0.5 \text{ fm}$ to reproduce the momentum space results.

In momentum space, we can try to understand this behavior at the HF level from the following discussion [254]. Consider NN interactions, where the momentum transfer \mathbf{q} is given as $\mathbf{p} - \mathbf{p}'$. As we use anti-symmetric wave functions, we have two terms for the Hartree-Fock energy: a direct and an exchange term. For the direct term, $\mathbf{p} = \mathbf{p}'$ and we find a vanishing momentum transfer \mathbf{q} . Local regulators of the form $\exp[-(q/\Lambda)^{2n}]$ evaluate to 1 for the direct term. For the exchange term, $\mathbf{p} = -\mathbf{p}'$ and we find $\mathbf{q} = 2\mathbf{p}$. Thus, for local regulators, the direct term to the

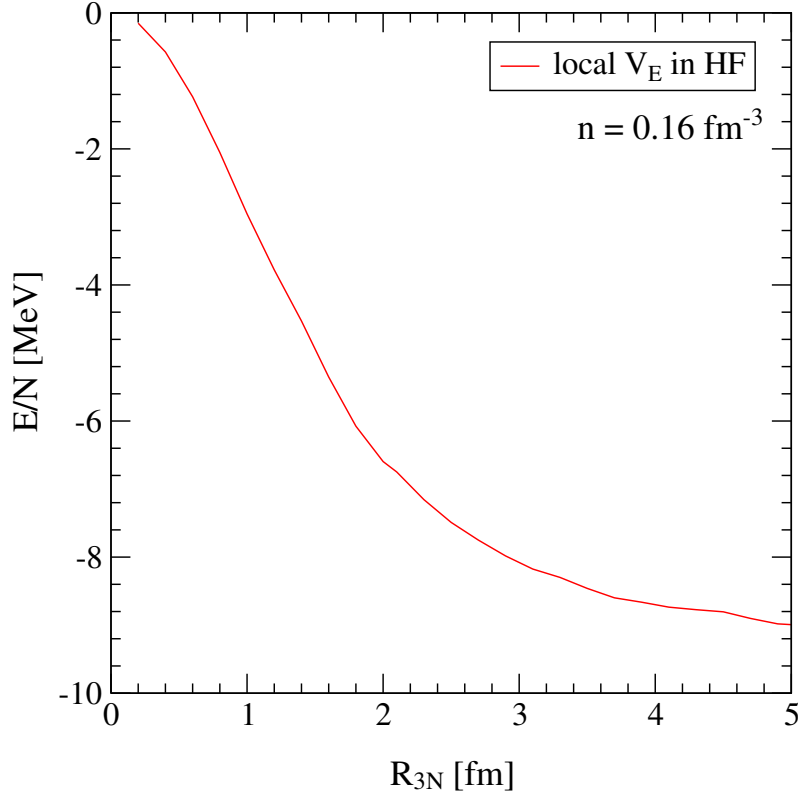


Figure 6.8: The 3N contact interaction V_E in pure neutron matter at saturation density on the Hartree-Fock level as a function of the 3N cutoff R_{3N} . The function approaches a constant value for $R_{3N} \rightarrow \infty$.

HF energy is unregulated while the exchange term is regulated with a momentum transfer of $2\mathbf{p}$. For $n = 2$, we find for the regulator in the exchange term $\exp[-16p^4/\Lambda^4]$. For nonlocal regulators instead one usually regularizes with regulators of the form $\exp[-(p/\Lambda)^{2n}]$ and $\exp[-(p'/\Lambda)^{2n}]$. Both for the direct as well as the exchange term, this leads to $\exp[-(p/\Lambda)^{2n}]^2$, and for $n = 2$, we find $\exp[-2p^4/\Lambda^4]$.

From this we can conclude two differences for local vs. nonlocal regulators: first, local regulators affect direct and exchange term differently, while nonlocal regulators affect both terms similarly. Second, in the exchange terms, for a certain cutoff, local regulators cut away more contributions compared to nonlocal regulators. This can be understood from the above example by the fact, that in the exchange term the regulator is $\exp[-2p^4/\Lambda^4]$ vs. $\exp[-16p^4/\Lambda^4]$ for nonlocal vs. local regulators, meaning, that for the same Λ , in the local case the cutoff is effectively smaller.

We want to illustrate these effects using two examples. In the Hartree-Fock approximation, for spin-dependent interactions, the direct term vanishes, because we sum over all possible spin states which effectively equals tracing over Pauli matrices. Thus, only the exchange terms survive. As they are regulated locally at a certain cutoff, the result will be smaller than for a nonlocal regulator with the same cutoff, see the previous discussion and Fig. 6.7. Thus, local regulators do not only regularize UV divergencies, but also cut away more IR physics compared to nonlocal regulators.

For spin-independent interactions, like V_E , the direct term contributes to the Hartree-Fock energy. For nonlocal regulators, direct and exchange terms are regulated in the same way. Because

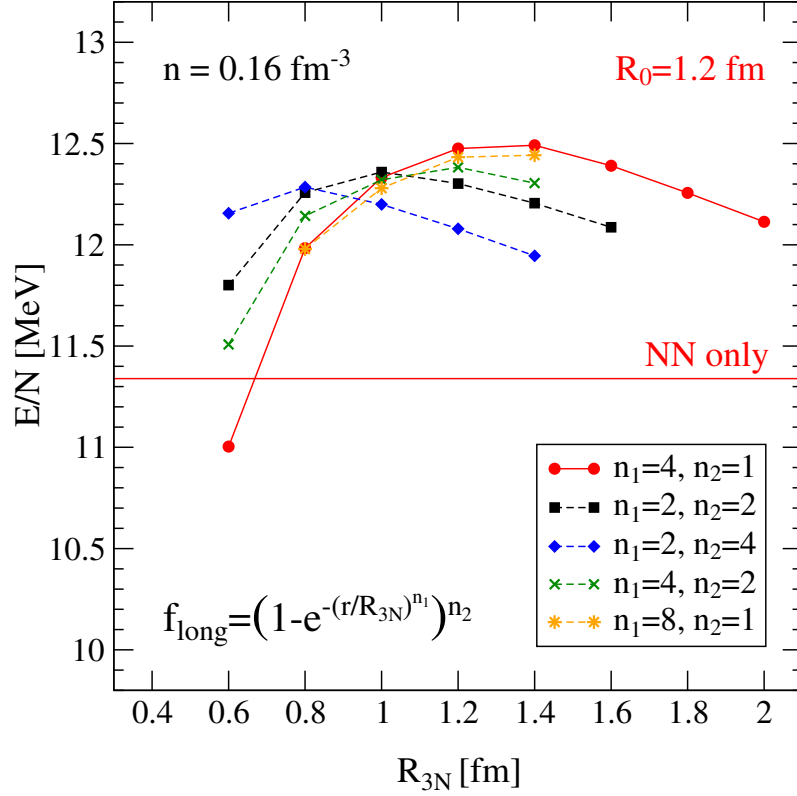


Figure 6.9: Dependence of the AFDMC energy per particle at saturation density as a function of the 3N cutoff R_{3N} on different long-range regulators. Results are shown for an NN cutoff $R_0 = 1.2$ fm. The long-range regulator is given by $[1 - e^{-(r/R_{3N})^{n_1}}]^{n_2}$ with different parameters n_1 and n_2 .

in the case of V_E the interaction is momentum-independent, all terms add up to 0. For the local V_E of this work

$$V_E(\mathbf{q}_i, \mathbf{q}_j) = \frac{c_E}{2f_\pi^4 \Lambda_\chi} \int d\mathbf{r}_{ij} e^{i\mathbf{q}_i \cdot \mathbf{r}_{ij}} \delta(\mathbf{r}_{ij}) \int d\mathbf{r}_{kj} e^{i\mathbf{q}_k \cdot \mathbf{r}_{kj}} \delta(\mathbf{r}_{kj}), \quad (6.54)$$

with normalized smeared-out δ functions, $q_i = 0$ for the direct term, leading to a constant independent of cutoff and momenta, while the exchange terms are cutoff dependent. When lowering the coordinate-space cutoff $R_{3N} \rightarrow 0$ all terms vanish, but when increasing the cutoff in coordinate space, the direct term is constant while the exchange terms vanish. V_E , thus, adds a sizeable contribution to neutron matter for high R_{3N} and already in the cutoff range of this work, see Fig. 6.8.

We investigated different forms for the local long-range regulators when choosing different parameters in the long-range regulator function. In Fig. 6.9 we show the dependence of the AFDMC energy per particle for V_C at saturation density as a function of the 3N cutoff R_{3N} on different long-range regulators. Results are shown for an NN cutoff $R_0 = 1.2$ fm. The long-range regulator is given by $(1 - e^{-(r/R_{3N})^{n_1}})^{n_2}$ with different parameters n_1 and n_2 . We find that the general picture is independent of the choice of the exponents in the regulator function. A consistent change of the short-range regulator has only a negligible effect on the energy. For different functions, the position of the plateau varies between 0.8 – 1.2 fm but the overall energies at the plateau are comparable, ranging between 12.3 – 12.5 MeV.

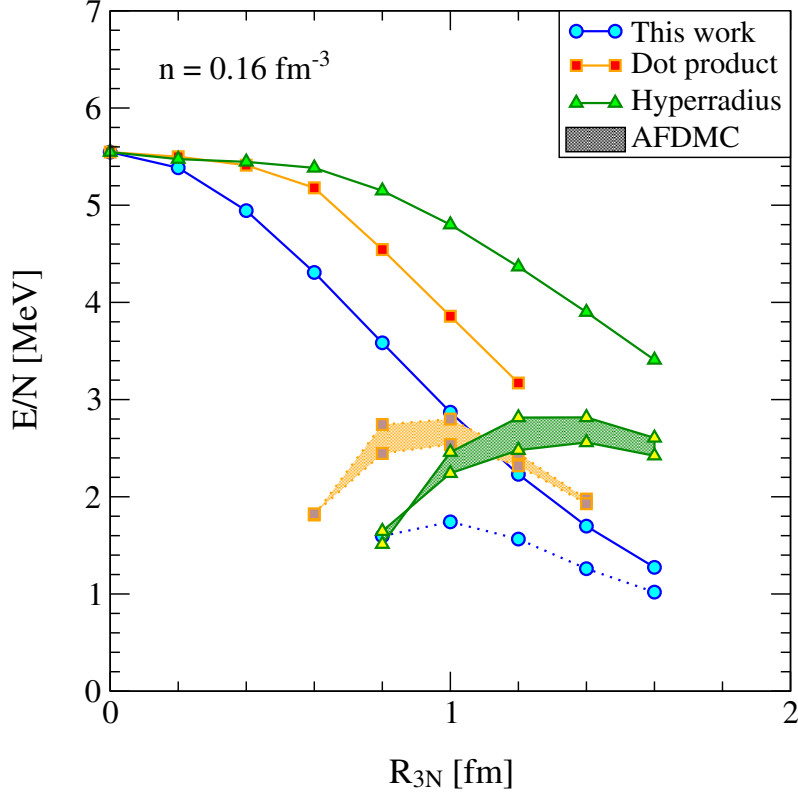


Figure 6.10: Dependence of the energy per particle of the LR V_C part $\sim c_3$ at saturation density as a function of the 3N cutoff R_{3N} on different long-range regulators. We show the HF as well as the AFDMC result for the original regulator of this work ($R_0 = 1.2$ fm) in comparison to a regulator of the form $[1 - e^{-(\mathbf{r}_{ij} \cdot \mathbf{r}_{kj}/R_{3N}^2)^4}]$ (Dot product) and a regulator of the form $[1 - e^{-(\mathbf{r}_{ij}^2 + \mathbf{r}_{kj}^2 - \mathbf{r}_{ik}^2)^4/R_{3N}^8}]$ (Hyperradius) (both for $R_0 = 1.0 - 1.2$ fm).

We furthermore investigated local regulators on the scalar product of the two radial vectors involved, $[1 - e^{-(\mathbf{r}_{ij} \cdot \mathbf{r}_{kj}/R_{3N}^2)^4}]$, and a regulator on the "hyperradius" $\mathbf{r}_{ij}^2 + \mathbf{r}_{kj}^2 - \mathbf{r}_{ik}^2$, given by $[1 - e^{-(\mathbf{r}_{ij}^2 + \mathbf{r}_{kj}^2 - \mathbf{r}_{ik}^2)^4/R_{3N}^8}]$ and show the energy per particle of the 3N V_C contribution $\sim c_3$ at saturation density as a function of the 3N cutoff R_{3N} for these regulators in Fig 6.10. Depicted are the HF results as well as the results obtained in the AFDMC method, where the bands are defined as before. As a comparison, we show the HF and the AFDMC result for $R_0 = 1.2$ fm for the original regulator of this work.

The particular definition of the "hyperradius" regulator is obtained by ensuring that the 3N contribution is suppressed if one radial vector vanishes. We find that the results vary strongly for the different regulator functions. Using the scalar product or the hyperradius in the regulator leads to HF results closer to the infinite cutoff limit for the cutoff range of this work. Especially the hyperradius regulator leads to 86% of the infinite cutoff result at $R_{3N} = 1.0$ fm.

Furthermore, these two regulators lead to $\approx 1.0 - 1.2$ MeV more repulsion from the LR V_C part in an AFDMC calculation within the regulator range of this work. This is highlighted also in Fig. 6.11, where we show the variation of the AFDMC energy per particle for the c_1 and LR c_3 part of V_C at saturation density as a function of the 3N cutoff R_{3N} for an NN cutoff 1.0 fm (black lines in the upper part) and 1.2 fm (red lines in the lower part) for the original regulator of this

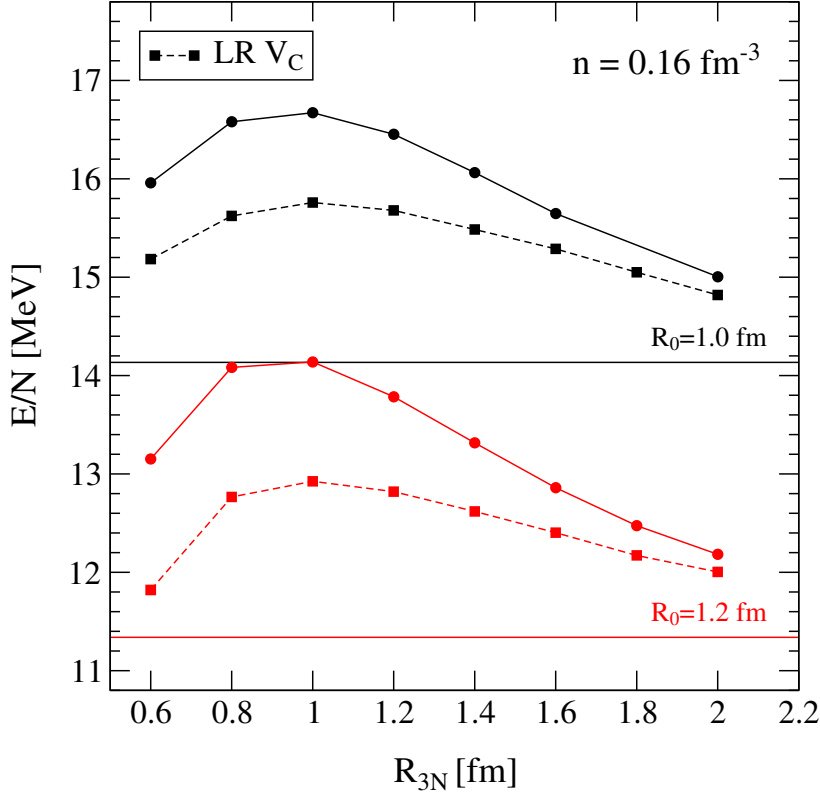


Figure 6.11: Variation of the AFDMC energy per particle for the c_1 and LR c_3 part of V_C at saturation density as a function of the 3N cutoff R_{3N} for an NN cutoff 1.0 fm (black lines in the upper part) and 1.2 fm (red lines in the lower part) for the original regulator of this work (squares) and the scalar product regulator (circles). The horizontal lines correspond to the NN-only energy.

work (squares) and the scalar product regulator (circles). The final energy range at saturation density changes from 12.3 – 15.6 MeV for the original regulator of this work to 13.8 – 16.7 MeV for the scalar-product regulator.

Both the scalar product as well as the hyperradius regulator also lead to a collapse in neutron matter and we find plateaus similar as before also for these regulators. Although the energies obtained on the plateau are comparable for both regulators, the position of the plateau varies from 0.8 – 1.0 fm for the scalar product regulator to 1.2 – 1.4 fm for the hyperradius regulator. Local vs. nonlocal regulators have to be further investigated to better understand the sources of the differences discussed above. In addition, it is necessary to find a possibility of assessing the quality of local regulators to be able to rule out certain forms of local regulators and design improved local regulators which do not suffer from the problems discussed above. Work in these directions is in progress.

7 Results at N²LO with local chiral NN and 3N interactions

In this Chapter we present our results for the equation of state of neutron matter and for neutron drops based on local chiral NN and 3N interactions. We will include all terms of V_C and adopt the c_i values of Refs. [213, 219]. Results including the shorter-range contributions V_D and V_E will be studied in future [253]. Finally, we will also present results including the shorter-range contributions V_D and V_E for light nuclei with all N²LO 3N contributions.

7.1 Equation of state of neutron matter using AFDMC

In Fig. 7.1 we present the final result of our AFDMC simulations for the equation of state in neutron matter. We show the energy per particle as a function of density including NN and the 3N V_C interactions for a variation of the two-body cutoff $R_0 = 1.0 - 1.2$ fm and a variation of the three-body cutoff R_{3N} in the same range. For the softer NN potential with $R_0 = 1.2$ fm (lower lines) we find the energy per particle to be 12.3 – 12.5 MeV at saturation density. The NN-only

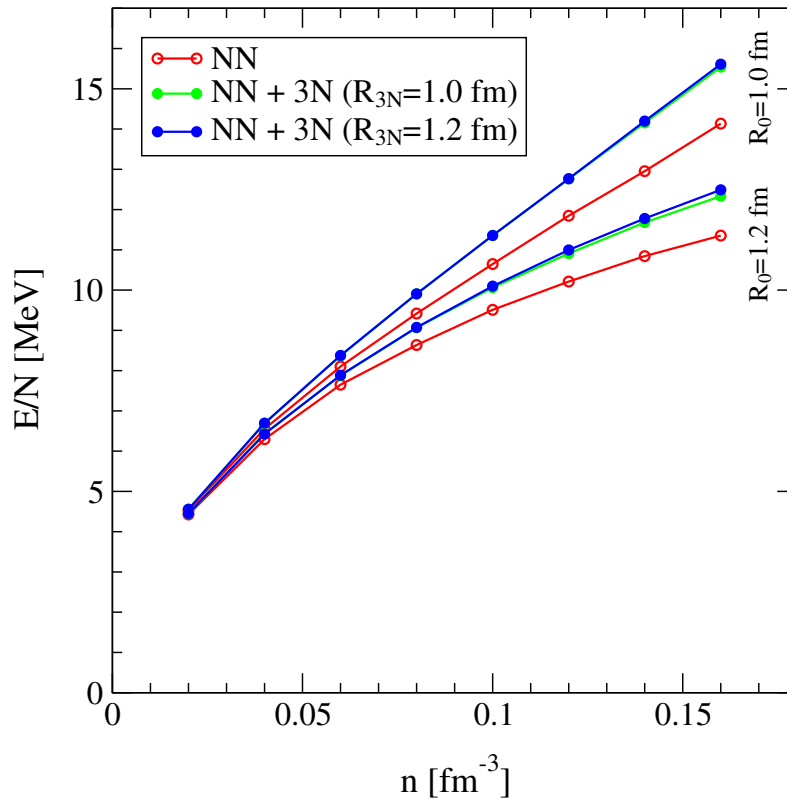


Figure 7.1: Energy per particle as a function of density for pure neutron matter at N²LO, including NN forces and the 3N V_C interaction in AFDMC. We vary the NN cutoff $R_0 = 1.0 - 1.2$ fm and the 3N cutoff R_{3N} in the same range.

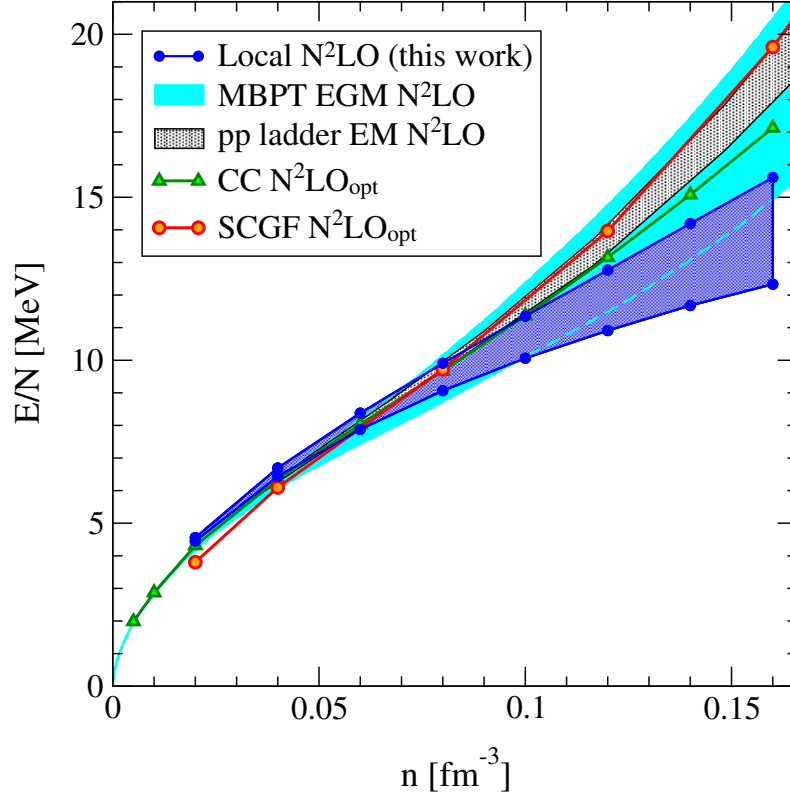


Figure 7.2: Comparison of the neutron matter energy at $N^2\text{LO}$ based on the local chiral NN+3N potentials in AFDMC (this work) with the $N^2\text{LO}$ calculation of Ref. [57] based on the EGM $N^2\text{LO}$ potentials and using many-body perturbation theory (MBPT), with the particle-particle (pp) ladder results of Ref. [255] based on the EM $N^2\text{LO}$ potential, and with results based on the $N^2\text{LO}_{\text{opt}}$ potential using self-consistent Green’s function (SCGF) methods [194] and using coupled-cluster (CC) theory [192].

energy is 11.4 MeV and the 3N V_C has an impact of ≈ 1 MeV. For the harder NN potential with $R_0 = 1.0$ fm (upper lines) we find an energy per particle of 15.5 – 15.6 MeV compared to 14.1 MeV for an NN-only calculation. Here, the impact of the 3N V_C is ≈ 1.5 MeV. Our total $N^2\text{LO}$ band is 12.3 – 15.6 MeV at $n = 0.16 \text{ fm}^{-3}$.

The variation of the total energy with the 3N cutoff is ~ 0.2 MeV in our cutoff range and considerably smaller than the variation with the NN cutoff because R_{3N} lies on the plateau described in Section 6.4.

We find the magnitude of the local 3N two-pion-exchange V_C forces to be at most about 1.5 MeV at saturation density which is smaller than a typical contribution of 4 MeV [54] in momentum space with non-local regulators, including 2nd and 3rd order corrections. As we have shown before, this difference can already be seen on the HF level and is most likely due to using these local regulators. A similar behavior was also seen in the coupled-cluster calculations of Ref. [192] where a difference of 2 MeV was found for the neutron matter energy per particle when choosing local vs. non-local regulators with a similar cutoff value of 500 MeV. For a local regulator on the scalar product of the radial vectors, the situation improves by ≈ 1 MeV, but these findings show clearly that local vs. nonlocal regulators need to be further investigated.

In Fig. 7.2 we compare the neutron matter energy at $N^2\text{LO}$ based on the local chiral NN+3N potentials in AFDMC with the $N^2\text{LO}$ calculation of Ref. [57] based on the EGM $N^2\text{LO}$ potentials

of Ref. [59] and using many-body perturbation theory, with the particle-particle (pp) ladder results of Ref. [255] based on the EM N^2 LO potential of Ref. [232], and with results based on the N^2 LO_{opt} potential of Ref. [239] using self-consistent Green's function (SCGF) methods [194] and using coupled-cluster (CC) theory [192]. At saturation density, the AFDMC energies are in general smaller than the other results, mainly due to the smaller contribution of the 3N forces for the local chiral potential. Furthermore, the density dependence of the AFDMC band is flatter than for the other calculations, which may be explained by differences in the NN phase shift predictions and which has also been seen on the NN level. We would expect the results to come closer when including chiral forces at N^3 LO. A comparison of AFDMC with MBPT results using the same local potential to benchmark MBPT with NN and 3N interactions, as in Sec. 5.2, is work in progress.

7.2 Variation of the c_i couplings

In the previous Section we found for the neutron matter equation of state at $n = 0.16 \text{ fm}^{-3}$ an energy range of 12.3 – 15.6 MeV. In our calculation of Ref. [17] using MBPT we found an energy range of 14.9 – 20.5 MeV, which is approximately two times as broad. In the MBPT calculation there are three major sources of uncertainty: the many-body method, the cutoff variation and the uncertainty of the c_i . It is difficult to clearly separate the sources of uncertainty but at saturation density $\approx 1 - 2 \text{ MeV}$ of the uncertainty stems from a variation of the couplings c_i in the two-pion exchange V_C , while a large part, $\approx 3 - 4 \text{ MeV}$, stems from the cutoff variation and $\approx 1 \text{ MeV}$ from the many-body method.

In the AFDMC calculation, we so far only include the uncertainty of the many-body method and the cutoff variation. The first is usually smaller than the points we plot and, thus negligible, while the latter accounts for all our uncertainty. This cutoff uncertainty is similar to the one in the MBPT calculation but we want to stress that the two cutoff ranges are not comparable. While in the AFDMC calculation the cutoff $R_0 = 1.0 - 1.2 \text{ fm}$ (400 – 500 MeV) and the SFR cutoff has almost no effect, in momentum space we can only choose the perturbative low-cutoff EGM potentials with $\Lambda_{3N} = 450 \text{ MeV}$ and the uncertainty originates in the SFR cutoff variation 500 – 700 MeV.

We now study the uncertainty in the couplings c_i for AFDMC and choose the range defined in Ref. [17] with $c_1 = -(0.37 - 0.81) \text{ GeV}^{-1}$ and $c_3 = -(2.71 - 3.4) \text{ GeV}^{-1}$. To be consistent with the NN sector it would be necessary to vary the c_i simultaneously in the NN two-pion exchange as well as in the 3N sector. We will only vary the c_i in the latter as in Ref. [17].

We calculated the c_i dependence for different combinations of the cutoffs R_0 and R_{3N} at saturation density and give the results in Tab. 7.2. While in the MBPT calculation we found a sizeable dependence of the result on the couplings c_i of $\approx 1 \text{ MeV}$, in AFDMC the c_i dependence is at most of the order of 0.3 MeV at saturation density and, thus, negligible compared to the cutoff variation.

This difference can be understood by the fact that local vs. nonlocal regulators lead to energies which are smaller by approximately a factor of two, which also decreases the variation with the c_i couplings.

Furthermore in MBPT, the energies were calculated at third order in perturbation theory and the inclusion of higher orders could also decrease the energy change in the c_i variation. To investigate this further, it would be interesting to study the perturbativeness of local chiral

Table 7.1: Variation of the neutron matter energy per particle at saturation density for different NN and 3N cutoffs and different values for the couplings c_i . All couplings are given in GeV^{-1} and all energies are given in MeV.

	$R_{3N} = 1.0 \text{ fm}$			$R_{3N} = 1.2 \text{ fm}$		
$R_0 = 1.0 \text{ fm}$	c_3/c_1	-0.37	-0.81	c_3/c_1	-0.37	-0.81
	-2.71	15.31	15.43	-2.71	15.31	15.42
	-3.40	15.42	15.54	-3.40	15.51	15.61
$R_0 = 1.2 \text{ fm}$	c_3/c_1	-0.37	-0.81	c_3/c_1	-0.37	-0.81
	-2.71	12.22	12.32	-2.71	12.30	12.39
	-3.40	12.24	12.33	-3.40	12.41	12.48

Hamiltonians with NN and 3N forces, similar to Sec. 5.2, for different cutoff combinations and c_i .

7.3 Light nuclei

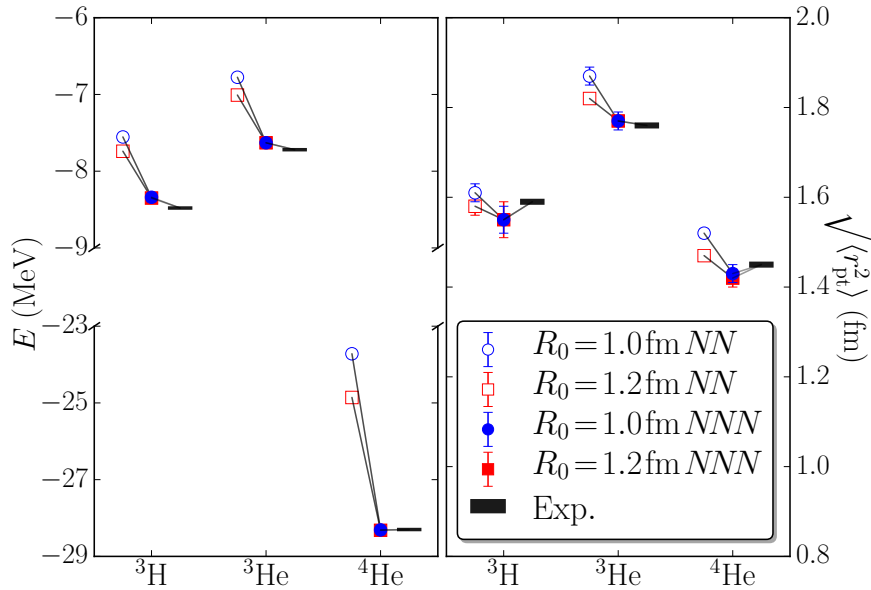


Figure 7.3: Ground-state energies and point-proton radii of light nuclei with $A = 3, 4$ calculated with the local chiral NN and 3N interactions in GFMC compared with experiment from Ref. [253].

In Ref. [253] the local chiral NN and 3N interactions presented in this work have been used to calculate the ground-state energies and point-proton radii of ${}^3\text{H}$, ${}^3\text{He}$, and ${}^4\text{He}$. The results are presented in Fig. 7.3.

After inclusion of consistent 3N forces, both the experimental ground-state energies and radii are well reproduced. The underbinding in the $A = 3$ system is $\approx 1\%$ and the agreement for the ${}^4\text{He}$ binding energy is perfect because the 3N forces were fitted to this data point. The radius of

^3He is well described. For ^3H and ^4He the radii are somewhat too small but still agree with the experimental result within the larger statistical error of the GFMC results.

7.4 Neutron drops

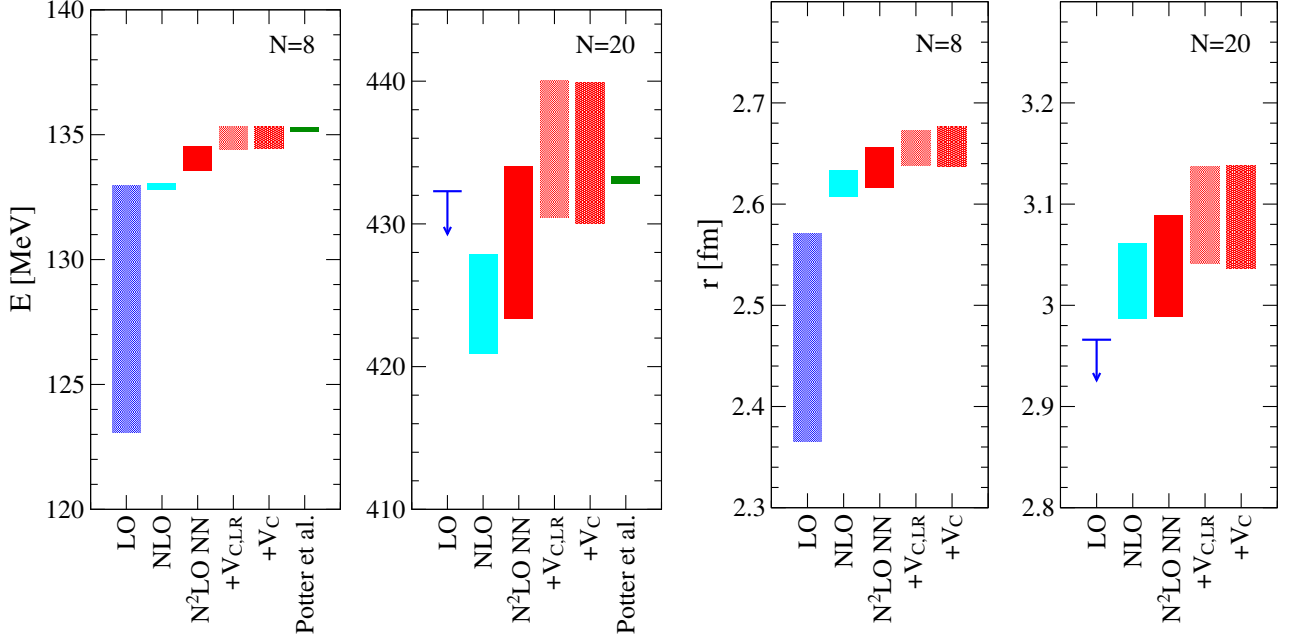


Figure 7.4: Neutron-drop energies and radii for neutron numbers of $N = 8$ or 20 in a harmonic oscillator well with oscillator parameter $\hbar\omega = 10\text{ MeV}$ using AFDMC. We used the same cutoff in the two- and three-nucleon sector, $R_0 = R_{3N}$. We give the results at different orders in the chiral expansion and, at $N^2\text{LO}$, for NN forces only, including only the LR c_1 and c_3 parts of V_C , and including also the SR and IR parts of V_C . The band is given by a cutoff variation of $R_0 = R_{3N} = 1.0 - 1.2\text{ fm}$. At LO with the softer cutoff and 20 neutrons, the system is collapsing. We compare our results with the calculations of Ref. [256], which use coupled-cluster theory at the ΛCCSD level, where the band is given by two different SRG evolution scales (for a fixed initial Hamiltonian).

Neutron drops in external potentials are an interesting system to constrain the properties of neutron-rich nuclei and energy-density functionals.

We have calculated neutron drops for neutron numbers of 8, 20, 40, and 70 in a harmonic oscillator well with oscillator parameter $\hbar\omega = 10\text{ MeV}$. For these calculations we used the same cutoff in the two- and three-nucleon sector, $R_0 = R_{3N}$, with a cutoff variation of $R_0 = R_{3N} = 1.0 - 1.2\text{ fm}$. The results for the energy and the radius of the neutron drops are tabulated in Tab. 7.2 and shown in Fig. 7.4. We give the results at different orders in the chiral expansion and, at $N^2\text{LO}$, for NN forces only, including only the LR c_1 and c_3 parts of V_C , and including also the SR and IR parts of V_C .

In systems with larger neutron numbers, the relative band of our calculations increases, at the level of $N^2\text{LO} + V_C$ it is 1% for $N = 8$, 2% at $N = 20$, 5% at $N = 40$, and 7% at $N = 70$. Furthermore, for larger systems and at low chiral orders, our calculations do not converge and collapses occur, due to the higher densities inside the larger neutron drops.

We have compared our results at $N^2\text{LO}$ with the calculations of Ref. [256], which use coupled-cluster theory at the ΛCCSD level, an SRG-evolved chiral Hamiltonian with the $N^3\text{LO}$ potential by Entem and Machleidt of Ref. [60] with a cutoff of 500 MeV, and $N^2\text{LO}$ 3N forces with the same cutoff, including also the V_D and V_E parts. The band is given by two different SRG evolution scales for a fixed initial Hamiltonian. We find very good agreement between the two approaches after inclusion of $N^2\text{LO}$ 3N forces whose contribution is small.

Table 7.2: Neutron-drop energies and radii for neutron numbers of 8, 20, 40, and 70 in a harmonic oscillator well with oscillator parameter $\hbar\omega = 10$ MeV. We used the same cutoff in the two- and three-nucleon sector, $R_0 = R_{3N}$. We give the results at different orders in the chiral expansion and, at N^2 LO, for NN forces only, including only the LR c_1 and c_3 parts of V_C , and including also the SR and IR parts of V_C . In systems with larger neutron numbers, collapses occur at low chiral-orders and the energies cannot be calculated.

#N	Hamiltonian	E	rms-radius
8	LO(1.0)	132.95(2)	2.571(1)
8	NLO(1.0)	133.07(3)	2.633(1)
8	N^2 LO(1.0) NN-only	134.53(2)	2.656(1)
8	N^2 LO(1.0) + $V_{C,LR}$	135.31(2)	2.673(1)
8	N^2 LO(1.0) + V_C	135.34(1)	2.677(1)
8	LO(1.2)	123.08(5)	2.365(1)
8	NLO(1.2)	132.82(2)	2.607(1)
8	N^2 LO(1.2) NN-only	133.53(1)	2.616(1)
8	N^2 LO(1.2) + $V_{C,LR}$	134.40(1)	2.638(1)
8	N^2 LO(1.2) + V_C	134.45(1)	2.637(1)
20	LO(1.0)	432.29(7)	2.966(1)
20	NLO(1.0)	427.90(9)	3.062(1)
20	N^2 LO(1.0) NN-only	434.04(8)	3.089(1)
20	N^2 LO(1.0) + $V_{C,LR}$	440.04(14)	3.137(1)
20	N^2 LO(1.0) + V_C	439.90(7)	3.138(2)
20	NLO(1.2)	420.92(4)	2.987(1)
20	N^2 LO(1.2) NN-only	423.38(3)	2.989(1)
20	N^2 LO(1.2) + $V_{C,LR}$	430.45(6)	3.041(1)
20	N^2 LO(1.2) + V_C	430.05(5)	3.036(1)
40	NLO(1.0)	1053.10(36)	3.459(1)
40	N^2 LO(1.0) NN-only	1068.31(13)	3.481(1)
40	N^2 LO(1.0) + $V_{C,LR}$	1091.97(23)	3.557(1)
40	N^2 LO(1.0) + V_C	1090.28(14)	3.556(1)
40	NLO(1.2)	1015.09(15)	3.318(1)
40	N^2 LO(1.2) NN-only	1015.35(17)	3.293(1)
40	N^2 LO(1.2) + $V_{C,LR}$	1045.77(12)	3.385(1)
40	N^2 LO(1.2) + V_C	1042.31(16)	3.377(1)
70	N^2 LO(1.0) NN-only	2230.26(26)	3.877(1)
70	N^2 LO(1.0) + $V_{C,LR}$	2296.42(64)	3.987(1)
70	N^2 LO(1.0) + V_C	2290.60(25)	3.991(1)
70	N^2 LO(1.2) NN-only	2062.93(59)	3.593(1)
70	N^2 LO(1.2) + $V_{C,LR}$	2155.56(48)	3.730(2)
70	N^2 LO(1.2) + V_C	2139.78(54)	3.711(2)

8 Summary and outlook

In this Thesis we have presented QMC calculations with local chiral EFT interactions. We followed Ref. [78] to construct improved local chiral NN potentials by using a freedom in chiral EFT to remove all sources of nonlocality to $N^2\text{LO}$. We have constructed new local LO, NLO, and $N^2\text{LO}$ NN interactions with improved fits for the low-energy couplings, which show a very good reproduction of the NN phase shifts as well as of deuteron properties compared to the momentum-space $N^2\text{LO}$ NN potentials of Ref. [59].

We then applied these local chiral NN interactions in AFDMC calculations of neutron matter. The results show a systematic order-by-order convergence. We have investigated the sensitivity of the results to the local regulator and to the SFR cutoff, to the influence of the Jastrow term, and also to finite size effects in AFDMC.

We studied the same potentials in MBPT calculations of neutron matter. Comparing MBPT and AFDMC results, we found excellent agreement of the results for the softer $R_0 = 1.1\text{ fm}$ and $R_0 = 1.2\text{ fm}$ potentials within the two many-body frameworks, which represents a direct validation of MBPT for neutron matter for soft interactions. These nonperturbative benchmarks for the neutron-matter equation of state at nuclear densities are one of the main conclusions of this Thesis.

Since for densities higher than $0.5n_0$ 3N forces become important, we presented the derivation of consistent local chiral 3N interactions at $N^2\text{LO}$ and included these forces into the QMC calculations. We investigated the individual contributions to neutron matter both at the Hartree-Fock level as well as in AFDMC and found that local regulators for 3N interactions lead to less repulsion from the 3N two-pion-exchange contribution, already at the Hartree-Fock level. We have investigated the influence of the cutoff on the results and found that the energy change for a cutoff variation $R_{3N} = 1.0 - 1.2\text{ fm}$ is very small compared to the NN cutoff variation.

We further found that the shorter-range contributions V_D and V_E can add sizeable contributions to neutron matter if local regulators are used.

We found that other forms of local regulators can lead to large differences in the result, leading to the conclusion, that local vs. nonlocal regulators have to be studied in more detail. It will be crucial to develop a method of assessing the quality of local regulators to find improved versions for these regulators.

We then presented the neutron-matter equation of state for local chiral NN and 3N interactions which is another major result of this Thesis. This calculation is consistent with previous determinations of the neutron-matter equation of state and has smaller theoretical uncertainties compared to previous determinations. However, we find smaller energies due to less repulsion from 3N interactions. We also simulated neutron drops and light nuclei with these local chiral Hamiltonians.

Future work will include further studies of local regulators to construct improved local 3N interactions. With improved regulators, AFDMC calculations with local $N^2\text{LO}$ NN+3N forces will provide nonperturbative benchmarks for nuclei, and nuclear matter. This will allow to study the perturbativeness of local chiral Hamiltonians with NN and 3N interactions and presents *ab initio* constraints for nuclear density functionals and for dense matter in astrophysics.

Furthermore, we plan to develop maximally-local chiral $N^3\text{LO}$ Hamiltonians to improve the theoretical uncertainty of our results. Because only eight out of the 15 new contact operators are local, we have to find a suitable set of seven nonlocal operators which can be treated perturbatively. In addition, the long-range pion exchange interactions at $N^3\text{LO}$ include nonlocal relativistic corrections, which also have to be treated perturbatively.

With these maximally local chiral $N^3\text{LO}$ potentials we will carry out precision studies of neutron and nuclear matter and of nuclei which can be expected to reduce the theoretical uncertainties, e.g., in the equation of state of pure neutron matter and the neutron-star mass-radius relation, by a factor of two compared to the determination in Ref. [17]. Additional astrophysics constraints, e.g., from future observations of heavier neutron stars or by the NICER mission, will help to constrain the equation of state even further. These calculations will serve as precise non-perturbative benchmarks for astrophysics. For instance, model equations of state for supernova simulations can be benchmarked and waveforms with an uncertainty band for the gravitational wave signal can be obtained.

Because the couplings in chiral EFT are fit to experiment, chiral EFT so far is not able to make predictions from first principles. By direct matching to lattice QCD results, for example for few-neutron systems in a box, and also varying the pion mass in chiral EFT, the approach presented here will be able to connect nuclear physics to the underlying theory of QCD. By determining the couplings in lattice QCD, chiral EFT predictions from first principles will be made available. The approach outlined in this Thesis will also help to study in detail the influence of the Δ isobar as an additional degree of freedom in chiral EFT. Due to the precision of continuum QMC methods, we can examine the perturbativeness of different chiral orders and investigate the order-by-order convergence in Δ -less and Δ -full chiral EFT. This will allow us to compare the convergence of chiral EFT in these two approaches, leading to insights into the employed power counting scheme.

Acknowledgements

I thank Prof. Achim Schwenk for his excellent supervision and tremendous support throughout the years. I am very thankful for the great time I had working in his group and the uncountable opportunities he offered, and I hope that we will continue to work together in the future.

I thank Prof. Alexandros Gezerlis for his help and time, especially in the beginning of this Thesis, and the many fruitful discussions until the final stages of this work.

My thanks also goes to Dr. Stefano Gandolfi with whom I have a great and productive collaboration. I thank him especially for inviting me to Los Alamos and for his hospitality. It was a great experience and I appreciate this very much.

I thank Dr. Kai Hebeler for many useful discussions, and a very pleasant and fruitful collaboration throughout the years.

Furthermore, I thank my other collaborators of this work: Prof. Evgeny Epelbaum and Dr. Andreas Nogga.

I thank Michael Freunek for the NN interaction fits performed in Ref. [78] and Prof. Joe Carlson, Prof. Richard Furnstahl, Thomas Krüger, Dr. Joel Lynn, and Dr. Alessandro Lovato for stimulating discussions.

My special thanks go to the members, old and new, of the STRONGINT group: Alexander Bartl, Liliana Caballero, Arianna Carbone, Christian Drischler, Victoria Durant, Svenja Greif, Martin Hoferichter, Jason D. Holt, Lukas Huth, Philipp Klos, Dmitry Kobayakov, Javier Menéndez, Johannes Simonis, Vittorio Somà, and Maria Voskresenskaya. Thank you for the wonderful atmosphere and the great time in and out of the offices.

My thanks also go to all the members of the theory center.

Finally, and most importantly, I thank my family and loved ones for their constant support in all situations.

This work was carried out within the ERC Grant No. 307986 STRONGINT. The computations were performed at the Jülich Supercomputing Center.



A Fourier transformation of contact interactions

In the following we give the Fourier transformation of the contact contributions. The LO contacts are momentum independent and their Fourier transformation is given by

$$\int \frac{d^3q}{(2\pi)^3} V_{\text{cont}}^{\text{LO}} f_{\text{local}}(q^2) e^{i\mathbf{q}\cdot\mathbf{r}} = V_{\text{cont}}^{\text{LO}} \int \frac{d^3q}{(2\pi)^3} f_{\text{local}}(q^2) e^{i\mathbf{q}\cdot\mathbf{r}} = V_{\text{cont}}^{\text{LO}} \delta_{R_0}(\mathbf{r}), \quad (\text{A.1})$$

where $f_{\text{local}}(q^2)$ is a local momentum space regulator.

The first four NLO contact interactions are proportional to q^2 and contain spin and isospin operators which are not dotted into momentum operators. Writing the q^2 dependence explicitly, the Fourier transformation is given by

$$\int \frac{d^3q}{(2\pi)^3} V_{\text{cont}}^{\text{NLO}} q^2 f_{\text{local}}(q^2) e^{i\mathbf{q}\cdot\mathbf{r}} = -V_{\text{cont}}^{\text{NLO}} \Delta \int \frac{d^3q}{(2\pi)^3} f_{\text{local}}(q^2) e^{i\mathbf{q}\cdot\mathbf{r}} = -V_{\text{cont}}^{\text{NLO}} \Delta \delta_{R_0}(\mathbf{r}). \quad (\text{A.2})$$

To Fourier transform the spin-orbit interaction we employ the test function ψ :

$$\begin{aligned} & \langle \mathbf{r} | \hat{O}_{\text{LS}} | \psi \rangle \\ &= \int \frac{d^3p}{(2\pi)^3} \frac{d^3p'}{(2\pi)^3} d^3r' \langle \mathbf{r} | \mathbf{p}' \rangle \langle \mathbf{p}' | \hat{O}_{\text{LS}} | \mathbf{p} \rangle \langle \mathbf{p} | \mathbf{r}' \rangle \langle \mathbf{r}' | \psi \rangle \\ &= \int \frac{d^3p}{(2\pi)^3} \frac{d^3p'}{(2\pi)^3} d^3r' e^{i\mathbf{p}'\cdot\mathbf{r}} e^{-i\mathbf{p}\cdot\mathbf{r}'} \langle \mathbf{p}' | \hat{O}_{\text{LS}} | \mathbf{p} \rangle \psi(\mathbf{r}') \\ &= \frac{C_5}{2} \int \frac{d^3q}{(2\pi)^3} \frac{d^3k}{(2\pi)^3} d^3r' i(\boldsymbol{\sigma}_1 + \boldsymbol{\sigma}_2) \cdot (\mathbf{q} \times \mathbf{k}) \mathbf{e}^{i\frac{\mathbf{q}}{2}\cdot(\mathbf{r}+\mathbf{r}')} \mathbf{e}^{i\mathbf{k}\cdot(\mathbf{r}-\mathbf{r}')} \psi(\mathbf{r}') f_{\text{local}}(q^2) \\ &= \frac{C_5}{2} \int \frac{d^3q}{(2\pi)^3} \frac{d^3k}{(2\pi)^3} d^3r' i\epsilon^{\alpha\beta\gamma} (\boldsymbol{\sigma}_1 + \boldsymbol{\sigma}_2)_\alpha q_\beta e^{i\frac{\mathbf{q}}{2}\cdot(\mathbf{r}+\mathbf{r}')} (i\partial'_\gamma e^{i\mathbf{k}\cdot(\mathbf{r}-\mathbf{r}')} \psi(\mathbf{r}')) f_{\text{local}}(q^2) \\ &= -\frac{C_5}{2} \int \frac{d^3q}{(2\pi)^3} \frac{d^3k}{(2\pi)^3} d^3r' i\epsilon^{\alpha\beta\gamma} (\boldsymbol{\sigma}_1 + \boldsymbol{\sigma}_2)_\alpha q_\beta (i\partial'_\gamma e^{i\frac{\mathbf{q}}{2}\cdot\mathbf{r}'} \psi(\mathbf{r}')) e^{i\mathbf{k}\cdot(\mathbf{r}-\mathbf{r}')} f_{\text{local}}(q^2) e^{i\frac{\mathbf{q}}{2}\cdot\mathbf{r}} \\ &= \frac{C_5}{4} \int \frac{d^3q}{(2\pi)^3} i\epsilon^{\alpha\beta\gamma} (\boldsymbol{\sigma}_1 + \boldsymbol{\sigma}_2)_\alpha q_\beta q_\gamma \psi(\mathbf{r}) f_{\text{local}}(q^2) e^{i\mathbf{q}\cdot\mathbf{r}} \\ &\quad - \frac{C_5}{2} \int \frac{d^3q}{(2\pi)^3} i\epsilon^{\alpha\beta\gamma} (\boldsymbol{\sigma}_1 + \boldsymbol{\sigma}_2)_\alpha q_\beta (i\partial_\gamma \psi(\mathbf{r})) f_{\text{local}}(q^2) e^{i\mathbf{q}\cdot\mathbf{r}} \\ &= -\frac{C_5}{2} \epsilon^{\alpha\beta\gamma} (\boldsymbol{\sigma}_1 + \boldsymbol{\sigma}_2)_\alpha \partial_\beta \left(\int \frac{d^3q}{(2\pi)^3} f_{\text{local}}(q^2) e^{i\mathbf{q}\cdot\mathbf{r}} \right) (i\partial_\gamma \psi(\mathbf{r})) \\ &= -\frac{C_5}{2} \frac{\partial_r \delta_{R_0}}{r} \epsilon^{\alpha\beta\gamma} (\boldsymbol{\sigma}_1 + \boldsymbol{\sigma}_2)_\alpha \mathbf{r}_\beta (i\partial_\gamma \psi(\mathbf{r})) \\ &= -\frac{C_5}{2} \frac{\partial_r \delta_{R_0}}{r} \mathbf{S} \cdot i\mathbf{r} \times \nabla \psi(\mathbf{r}) = \frac{C_5}{2} \frac{\partial_r \delta_{R_0}}{r} \mathbf{L} \cdot \mathbf{S} \psi(\mathbf{r}). \end{aligned} \quad (\text{A.3})$$

Here we used partial integration and the antisymmetry of $\epsilon^{\alpha\beta\gamma}$ in line 5 and 6, respectively, and $\mathbf{L} = -i\mathbf{r} \times \nabla$ in the last line.

The Fourier transformation of the tensorial contact operators is given by

$$\begin{aligned}
& \int \frac{d^3q}{(2\pi)^3} V_{\text{cont}}^{\text{tens}} f_{\text{local}}(q^2) \boldsymbol{\sigma}_1 \cdot \mathbf{q} \boldsymbol{\sigma}_2 \cdot \mathbf{q} e^{i\mathbf{q} \cdot \mathbf{r}} \\
&= -V_{\text{cont}}^{\text{tens}} \sigma_1^i \sigma_2^j \partial^i \partial^j \int \frac{d^3q}{(2\pi)^3} f_{\text{local}}(q^2) e^{i\mathbf{q} \cdot \mathbf{r}} \\
&= -V_{\text{cont}}^{\text{tens}} \sigma_1^i \sigma_2^j \partial^i \partial^j \delta_{R_0}(\mathbf{r}) \\
&= -V_{\text{cont}}^{\text{tens}} \sigma_1^i \sigma_2^j \partial^i \left(\frac{x^j}{r} \partial_r \delta_{R_0}(\mathbf{r}) \right) \\
&= V_{\text{cont}}^{\text{tens}} \left[\boldsymbol{\sigma}_1 \cdot \hat{\mathbf{r}} \boldsymbol{\sigma}_2 \cdot \hat{\mathbf{r}} \left(\frac{\partial_r \delta_{R_0}(\mathbf{r})}{r} - \partial_r^2 \delta_{R_0}(\mathbf{r}) \right) - \boldsymbol{\sigma}_1 \cdot \boldsymbol{\sigma}_2 \frac{\partial_r \delta_{R_0}(\mathbf{r})}{r} \right].
\end{aligned} \tag{A.4}$$

B Partial-wave-decomposed contact interactions

In Refs. [213, 219], we fit the LECs C_S, C_T , and C_{1-7} to NN phase shifts. In every partial wave only certain LECs contribute. In the following we give the partial wave decomposition for all relevant channels. We use spectroscopic LECs given in terms of C_S, C_T , and C_{1-7} as follows:

$$\begin{aligned}
 d_{11} &= C_S + C_T, \\
 d_{22} &= C_S - 3C_T, \\
 d_1 &= C_1 - 3C_2 + C_3 - 3C_4, \\
 d_2 &= C_6 - 3C_7, \\
 d_3 &= C_1 + C_2 - 3C_3 - 3C_4, \\
 d_4 &= C_1 + C_2 + C_3 + C_4, \\
 d_5 &= C_1 - 3C_2 - 3C_3 + 9C_4, \\
 d_6 &= \frac{1}{2}C_5, \\
 d_7 &= C_6 + C_7.
 \end{aligned}$$

For the partial-wave-decomposed matrix elements we find

$$\langle {}^1S_0 | V_{\text{cont}} | {}^1S_0 \rangle = d_{22}\delta_{R_0} + (d_3 - d_7)20\frac{r^2}{R_0^4}\delta_{R_0} - (d_3 - d_7)16\frac{r^6}{R_0^8}\delta_{R_0}, \quad (\text{B.1})$$

$$\langle {}^3S_1 | V_{\text{cont}} | {}^3S_1 \rangle = d_{11}\delta_{R_0} + (d_1 + \frac{1}{3}d_2)20\frac{r^2}{R_0^4}\delta_{R_0} - (d_1 + \frac{1}{3}d_2)16\frac{r^6}{R_0^8}\delta_{R_0}, \quad (\text{B.2})$$

$$\begin{aligned}
 \langle {}^3S_1 | V_{\text{cont}} | {}^3D_1 \rangle &= \langle {}^3D_1 | V_{\text{cont}} | {}^3S_1 \rangle \\
 &= d_2\frac{\sqrt{8}}{3}8\frac{r^2}{R_0^4}\delta_{R_0} - d_2\frac{\sqrt{8}}{3}16\frac{r^6}{R_0^8}\delta_{R_0},
 \end{aligned} \quad (\text{B.3})$$

$$\langle {}^3D_1 | V_{\text{cont}} | {}^3D_1 \rangle = d_{11}\delta_{R_0} - (d_1 - \frac{1}{3}d_2)16\frac{r^6}{R_0^8}\delta_{R_0} + (d_1 + \frac{3}{5}d_6 + \frac{1}{15}d_2)20\frac{r^2}{R_0^4}\delta_{R_0}, \quad (\text{B.4})$$

$$\langle {}^1P_1 | V_{\text{cont}} | {}^1P_1 \rangle = d_{22}\delta_{R_0} + (d_5 - d_2)20\frac{r^2}{R_0^4}\delta_{R_0} - (d_5 - d_2)16\frac{r^6}{R_0^8}\delta_{R_0}, \quad (\text{B.5})$$

$$\langle {}^3P_0 | V_{\text{cont}} | {}^3P_0 \rangle = d_{11}\delta_{R_0} - (d_4 - d_7)16\frac{r^6}{R_0^8}\delta_{R_0} + (d_4 + \frac{2}{5}d_6 - \frac{1}{5}d_7)20\frac{r^2}{R_0^4}\delta_{R_0}, \quad (\text{B.6})$$

$$\langle {}^3P_1 | V_{\text{cont}} | {}^3P_1 \rangle = d_{11}\delta_{R_0} - (d_4 + d_7)16\frac{r^6}{R_0^8}\delta_{R_0} + (d_4 + \frac{1}{5}d_6 + \frac{3}{5}d_7)20\frac{r^2}{R_0^4}\delta_{R_0}, \quad (\text{B.7})$$

$$\langle {}^3P_2 | V_{\text{cont}} | {}^3P_2 \rangle = d_{11} \delta_{R_0} - (d_4 + \frac{1}{5}d_7) 16 \frac{r^6}{R_0^8} \delta_{R_0} + (d_4 - \frac{1}{5}d_6 + \frac{7}{25}d_7) 20 \frac{r^2}{R_0^4} \delta_{R_0}, \quad (\text{B.8})$$

$$\begin{aligned} \langle {}^3P_2 | V_{\text{cont}} | {}^3F_2 \rangle &= \langle {}^3F_2 | V_{\text{cont}} | {}^3P_2 \rangle \\ &= d_7 \sqrt{6} \frac{16}{5} \frac{r^2}{R_0^4} \delta_{R_0} - d_7 \sqrt{6} \frac{32}{5} \frac{r^6}{R_0^8} \delta_{R_0}, \end{aligned} \quad (\text{B.9})$$

$$\langle {}^3F_2 | V_{\text{cont}} | {}^3F_2 \rangle = d_{11} \delta_{R_0} - (d_4 - \frac{1}{5}d_7) 16 \frac{r^6}{R_0^8} \delta_{R_0} + (d_4 + \frac{4}{5}d_6 + \frac{3}{25}d_7) 20 \frac{r^2}{R_0^4} \delta_{R_0}. \quad (\text{B.10})$$

C Two-body matrix elements for MBPT calculations in pure neutron matter

We want to calculate the energy per particle E/N perturbatively in pure neutron matter, using the local coordinate space NN potential. In neutron matter, the antisymmetrized potential is given by

$$V_{\text{as}} = (1 - \mathcal{P}_{12})V = V - \mathcal{P}_{12}V. \quad (\text{C.1})$$

The antisymmetrizer in neutron matter only has momentum and spin parts $\mathcal{P}_{12} = \mathcal{P}_{12}^{\text{mom}}\mathcal{P}_{12}^{\text{spin}} = \mathcal{P}_{12}^{\text{mom}} \frac{1 + \boldsymbol{\sigma}_1 \cdot \boldsymbol{\sigma}_2}{2}$.

We only consider the spin part and find

$$\begin{aligned} \frac{1 + \boldsymbol{\sigma}_1 \cdot \boldsymbol{\sigma}_2}{2} V(\mathbf{r}) &= \frac{1 + \boldsymbol{\sigma}_1 \cdot \boldsymbol{\sigma}_2}{2} (V_C(\mathbf{r}) + \boldsymbol{\sigma}_1 \cdot \boldsymbol{\sigma}_2 V_S(\mathbf{r}) + \mathbf{L} \cdot \mathbf{S} V_{\text{LS}}(\mathbf{r}) + S_{12}(\mathbf{r}) V_T(\mathbf{r})) \\ &= \frac{1}{2} (V_C(\mathbf{r}) + \boldsymbol{\sigma}_1 \cdot \boldsymbol{\sigma}_2 V_S(\mathbf{r}) + \mathbf{L} \cdot \mathbf{S} V_{\text{LS}}(\mathbf{r}) + S_{12}(\mathbf{r}) V_T(\mathbf{r}) \\ &\quad + \boldsymbol{\sigma}_1 \cdot \boldsymbol{\sigma}_2 V_C(\mathbf{r}) + (3 - 2\boldsymbol{\sigma}_1 \cdot \boldsymbol{\sigma}_2) V_S(\mathbf{r}) + \mathbf{L} \cdot \mathbf{S} V_{\text{LS}}(\mathbf{r}) + S_{12}(\mathbf{r}) V_T(\mathbf{r})), \end{aligned} \quad (\text{C.2})$$

because $\boldsymbol{\sigma}_1 \cdot \boldsymbol{\sigma}_2 \mathbf{L} \cdot \mathbf{S} = \mathbf{L} \cdot \mathbf{S}$ and $\boldsymbol{\sigma}_1 \cdot \boldsymbol{\sigma}_2 S_{12}(\mathbf{r}) V_T(\mathbf{r}) = S_{12}(\mathbf{r}) V_T(\mathbf{r})$.

Since $\boldsymbol{\sigma}_1 \cdot \boldsymbol{\sigma}_2 \rightarrow -3, 1$ for $S = 0$ and $S = 1$, respectively, we find

$$\frac{1 + \boldsymbol{\sigma}_1 \cdot \boldsymbol{\sigma}_2}{2} V(\mathbf{r}) = (-1)^{S+1} V(\mathbf{r}) = \begin{cases} -V(\mathbf{r}) & \text{if } S = 0 \\ V(\mathbf{r}) & \text{if } S = 1 \end{cases}, \quad (\text{C.3})$$

and

$$V_{\text{as}} = V - \mathcal{P}_{12}V = V - \mathcal{P}_{12}^{\text{mom}} \frac{1 + \boldsymbol{\sigma}_1 \cdot \boldsymbol{\sigma}_2}{2} V = V - \mathcal{P}_{12}^{\text{mom}} V (-1)^{S+1}. \quad (\text{C.4})$$

We need to calculate the matrix element $\langle \mathbf{k}' S m_{S'} | V_{\text{as}} | \mathbf{k} S m_S \rangle$ and make use the plane wave expansion and the spherical harmonic addition theorem

$$\begin{aligned} \langle \mathbf{r} | \mathbf{k} \rangle &= e^{i\mathbf{k} \cdot \mathbf{r}} = \sum_l i^l (2l+1) j_l(kr) P_l(\hat{\mathbf{k}} \cdot \hat{\mathbf{r}}) \\ &= \sum_l i^l (2l+1) j_l(kr) \frac{4\pi}{(2l+1)} \sum_{m_l} Y_{lm_l}^*(\Omega_{\mathbf{k}}) Y_{lm_l}(\Omega_{\mathbf{r}}) \\ &= 4\pi \sum_{l, m_l} i^l j_l(kr) Y_{lm_l}^*(\Omega_{\mathbf{k}}) Y_{lm_l}(\Omega_{\mathbf{r}}). \end{aligned} \quad (\text{C.5})$$

The momentum exchange operator $\mathcal{P}_{12}^{\text{mom}}$ acts on the momenta and leads to $\mathcal{P}_{12}^{\text{mom}}\mathbf{k} = \mathcal{P}_{12}^{\text{mom}}(\mathbf{k}_1 - \mathbf{k}_2) = \mathbf{k}_2 - \mathbf{k}_1 = -\mathbf{k}$. For the matrix element we then find

$$\begin{aligned}
\langle \mathbf{k}' S m_{S'} | \mathcal{P}_{12}^{\text{mom}} V | \mathbf{k} S m_S \rangle &= \langle -\mathbf{k}' S m_{S'} | V | \mathbf{k} S m_S \rangle \\
&= \int d^3\mathbf{r} \langle S m_{S'} | \langle -\mathbf{k}' | \mathbf{r} \rangle V(\mathbf{r}) \langle \mathbf{r} | \mathbf{k} \rangle | S m_S \rangle \\
&= \int d^3\mathbf{r} \langle S m_{S'} | (4\pi) \sum_{l, m_l} i^{-l} j_l(k'r) Y_{lm_l}(\Omega_{-\mathbf{k}}) Y_{lm_l}^*(\Omega_{\mathbf{r}}) V(\mathbf{r}) \langle \mathbf{r} | \mathbf{k} \rangle | S m_S \rangle \\
&= \int d^3\mathbf{r} \langle S m_{S'} | (4\pi) \sum_{l, m_l} i^{-l} j_l(k'r) (-1)^l Y_{lm_l}(\Omega_{\mathbf{k}}) Y_{lm_l}^*(\Omega_{\mathbf{r}}) V(\mathbf{r}) \langle \mathbf{r} | \mathbf{k} \rangle | S m_S \rangle \\
&= (-1)^l \langle \mathbf{k}' S m_{S'} | V | \mathbf{k} S m_S \rangle.
\end{aligned} \tag{C.6}$$

This leads to $V_{\text{as}} = V - (-1)^{L+S+1}V = 2V$ for antisymmetric states in pure neutron matter ($T=1$). We then find for the matrix element

$$\begin{aligned}
\langle \mathbf{k}' S m_{S'} | V_{\text{as}} | \mathbf{k} S m_S \rangle &= \langle S m_{S'} | \langle \mathbf{k}' | V_{\text{as}} | \mathbf{k} \rangle | S m_S \rangle \\
&= \int d^3\mathbf{r} \langle S m_{S'} | \langle \mathbf{k}' | \mathbf{r} \rangle V_{\text{as}}(\mathbf{r}) \langle \mathbf{r} | \mathbf{k} \rangle | S m_S \rangle \\
&= 2 \int d^3\mathbf{r} \langle S m_{S'} | (4\pi)^2 \sum_{l', m_{l'}} i^{-l'} j_{l'}(k'r) Y_{l'm_{l'}}(\Omega_{\mathbf{k}'}) Y_{l'm_{l'}}^*(\Omega_{\mathbf{r}}) V(\mathbf{r}) \sum_{l, m_l} i^l j_l(kr) Y_{lm_l}^*(\Omega_{\mathbf{k}}) Y_{lm_l}(\Omega_{\mathbf{r}}) | S m_S \rangle \\
&= 2 \sum_{lm_l l' m_{l'}} (4\pi)^2 i^{l-l'} Y_{l'm_{l'}}(\Omega_{\mathbf{k}'}) Y_{lm_l}^*(\Omega_{\mathbf{k}}) \int d^3\mathbf{r} \langle S m_{S'} | j_{l'}(k'r) j_l(kr) Y_{l'm_{l'}}^*(\Omega_{\mathbf{r}}) V(\mathbf{r}) Y_{lm_l}(\Omega_{\mathbf{r}}) | S m_S \rangle \\
&= 2 \sum_{lm_l l' m_{l'}} (4\pi)^2 i^{l-l'} Y_{l'm_{l'}}(\Omega_{\mathbf{k}'}) Y_{lm_l}^*(\Omega_{\mathbf{k}}) \int d^3\mathbf{r} \langle S m_{S'} | j_{l'}(k'r) j_l(kr) \langle l' m_{l'} | \theta \phi \rangle V(\mathbf{r}) \langle \theta \phi | lm_l \rangle | S m_S \rangle \\
&= 2 \sum_{lm_l l' m_{l'}} (4\pi)^2 i^{l-l'} Y_{l'm_{l'}}(\Omega_{\mathbf{k}'}) Y_{lm_l}^*(\Omega_{\mathbf{k}}) \int d^3\mathbf{r} j_{l'}(k'r) j_l(kr) \langle l' m_{l'} S m_{S'} | \theta \phi \rangle \\
&\quad \times \left(\sum_{J' m_{J'}} | (l'S) J' m_{J'} \rangle \langle (l'S) J' m_{J'} | \right) V(\mathbf{r}) \left(\sum_{J m_J} | (lS) J m_J \rangle \langle (lS) J m_J | \right) \langle \theta \phi | lm_l S m_S \rangle \\
&= 2 \sum_{lm_l l' m_{l'}} \sum_{J m_J J' m_{J'}} (4\pi)^2 i^{l-l'} Y_{l'm_{l'}}(\Omega_{\mathbf{k}'}) Y_{lm_l}^*(\Omega_{\mathbf{k}}) \int d^3\mathbf{r} j_{l'}(k'r) j_l(kr) \langle l' m_{l'} S m_{S'} | (l'S) J' m_{J'} \rangle | \theta \phi \rangle \\
&\quad \times V_{Sl'l'J}(\mathbf{r}) \delta_{JJ'} \delta_{m_J m_{J'}} \langle \theta \phi | \langle (lS) J m_J | lm_l S m_S \rangle,
\end{aligned} \tag{C.7}$$

because the chiral interaction at N²LO does not change total angular momentum or its projection.

We finally get

$$\begin{aligned}
& \langle \mathbf{k}' S m_{S'} | V_{\text{as}} | \mathbf{k} S m_S \rangle \tag{C.8} \\
&= 2 \sum_{l m_l l' m_{l'}} \sum_{J m_J} (4\pi)^2 i^{l-l'} Y_{l' m_{l'}}(\Omega_{\mathbf{k}'}) Y_{l m_l}^*(\Omega_{\mathbf{k}}) \int d^3 \mathbf{r} j_{l'}(k' r) j_l(k r) \langle l' m_{l'} S m_{S'} | (l' S) J m_J \rangle | \theta \phi \rangle \langle \theta \phi | \\
&\quad \times V_{S l l' J}(\mathbf{r}) \langle (l S) J m_J | l m_l S m_S \rangle \\
&= 2 \sum_{l m_l l' m_{l'}} \sum_{J m_J} (4\pi)^2 i^{l-l'} Y_{l' m_{l'}}(\Omega_{\mathbf{k}'}) Y_{l m_l}^*(\Omega_{\mathbf{k}}) \int d r r^2 j_{l'}(k' r) j_l(k r) V_{S l l' J}(\mathbf{r}) \mathcal{C}_{l' m_{l'} S m_{S'}}^{J m_J} \mathcal{C}_{l m_l S m_S}^{J m_J} \\
&= 2 \sum_{l m_l l' m_{l'}} \sum_{J m_J} (4\pi)^2 i^{l-l'} Y_{l' m_{l'}}(\Omega_{\mathbf{k}'}) Y_{l m_l}^*(\Omega_{\mathbf{k}}) V_0(k, k', S, l, l', J) \mathcal{C}_{l' m_{l'} S m_{S'}}^{J m_J} \mathcal{C}_{l m_l S m_S}^{J m_J},
\end{aligned}$$

where $V_0(k, k', S, l, l', J)$ encodes the potential in a certain partial wave channel with incoming and outgoing momenta \mathbf{k} and \mathbf{k}' and $V_{S l l' J}(\mathbf{r})$ is the partial-wave decomposed potential in coordinate space.

D Fourier transformation of chiral momentum-space 3N forces

In the following, we show how to do the Fourier transformation of the chiral 3N forces which are naturally formulated in momentum space, see Sec. 2.2.5. We use some general functions in coordinate space:

$$Y(r) = \frac{\exp(-m_\pi \cdot r)}{r}, \quad (\text{D.1})$$

$$U(r) = 1 + \frac{1}{m_\pi r}, \quad (\text{D.2})$$

$$T(r) = 1 + \frac{3}{m_\pi r} + \frac{3}{(m_\pi r)^2}, \quad (\text{D.3})$$

$$S_{ij}(\mathbf{r}) = 3\boldsymbol{\sigma}_i \cdot \hat{\mathbf{r}} \boldsymbol{\sigma}_j \cdot \hat{\mathbf{r}} - \boldsymbol{\sigma}_i \cdot \boldsymbol{\sigma}_j, \quad (\text{D.4})$$

$$X_{ij}(\mathbf{r}) = \left(S_{ij}(\mathbf{r}) T(r) + \boldsymbol{\sigma}_i \cdot \boldsymbol{\sigma}_j \right) Y(r). \quad (\text{D.5})$$

D.1 Two-pion-exchange interaction V_C

D.1.1 $V_C^{c_1}$

We begin with the part $\sim c_1$ from Eqs. (2.33) and (2.32):

$$\begin{aligned} & V_C^{c_1}(\mathbf{r}_{ij}, \mathbf{r}_{kj}) \\ &= \int \frac{d^3 \mathbf{q}_i}{(2\pi)^3} \frac{d^3 \mathbf{q}_k}{(2\pi)^3} \exp(i\mathbf{q}_i \cdot \mathbf{r}_{ij}) \exp(i\mathbf{q}_k \cdot \mathbf{r}_{kj}) V_C^{c_1}(\mathbf{q}_i, \mathbf{q}_k) \\ &= -\frac{1}{2} \frac{4c_1 m_\pi^2}{f_\pi^2} \left(\frac{g_A}{2f_\pi} \right)^2 \boldsymbol{\tau}_i \cdot \boldsymbol{\tau}_k \int \frac{d^3 \mathbf{q}_i}{(2\pi)^3} \frac{\boldsymbol{\sigma}_i \cdot \mathbf{q}_i}{q_i^2 + m_\pi^2} \exp(i\mathbf{q}_i \cdot \mathbf{r}_{ij}) \int \frac{d^3 \mathbf{q}_k}{(2\pi)^3} \frac{\boldsymbol{\sigma}_k \cdot \mathbf{q}_k}{q_k^2 + m_\pi^2} \exp(i\mathbf{q}_k \cdot \mathbf{r}_{kj}). \end{aligned} \quad (\text{D.6})$$

The two integrals have an identical structure. Using greek letters for cartesian components and implicitly sum over repeated greek indices, the integrals can be evaluated as follows:

$$\begin{aligned}
& \int \frac{d^3 \mathbf{q}_i}{(2\pi)^3} \frac{\boldsymbol{\sigma}_i \cdot \mathbf{q}_i}{q_i^2 + m_\pi^2} \exp(i\mathbf{q}_i \cdot \mathbf{r}_{ij}) \\
&= -i\sigma_i^\alpha \partial^\alpha \int \frac{d^3 \mathbf{q}_i}{(2\pi)^3} \frac{1}{q_i^2 + m_\pi^2} \exp(i\mathbf{q}_i \cdot \mathbf{r}_{ij}) \\
&= -i\sigma_i^\alpha \partial^\alpha \left[\frac{1}{4\pi r_{12}} \exp(-m_\pi r_{12}) \right] \\
&= \frac{i}{4\pi} \sigma_i^\alpha \frac{x_{ij}^\alpha}{r_{ij}} \left(\frac{1}{r_{ij}^2} + \frac{m_\pi}{r_{ij}} \right) \exp(-m_\pi r_{ij}) \\
&= \frac{i}{4\pi} \boldsymbol{\sigma}_i \cdot \hat{\mathbf{r}}_{ij} m_\pi U(r_{ij}) Y(r_{ij}).
\end{aligned} \tag{D.7}$$

Inserting the integrals into Eq. (D.7) we find for the c_1 part

$$V_{C,c_1}^{ijk} = \sum_{\pi(ijk)} \frac{1}{2} \left(\frac{g_A}{2f_\pi} \right)^2 \left(\frac{m_\pi}{4\pi} \right)^2 \left(\frac{4c_1 m_\pi^2}{f_\pi^2} \right) \boldsymbol{\tau}_i \cdot \boldsymbol{\tau}_k (\boldsymbol{\sigma}_i \cdot \hat{\mathbf{r}}_{ij}) (\boldsymbol{\sigma}_k \cdot \hat{\mathbf{r}}_{kj}) U(r_{ij}) Y(r_{ij}) U(r_{kj}) Y(r_{kj}). \tag{D.8}$$

D.1.2 $V_C^{c_3}$

We now turn to the more complicated c_3 part of the 3N two-pion-exchange interaction. Its Fourier transformation is given by

$$\begin{aligned}
V_{C,c_3}(\mathbf{r}_{ij}, \mathbf{r}_{kj}) &= \int \frac{d^3 \mathbf{q}_i}{(2\pi)^3} \frac{d^3 \mathbf{q}_k}{(2\pi)^3} \exp(i\mathbf{q}_i \cdot \mathbf{r}_{ij}) \exp(i\mathbf{q}_k \cdot \mathbf{r}_{kj}) V_C^{c_3}(\mathbf{q}_i, \mathbf{q}_k) \\
&= \frac{1}{2} \left(\frac{g_A}{2f_\pi} \right)^2 \left(\frac{2c_3}{f_\pi^2} \right) \boldsymbol{\tau}_i \cdot \boldsymbol{\tau}_k \int \frac{d^3 \mathbf{q}_i}{(2\pi)^3} \frac{\boldsymbol{\sigma}_i \cdot \mathbf{q}_i}{q_i^2 + m_\pi^2} q_i^\alpha \exp(i\mathbf{q}_i \cdot \mathbf{r}_{ij}) \\
&\quad \times \int \frac{d^3 \mathbf{q}_k}{(2\pi)^3} \frac{\boldsymbol{\sigma}_k \cdot \mathbf{q}_k}{q_k^2 + m_\pi^2} q_k^\alpha \exp(i\mathbf{q}_k \cdot \mathbf{r}_{kj}).
\end{aligned} \tag{D.9}$$

The two integrals have a similar structure and are similar to the one-pion-exchange case. Thus, we find for the integral

$$\begin{aligned}
& \int \frac{d^3 \mathbf{q}}{(2\pi)^3} \frac{\boldsymbol{\sigma} \cdot \mathbf{q}}{q^2 + m_\pi^2} q^\alpha \exp(i\mathbf{q} \cdot \mathbf{r}) \\
&= -\sigma^\beta \partial^\alpha \partial^\beta \int \frac{d^3 \mathbf{q}}{(2\pi)^3} \frac{1}{q^2 + m_\pi^2} \exp(i\mathbf{q} \cdot \mathbf{r}) \\
&= -\frac{1}{4\pi} \sigma^\beta \partial^\alpha \partial^\beta \left(\frac{1}{r} \exp(-m_\pi r) \right) \\
&= -\frac{m_\pi^2}{4\pi} \sigma^\beta \left[\left(\frac{x^\alpha x^\beta}{r} - \frac{1}{3} \delta^{\alpha\beta} \right) T(r) Y(r) + \frac{1}{3} \delta^{\alpha\beta} Y(r) - \frac{1}{3} \frac{4\pi}{m_\pi^2} \delta^{\alpha\beta} \delta(\mathbf{r}) \right].
\end{aligned} \tag{D.10}$$

Inserting this integral into Eq. (D.10) we find

$$\begin{aligned}
V_{C,c_3}(\mathbf{r}_{ij}, \mathbf{r}_{kj}) &= \frac{1}{2} \left(\frac{g_A}{2f_\pi} \right)^2 \left(\frac{2c_3}{f_\pi^2} \right) \boldsymbol{\tau}_i \cdot \boldsymbol{\tau}_k \\
&\times \left(-\frac{m_\pi^2}{4\pi} \sigma_i^\beta \left[\left(\frac{x_{ij}^\alpha x_{ij}^\beta}{r_{ij} r_{ij}} - \frac{1}{3} \delta^{\alpha\beta} \right) T(r_{ij}) Y(r_{ij}) + \frac{1}{3} \delta^{\alpha\beta} Y(r_{ij}) - \frac{1}{3} \frac{4\pi}{m_\pi^2} \delta^{\alpha\beta} \delta(\mathbf{r}_{ij}) \right] \right) \\
&\times \left(-\frac{m_\pi^2}{4\pi} \sigma_k^\gamma \left[\left(\frac{x_{kj}^\alpha x_{kj}^\gamma}{r_{kj} r_{kj}} - \frac{1}{3} \delta^{\alpha\gamma} \right) T(r_{kj}) Y(r_{kj}) + \frac{1}{3} \delta^{\alpha\gamma} Y(r_{kj}) - \frac{1}{3} \frac{4\pi}{m_\pi^2} \delta^{\alpha\gamma} \delta(\mathbf{r}_{kj}) \right] \right) \\
&= \frac{1}{2} \left(\frac{g_A}{2f_\pi} \right)^2 \left(\frac{2c_3}{f_\pi^2} \right) \boldsymbol{\tau}_i \cdot \boldsymbol{\tau}_k \left(\frac{m_\pi^2}{4\pi} \right)^2 \sigma_i^\beta \sigma_k^\gamma \frac{1}{9} \left[\left(\frac{4\pi}{m_\pi^2} \right)^2 \delta^{\beta\gamma} \delta(\mathbf{r}_{ij}) \delta(\mathbf{r}_{kj}) \right. \\
&- \left[\left(3 \frac{x_{ij}^\alpha x_{ij}^\beta}{r_{ij} r_{ij}} - \delta^{\alpha\beta} \right) T(r_{ij}) Y(r_{ij}) + \delta^{\alpha\beta} Y(r_{ij}) \right] \frac{4\pi}{m_\pi^2} \delta^{\alpha\gamma} \delta(\mathbf{r}_{kj}) \\
&- \left[\left(3 \frac{x_{kj}^\alpha x_{kj}^\gamma}{r_{kj} r_{kj}} - \delta^{\alpha\gamma} \right) T(r_{kj}) Y(r_{kj}) + \delta^{\alpha\gamma} Y(r_{kj}) \right] \frac{4\pi}{m_\pi^2} \delta^{\alpha\beta} \delta(\mathbf{r}_{ij}) \\
&+ \left[\left(3 \frac{x_{ij}^\alpha x_{ij}^\beta}{r_{ij} r_{ij}} - \delta^{\alpha\beta} \right) T(r_{ij}) Y(r_{ij}) + \delta^{\alpha\beta} Y(r_{ij}) \right] \\
&\times \left. \left[\left(3 \frac{x_{kj}^\alpha x_{kj}^\gamma}{r_{kj} r_{kj}} - \delta^{\alpha\gamma} \right) T(r_{kj}) Y(r_{kj}) + \delta^{\alpha\gamma} Y(r_{kj}) \right] \right].
\end{aligned}
\tag{D.11}$$

The first term in the sum simply leads to

$$V_{C,c_3}^1 \sim \boldsymbol{\sigma}_i \cdot \boldsymbol{\sigma}_k \delta(\mathbf{r}_{ij}) \delta(\mathbf{r}_{kj}), \tag{D.12}$$

which is similar to a spin-dependent three-nucleon-contact part. Its origin is the short-range contribution of the pion-exchange interaction. The second and third term have the same structure. For the second term we find

$$\begin{aligned}
V_{C,c_3}^2 &\sim \sigma_i^\beta \sigma_k^\gamma \left[\left(3 \frac{x_{ij}^\alpha x_{ij}^\beta}{r_{ij} r_{ij}} - \delta^{\alpha\beta} \right) T(r_{ij}) Y(r_{ij}) + \delta^{\alpha\beta} Y(r_{ij}) \right] \delta^{\alpha\gamma} \delta(\mathbf{r}_{kj}) \\
&= \left[(3\sigma_i \cdot \hat{\mathbf{r}}_{ij} \sigma_k \cdot \hat{\mathbf{r}}_{ij} - \boldsymbol{\sigma}_i \cdot \boldsymbol{\sigma}_k) T(r_{ij}) Y(r_{ij}) + \boldsymbol{\sigma}_i \cdot \boldsymbol{\sigma}_k Y(r_{ij}) \right] \delta(\mathbf{r}_{kj}) \\
&= [S_{ik}(\mathbf{r}_{ij}) T(r_{ij}) Y(r_{ij}) + \boldsymbol{\sigma}_i \cdot \boldsymbol{\sigma}_k Y(r_{ij})] \delta(\mathbf{r}_{kj}) \\
&= X_{ik}(\mathbf{r}_{ij}) \delta(\mathbf{r}_{kj})
\end{aligned}
\tag{D.13}$$

The result for the third term is only different in the indices. For the last term we find

$$\begin{aligned}
V_{C,c_3}^4 &\sim \sigma_i^\beta \sigma_k^\gamma \left[\left(3 \frac{x_{ij}^\alpha x_{ij}^\beta}{r_{ij} r_{ij}} - \delta^{\alpha\beta} \right) T(r_{ij})Y(r_{ij}) + \delta^{\alpha\beta} Y(r_{ij}) \right] \\
&\times \left[\left(3 \frac{x_{kj}^\alpha x_{kj}^\gamma}{r_{kj} r_{kj}} - \delta^{\alpha\gamma} \right) T(r_{kj})Y(r_{kj}) + \delta^{\alpha\gamma} Y(r_{kj}) \right] \\
&= \sigma_i^\beta \sigma_k^\gamma \left(3 \frac{x_{ij}^\alpha x_{ij}^\beta}{r_{ij} r_{ij}} - \delta^{\alpha\beta} \right) T(r_{ij})Y(r_{ij}) \left(3 \frac{x_{kj}^\alpha x_{kj}^\gamma}{r_{kj} r_{kj}} - \delta^{\alpha\gamma} \right) T(r_{kj})Y(r_{kj}) \\
&\quad + \sigma_i^\beta \sigma_k^\gamma \delta^{\alpha\beta} Y(r_{ij}) \delta^{\alpha\gamma} Y(r_{kj}) + \sigma_i^\beta \sigma_k^\gamma \left(3 \frac{x_{ij}^\alpha x_{ij}^\beta}{r_{ij} r_{ij}} - \delta^{\alpha\beta} \right) T(r_{ij})Y(r_{ij}) \delta^{\alpha\gamma} Y(r_{kj}) \\
&\quad + \sigma_i^\beta \sigma_k^\gamma \delta^{\alpha\beta} Y(r_{ij}) \left(3 \frac{x_{kj}^\alpha x_{kj}^\gamma}{r_{kj} r_{kj}} - \delta^{\alpha\gamma} \right) T(r_{kj})Y(r_{kj}) \\
&= \left(9 \sigma_i \cdot \hat{\mathbf{r}}_{ij} \sigma_k \cdot \hat{\mathbf{r}}_{kj} \hat{\mathbf{r}}_{ij} \cdot \hat{\mathbf{r}}_{kj} - 3 \sigma_i \cdot \hat{\mathbf{r}}_{ij} \sigma_k \cdot \hat{\mathbf{r}}_{kj} - 3 \sigma_i \cdot \hat{\mathbf{r}}_{ij} \sigma_k \cdot \hat{\mathbf{r}}_{ij} + \sigma_i \cdot \sigma_k \right) T(r_{ij})Y(r_{ij})T(r_{kj})Y(r_{kj}) \\
&\quad + \sigma_i \cdot \sigma_k Y(r_{ij})Y(r_{kj}) + S_{ik}(\mathbf{r}_{ij})T(r_{ij})Y(r_{ij})Y(r_{kj}) + S_{ik}(\mathbf{r}_{kj})T(r_{kj})Y(r_{ij})Y(r_{kj}) \\
&= X_{ij}(\mathbf{r}_{ij})X_{kj}(\mathbf{r}_{kj}),
\end{aligned} \tag{D.14}$$

where we have used

$$\begin{aligned}
X_{ij}(\mathbf{r}_{ij})X_{kj}(\mathbf{r}_{kj}) &= Y(r_{ij})Y(r_{kj}) \left(S_{ij}(\mathbf{r}_{ij})T(r_{ij}) + \sigma_i \cdot \sigma_j \right) \left(S_{kj}(\mathbf{r}_{kj})T(r_{kj}) + \sigma_k \cdot \sigma_j \right) \\
&= Y(r_{ij})Y(r_{kj}) \left[S_{ij}(\mathbf{r}_{ij})T(r_{ij})\sigma_k \cdot \sigma_j + \sigma_i \cdot \sigma_j \sigma_k \cdot \sigma_j \right. \\
&\quad \left. + \sigma_i \cdot \sigma_j S_{kj}(\mathbf{r}_{kj})T(r_{kj}) + S_{ij}(\mathbf{r}_{ij})S_{kj}(\mathbf{r}_{kj})T(r_{ij})T(r_{kj}) \right].
\end{aligned} \tag{D.15}$$

For the individual products involving the spin matrices we find

$$\sigma_i \cdot \sigma_j \sigma_k \cdot \sigma_j = \sigma_i^\alpha \sigma_k^\beta \sigma_j^\alpha \sigma_j^\beta = \sigma_i^\alpha \sigma_k^\beta (\delta^{\alpha\beta} + i \epsilon^{\alpha\beta\gamma} \sigma_j^\gamma) = \sigma_i \cdot \sigma_k + i \sigma_i \cdot (\sigma_k \times \sigma_j) \tag{D.16}$$

$$\begin{aligned}
S_{ij}(\mathbf{r}_{ij})\sigma_k \cdot \sigma_j &= \left(3 \sigma_i \cdot \hat{\mathbf{r}}_{ij} \sigma_j \cdot \hat{\mathbf{r}}_{ij} - \sigma_i \cdot \sigma_j \right) \sigma_k \cdot \sigma_j \\
&= \left(3 \sigma_i \cdot \hat{\mathbf{r}}_{ij} \sigma_k \cdot \hat{\mathbf{r}}_{ij} + 3i \sigma_i \cdot \hat{\mathbf{r}}_{ij} \hat{\mathbf{r}}_{ij} \cdot (\sigma_k \times \sigma_j) - \sigma_i \cdot \sigma_k - i \sigma_i \cdot (\sigma_k \times \sigma_j) \right) \\
&= S_{ik}(\mathbf{r}_{ij}) + i \left(3 \sigma_i \cdot \hat{\mathbf{r}}_{ij} \hat{\mathbf{r}}_{ij} \cdot (\sigma_k \times \sigma_j) - \sigma_i \cdot (\sigma_k \times \sigma_j) \right)
\end{aligned} \tag{D.17}$$

$$\sigma_i \cdot \sigma_j S_{kj}(\mathbf{r}_{kj}) = S_{ik}(\mathbf{r}_{kj}) + i \left(3 \sigma_k \cdot \hat{\mathbf{r}}_{kj} \hat{\mathbf{r}}_{kj} \cdot (\sigma_j \times \sigma_i) - \sigma_i \cdot (\sigma_k \times \sigma_j) \right) \tag{D.18}$$

$$\begin{aligned}
S_{ij}(\mathbf{r}_{ij})S_{ik}(\mathbf{r}_{ij}) &= \left(3 \sigma_i \cdot \hat{\mathbf{r}}_{ij} \sigma_j \cdot \hat{\mathbf{r}}_{ij} - \sigma_i \cdot \sigma_j \right) \left(3 \sigma_k \cdot \hat{\mathbf{r}}_{kj} \sigma_j \cdot \hat{\mathbf{r}}_{kj} - \sigma_k \cdot \sigma_j \right) \\
&= \left(9 \sigma_i \cdot \hat{\mathbf{r}}_{ij} \sigma_k \cdot \hat{\mathbf{r}}_{kj} (\hat{\mathbf{r}}_{ij} \cdot \hat{\mathbf{r}}_{kj} + i \sigma_j \cdot (\hat{\mathbf{r}}_{ij} \times \hat{\mathbf{r}}_{kj})) - 3 \sigma_k \cdot \hat{\mathbf{r}}_{kj} (\sigma_i \cdot \hat{\mathbf{r}}_{kj} + i \hat{\mathbf{r}}_{kj} \cdot (\sigma_j \times \sigma_i)) \right. \\
&\quad \left. - 3 \sigma_i \cdot \hat{\mathbf{r}}_{ij} (\sigma_k \cdot \hat{\mathbf{r}}_{ij} + i \hat{\mathbf{r}}_{ij} \cdot (\sigma_k \times \sigma_j)) + \sigma_i \cdot \sigma_k + i \sigma_i \cdot (\sigma_k \times \sigma_j) \right).
\end{aligned} \tag{D.19}$$

For the full three body force we have to sum over all permutations of the particle indices i, j and k . This will also lead to a term in the sum with $X_{kj}(\mathbf{r}_{kj})X_{ij}(\mathbf{r}_{ij})$. The cross products in this

term will have the opposite sign as the cross products in Eqs. (D.16)-(D.19), leading to the cancellation of all appearing cross products, which, thus, can be neglected. This was used in the last step of Eq. (D.14).

Putting everything together we find for the contribution $\sim c_3$

$$V_{C,c_3}^{ijk} = \sum_{\pi(ijk)} \frac{1}{2} \left(\frac{g_A}{2f_\pi} \right)^2 \left(\frac{2c_3}{f_\pi^2} \right) \boldsymbol{\tau}_i \cdot \boldsymbol{\tau}_k \left(\frac{m_\pi^2}{4\pi} \right)^2 \frac{1}{9} \left[\left(\frac{4\pi}{m_\pi^2} \right)^2 \boldsymbol{\sigma}_i \cdot \boldsymbol{\sigma}_k \delta(\mathbf{r}_{ij}) \delta(\mathbf{r}_{kj}) - \frac{4\pi}{m_\pi^2} X_{ik}(\mathbf{r}_{ij}) \delta(\mathbf{r}_{kj}) - \frac{4\pi}{m_\pi^2} X_{ik}(\mathbf{r}_{kj}) \delta(\mathbf{r}_{ij}) + X_{ij}(\mathbf{r}_{ij}) X_{kj}(\mathbf{r}_{kj}) \right].$$

D.1.3 $V_C^{c_4}$

We now turn to the last part $\sim c_4$ of the 3N two-pion-exchange interaction. Its Fourier transformation is given by

$$\begin{aligned} V_{C,c_4}(\mathbf{r}_{ij}, \mathbf{r}_{kj}) &= \int \frac{d^3 \mathbf{q}_i}{(2\pi)^3} \frac{d^3 \mathbf{q}_k}{(2\pi)^3} \exp(i\mathbf{q}_i \cdot \mathbf{r}_{ij}) \exp(i\mathbf{q}_k \cdot \mathbf{r}_{kj}) V_C^{c_4}(\mathbf{q}_i, \mathbf{q}_k) \\ &= \frac{1}{2} \left(\frac{g_A}{2f_\pi} \right)^2 \frac{c_4}{f_\pi^2} \boldsymbol{\tau}_i \cdot (\boldsymbol{\tau}_k \times \boldsymbol{\tau}_j) \epsilon^{abc} \sigma_2^a \int \frac{d^3 \mathbf{q}_i}{(2\pi)^3} \frac{\boldsymbol{\sigma}_i \cdot \mathbf{q}_i}{q_i^2 + m_\pi^2} \mathbf{q}_i^b \exp(i\mathbf{q}_i \cdot \mathbf{r}_{ij}) \\ &\quad \times \int \frac{d^3 \mathbf{q}_k}{(2\pi)^3} \frac{\boldsymbol{\sigma}_k \cdot \mathbf{q}_k}{q_k^2 + m_\pi^2} \mathbf{q}_k^c \exp(i\mathbf{q}_k \cdot \mathbf{r}_{kj}) \\ &= \frac{1}{9} \frac{1}{2} \left(\frac{g_A}{2f_\pi} \right)^2 \frac{c_4}{f_\pi^2} \boldsymbol{\tau}_i \cdot (\boldsymbol{\tau}_k \times \boldsymbol{\tau}_j) \left(\frac{m_\pi^2}{4\pi} \right)^2 \epsilon^{abc} \sigma_i^a \sigma_j^a \sigma_k^\beta \\ &\quad \times \left[\left(\frac{4\pi}{m_\pi^2} \right)^2 \delta^{ab} \delta^{\beta c} \delta(\mathbf{r}_{ij}) \delta(\mathbf{r}_{kj}) \right. \\ &\quad - \left[\left(3 \frac{x_{ij}^a x_{ij}^b}{r_{ij} r_{ij}} - \delta^{ab} \right) T(r_{ij}) Y(r_{ij}) + \delta^{ab} Y(r_{ij}) \right] \frac{4\pi}{m_\pi^2} \delta^{\beta c} \delta(\mathbf{r}_{kj}) \\ &\quad - \left[\left(3 \frac{x_{kj}^\beta x_{kj}^c}{r_{kj} r_{kj}} - \delta^{\beta c} \right) T(r_{kj}) Y(r_{kj}) + \delta^{\beta c} Y(r_{kj}) \right] \frac{4\pi}{m_\pi^2} \delta^{ab} \delta(\mathbf{r}_{ij}) \\ &\quad + \left[\left(3 \frac{x_{ij}^a x_{ij}^b}{r_{ij} r_{ij}} - \delta^{ab} \right) T(r_{ij}) Y(r_{ij}) + \delta^{ab} Y(r_{ij}) \right] \\ &\quad \left. \times \left[\left(3 \frac{x_{kj}^\beta x_{kj}^c}{r_{kj} r_{kj}} - \delta^{\beta c} \right) T(r_{kj}) Y(r_{kj}) + \delta^{\beta c} Y(r_{kj}) \right] \right] \end{aligned} \quad (\text{D.20})$$

We again look at the individual terms and find for the first term

$$\epsilon^{abc} \sigma_i^a \sigma_j^a \sigma_k^\beta \left(\frac{4\pi}{m_\pi^2} \right)^2 \delta^{ab} \delta^{\beta c} \delta(\mathbf{r}_{ij}) \delta(\mathbf{r}_{kj}) = \boldsymbol{\sigma}_i \cdot (\boldsymbol{\sigma}_k \times \boldsymbol{\sigma}_j) \left(\frac{4\pi}{m_\pi^2} \right)^2 \delta(\mathbf{r}_{ij}) \delta(\mathbf{r}_{kj}). \quad (\text{D.21})$$

For the second and third term we find the expressions

$$\begin{aligned}
& -\epsilon^{abc}\sigma_i^\alpha\sigma_j^a\sigma_k^\beta\left[\left(3\frac{x_{ij}^\alpha x_{ij}^b}{r_{ij}r_{ij}}-\delta^{ab}\right)T(r_{ij})Y(r_{ij})+\delta^{ab}Y(r_{ij})\right]\frac{4\pi}{m_\pi^2}\delta^{\beta c}\delta(\mathbf{r}_{kj}) \quad (\text{D.22}) \\
& = -\left[\epsilon^{abc}\sigma_i^\alpha\sigma_j^a\sigma_k^\beta 3\frac{x_{ij}^\alpha x_{ij}^b}{r_{ij}r_{ij}}T(r_{ij})Y(r_{ij})+\boldsymbol{\sigma}_i\cdot(\boldsymbol{\sigma}_k\times\boldsymbol{\sigma}_j)(1-T(r_{ij}))Y(r_{ij})\right]\frac{4\pi}{m_\pi^2}\delta(\mathbf{r}_{kj}) \\
& = -\frac{12\pi}{m_\pi^2}\boldsymbol{\sigma}_i\cdot\hat{\mathbf{r}}_{ij}\hat{\mathbf{r}}_{ij}\cdot(\boldsymbol{\sigma}_k\times\boldsymbol{\sigma}_j)T(r_{ij})Y(r_{ij})\delta(\mathbf{r}_{kj})-\frac{4\pi}{m_\pi^2}\boldsymbol{\sigma}_i\cdot(\boldsymbol{\sigma}_k\times\boldsymbol{\sigma}_j)(1-T(r_{ij}))Y(r_{ij})\delta(\mathbf{r}_{kj}) \\
& \quad -\epsilon^{abc}\sigma_i^\alpha\sigma_j^a\sigma_k^\beta\left[\left(3\frac{x_{kj}^\beta x_{kj}^c}{r_{kj}r_{kj}}-\delta^{\beta c}\right)T(r_{kj})Y(r_{kj})+\delta^{\beta c}Y(r_{kj})\right]\frac{4\pi}{m_\pi^2}\delta^{ab}\delta(\mathbf{r}_{ij}) \\
& = -\frac{12\pi}{m_\pi^2}\boldsymbol{\sigma}_k\cdot\hat{\mathbf{r}}_{kj}\hat{\mathbf{r}}_{kj}\cdot(\boldsymbol{\sigma}_j\times\boldsymbol{\sigma}_i)T(r_{kj})Y(r_{kj})\delta(\mathbf{r}_{ij})-\frac{4\pi}{m_\pi^2}\boldsymbol{\sigma}_i\cdot(\boldsymbol{\sigma}_k\times\boldsymbol{\sigma}_j)(1-T(r_{kj}))Y(r_{kj})\delta(\mathbf{r}_{ij}).
\end{aligned}$$

For the last term we obtain the following result:

$$\begin{aligned}
& \epsilon^{abc}\sigma_i^\alpha\sigma_j^a\sigma_k^\beta\left[\left(3\frac{x_{ij}^\alpha x_{ij}^b}{r_{ij}r_{ij}}-\delta^{ab}\right)T(r_{ij})Y(r_{ij})+\delta^{ab}Y(r_{ij})\right] \quad (\text{D.23}) \\
& \quad \times\left[\left(3\frac{x_{kj}^\beta x_{kj}^c}{r_{kj}r_{kj}}-\delta^{\beta c}\right)T(r_{kj})Y(r_{kj})+\delta^{\beta c}Y(r_{kj})\right] \\
& = 9\boldsymbol{\sigma}_i\cdot\hat{\mathbf{r}}_{ij}\boldsymbol{\sigma}_i\cdot\hat{\mathbf{r}}_{kj}\boldsymbol{\sigma}_j\cdot(\hat{\mathbf{r}}_{ij}\times\hat{\mathbf{r}}_{kj})T(r_{ij})Y(r_{ij})T(r_{kj})Y(r_{kj}) \\
& \quad + 3\boldsymbol{\sigma}_i\cdot\hat{\mathbf{r}}_{ij}\hat{\mathbf{r}}_{ij}\cdot(\boldsymbol{\sigma}_k\times\boldsymbol{\sigma}_j)T(r_{ij})Y(r_{ij})(1-T(r_{kj}))Y(r_{kj}) \\
& \quad + 3\boldsymbol{\sigma}_k\cdot\hat{\mathbf{r}}_{kj}\hat{\mathbf{r}}_{kj}\cdot(\boldsymbol{\sigma}_j\times\boldsymbol{\sigma}_i)T(r_{kj})Y(r_{kj})(1-T(r_{ij}))Y(r_{ij}) \\
& \quad + \boldsymbol{\sigma}_j\cdot(\boldsymbol{\sigma}_i\times\boldsymbol{\sigma}_k)(1-T(r_{ij}))(1-T(r_{kj}))Y(r_{ij})Y(r_{kj})
\end{aligned}$$

The final contribution is, thus,

$$\begin{aligned}
V_{C,c_4} & = \sum_{\pi(ijk)} \frac{1}{9} \frac{1}{2} \left(\frac{g_A}{2f_\pi}\right)^2 \frac{c_4}{f_\pi^2} \boldsymbol{\tau}_i\cdot(\boldsymbol{\tau}_k\times\boldsymbol{\tau}_j) \left(\frac{m_\pi^2}{4\pi}\right)^2 \quad (\text{D.24}) \\
& \quad \times \left[\left(\frac{4\pi}{m_\pi^2}\right)^2 \boldsymbol{\sigma}_i\cdot(\boldsymbol{\sigma}_k\times\boldsymbol{\sigma}_j)\delta(\mathbf{r}_{ij})\delta(\mathbf{r}_{kj}) \right. \\
& \quad - \frac{4\pi}{m_\pi^2}\boldsymbol{\sigma}_i\cdot(\boldsymbol{\sigma}_k\times\boldsymbol{\sigma}_j)(1-T(r_{ij}))Y(r_{ij})\delta(\mathbf{r}_{kj}) - \frac{12\pi}{m_\pi^2}\boldsymbol{\sigma}_i\cdot\hat{\mathbf{r}}_{ij}\hat{\mathbf{r}}_{ij}\cdot(\boldsymbol{\sigma}_k\times\boldsymbol{\sigma}_j)T(r_{ij})Y(r_{ij})\delta(\mathbf{r}_{kj}) \\
& \quad - \frac{4\pi}{m_\pi^2}\boldsymbol{\sigma}_i\cdot(\boldsymbol{\sigma}_k\times\boldsymbol{\sigma}_j)(1-T(r_{kj}))Y(r_{kj})\delta(\mathbf{r}_{ij}) - \frac{12\pi}{m_\pi^2}\boldsymbol{\sigma}_k\cdot\hat{\mathbf{r}}_{kj}\hat{\mathbf{r}}_{kj}\cdot(\boldsymbol{\sigma}_j\times\boldsymbol{\sigma}_i)T(r_{kj})Y(r_{kj})\delta(\mathbf{r}_{ij}) \\
& \quad + 9\boldsymbol{\sigma}_i\cdot\hat{\mathbf{r}}_{ij}\boldsymbol{\sigma}_k\cdot\hat{\mathbf{r}}_{kj}\boldsymbol{\sigma}_j\cdot(\hat{\mathbf{r}}_{ij}\times\hat{\mathbf{r}}_{kj})T(r_{ij})T(r_{kj})Y(r_{ij})Y(r_{kj}) \\
& \quad + 3\boldsymbol{\sigma}_i\cdot\hat{\mathbf{r}}_{ij}\hat{\mathbf{r}}_{ij}\cdot(\boldsymbol{\sigma}_k\times\boldsymbol{\sigma}_j)T(r_{ij})(1-T(r_{kj}))Y(r_{ij})Y(r_{kj}) \\
& \quad + 3\boldsymbol{\sigma}_k\cdot\hat{\mathbf{r}}_{kj}\hat{\mathbf{r}}_{kj}\cdot(\boldsymbol{\sigma}_j\times\boldsymbol{\sigma}_i)T(r_{kj})(1-T(r_{ij}))Y(r_{ij})Y(r_{kj}) \\
& \quad \left. + \boldsymbol{\sigma}_j\cdot(\boldsymbol{\sigma}_i\times\boldsymbol{\sigma}_k)(1-T(r_{ij}))(1-T(r_{kj}))Y(r_{ij})Y(r_{kj})\right].
\end{aligned}$$

Making use of Eqs. (D.15)-(D.19) we calculate $[X_{ij}(\mathbf{r}_{ij}), X_{kj}(\mathbf{r}_{kj})]$ and find

$$\begin{aligned}
& [X_{ij}(\mathbf{r}_{ij}), X_{kj}(\mathbf{r}_{kj})] \\
&= 2Y(r_{ij})Y(r_{kj})i\boldsymbol{\sigma}_i \cdot (\boldsymbol{\sigma}_k \times \boldsymbol{\sigma}_j) \\
&\quad + 2Y(r_{ij})Y(r_{kj})T(r_{ij}) \left(3i\boldsymbol{\sigma}_i \cdot \hat{\mathbf{r}}_{ij}\hat{\mathbf{r}}_{ij} \cdot (\boldsymbol{\sigma}_k \times \boldsymbol{\sigma}_j) - i\boldsymbol{\sigma}_i \cdot (\boldsymbol{\sigma}_k \times \boldsymbol{\sigma}_j) \right) \\
&\quad + 2Y(r_{ij})Y(r_{kj})T(r_{kj}) \left(3i\boldsymbol{\sigma}_k \cdot \hat{\mathbf{r}}_{kj}\hat{\mathbf{r}}_{kj} \cdot (\boldsymbol{\sigma}_j \times \boldsymbol{\sigma}_i) - i\boldsymbol{\sigma}_i \cdot (\boldsymbol{\sigma}_k \times \boldsymbol{\sigma}_j) \right) \\
&\quad + 2Y(r_{ij})Y(r_{kj})T(r_{ij})T(r_{kj}) \left(9i\boldsymbol{\sigma}_i \cdot \hat{\mathbf{r}}_{ij}\boldsymbol{\sigma}_k \cdot \hat{\mathbf{r}}_{kj}\boldsymbol{\sigma}_j \cdot (\hat{\mathbf{r}}_{ij} \times \hat{\mathbf{r}}_{kj}) - 3i\boldsymbol{\sigma}_i \cdot \hat{\mathbf{r}}_{ij}\hat{\mathbf{r}}_{ij} \cdot (\boldsymbol{\sigma}_k \times \boldsymbol{\sigma}_j) \right. \\
&\quad \left. - 3i\boldsymbol{\sigma}_k \cdot \hat{\mathbf{r}}_{kj}\hat{\mathbf{r}}_{kj} \cdot (\boldsymbol{\sigma}_j \times \boldsymbol{\sigma}_i) + i\boldsymbol{\sigma}_i \cdot (\boldsymbol{\sigma}_k \times \boldsymbol{\sigma}_j) \right).
\end{aligned} \tag{D.25}$$

Putting everything together, we find for the c_4 part

$$\begin{aligned}
V_{C,c_4}^{ijk} &= \sum_{\pi(ijk)} \frac{1}{9} \frac{1}{2} \left(\frac{g_A}{2f_\pi} \right)^2 \frac{c_4}{f_\pi^2} \boldsymbol{\tau}_i \cdot (\boldsymbol{\tau}_k \times \boldsymbol{\tau}_j) \left(\frac{m_\pi^2}{4\pi} \right)^2 \\
&\quad \times \left[\left(\frac{4\pi}{m_\pi^2} \right)^2 \boldsymbol{\sigma}_i \cdot (\boldsymbol{\sigma}_k \times \boldsymbol{\sigma}_j) \delta(\mathbf{r}_{ij})\delta(\mathbf{r}_{kj}) \right. \\
&\quad - \frac{4\pi}{m_\pi^2} \boldsymbol{\sigma}_i \cdot (\boldsymbol{\sigma}_k \times \boldsymbol{\sigma}_j) (1 - T(r_{ij})) Y(r_{ij})\delta(\mathbf{r}_{kj}) - \frac{12\pi}{m_\pi^2} \boldsymbol{\sigma}_i \cdot \hat{\mathbf{r}}_{ij}\hat{\mathbf{r}}_{ij} \cdot (\boldsymbol{\sigma}_k \times \boldsymbol{\sigma}_j) T(r_{ij})Y(r_{ij})\delta(\mathbf{r}_{kj}) \\
&\quad - \frac{4\pi}{m_\pi^2} \boldsymbol{\sigma}_i \cdot (\boldsymbol{\sigma}_k \times \boldsymbol{\sigma}_j) (1 - T(r_{kj})) Y(r_{kj})\delta(\mathbf{r}_{ij}) - \frac{12\pi}{m_\pi^2} \boldsymbol{\sigma}_k \cdot \hat{\mathbf{r}}_{kj}\hat{\mathbf{r}}_{kj} \cdot (\boldsymbol{\sigma}_j \times \boldsymbol{\sigma}_i) T(r_{kj})Y(r_{kj})\delta(\mathbf{r}_{ij}) \\
&\quad \left. + \frac{1}{2i} [X_{ij}(\mathbf{r}_{ij}), X_{kj}(\mathbf{r}_{kj})] \right].
\end{aligned}$$

D.2 One-pion-exchange–contact interaction V_D

Next, we transform the one-pion-exchange–contact interaction V_D :

$$\begin{aligned}
V_D(\mathbf{r}_{ij}, \mathbf{r}_{kj}) &= \int \frac{d^3\mathbf{q}_i}{(2\pi)^3} \frac{d^3\mathbf{q}_k}{(2\pi)^3} \exp(i\mathbf{q}_i \cdot \mathbf{r}_{ij}) \exp(i\mathbf{q}_k \cdot \mathbf{r}_{kj}) V_D(\mathbf{q}_i, \mathbf{q}_k) \\
&= -\frac{g_A}{8f_\pi^2} \frac{c_D}{f_\pi^2 \Lambda_\chi} \boldsymbol{\tau}_i \cdot \boldsymbol{\tau}_k \int \frac{d^3\mathbf{q}_i}{(2\pi)^3} \exp(i\mathbf{q}_i \cdot \mathbf{r}_{ij}) \int \frac{d^3\mathbf{q}_k}{(2\pi)^3} \frac{\boldsymbol{\sigma}_k \cdot \mathbf{q}_k \boldsymbol{\sigma}_i \cdot \mathbf{q}_k}{q_k^2 + m_\pi^2} \exp(i\mathbf{q}_k \cdot \mathbf{r}_{kj}).
\end{aligned} \tag{D.26}$$

The first integral will lead to a δ function, while for the second integral we find analogue to the one-pion-exchange case:

$$\begin{aligned}
& \int \frac{d^3\mathbf{q}}{(2\pi)^3} \frac{\boldsymbol{\sigma}_k \cdot \mathbf{q} \boldsymbol{\sigma}_i \cdot \mathbf{q}}{q^2 + m_\pi^2} \exp(i\mathbf{q} \cdot \mathbf{r}) \\
&= -\frac{m_\pi^2}{12\pi} Y(r) T(r) S_{ik}(\mathbf{r}) - \frac{m_\pi^2}{12\pi} Y(r) \boldsymbol{\sigma}_i \cdot \boldsymbol{\sigma}_k + \frac{1}{3} \delta(\mathbf{r}) \boldsymbol{\sigma}_i \cdot \boldsymbol{\sigma}_k \\
&= -\frac{m_\pi^2}{12\pi} X_{ik}(\mathbf{r}) + \frac{1}{3} \delta(\mathbf{r}) \boldsymbol{\sigma}_i \cdot \boldsymbol{\sigma}_k.
\end{aligned} \tag{D.27}$$

Inserting the integrals, we find for V_D

$$\begin{aligned}
V_D(\mathbf{r}_{ij}, \mathbf{r}_{kj}) &= -\frac{g_A}{8f_\pi^2} \frac{c_D}{f_\pi^2 \Lambda_\chi} \boldsymbol{\tau}_i \cdot \boldsymbol{\tau}_k \int \frac{d^3 \mathbf{q}_i}{(2\pi)^3} \exp(i\mathbf{q}_i \cdot \mathbf{r}_{ij}) \int \frac{d^3 \mathbf{q}_k}{(2\pi)^3} \frac{\boldsymbol{\sigma}_k \cdot \mathbf{q}_k \boldsymbol{\sigma}_i \cdot \mathbf{q}_k}{q_k^2 + m_\pi^2} \exp(i\mathbf{q}_k \cdot \mathbf{r}_{kj}) \\
&= -\frac{g_A}{8f_\pi^2} \frac{c_D}{f_\pi^2 \Lambda_\chi} \boldsymbol{\tau}_i \cdot \boldsymbol{\tau}_k \delta(\mathbf{r}_{ij}) \left(-\frac{m_\pi^2}{12\pi} X_{ik}(\mathbf{r}_{kj}) + \frac{1}{3} \delta(\mathbf{r}_{kj}) \boldsymbol{\sigma}_i \cdot \boldsymbol{\sigma}_k \right).
\end{aligned} \tag{D.28}$$

E Fourier transformation of local coordinate-space 3N forces to momentum space

In the following Section we present the Fourier transformation of the regularized coordinate expressions for the local 3N forces back to momentum space for neutron matter to use in our MBPT machinery. We begin with the V_E -like part of V_C :

$$V_{C,c_3,V_E}^{ijk} = \sum_{\pi(ijk)} \frac{1}{2} \left(\frac{g_A}{2f_\pi} \right)^2 \left(\frac{2c_3}{f_\pi^2} \right) \frac{1}{9} \sigma_i \cdot \sigma_k \delta(\mathbf{r}_{ij}) \delta(\mathbf{r}_{kj}). \quad (\text{E.1})$$

Fourier transformation to momentum space leads to

$$\begin{aligned} V_{C,c_3,V_E,MS}^{ijk} &= \sum_{\pi(ijk)} \frac{1}{2} \left(\frac{g_A}{2f_\pi} \right)^2 \left(\frac{2c_3}{f_\pi^2} \right) \frac{1}{9} \sigma_i \cdot \sigma_k \int d\mathbf{r}_{ij} \int d\mathbf{r}_{kj} e^{i\mathbf{q}_i \cdot \mathbf{r}_{ij}} e^{i\mathbf{q}_k \cdot \mathbf{r}_{kj}} \delta(\mathbf{r}_{ij}) \delta(\mathbf{r}_{kj}) \\ &= \sum_{\pi(ijk)} \frac{g_A^2}{4f_\pi^4} \frac{c_3}{9} \sigma_i \cdot \sigma_k \int d\mathbf{r}_{ij} e^{i\mathbf{q}_i \cdot \mathbf{r}_{ij}} \delta(\mathbf{r}_{ij}) \int d\mathbf{r}_{kj} e^{i\mathbf{q}_k \cdot \mathbf{r}_{kj}} \delta(\mathbf{r}_{kj}), \end{aligned} \quad (\text{E.2})$$

where the integral

$$\int d\mathbf{r} e^{i\mathbf{q} \cdot \mathbf{r}} \delta(\mathbf{r}) = 2\pi \frac{1}{\pi \Gamma(3/4) R_0^3} \int dr r^2 \frac{2 \sin(q r)}{q r} e^{-r^4/R_0^4} = 4\pi F_{\text{cont}}(q, R_0) \quad (\text{E.3})$$

is the Fourier transformed regularized contact interaction and will be evaluated numerically. Putting everything together, we get

$$V_{C,c_3,V_E,MS}^{ijk} = \sum_{\pi(ijk)} (4\pi)^2 \frac{g_A^2}{4f_\pi^4} \frac{c_3}{9} \sigma_i \cdot \sigma_k F_{\text{cont}}(q_i, R_0) F_{\text{cont}}(q_k, R_0). \quad (\text{E.4})$$

The Fourier transformation of V_E can be performed analogous.

We will now turn to the V_D -like part of V_C . In coordinate space, it is given by

$$V_{C,c_3,V_D}^{ijk} = - \sum_{\pi(ijk)} \frac{g_A^2}{4f_\pi^4} \frac{m_\pi^2}{4\pi} \frac{c_3}{9} \left[X_{ik}(\mathbf{r}_{ij}) \delta(\mathbf{r}_{kj}) + X_{ik}(\mathbf{r}_{kj}) \delta(\mathbf{r}_{ij}) \right], \quad (\text{E.5})$$

when we use our convention for the spin-isospin structure. For the Fourier transformation we find

$$\begin{aligned}
V_{C,c_3,V_D,MS}^{ijk} &= - \sum_{\pi(ijk)} \frac{g_A^2 m_\pi^2 c_3}{4f_\pi^4 4\pi 9} \int d\mathbf{r}_{ij} \int d\mathbf{r}_{kj} e^{i\mathbf{q}_i \cdot \mathbf{r}_{ij}} e^{i\mathbf{q}_k \cdot \mathbf{r}_{kj}} [X_{ik}(\mathbf{r}_{ij})\delta(\mathbf{r}_{kj}) + X_{ik}(\mathbf{r}_{kj})\delta(\mathbf{r}_{ij})] \\
&= - \sum_{\pi(ijk)} \frac{g_A^2 m_\pi^2 c_3}{4f_\pi^4 4\pi 9} \left[4\pi F_{\text{cont}}(q_k, R_0) \int d\mathbf{r}_{ij} e^{i\mathbf{q}_i \cdot \mathbf{r}_{ij}} X_{ik}(\mathbf{r}_{ij}) \right. \\
&\quad \left. + 4\pi F_{\text{cont}}(q_i, R_0) \int d\mathbf{r}_{kj} e^{i\mathbf{q}_k \cdot \mathbf{r}_{kj}} X_{ik}(\mathbf{r}_{kj}) \right]. \tag{E.6}
\end{aligned}$$

The appearing integral can be separated in two parts

$$\begin{aligned}
&\int d\mathbf{r}_{ij} e^{i\mathbf{q}_i \cdot \mathbf{r}_{ij}} X_{ik}(\mathbf{r}_{ij}) \tag{E.7} \\
&= \int d\mathbf{r}_{ij} e^{i\mathbf{q}_i \cdot \mathbf{r}_{ij}} \left(S_{ik}(\mathbf{r}_{ij}) T(r_{ij}) + \boldsymbol{\sigma}_i \cdot \boldsymbol{\sigma}_k \right) Y(r_{ij}) \left(1 - e^{-\left(\frac{r_{ij}}{R_0}\right)^4} \right) \\
&= \int d\mathbf{r}_{ij} e^{i\mathbf{q}_i \cdot \mathbf{r}_{ij}} S_{ik}(\mathbf{r}_{ij}) T(r_{ij}) Y(r_{ij}) \left(1 - e^{-\left(\frac{r_{ij}}{R_0}\right)^4} \right) + \boldsymbol{\sigma}_i \cdot \boldsymbol{\sigma}_k \int d\mathbf{r}_{ij} e^{i\mathbf{q}_i \cdot \mathbf{r}_{ij}} Y(r_{ij}) \left(1 - e^{-\left(\frac{r_{ij}}{R_0}\right)^4} \right).
\end{aligned}$$

The first integral can be solved like

$$\begin{aligned}
&\int d\mathbf{r}_{ij} e^{i\mathbf{q}_i \cdot \mathbf{r}_{ij}} S_{ik}(\mathbf{r}_{ij}) T(r_{ij}) Y(r_{ij}) \left(1 - e^{-\left(\frac{r_{ij}}{R_0}\right)^4} \right) \tag{E.8} \\
&= \sum_{\alpha\beta} \sigma_i^\alpha \sigma_k^\beta \int d\mathbf{r}_{ij} e^{i\mathbf{q}_i \cdot \mathbf{r}_{ij}} \left(3\hat{r}_{ij}^\alpha \hat{r}_{ij}^\beta - \delta^{\alpha\beta} \right) T(r_{ij}) Y(r_{ij}) \left(1 - e^{-\left(\frac{r_{ij}}{R_0}\right)^4} \right).
\end{aligned}$$

The part $\left(3\hat{r}_{ij}^\alpha \hat{r}_{ij}^\beta - \delta^{\alpha\beta} \right)$ can be expressed as a sum of spherical harmonics $\sum_{lm} c_{lm}^{\alpha\beta} Y_{lm}$ where contributions with $l \neq 2$ vanish. The function $e^{i\mathbf{q}_i \cdot \mathbf{r}_{ij}}$ can be rewritten using Eq. (C.5). We find

$$\begin{aligned}
&\sum_{\alpha\beta} \sigma_i^\alpha \sigma_k^\beta \int d\mathbf{r}_{ij} e^{i\mathbf{q}_i \cdot \mathbf{r}_{ij}} \left(3\hat{r}_{ij}^\alpha \hat{r}_{ij}^\beta - \delta^{\alpha\beta} \right) T(r_{ij}) Y(r_{ij}) \left(1 - e^{-\left(\frac{r_{ij}}{R_0}\right)^4} \right) \tag{E.9} \\
&= 4\pi \sum_{\alpha\beta} \sum_{lm} \sum_{l'm'} i^{l'} c_{lm}^{\alpha\beta} Y_{l'm'}(\Omega_{\mathbf{q}_i}) \sigma_i^\alpha \sigma_k^\beta \int dr_{ij} r_{ij}^2 j_{l'}(q_i r_{ij}) T(r_{ij}) Y(r_{ij}) \left(1 - e^{-\left(\frac{r_{ij}}{R_0}\right)^4} \right) \\
&\quad \times \int d\cos(\theta) d\phi Y_{l'm'}^*(\Omega_{\mathbf{r}_{ij}}) Y_{lm}(\Omega_{\mathbf{r}_{ij}}).
\end{aligned}$$

Using the orthonormality of the spherical harmonics and $l = 2$, we finally get

$$\begin{aligned}
& \int d\mathbf{r}_{ij} e^{i\mathbf{q}_i \cdot \mathbf{r}_{ij}} S_{ik}(\mathbf{r}_{ij}) T(r_{ij}) Y(r_{ij}) \left(1 - e^{-\left(\frac{r_{ij}}{R_0}\right)^4}\right) \\
&= 4\pi \sum_{\alpha\beta} \sum_{lm} \sum_{l'm'} i^{l'} c_{lm}^{\alpha\beta} Y_{l'm'}(\Omega_{\mathbf{q}_i}) \sigma_i^\alpha \sigma_k^\beta \int dr_{ij} r_{ij}^2 j_{l'}(q_i r_{ij}) T(r_{ij}) Y(r_{ij}) \left(1 - e^{-\left(\frac{r_{ij}}{R_0}\right)^4}\right) \delta_{ll'} \delta_{mm'} \\
&= -4\pi \sum_{\alpha\beta} \left(3\hat{q}_i^\alpha \hat{q}_i^\beta - \delta^{\alpha\beta}\right) \sigma_i^\alpha \sigma_k^\beta \int dr_{ij} r_{ij}^2 j_2(q_i r_{ij}) T(r_{ij}) Y(r_{ij}) \left(1 - e^{-\left(\frac{r_{ij}}{R_0}\right)^4}\right) \\
&= -4\pi (3\boldsymbol{\sigma}_i \cdot \hat{\mathbf{q}}_i \boldsymbol{\sigma}_k \cdot \hat{\mathbf{q}}_i - \boldsymbol{\sigma}_i \cdot \boldsymbol{\sigma}_k) F_S(q, R_0).
\end{aligned} \tag{E.10}$$

The second integral gives

$$\begin{aligned}
& \boldsymbol{\sigma}_i \cdot \boldsymbol{\sigma}_k \int d\mathbf{r}_{ij} e^{i\mathbf{q}_i \cdot \mathbf{r}_{ij}} Y(r_{ij}) \left(1 - e^{-\left(\frac{r_{ij}}{R_0}\right)^4}\right) \\
&= 4\pi \boldsymbol{\sigma}_i \cdot \boldsymbol{\sigma}_k \int dr_{ij} \frac{\sin(q_i r_{ij})}{q_i} \exp(-m_\pi r_{ij}) \left(1 - e^{-\left(\frac{r_{ij}}{R_0}\right)^4}\right) \\
&= 4\pi \boldsymbol{\sigma}_i \cdot \boldsymbol{\sigma}_k F_Y(q_i, R_0).
\end{aligned} \tag{E.11}$$

Putting all pieces together we find for the integral

$$\begin{aligned}
& \int d\mathbf{r}_{ij} e^{i\mathbf{q}_i \cdot \mathbf{r}_{ij}} X_{ik}(\mathbf{r}_{ij}) \\
&= -4\pi (3\boldsymbol{\sigma}_i \cdot \hat{\mathbf{q}}_i \boldsymbol{\sigma}_k \cdot \hat{\mathbf{q}}_i - \boldsymbol{\sigma}_i \cdot \boldsymbol{\sigma}_k) F_S(q_i, R_0) + 4\pi \boldsymbol{\sigma}_i \cdot \boldsymbol{\sigma}_k F_Y(q_i, R_0).
\end{aligned} \tag{E.12}$$

and

$$\begin{aligned}
V_{C, c_3, V_D, MS}^{ijk} &= \sum_{\pi(ijk)} \frac{g_A^2}{4f_\pi^4} \frac{c_3 m_\pi^2}{9} [12\pi \boldsymbol{\sigma}_i \cdot \hat{\mathbf{q}}_i \boldsymbol{\sigma}_k \cdot \hat{\mathbf{q}}_i F_S(q_i, R_0) F_{\text{cont}}(q_k, R_0) \\
&\quad - 4\pi \boldsymbol{\sigma}_i \cdot \boldsymbol{\sigma}_k F_{\text{cont}}(q_k, R_0) (F_Y(q_i, R_0) + F_S(q_i, R_0)) \\
&\quad + 12\pi \boldsymbol{\sigma}_i \cdot \hat{\mathbf{q}}_k \boldsymbol{\sigma}_k \cdot \hat{\mathbf{q}}_k F_{\text{cont}}(q_i, R_0) F_S(q_k, R_0) \\
&\quad - 4\pi \boldsymbol{\sigma}_i \cdot \boldsymbol{\sigma}_k F_{\text{cont}}(q_i, R_0) (F_S(q_k, R_0) + F_Y(q_k, R_0))] \\
&= 2 \sum_{\pi(ijk)} \frac{g_A^2}{4f_\pi^4} \frac{c_3 m_\pi^2}{9} [12\pi \boldsymbol{\sigma}_i \cdot \hat{\mathbf{q}}_i \boldsymbol{\sigma}_k \cdot \hat{\mathbf{q}}_i F_S(q_i, R_0) F_{\text{cont}}(q_k, R_0) \\
&\quad - 4\pi \boldsymbol{\sigma}_i \cdot \boldsymbol{\sigma}_k F_{\text{cont}}(q_k, R_0) (F_Y(q_i, R_0) + F_S(q_i, R_0))] .
\end{aligned} \tag{E.13}$$

For V_D the Fourier transformation is similar and only differs in the prefactor.

We will now transform the last part of V_C proportional to c_3 . It is the long-range contribution, which in coordinate space is given by

$$V_{C, c_3, \text{LR}}^{ijk} = \sum_{\pi(ijk)} \frac{g_A^2}{4f_\pi^4} \frac{m_\pi^4}{(4\pi)^2} \frac{c_3}{9} X_{ij}(\mathbf{r}_{ij}) X_{kj}(\mathbf{r}_{kj}). \tag{E.14}$$

We again do the Fourier transformation:

$$\begin{aligned}
V_{C,c_3,LR,MS}^{ijk} &= \sum_{\pi(ijk)} \frac{g_A^2}{4f_\pi^4} \frac{m_\pi^4}{(4\pi)^2} \frac{c_3}{9} \int d\mathbf{r}_{ij} e^{i\mathbf{q}_i \cdot \mathbf{r}_{ij}} X_{ij}(\mathbf{r}_{ij}) \int d\mathbf{r}_{kj} e^{i\mathbf{q}_k \cdot \mathbf{r}_{kj}} X_{kj}(\mathbf{r}_{kj}) \\
&= \sum_{\pi(ijk)} \frac{g_A^2}{4f_\pi^4} \frac{m_\pi^4}{(4\pi)^2} \frac{c_3}{9} (4\pi)^2 \left(- \left(3\boldsymbol{\sigma}_i \cdot \hat{\mathbf{q}}_i \boldsymbol{\sigma}_j \cdot \hat{\mathbf{q}}_i - \boldsymbol{\sigma}_i \cdot \boldsymbol{\sigma}_j \right) F_S(q_i, R_0) + \boldsymbol{\sigma}_i \cdot \boldsymbol{\sigma}_j F_Y(q_i, R_0) \right) \\
&\quad \times \left(- \left(3\boldsymbol{\sigma}_k \cdot \hat{\mathbf{q}}_k \boldsymbol{\sigma}_j \cdot \hat{\mathbf{q}}_k - \boldsymbol{\sigma}_k \cdot \boldsymbol{\sigma}_j \right) F_S(q_k, R_0) + \boldsymbol{\sigma}_k \cdot \boldsymbol{\sigma}_j F_Y(q_k, R_0) \right) \\
&= \sum_{\pi(ijk)} \frac{g_A^2}{4f_\pi^4} \frac{m_\pi^4}{(4\pi)^2} \frac{c_3}{9} (4\pi)^2 \left[9\boldsymbol{\sigma}_i \cdot \hat{\mathbf{q}}_i \boldsymbol{\sigma}_j \cdot \hat{\mathbf{q}}_i \boldsymbol{\sigma}_k \cdot \hat{\mathbf{q}}_k \boldsymbol{\sigma}_j \cdot \hat{\mathbf{q}}_k F_S(q_i, R_0) F_S(q_k, R_0) \right. \\
&\quad - 3\boldsymbol{\sigma}_i \cdot \hat{\mathbf{q}}_i \boldsymbol{\sigma}_j \cdot \hat{\mathbf{q}}_i \boldsymbol{\sigma}_k \cdot \boldsymbol{\sigma}_j F_S(q_i, R_0) (F_Y(q_k, R_0) + F_S(q_k, R_0)) \\
&\quad - 3\boldsymbol{\sigma}_i \cdot \boldsymbol{\sigma}_j \boldsymbol{\sigma}_k \cdot \hat{\mathbf{q}}_k \boldsymbol{\sigma}_j \cdot \hat{\mathbf{q}}_k (F_Y(q_i, R_0) + F_S(q_i, R_0)) F_S(q_k, R_0) \\
&\quad \left. + \boldsymbol{\sigma}_i \cdot \boldsymbol{\sigma}_j \boldsymbol{\sigma}_k \cdot \boldsymbol{\sigma}_j (F_Y(q_i, R_0) + F_S(q_i, R_0)) (F_Y(q_k, R_0) + F_S(q_k, R_0)) \right].
\end{aligned} \tag{E.15}$$

Using the relation $\sigma_i^\alpha \sigma_i^\beta = \delta^{\alpha\beta} + i\epsilon^{\alpha\beta\gamma} \sigma_i^\gamma$ the individual terms can be simplified. Since the terms involving vector products vanish when summing over all permutations, we arrive at

$$\begin{aligned}
V_{C,c_3,LR,MS}^{ijk} &= \sum_{\pi(ijk)} \frac{g_A^2}{4f_\pi^4} \frac{m_\pi^4}{(4\pi)^2} \frac{c_3}{9} \left[9\boldsymbol{\sigma}_i \cdot \hat{\mathbf{q}}_i \boldsymbol{\sigma}_k \cdot \hat{\mathbf{q}}_k \hat{\mathbf{q}}_i \cdot \hat{\mathbf{q}}_k F_S(q_i, R_0) F_S(q_k, R_0) \right. \\
&\quad - 3\boldsymbol{\sigma}_i \cdot \hat{\mathbf{q}}_i \boldsymbol{\sigma}_k \cdot \hat{\mathbf{q}}_i F_S(q_i, R_0) (F_Y(q_k, R_0) + F_S(q_k, R_0)) \\
&\quad - 3\boldsymbol{\sigma}_i \cdot \hat{\mathbf{q}}_k \boldsymbol{\sigma}_k \cdot \hat{\mathbf{q}}_k (F_Y(q_i, R_0) + F_S(q_i, R_0)) F_S(q_k, R_0) \\
&\quad \left. + \boldsymbol{\sigma}_i \cdot \boldsymbol{\sigma}_k (F_Y(q_i, R_0) + F_S(q_i, R_0)) (F_Y(q_k, R_0) + F_S(q_k, R_0)) \right].
\end{aligned} \tag{E.16}$$

Finally we transform the part proportional to c_1 which is given in neutron matter as

$$V_{C,c_1}^{ijk} = \sum_{\pi(ijk)} \frac{1}{2} \left(\frac{g_A}{2f_\pi} \right)^2 \left(\frac{m_\pi}{4\pi} \right)^2 \left(\frac{4c_1 m_\pi^2}{f_\pi^2} \right) (\boldsymbol{\sigma}_i \cdot \hat{\mathbf{r}}_{ij}) (\boldsymbol{\sigma}_k \cdot \hat{\mathbf{r}}_{kj}) U(r_{ij}) Y(r_{ij}) U(r_{kj}) Y(r_{kj}). \tag{E.17}$$

The Fourier transformation is given by

$$V_{C,c_1,MS}^{ijk} = \sum_{\pi(ijk)} c_1 \frac{g_A^2}{2f_\pi^4} \frac{m_\pi^4}{(4\pi)^2} \int d\mathbf{r}_{ij} e^{i\mathbf{q}_i \cdot \mathbf{r}_{ij}} \boldsymbol{\sigma}_i \cdot \hat{\mathbf{r}}_{ij} U(r_{ij}) Y(r_{ij}) \int d\mathbf{r}_{kj} e^{i\mathbf{q}_k \cdot \mathbf{r}_{kj}} \boldsymbol{\sigma}_k \cdot \hat{\mathbf{r}}_{kj} U(r_{kj}) Y(r_{kj}). \tag{E.18}$$

For the integral, we can use a similar strategy as before and rewrite the r unit vector in spherical harmonics with $l = 1$. We then find

$$\int d\mathbf{r}_{ij} e^{i\mathbf{q}_i \cdot \mathbf{r}_{ij}} \boldsymbol{\sigma}_i \cdot \hat{\mathbf{r}}_{ij} U(r_{ij}) Y(r_{ij}) = 4\pi i \boldsymbol{\sigma}_i \cdot \hat{\mathbf{q}}_i \int dr_{ij} r_{ij}^2 j_1(q_i r_{ij}) U(r_{ij}) Y(r_{ij}) = 4\pi i \boldsymbol{\sigma}_i \cdot \hat{\mathbf{q}}_i F_{c_1}(q_i). \tag{E.19}$$

We, thus, find

$$V_{C,c_1,MS}^{ijk} = - \sum_{\pi(ijk)} c_1 \frac{g_A^2}{2f_\pi^4} m_\pi^4 \boldsymbol{\sigma}_i \cdot \hat{\mathbf{q}}_i \boldsymbol{\sigma}_k \cdot \hat{\mathbf{q}}_k F_{c_1}(q_i) F_{c_1}(q_k). \tag{E.20}$$

Bibliography

- [1] J. M. Lattimer, “The nuclear equation of state and neutron star masses,” *Ann.Rev.Nucl.Part.Sci.*, vol. 62, pp. 485–515, 2012. Updated version: <http://stellarcollapse.org/nsmasses>, downloaded 03.03.2015.
- [2] P. Demorest, T. Pennucci, S. Ransom, M. Roberts, and J. Hessels, “Shapiro Delay Measurement of A Two Solar Mass Neutron Star,” *Nature*, vol. 467, pp. 1081–1083, 2010.
- [3] J. Antoniadis, P. C. Freire, N. Wex, T. M. Tauris, R. S. Lynch, *et al.*, “A Massive Pulsar in a Compact Relativistic Binary,” *Science*, vol. 340, p. 6131, 2013.
- [4] J. M. Lattimer, “Neutron stars,” *Gen.Rel.Grav.*, vol. 46, p. 1713, 2014.
- [5] A. W. Steiner, J. M. Lattimer, and E. F. Brown, “The Neutron Star Mass-Radius Relation and the Equation of State of Dense Matter,” *Astrophys.J.*, vol. 765, p. L5, 2013.
- [6] D. Page, M. Prakash, J. M. Lattimer, and A. W. Steiner, “Rapid Cooling of the Neutron Star in Cassiopeia A Triggered by Neutron Superfluidity in Dense Matter,” *Phys.Rev.Lett.*, vol. 106, p. 081101, 2011.
- [7] J. Lattimer and M. Prakash, “The physics of neutron stars,” *Science*, vol. 304, pp. 536–542, 2004.
- [8] A. B. Migdal, “Pion Fields in Nuclear Matter,” *Rev.Mod.Phys.*, vol. 50, pp. 107–172, 1978.
- [9] N. K. Glendenning and J. Schaffner-Bielich, “First order kaon condensate,” *Phys.Rev.*, vol. C60, p. 025803, 1999.
- [10] D. Voskresensky, “On the possibility of the condensation of the charged rho meson field in dense isospin asymmetric baryon matter,” *Phys.Lett.*, vol. B392, pp. 262–266, 1997.
- [11] J. M. Lattimer and F. D. Swesty, “A Generalized equation of state for hot, dense matter,” *Nucl.Phys.*, vol. A535, pp. 331–376, 1991.
- [12] S. Typel, G. Ropke, T. Klahn, D. Blaschke, and H. Wolter, “Composition and thermodynamics of nuclear matter with light clusters,” *Phys.Rev.*, vol. C81, p. 015803, 2010.
- [13] H. Shen, H. Toki, K. Oyamatsu, and K. Sumiyoshi, “Relativistic Equation of State for Core-Collapse Supernova Simulations,” *Astrophys.J.Suppl.*, vol. 197, p. 20, 2011.
- [14] G. Shen, C. Horowitz, and S. Teige, “A New Equation of State for Astrophysical Simulations,” *Phys.Rev.*, vol. C83, p. 035802, 2011.
- [15] G. Shen, C. Horowitz, and E. O’Connor, “A Second Relativistic Mean Field and Virial Equation of State for Astrophysical Simulations,” *Phys.Rev.*, vol. C83, p. 065808, 2011.
- [16] S. Gandolfi, J. Carlson, and S. Reddy, “The maximum mass and radius of neutron stars and the nuclear symmetry energy,” *Phys.Rev.*, vol. C85, p. 032801, 2012.

-
- [17] T. Krüger, I. Tews, B. Friman, K. Hebeler, and A. Schwenk, “The chiral condensate in neutron matter,” *Phys.Lett.*, vol. B726, pp. 412–416, 2013.
- [18] S. Guillot, M. Servillat, N. A. Webb, and R. E. Rutledge, “Measurement of the Radius of Neutron Stars with High S/N Quiescent Low-mass X-ray Binaries in Globular Clusters,” *Astrophys.J.*, vol. 772, p. 7, 2013.
- [19] K. O’Hara, S. Hemmer, M. Gehm, S. Granade, and J. Thomas, “Observation of a Strongly Interacting Degenerate Fermi Gas of Atoms,” *Science*, vol. 298, pp. 2179–2182, 2002.
- [20] C. Chin, R. Grimm, P. Julienne, and E. Tiesinga, “Feshbach resonances in ultracold gases,” *Rev. Mod. Phys.*, vol. 82, pp. 1225–1286, Apr 2010.
- [21] C. Chin, M. Bartenstein, A. Altmeyer, S. Riedl, S. Jochim, J. Hecker Denschlag, and R. Grimm, “Observation of the Pairing Gap in a Strongly Interacting Fermi Gas,” *Science*, vol. 305, pp. 1128–1130, 2004.
- [22] M. Zwierlein, J. Abo-Shaeer, A. Schirotzek, C. Schunck, and W. Ketterle, “Vortices and superfluidity in a strongly interacting Fermi gas,” *Nature*, vol. 435, pp. 1047–1051, 2005.
- [23] A. Gezerlis and J. Carlson, “Strongly paired fermions: Cold atoms and neutron matter,” *Phys.Rev.*, vol. C77, p. 032801, 2008.
- [24] M. Ku, A. Sommer, L. Cheuk, and M. Zwierlein, “Revealing the Superfluid Lambda Transition in the Universal Thermodynamics of a Unitary Fermi Gas,” *Science*, vol. 335, pp. 563–567, 2012.
- [25] N. Navon, S. Nascimbene, F. Chevy, and C. Salomon, “The Equation of State of a Low-Temperature Fermi Gas with Tunable Interactions,” *Science*, vol. 328, no. 5979, pp. 729–732, 2010.
- [26] L. Luo and J. Thomas, “Thermodynamic measurements in a strongly interacting Fermi gas,” *Journal of Low Temperature Physics*, vol. 154, no. 1-2, pp. 1–29, 2009.
- [27] P. Danielewicz, R. Lacey, and W. G. Lynch, “Determination of the equation of state of dense matter,” *Science*, vol. 298, pp. 1592–1596, 2002.
- [28] M. G. Endres, D. B. Kaplan, J.-W. Lee, and A. N. Nicholson, “Lattice Monte Carlo calculations for unitary fermions in a finite box,” *Phys.Rev.*, vol. A87, no. 2, p. 023615, 2013.
- [29] M. E. Burbidge, G. Burbidge, W. A. Fowler, and F. Hoyle, “Synthesis of the elements in stars,” *Rev.Mod.Phys.*, vol. 29, pp. 547–650, 1957.
- [30] P. Seeger, W. Fowler, and D. Clayton, “Nucleosynthesis of Heavy Elements by Neutron Capture,” *Ap.J.Suppl.*, vol. 11, p. 121, 1965.
- [31] D. Page and S. Reddy, “Thermal and transport properties of the neutron star inner crust,” 2012.
- [32] E. Anders and N. Grevesse, “Abundances of the elements: Meteoritic and solar,” *Geochim.Cosmochim.Acta*, vol. 53, pp. 197–214, 1989.

-
- [33] A. Arcones and F. K. Thielemann, “Neutrino-driven wind simulations and nucleosynthesis of heavy elements,” *J. Phys.*, vol. G40, p. 013201, 2013.
- [34] F. Wienholtz, D. Beck, K. Blaum, C. Borgmann, M. Breitenfeldt, *et al.*, “Masses of exotic calcium isotopes pin down nuclear forces,” *Nature*, vol. 498, no. 7454, pp. 346–349, 2013.
- [35] K. Hebeler, J. Holt, J. Menéndez, and A. Schwenk, “Nuclear forces and their impact on neutron-rich nuclei and neutron-rich matter,” *Annu.Rev.Nucl.Part.Sci.*, vol. xx, p. zz, 2015.
- [36] E. Epelbaum, H.-W. Hammer, and U.-G. Meissner, “Modern Theory of Nuclear Forces,” *Rev.Mod.Phys.*, vol. 81, pp. 1773–1825, 2009.
- [37] R. Machleidt and D. Entem, “Chiral effective field theory and nuclear forces,” *Phys.Rept.*, vol. 503, pp. 1–75, 2011.
- [38] N. Kalantar-Nayestanaki, E. Epelbaum, J. Messchendorp, and A. Nogga, “Signatures of three-nucleon interactions in few-nucleon systems,” *Rept.Prog.Phys.*, vol. 75, p. 016301, 2012.
- [39] B. R. Barrett, P. Navratil, and J. P. Vary, “Ab initio no core shell model,” *Prog.Part.Nucl.Phys.*, vol. 69, pp. 131–181, 2013.
- [40] R. Roth, J. Langhammer, A. Calci, S. Binder, and P. Navratil, “Similarity-Transformed Chiral NN+3N Interactions for the Ab Initio Description of 12-C and 16-O,” *Phys.Rev.Lett.*, vol. 107, p. 072501, 2011.
- [41] E. Epelbaum, H. Krebs, D. Lee, and U.-G. Meissner, “Ab initio calculation of the Hoyle state,” *Phys.Rev.Lett.*, vol. 106, p. 192501, 2011.
- [42] E. Epelbaum, H. Krebs, T. A. Lähde, D. Lee, U.-G. Meißner, *et al.*, “Ab Initio Calculation of the Spectrum and Structure of ^{16}O ,” *Phys.Rev.Lett.*, vol. 112, no. 10, p. 102501, 2014.
- [43] T. Otsuka, T. Suzuki, J. D. Holt, A. Schwenk, and Y. Akaishi, “Three-body forces and the limit of oxygen isotopes,” *Phys.Rev.Lett.*, vol. 105, p. 032501, 2010.
- [44] J. D. Holt, T. Otsuka, A. Schwenk, and T. Suzuki, “Three-body forces and shell structure in calcium isotopes,” *J.Phys.*, vol. G39, p. 085111, 2012.
- [45] J. Holt, J. Menendez, and A. Schwenk, “The role of three-nucleon forces and many-body processes in nuclear pairing,” *J.Phys.*, vol. G40, p. 075105, 2013.
- [46] G. Hagen, M. Hjorth-Jensen, G. Jansen, R. Machleidt, and T. Papenbrock, “Continuum effects and three-nucleon forces in neutron-rich oxygen isotopes,” *Phys.Rev.Lett.*, vol. 108, p. 242501, 2012.
- [47] G. Hagen, M. Hjorth-Jensen, G. Jansen, R. Machleidt, and T. Papenbrock, “Evolution of shell structure in neutron-rich calcium isotopes,” *Phys.Rev.Lett.*, vol. 109, p. 032502, 2012.
- [48] R. Roth, S. Binder, K. Vobig, A. Calci, J. Langhammer, *et al.*, “Ab Initio Calculations of Medium-Mass Nuclei with Normal-Ordered Chiral NN+3N Interactions,” *Phys.Rev.Lett.*, vol. 109, p. 052501, 2012.

-
- [49] H. Hergert, S. Bogner, S. Binder, A. Calci, J. Langhammer, *et al.*, “In-Medium Similarity Renormalization Group with Chiral Two- Plus Three-Nucleon Interactions,” *Phys.Rev.*, vol. C87, no. 3, p. 034307, 2013.
 - [50] S. Bogner, H. Hergert, J. Holt, A. Schwenk, S. Binder, *et al.*, “Nonperturbative shell-model interactions from the in-medium similarity renormalization group,” *Phys.Rev.Lett.*, vol. 113, p. 142501, 2014.
 - [51] V. Somà, A. Cipollone, C. Barbieri, P. Navrátil, and T. Duguet, “Chiral two- and three-nucleon forces along medium-mass isotope chains,” *Phys.Rev.*, vol. C89, no. 6, p. 061301, 2014.
 - [52] N. Kaiser, S. Fritsch, and W. Weise, “Chiral dynamics and nuclear matter,” *Nucl.Phys.*, vol. A697, pp. 255–276, 2002.
 - [53] E. Epelbaum, H. Krebs, D. Lee, and U.-G. Meissner, “Ground state energy of dilute neutron matter at next-to-leading order in lattice chiral effective field theory,” *Eur.Phys.J.*, vol. A40, pp. 199–213, 2009.
 - [54] K. Hebeler and A. Schwenk, “Chiral three-nucleon forces and neutron matter,” *Phys.Rev.*, vol. C82, p. 014314, 2010.
 - [55] K. Hebeler, S. Bogner, R. Furnstahl, A. Nogga, and A. Schwenk, “Improved nuclear matter calculations from chiral low-momentum interactions,” *Phys.Rev.*, vol. C83, p. 031301, 2011.
 - [56] K. Hebeler, J. Lattimer, C. Pethick, and A. Schwenk, “Constraints on neutron star radii based on chiral effective field theory interactions,” *Phys.Rev.Lett.*, vol. 105, p. 161102, 2010.
 - [57] I. Tews, T. Krüger, K. Hebeler, and A. Schwenk, “Neutron matter at next-to-next-to-next-to-leading order in chiral effective field theory,” *Phys.Rev.Lett.*, vol. 110, no. 3, p. 032504, 2013.
 - [58] J. Holt, N. Kaiser, and W. Weise, “Chiral Fermi liquid approach to neutron matter,” *Phys.Rev.*, vol. C87, no. 1, p. 014338, 2013.
 - [59] E. Epelbaum, W. Glockle, and U.-G. Meissner, “The Two-nucleon system at next-to-next-to-next-to-leading order,” *Nucl.Phys.*, vol. A747, pp. 362–424, 2005.
 - [60] D. Entem and R. Machleidt, “Accurate charge dependent nucleon nucleon potential at fourth order of chiral perturbation theory,” *Phys.Rev.*, vol. C68, p. 041001, 2003.
 - [61] G. Hagen, T. Papenbrock, M. Hjorth-Jensen, and D. Dean, “Coupled-cluster computations of atomic nuclei,” *Rept.Prog.Phys.*, vol. 77, no. 9, p. 096302, 2014.
 - [62] H.-W. Hammer, A. Nogga, and A. Schwenk, “Three-body forces: From cold atoms to nuclei,” *Rev.Mod.Phys.*, vol. 85, p. 197, 2013.
 - [63] D. Ceperley, “Path integrals in the theory of condensed helium,” *Rev.Mod.Phys.*, vol. 67, pp. 279–355, 1995.

-
- [64] J. Carlson, S. Gandolfi, and A. Gezerlis, “Quantum Monte Carlo approaches to nuclear and atomic physics,” *PTEP*, vol. 2012, p. 01A209, 2012.
 - [65] J. Carlson, S. Gandolfi, F. Pederiva, S. C. Pieper, R. Schiavilla, *et al.*, “Quantum Monte Carlo methods for nuclear physics,” 2014.
 - [66] G. Wlazlowski and P. Magierski, “Quantum Monte Carlo study of dilute neutron matter at finite temperatures,” *Phys.Rev.*, vol. C83, p. 012801, 2011.
 - [67] A. Gezerlis, “Spin-polarized low-density neutron matter,” *Phys.Rev.*, vol. C83, p. 065801, 2011.
 - [68] A. Gezerlis and R. Sharma, “Phase separation in low-density neutron matter,” *Phys.Rev.*, vol. C85, p. 015806, 2012.
 - [69] B. Pudliner, V. Pandharipande, J. Carlson, S. C. Pieper, and R. B. Wiringa, “Quantum Monte Carlo calculations of nuclei with $A \leq 7$,” *Phys.Rev.*, vol. C56, pp. 1720–1750, 1997.
 - [70] S. C. Pieper, “Quantum Monte Carlo calculations of light nuclei,” *Riv.Nuovo Cim.*, vol. 31, pp. 709–740, 2008.
 - [71] M. Ulybyshev and M. Katsnelson, “Magnetism and interaction-induced gap opening in graphene with vacancies or hydrogen adatoms: Quantum Monte Carlo study,” *Phys.Rev.Lett.*, vol. 114, no. 24, p. 246801, 2015.
 - [72] J. Kolorenc and L. Mitas, “Applications of quantum Monte Carlo methods in condensed systems,” *Rept.Prog.Phys.*, vol. 74, p. 026502, 2011.
 - [73] K. M. Nollett, S. C. Pieper, R. B. Wiringa, J. Carlson, and G. Hale, “Quantum Monte Carlo calculations of neutron-alpha scattering,” *Phys.Rev.Lett.*, vol. 99, p. 022502, 2007.
 - [74] J. Carlson, “Green’s function Monte Carlo study of light nuclei,” *Phys.Rev.*, vol. C36, pp. 2026–2033, 1987.
 - [75] S. C. Pieper and R. B. Wiringa, “Quantum Monte Carlo calculations of light nuclei,” *Ann.Rev.Nucl.Part.Sci.*, vol. 51, pp. 53–90, 2001.
 - [76] A. Lovato, S. Gandolfi, R. Butler, J. Carlson, E. Lusk, *et al.*, “Charge Form Factor and Sum Rules of Electromagnetic Response Functions in ^{12}C ,” *Phys.Rev.Lett.*, vol. 111, no. 9, p. 092501, 2013.
 - [77] K. Schmidt and S. Fantoni, “A quantum Monte Carlo method for nucleon systems,” *Phys.Lett.*, no. B446, pp. 99–103, 1999.
 - [78] M. Freunek, “Nucleon-nucleon interaction in chiral effective field theory in configuration space,” Master’s thesis, Universität Bonn and Forschungszentrum Jülich, 2007.
 - [79] S. Gandolfi, J. Carlson, and S. C. Pieper, “Cold neutrons trapped in external fields,” *Phys.Rev.Lett.*, vol. 106, p. 012501, 2011.
 - [80] N. Chamel, S. Goriely, and J. Pearson, “Further explorations of Skyrme-Hartree-Fock-Bogoliubov mass formulas. IX. Constraint of pairing force to S(0)-1 neutron-matter gap,” *Nucl.Phys.*, vol. A812, pp. 72–98, 2008.

-
- [81] K. Hebeler, J. Lattimer, C. Pethick, and A. Schwenk, “Equation of state and neutron star properties constrained by nuclear physics and observation,” *Astrophys.J.*, vol. 773, p. 11, 2013.
- [82] L. D. Landau, “On the theory of stars,” *Phys.Z. Sowjetunion*, vol. 1, p. 285, 1932.
- [83] J. Chadwick, “Possible Existence of a Neutron,” *Nature*, vol. 129, p. 312, 1932.
- [84] W. Baade and F. Zwicky, “On Super-novae,” *Phys.Rev.*, vol. 45, p. 138, 1934.
- [85] A. Hewish, S. Bell, J. Pilkington, P. Scott, and R. Collins, “Observation of a rapidly pulsating radio source,” *Nature*, vol. 217, pp. 709–713, 1968.
- [86] P. Haensel, A. Y. Potekhin, and D. Yakovlev, *Neutron Stars 1*. Springer, 2007.
- [87] S. Chandrasekhar, “The maximum mass of ideal white dwarfs,” *Astrophys.J.*, vol. 74, pp. 81–82, 1931.
- [88] H.-T. Janka, K. Langanke, A. Marek, G. Martinez-Pinedo, and B. Mueller, “Theory of Core-Collapse Supernovae,” *Phys.Rept.*, vol. 442, pp. 38–74, 2007.
- [89] H.-T. Janka, “Explosion mechanisms of core-collapse supernovae,” *Annual Review of Nuclear and Particle Science*, vol. 62, no. 1, pp. 407–451, 2012.
- [90] R. C. Tolman, “Static solutions of Einstein’s field equations for spheres of fluid,” *Phys.Rev.*, vol. 55, pp. 364–373, 1939.
- [91] J. Oppenheimer and G. Volkoff, “On Massive neutron cores,” *Phys.Rev.*, vol. 55, pp. 374–381, 1939.
- [92] C. Drischler, “Asymmetric nuclear matter based on chiral effective fieldtheory interactions,” Master’s thesis, Technische Universität Darmstadt, 1998.
- [93] F. Weber, “Strange quark matter and compact stars,” *Prog.Part.Nucl.Phys.*, vol. 54, pp. 193–288, 2005.
- [94] W. Becker, *Neutron Stars and Pulsars*. Springer, 2009.
- [95] A. Dieperink and C. Korpa, “Nuclear constraints on the EoS and rotating neutron stars,” *J.Phys.Conf.Ser.*, vol. 496, p. 012004, 2014.
- [96] J. Aasi *et al.*, “Advanced LIGO,” *Class.Quant.Grav.*, vol. 32, p. 074001, 2015.
- [97] A. Bauswein and H.-T. Janka, “Measuring neutron-star properties via gravitational waves from binary mergers,” *Phys.Rev.Lett.*, vol. 108, p. 011101, 2012.
- [98] A. Bauswein, H. Janka, K. Hebeler, and A. Schwenk, “Equation-of-state dependence of the gravitational-wave signal from the ring-down phase of neutron-star mergers,” *Phys.Rev.*, vol. D86, p. 063001, 2012.
- [99] A. Bauswein, N. Stergioulas, and H.-T. Janka, “Revealing the high-density equation of state through binary neutron star mergers,” *Phys.Rev.*, vol. D90, no. 2, p. 023002, 2014.

-
- [100] J. Weisberg, D. Nice, and J. Taylor, “Timing Measurements of the Relativistic Binary Pulsar PSR B1913+16,” *Astrophys.J.*, vol. 722, pp. 1030–1034, 2010.
- [101] M. Kramer, I. H. Stairs, R. Manchester, M. McLaughlin, A. Lyne, *et al.*, “Tests of general relativity from timing the double pulsar,” *Science*, vol. 314, pp. 97–102, 2006.
- [102] M. Burgay, N. D’Amico, A. Possenti, R. Manchester, A. Lyne, *et al.*, “An Increased estimate of the merger rate of double neutron stars from observations of a highly relativistic system,” *Nature*, vol. 426, pp. 531–533, 2003.
- [103] A. Lyne, M. Burgay, M. Kramer, A. Possenti, R. Manchester, *et al.*, “A Double - pulsar system - A Rare laboratory for relativistic gravity and plasma physics,” *Science*, vol. 303, pp. 1153–1157, 2004.
- [104] G. Israel, T. Belloni, L. Stella, Y. Rephaeli, D. Gruber, *et al.*, “Discovery of rapid x-ray oscillations in the tail of the SGR 1806-20 hyperflare,” *Astrophys.J.*, vol. 628, pp. L53–L56, 2005.
- [105] T. E. Strohmayer and A. L. Watts, “Discovery of fast x-ray oscillations during the 1998 giant flare from SGR 1900+14,” *Astrophys.J.*, vol. 632, pp. L111–L114, 2005.
- [106] A. L. Watts and T. E. Strohmayer, “Detection with rhessi of high frequency x-ray oscillations in the tail of the 2004 hyperflare from sgr 1806-20,” *Astrophys.J.*, vol. 637, pp. L117–L120, 2006.
- [107] T. E. Strohmayer and A. L. Watts, “The 2004 Hyperflare from SGR 1806-20: Further Evidence for Global Torsional Vibrations,” *Astrophys.J.*, vol. 653, pp. 593–601, 2006.
- [108] A. W. Steiner and A. L. Watts, “Constraints on Neutron Star Crusts From Oscillations in Giant Flares,” *Phys.Rev.Lett.*, vol. 103, p. 181101, 2009.
- [109] K. Gendreau, Z. Arzoumanian, and T. Okaajima, “The Neutron star Interior Composition ExploreR (NICER): an Explorer mission of opportunity for soft x-ray timing spectroscopy,” *Proc. SPIE*, vol. 8443, p. 844313, 2012.
- [110] Z. Arzoumanian *et al.*, “The neutron star interior composition explorer (NICER): mission definition ,” *Proc. SPIE*, vol. 9144, p. 914420, 2014.
- [111] J. Erler, N. Birge, M. Kortelainen, W. Nazarewicz, E. Olsen, A. Perhac, and M. Stoitsov, “The limits of the nuclear landscape,” *Nature*, vol. 486, pp. 509–512, 2012.
- [112] C. Weizsäcker, “Zur Theorie der Kernmassen,” *Zeitschrift für Physik*, vol. 96, no. 7-8, pp. 431–458, 1935.
- [113] H. A. Bethe and R. F. Bacher, “Nuclear physics a. stationary states of nuclei,” *Rev. Mod. Phys.*, vol. 8, pp. 82–229, Apr 1936.
- [114] D. Steppenbeck, S. Takeuchi, N. Aoi, P. Doornenbal, M. Matsushita, *et al.*, “Evidence for a new nuclear ‘magic number’ from the level structure of ^{54}Ca ,” *Nature*, vol. 502, no. 7470, pp. 207–210, 2013.
- [115] M. Arnould and S. Goriely, “The p-process of stellar nucleosynthesis: astrophysics and nuclear physics status,” *Physics Reports*, vol. 384, no. 1–2, pp. 1 – 84, 2003.

-
- [116] P. Merrill, “Spectroscopic observations of stars of Class-S,” *Astrophys. J.*, vol. 116, p. 21, 1952.
 - [117] F.-K. Thielemann, A. Arcones, R. Käppeli, M. Liebendörfer, T. Rauscher, C. Winteler, C. Fröhlich, I. Dillmann, T. Fischer, G. Martinez-Pinedo, K. Langanke, K. Farouqi, K.-L. Kratz, I. Panov, and I. Korneev, “What are the astrophysical sites for the r-process and the production of heavy elements?,” *Progress in Particle and Nuclear Physics*, vol. 66, no. 2, pp. 346 – 353, 2011. Particle and Nuclear Astrophysics International Workshop on Nuclear Physics, 32nd Course.
 - [118] A. Akmal, V. Pandharipande, and D. Ravenhall, “The Equation of state of nucleon matter and neutron star structure,” *Phys.Rev.*, vol. C58, pp. 1804–1828, 1998.
 - [119] J. Lattimer and M. Prakash, “Neutron star structure and the equation of state,” *Astrophys.J.*, vol. 550, p. 426, 2001.
 - [120] C. Drischler, V. Soma, and A. Schwenk, “Microscopic calculations and energy expansions for neutron-rich matter,” *Phys.Rev.*, vol. C89, no. 2, p. 025806, 2014.
 - [121] J. M. Lattimer and Y. Lim, “Constraining the Symmetry Parameters of the Nuclear Interaction,” *Astrophys.J.*, vol. 771, p. 51, 2013.
 - [122] M. Centelles, X. Roca-Maza, X. Vinas, and M. Warda, “Origin of the neutron skin thickness of 208Pb in nuclear mean-field models,” *Phys.Rev.*, vol. C82, p. 054314, 2010.
 - [123] A. Meucci, M. Vorabbi, C. Giusti, and P. Finelli, “Neutron density distribution and neutron skin thickness of ^{208}Pb ,” *Phys.Rev.*, vol. C90, no. 2, p. 027301, 2014.
 - [124] S. Abrahamyan, Z. Ahmed, H. Albataineh, K. Aniol, D. Armstrong, *et al.*, “Measurement of the Neutron Radius of 208Pb Through Parity-Violation in Electron Scattering,” *Phys.Rev.Lett.*, vol. 108, p. 112502, 2012.
 - [125] J. Zenihiro, H. Sakaguchi, T. Murakami, M. Yosoi, Y. Yasuda, *et al.*, “Neutron density distributions of Pb-204, Pb-206, Pb-208 deduced via proton elastic scattering at $E_p=295$ MeV,” *Phys.Rev.*, vol. C82, p. 044611, 2010.
 - [126] C. Tarbert, D. Watts, D. Glazier, P. Aguar, J. Ahrens, *et al.*, “Neutron skin of ^{208}Pb from Coherent Pion Photoproduction,” *Phys.Rev.Lett.*, vol. 112, no. 24, p. 242502, 2014.
 - [127] A. Klimkiewicz *et al.*, “Nuclear symmetry energy and neutron skins derived from pygmy dipole resonances,” *Phys. Rev.*, vol. C76, p. 051603, 2007.
 - [128] D. Rossi, P. Adrich, F. Aksouh, H. Alvarez-Pol, T. Aumann, *et al.*, “Measurement of the Dipole Polarizability of the Unstable Neutron-Rich Nucleus Ni68,” *Phys.Rev.Lett.*, vol. 111, no. 24, p. 242503, 2013.
 - [129] P. Souder *et al.* *PREX-II, Proposal to Jefferson Lab PAC 38*, vol. <http://hallaweb.jlab.org/parity/prex/prexII.pdf>.
 - [130] J. Schwinger *Phys.Rev.*, vol. 72, p. 742A, 1947.
 - [131] G. Baker, “Recent Progress in Many-Body Theories: The proceedings of the 10th International Conference,” Seattle, USA, September 10-15, 1999.

-
- [132] G. Zürn, T. Lompe, A. N. Wenz, S. Jochim, P. S. Julienne, and J. M. Hutson, “Precise characterization of ^6Li feshbach resonances using trap-sideband-resolved rf spectroscopy of weakly bound molecules,” *Phys. Rev. Lett.*, vol. 110, p. 135301, Mar 2013.
- [133] F. Wilczek, “Resonating with Feshbach,” *MIT Phys. Annu. 2006*, p. 32, 2006.
- [134] R. Machleidt, Q. MacPherson, E. Marji, R. Winzer, C. Zeoli, *et al.*, “Recent Progress in the Theory of Nuclear Forces,” 2012.
- [135] P. F. Bedaque and U. van Kolck, “Effective field theory for few nucleon systems,” *Ann.Rev.Nucl.Part.Sci.*, vol. 52, pp. 339–396, 2002.
- [136] E. Epelbaum, H.-W. Hammer, and U.-G. Meissner, “Modern Theory of Nuclear Forces,” *Rev.Mod.Phys.*, vol. 81, pp. 1773–1825, 2009.
- [137] D. Entem and R. Machleidt, “Accurate charge dependent nucleon nucleon potential at fourth order of chiral perturbation theory,” *Phys.Rev.*, vol. C68, p. 041001, 2003.
- [138] R. Machleidt and D. Entem, “Chiral effective field theory and nuclear forces,” *Phys.Rept.*, vol. 503, pp. 1–75, 2011.
- [139] S. Wong, *Introductory Nuclear Physics*. John Wiley & Sons, Inc., New York, 1998.
- [140] D. B. Kaplan, “Five lectures on effective field theory,” *nucl-th/0510023*, 2005.
- [141] W. Weise, “Nuclear chiral dynamics and phases of QCD,” *Prog.Part.Nucl.Phys.*, vol. 67, pp. 299–311, 2012.
- [142] A. Kurkela, E. S. Fraga, J. Schaffner-Bielich, and A. Vuorinen, “Constraining neutron star matter with Quantum Chromodynamics,” *Astrophys.J.*, vol. 789, p. 127, 2014.
- [143] S. Durr, Z. Fodor, J. Frison, C. Hoelbling, R. Hoffmann, *et al.*, “Ab-Initio Determination of Light Hadron Masses,” *Science*, vol. 322, pp. 1224–1227, 2008.
- [144] A. Kurkela, P. Romatschke, and A. Vuorinen, “Cold Quark Matter,” *Phys.Rev.*, vol. D81, p. 105021, 2010.
- [145] E. S. Fraga, A. Kurkela, and A. Vuorinen, “Interacting quark matter equation of state for compact stars,” *Astrophys.J.*, vol. 781, no. 2, p. L25, 2014.
- [146] K. G. Wilson, “Confinement of Quarks,” *Phys.Rev.*, vol. D10, pp. 2445–2459, 1974.
- [147] S. Beane, W. Detmold, K. Orginos, and M. Savage, “Nuclear Physics from Lattice QCD,” *Prog.Part.Nucl.Phys.*, vol. 66, pp. 1–40, 2011.
- [148] S. Beane *et al.*, “Light Nuclei and Hypernuclei from Quantum Chromodynamics in the Limit of SU(3) Flavor Symmetry,” *Phys.Rev.*, vol. D87, no. 3, p. 034506, 2013.
- [149] S. Beane *et al.*, “Nucleon-Nucleon Scattering Parameters in the Limit of SU(3) Flavor Symmetry,” *Phys.Rev.*, vol. C88, no. 2, p. 024003, 2013.
- [150] S. Beane, E. Chang, S. Cohen, W. Detmold, H. Lin, *et al.*, “Magnetic moments of light nuclei from lattice quantum chromodynamics,” *Phys.Rev.Lett.*, vol. 113, no. 25, p. 252001, 2014.

-
- [151] E. Epelbaum, “Few-nucleon forces and systems in chiral effective field theory,” *Prog.Part.Nucl.Phys.*, vol. 57, pp. 654–741, 2006.
- [152] N. Barnea, L. Contessi, D. Gazit, F. Pederiva, and U. van Kolck, “Effective Field Theory for Lattice Nuclei,” *Phys.Rev.Lett.*, vol. 114, no. 5, p. 052501, 2015.
- [153] J. Holt, J. Menendez, and A. Schwenk, “Chiral three-nucleon forces and bound excited states in neutron-rich oxygen isotopes,” *Eur.Phys.J.*, vol. A49, p. 39, 2013.
- [154] S. C. Pieper, R. B. Wiringa, and J. Carlson, “Quantum Monte Carlo calculations of excited states in $A = 6 - 8$ nuclei,” *Phys.Rev.*, vol. C70, p. 054325, 2004.
- [155] S. König, H. W. Griedhammer, and H. W. Hammer, “The proton-deuteron system in pionless EFT revisited,” *J.Phys.*, vol. G42, p. 045101, 2015.
- [156] S. Weinberg, “Phenomenological Lagrangians,” *Physica*, vol. A96, p. 327, 1979.
- [157] S. Weinberg, “Nuclear forces from chiral Lagrangians,” *Phys.Lett.*, vol. B251, pp. 288–292, 1990.
- [158] S. Weinberg, “Effective chiral Lagrangians for nucleon - pion interactions and nuclear forces,” *Nucl.Phys.*, vol. B363, pp. 3–18, 1991.
- [159] S. Weinberg, “Three body interactions among nucleons and pions,” *Phys.Lett.*, vol. B295, pp. 114–121, 1992.
- [160] U. van Kolck, “Few nucleon forces from chiral Lagrangians,” *Phys.Rev.*, vol. C49, pp. 2932–2941, 1994.
- [161] H. Krebs, A. Gasparyan, and E. Epelbaum, “Chiral three-nucleon force at N^4 LO I: Longest-range contributions,” *Phys.Rev.*, vol. C85, p. 054006, 2012.
- [162] S. Fiorilla, N. Kaiser, and W. Weise, “Chiral thermodynamics of nuclear matter,” *Nucl.Phys.*, vol. A880, pp. 65–87, 2012.
- [163] V. Bernard, E. Epelbaum, H. Krebs, and U.-G. Meissner, “Subleading contributions to the chiral three-nucleon force II: Short-range terms and relativistic corrections,” *Phys.Rev.*, vol. C84, p. 054001, 2011.
- [164] H. Krebs, A. Gasparyan, and E. Epelbaum, “Chiral three-nucleon force at N^4 LO II: Intermediate-range contributions,” *Phys.Rev.*, vol. C87, no. 5, p. 054007, 2013.
- [165] S. Kolling, E. Epelbaum, H. Krebs, and U.-G. Meissner, “Two-pion exchange electromagnetic current in chiral effective field theory using the method of unitary transformation,” *Phys.Rev.*, vol. C80, p. 045502, 2009.
- [166] S. Kolling, E. Epelbaum, H. Krebs, and U.-G. Meissner, “Two-nucleon electromagnetic current in chiral effective field theory: One-pion exchange and short-range contributions,” *Phys.Rev.*, vol. C84, p. 054008, 2011.
- [167] S. Weinberg, “Effective chiral Lagrangians for nucleon - pion interactions and nuclear forces,” *Nucl.Phys.*, vol. B363, pp. 3–18, 1991.

-
- [168] N. Fettes, U.-G. Meissner, and S. Steininger, “Pion - nucleon scattering in chiral perturbation theory. 1. Isospin symmetric case,” *Nucl.Phys.*, vol. A640, pp. 199–234, 1998.
 - [169] E. Epelbaum, U.-G. Meissner, and W. Gloeckle, “Nuclear forces in the chiral limit,” *Nucl.Phys.*, vol. A714, pp. 535–574, 2003.
 - [170] N. Kaiser, R. Brockmann, and W. Weise, “Peripheral nucleon-nucleon phase shifts and chiral symmetry,” *Nucl.Phys.*, vol. A625, pp. 758–788, 1997.
 - [171] E. Epelbaum, W. Gloeckle, and U.-G. Meissner, “Improving the convergence of the chiral expansion for nuclear forces. 1. Peripheral phases,” *Eur.Phys.J.*, vol. A19, pp. 125–137, 2004.
 - [172] V. Bernard, N. Kaiser, and U.-G. Meissner, “Chiral dynamics in nucleons and nuclei,” *Int.J.Mod.Phys.*, vol. E4, pp. 193–346, 1995.
 - [173] E. Epelbaum, A. Nogga, W. Gloeckle, H. Kamada, U. G. Meissner, *et al.*, “Three nucleon forces from chiral effective field theory,” *Phys.Rev.*, vol. C66, p. 064001, 2002.
 - [174] V. Bernard, E. Epelbaum, H. Krebs, and U.-G. Meissner, “Subleading contributions to the chiral three-nucleon force. I. Long-range terms,” *Phys.Rev.*, vol. C77, p. 064004, 2008.
 - [175] V. Bernard, E. Epelbaum, H. Krebs, and U.-G. Meissner, “Subleading contributions to the chiral three-nucleon force II: Short-range terms and relativistic corrections,” *Phys.Rev.*, vol. C84, p. 054001, 2011.
 - [176] P. Navratil, “Local three-nucleon interaction from chiral effective field theory,” *Few Body Syst.*, vol. 41, pp. 117–140, 2007.
 - [177] M. Hjorth-Jensen, T. Kuo, and E. Osnes, “Realistic effective interactions for nuclear systems,” *Phys.Rept.*, vol. 261, pp. 125–270, 1995.
 - [178] A. Gezerlis and J. Carlson, “Low-density neutron matter,” *Phys.Rev.*, vol. C81, p. 025803, 2010.
 - [179] C. Drischler, K. Hebeler, and A. Schwenk, *in preparation*.
 - [180] J. Holt, J. Menendez, J. Simonis, and A. Schwenk, “Three-nucleon forces and spectroscopy of neutron-rich calcium isotopes,” *Phys.Rev.*, vol. C90, no. 2, p. 024312, 2014.
 - [181] A. Gallant, J. Bale, T. Brunner, U. Chowdhury, S. Ettenauer, *et al.*, “New precision mass measurements of neutron-rich calcium and potassium isotopes and three-nucleon forces,” *Phys.Rev.Lett.*, vol. 109, p. 032506, 2012.
 - [182] W. Dickhoff and C. Barbieri, “Selfconsistent Green’s function method for nuclei and nuclear matter,” *Prog.Part.Nucl.Phys.*, vol. 52, pp. 377–496, 2004.
 - [183] C. Barbieri and M. Hjorth-Jensen, “Quasiparticle and quasihole states of nuclei around Ni-56,” *Phys.Rev.*, vol. C79, p. 064313, 2009.
 - [184] V. Soma, T. Duguet, and C. Barbieri, “Ab-initio self-consistent Gorkov-Green’s function calculations of semi-magic nuclei. I. Formalism at second order with a two-nucleon interaction,” *Phys.Rev.*, vol. C84, p. 064317, 2011.

-
- [185] V. Soma, C. Barbieri, and T. Duguet, “Ab-initio Gorkov-Green’s function calculations of open-shell nuclei,” *Phys.Rev.*, vol. C87, no. 1, p. 011303, 2013.
- [186] K. Tsukiyama, S. Bogner, and A. Schwenk, “In-Medium Similarity Renormalization Group for Nuclei,” *Phys.Rev.Lett.*, vol. 106, p. 222502, 2011.
- [187] H. Hergert, S. Bogner, S. Binder, A. Calci, J. Langhammer, *et al.*, “In-Medium Similarity Renormalization Group with Chiral Two- Plus Three-Nucleon Interactions,” *Phys.Rev.*, vol. C87, no. 3, p. 034307, 2013.
- [188] H. Hergert, S. Binder, A. Calci, J. Langhammer, and R. Roth, “Ab Initio Calculations of Even Oxygen Isotopes with Chiral Two-Plus-Three-Nucleon Interactions,” *Phys.Rev.Lett.*, vol. 110, no. 24, p. 242501, 2013.
- [189] R. Roth, “Importance Truncation for Large-Scale Configuration Interaction Approaches,” *Phys.Rev.*, vol. C79, p. 064324, 2009.
- [190] N. Barnea, W. Leidemann, and G. Orlandini, “Ground state wave functions in the hyper-spherical formalism for nuclei with A greater than 4,” *Nucl.Phys.*, vol. A650, pp. 427–442, 1999.
- [191] G. Baardsen, A. Ekström, G. Hagen, and M. Hjorth-Jensen, “Coupled-cluster studies of infinite nuclear matter,” *Phys.Rev.*, vol. C88, p. 054312, 2013.
- [192] G. Hagen, T. Papenbrock, A. Ekström, K. Wendt, G. Baardsen, *et al.*, “Coupled-cluster calculations of nucleonic matter,” *Phys.Rev.*, vol. C89, no. 1, p. 014319, 2014.
- [193] A. Carbone, A. Rios, and A. Polls, “Symmetric nuclear matter with chiral three-nucleon forces in the self-consistent Green’s functions approach,” *Phys.Rev.*, vol. C88, p. 044302, 2013.
- [194] A. Carbone, A. Rios, and A. Polls, “Correlated density-dependent chiral forces for infinite matter calculations within the Green’s function approach,” *Phys.Rev.*, vol. C90, no. 5, p. 054322, 2014.
- [195] S. C. Pieper, “Quantum Monte Carlo calculations of light nuclei,” *Nucl.Phys.*, vol. A751, pp. 516–532, 2005.
- [196] M. Kalos, “Monte Carlo Calculations of the Ground State of Three- and Four-Body Nuclei,” *Phys.Rev.*, vol. 128, p. 1732, 1962.
- [197] R. B. Wiringa, V. Stoks, and R. Schiavilla, “An Accurate nucleon-nucleon potential with charge independence breaking,” *Phys.Rev.*, vol. C51, pp. 38–51, 1995.
- [198] R. B. Wiringa and S. C. Pieper, “Evolution of nuclear spectra with nuclear forces,” *Phys.Rev.Lett.*, vol. 89, p. 182501, 2002.
- [199] B. Pudliner, V. Pandharipande, J. Carlson, and R. B. Wiringa, “Quantum Monte Carlo calculations of $A \leq 6$ nuclei,” *Phys.Rev.Lett.*, vol. 74, pp. 4396–4399, 1995.
- [200] S. C. Pieper, V. Pandharipande, R. B. Wiringa, and J. Carlson, “Realistic models of pion exchange three nucleon interactions,” *Phys.Rev.*, vol. C64, p. 014001, 2001.

-
- [201] M. Suzuki, “On the convergence of exponential operators- the Zassenhaus formula, BCH formula and systematic approximants,” *Comm. Math. Phys.*, vol. 57, pp. 193–200, 1977.
- [202] J. Lynn and K. Schmidt, “Real-Space Imaginary-Time Propagators for Non-Local Nucleon-Nucleon Potentials,” *Phys.Rev.*, vol. C86, p. 014324, 2012.
- [203] S. Gandolfi, *The Auxiliary Field Diffusion Monte Carlo Method for Nuclear Physics and Nuclear Astrophysics*. PhD thesis, University of Trento, 2007.
- [204] K. Schmidt and M. Kalos, *Applications of the Monte Carlo method in statistical physics, Topics in Applied Physics N.36*. Springer, New York, 1984.
- [205] J. Anderson, “Quantum Chemistry by Random Walk,” *J.Chem.Phys.*, vol. 65, pp. 4121–4127, 1976.
- [206] S. Zhang, J. Carlson, and J. Gubernatis, “Constrained Path Quantum Monte Carlo Method for Fermion Ground States,” *Phys.Rev.Lett.*, vol. 74, pp. 3652–3655, 1995.
- [207] S. Zhang, J. Carlson, and J. Gubernatis, “A Constrained path Monte Carlo method for fermion ground states,” *Phys.Rev.*, vol. B55, p. 7464, 1997.
- [208] S. Zhang and H. Krakauer, “Quantum Monte Carlo method using phase-free random walks with Slater determinants,” *Phys.Rev.Lett.*, vol. 90, p. 136401, 2003.
- [209] N. Metropolis, A. Rosenbluth, M. Rosenbluth, A. Teller, and E. Teller, “Equation of state calculations by fast computing machines,” *J.Chem.Phys.*, vol. 21, pp. 1087–1092, 1953.
- [210] A. Sarsa, S. Fantoni, K. Schmidt, and F. Pederiva, “Neutron matter at zero temperature with auxiliary field diffusion Monte Carlo,” *Phys.Rev.*, vol. C68, p. 024308, 2003.
- [211] S. Gandolfi, A. Y. Illarionov, K. Schmidt, F. Pederiva, and S. Fantoni, “Quantum Monte Carlo calculation of the equation of state of neutron matter,” *Phys.Rev.*, vol. C79, p. 054005, 2009.
- [212] S. Gandolfi, A. Lovato, J. Carlson, and K. E. Schmidt, “From the lightest nuclei to the equation of state of asymmetric nuclear matter with realistic nuclear interactions,” *Phys.Rev.*, vol. C90, no. 6, p. 061306, 2014.
- [213] A. Gezerlis, I. Tews, E. Epelbaum, S. Gandolfi, K. Hebeler, *et al.*, “Quantum Monte Carlo Calculations with Chiral Effective Field Theory Interactions,” *Phys.Rev.Lett.*, vol. 111, no. 3, p. 032501, 2013.
- [214] V. G. Stoks, R. Timmermans, and J. de Swart, “On the pion - nucleon coupling constant,” *Phys.Rev.*, vol. C47, pp. 512–520, 1993.
- [215] A. Lovato, S. Gandolfi, J. Carlson, S. C. Pieper, and R. Schiavilla, “Neutral weak current two-body contributions in inclusive scattering from ^{12}C ,” *Phys.Rev.Lett.*, vol. 112, no. 18, p. 182502, 2014.
- [216] P. Magierski, G. Wlazlowski, A. Bulgac, and J. E. Drut, “The Finite Temperature Pairing Gap of a Unitary Fermi Gas by Quantum Monte Carlo,” *Phys.Rev.Lett.*, vol. 103, p. 210403, 2009.

-
- [217] A. Roggero, A. Mukherjee, and F. Pederiva, “Quantum Monte Carlo calculations of neutron matter with non-local chiral interactions,” *Phys.Rev.Lett.*, vol. 112, p. 221103, 2014.
- [218] K. Wendt, R. Furnstahl, and S. Ramanan, “Local Projections of Low-Momentum Potentials,” *Phys.Rev.*, vol. C86, p. 014003, 2012.
- [219] A. Gezerlis, I. Tews, E. Epelbaum, M. Freunek, S. Gandolfi, *et al.*, “Local chiral effective field theory interactions and quantum Monte Carlo applications,” *Phys.Rev.*, vol. C90, no. 5, p. 054323, 2014.
- [220] E. Epelbaum, H. Krebs, and U. Meißner, “Improved chiral nucleon-nucleon potential up to next-to-next-to-next-to-leading order,” *Eur.Phys.J.*, vol. A51, no. 5, p. 53, 2015.
- [221] E. Epelbaum, H. Krebs, and U. G. Meißner, “Precision nucleon-nucleon potential at fifth order in the chiral expansion,” 2014.
- [222] G. Lepage, “How to renormalize the Schrodinger equation,” *nucl-th/9706029*, pp. 135–180, 1997.
- [223] A. Nogga, R. Timmermans, and U. van Kolck, “Renormalization of one-pion exchange and power counting,” *Phys.Rev.*, vol. C72, p. 054006, 2005.
- [224] B. Long and C. Yang, “Short-range nuclear forces in singlet channels,” *Phys.Rev.*, vol. C86, p. 024001, 2012.
- [225] J. Kirscher, H. W. Griesshammer, D. Shukla, and H. M. Hofmann, “Universal Correlations in Pion-less EFT with the Resonating Group Model: Three and Four Nucleons,” *Eur.Phys.J.*, vol. A44, pp. 239–256, 2010.
- [226] A. Lacour, J. Oller, and U.-G. Meissner, “Non-perturbative methods for a chiral effective field theory of finite density nuclear systems,” *Annals Phys.*, vol. 326, pp. 241–306, 2011.
- [227] E. Oset, A. Martinez Torres, K. Khemchandani, L. Roca, and J. Yamagata, “Two, three, many body systems involving mesons,” *Prog.Part.Nucl.Phys.*, vol. 67, pp. 455–460, 2012.
- [228] E. Epelbaum and U.-G. Meissner, “Isospin-violating nucleon-nucleon forces using the method of unitary transformation,” *Phys.Rev.*, vol. C72, p. 044001, 2005.
- [229] M. Piarulli, L. Girlanda, R. Schiavilla, R. Navarro Pérez, J. Amaro, *et al.*, “Minimally non-local nucleon-nucleon potentials with chiral two-pion exchange including Δ resonances,” *Phys.Rev.*, vol. C91, no. 2, p. 024003, 2015.
- [230] V. Baru, E. Epelbaum, C. Hanhart, M. Hoferichter, A. Kudryavtsev, *et al.*, “The Multiple-scattering series in pion-deuteron scattering and the nucleon-nucleon potential: Perspectives from effective field theory,” *Eur.Phys.J.*, vol. A48, p. 69, 2012.
- [231] M. Rentmeester, R. Timmermans, J. L. Friar, and J. de Swart, “Chiral two pion exchange and proton proton partial wave analysis,” *Phys.Rev.Lett.*, vol. 82, pp. 4992–4995, 1999.
- [232] E. Marji, A. Canul, Q. MacPherson, R. Winzer, C. Zeoli, *et al.*, “Nonperturbative renormalization of the chiral nucleon-nucleon interaction up to next-to-next-to-leading order,” *Phys.Rev.*, vol. C88, no. 5, p. 054002, 2013.

-
- [233] E. Epelbaum and J. Gegelia, “Regularization, renormalization and ‘peratization’ in effective field theory for two nucleons,” *Eur.Phys.J.*, vol. A41, pp. 341–354, 2009.
 - [234] C. Zeoli, R. Machleidt, and D. Entem, “Infinite-cutoff renormalization of the chiral nucleon-nucleon interaction at N^3LO ,” *Few Body Syst.*, vol. 54, pp. 2191–2205, 2013.
 - [235] E. Epelbaum, W. Gloeckle, and U.-G. Meissner, “Improving the convergence of the chiral expansion for nuclear forces. 2. Low phases and the deuteron,” *Eur.Phys.J.*, vol. A19, pp. 401–412, 2004.
 - [236] R. Timmermans, T. Rijken, and J. de Swart, “Determination of the charged pion coupling constant from data on the charge exchange reaction anti-p p \rightarrow anti-n n,” *Phys.Rev.Lett.*, vol. 67, pp. 1074–1077, 1991.
 - [237] V. Baru, C. Hanhart, M. Hoferichter, B. Kubis, A. Nogga, *et al.*, “Precision calculation of the π^- -deuteron scattering length and its impact on threshold pi-N scattering,” *Phys.Lett.*, vol. B694, pp. 473–477, 2011.
 - [238] V. Stoks, R. Kompl, M. Rentmeester, and J. de Swart, “Partial wave analysis of all nucleon-nucleon scattering data below 350-MeV,” *Phys.Rev.*, vol. C48, pp. 792–815, 1993.
 - [239] A. Ekström, G. Baardsen, C. Forssén, G. Hagen, M. Hjorth-Jensen, *et al.*, “Optimized Chiral Nucleon-Nucleon Interaction at Next-to-Next-to-Leading Order,” *Phys.Rev.Lett.*, vol. 110, no. 19, p. 192502, 2013.
 - [240] A. Ekström, G. Jansen, K. Wendt, G. Hagen, T. Papenbrock, and others, “Effects of three-nucleon forces and two-body currents on Gamow-Teller strengths,” *Phys.Rev.Lett.*, vol. 113, no. 26, p. 262504, 2014.
 - [241] R. Navarro Perez, J. Amaro, and E. Ruiz Arriola, “Statistical error analysis for phenomenological nucleon-nucleon potentials,” *Phys.Rev.*, vol. C89, no. 6, p. 064006, 2014.
 - [242] R. Navarro Pérez, J. Amaro, and E. Ruiz Arriola, “Error analysis of nuclear forces and effective interactions,” *J.Phys.*, vol. G42, no. 3, p. 034013, 2015.
 - [243] C. V. D. Leun and C. Alderliesten, “The deuteron binding energy,” *Nuclear Physics A*, vol. 380, no. 2, pp. 261 – 269, 1982.
 - [244] P. J. Mohr, B. N. Taylor, and D. B. Newell, “CODATA Recommended Values of the Fundamental Physical Constants: 2006,” *Rev.Mod.Phys.*, vol. 80, pp. 633–730, 2008.
 - [245] D. M. Bishop and L. M. Cheung, “Quadrupole moment of the deuteron from a precise calculation of the electric field gradient in D-2,” *Phys.Rev.*, vol. A20, pp. 381–384, 1979.
 - [246] N. Rodning and L. Knutson, “Asymptotic D-state to S-state ratio of the deuteron,” *Phys.Rev.*, vol. C41, pp. 898–909, 1990.
 - [247] G. Simon, C. Schmitt, and V. Walther, “Elastic Electric and Magnetic eD Scattering at Low Momentum Transfer,” *Nucl.Phys.*, vol. A364, pp. 285–296, 1981.
 - [248] T. E. O. Ericson and M. Rosa-Clot, “The Deuteron Asymptotic D State as a Probe of the Nucleon-nucleon Force,” *Nucl.Phys.*, vol. A405, p. 497, 1983.

-
- [249] J. Carlson, J. Morales, J., V. Pandharipande, and D. Ravenhall, “Quantum Monte Carlo calculations of neutron matter,” *Phys.Rev.*, vol. C68, p. 025802, 2003.
- [250] I. Tews, T. Krüger, A. Gezerlis, K. Hebeler, and A. Schwenk, “Neutron matter with chiral EFT interactions: Perturbative and first QMC calculations,” p. 302, 2013.
- [251] J. Lynn, J. Carlson, E. Epelbaum, S. Gandolfi, A. Gezerlis, *et al.*, “Quantum Monte Carlo Calculations of Light Nuclei Using Chiral Potentials,” *Phys.Rev.Lett.*, vol. 113, no. 19, p. 192501, 2014.
- [252] A. Lovato, O. Benhar, S. Fantoni, and K. E. Schmidt, “Comparative study of three-nucleon potentials in nuclear matter,” *Phys.Rev.*, vol. C85, p. 024003, 2012.
- [253] J. Lynn, I. Tews, J. Carlson, S. Gandolfi, A. Gezerlis, K. Schmidt, and A. Schwenk, “Chiral three-nucleon interactions in light nuclei, neutron- α scattering, and neutron matter,” *arXiv:1509.03470*, 2015.
- [254] R. Furnstahl and A. Dyhdalo , *private communications*.
- [255] F. Sammarruca, L. Coraggio, J. Holt, N. Itaco, R. Machleidt, *et al.*, “Toward order-by-order calculations of the nuclear and neutron matter equations of state in chiral effective field theory,” *Phys.Rev.*, vol. C91, no. 5, p. 054311, 2015.
- [256] H. Potter, S. Fischer, P. Maris, J. Vary, S. Binder, *et al.*, “Ab Initio study of neutron drops with chiral Hamiltonians,” *Phys.Lett.*, vol. B739, pp. 445–450, 2014.

Curriculum Vitae

Name: Ingo Tews
Date of Birth: November 12, 1986
Place of Birth: Greifswald, Germany
Citizenship: German

Employment:

since 2012 Research associate (2/3 E13) at Technische Universität Darmstadt

Education:

since 2012 Ph.D. research in physics at Technische Universität Darmstadt
Supervisor: Achim Schwenk

2011-2012 Master's studies in physics at Technische Universität Darmstadt,
Master's degree with Honors (final mark: 1.0),
Thesis: *Chiral three-nucleon forces at next-to-next-to-next-to-leading order
in nucleonic matter*,
Advisor: Achim Schwenk

2007-2010 Bachelor's studies in physics at Technische Universität Darmstadt,
Bachelor's degree (final mark: 1.1),
Thesis: *Deconvolution of (γ, n) cross sections from experiments
with bremsstrahlung photons*,
Supervisor: Norbert Pietralla

1997-2006 Alexander-von-Humboldt Gymnasium Greifswald,
Abitur (final mark: 1.2)

Awards and Honors:

2014 Our Quantum Monte Carlo studies were part of the "John von Neumann
Excellence Project 2014" of the John von Neumann-Institute for Computing,
FZ Jülich

2013 M.Sc. Research Prize of the Gerhard-Herzberg-Gesellschaft, Darmstadt,
for the best Master's thesis

2006 School award of the Alexander-von-Humboldt Gymnasium, Greifswald,
for the best Abitur results

Teaching Activities:

- | | |
|------|---|
| 2014 | Tutor for statistical mechanics at Technische Universität Darmstadt |
| 2010 | Tutor for linear algebra at Technische Universität Darmstadt |

Collaboration Visits:

- | | |
|------|--|
| 2014 | Visitor, Theory Division, Los Alamos National Laboratory, New Mexico, USA
March 24 - April 11 |
|------|--|

Schools and Training Programs:

- | | |
|------|--|
| 2013 | ECT* Doctoral Training Program 2013: Neutron-rich matter:
constraints from nuclear physics and astrophysics,
April 2013, Trento, Italy |
| 2012 | National Nuclear Physics Summer School 2012,
July 2012, Santa Fe, New Mexico, USA |

Memberships:

Member of the German Physical Society since 2006

Erklärung zur Dissertation

Hiermit versichere ich, die vorliegende Dissertation ohne Hilfe Dritter nur mit den angegebenen Quellen und Hilfsmitteln angefertigt zu haben. Alle Stellen, die aus Quellen entnommen wurden, sind als solche kenntlich gemacht. Diese Arbeit hat in gleicher oder ähnlicher Form noch keiner Prüfungsbehörde vorgelegen.

Darmstadt, den 15.10.2015

(Ingo Tews)